University of Bath

PHD

Low Temperature Precursors for SnOx Thin Films

Wildsmith, Thomas

Award date:
2014

Awarding institution:
University of Bath

Link to publication

Alternative formats
If you require this document in an alternative format, please contact:
openaccess@bath.ac.uk

Copyright of this thesis rests with the author. Access is subject to the above licence, if given. If no licence is specified above, original content in this thesis is licensed under the terms of the Creative Commons Attribution-NonCommercial 4.0 International (CC BY-NC-ND 4.0) Licence (https://creativecommons.org/licenses/by-nc-nd/4.0/). Any third-party copyright material present remains the property of its respective owner(s) and is licensed under its existing terms.

Take down policy
If you consider content within Bath's Research Portal to be in breach of UK law, please contact: openaccess@bath.ac.uk with the details. Your claim will be investigated and, where appropriate, the item will be removed from public view as soon as possible.

Download date: 05. May. 2023

Low Temperature Precursors for SnO_x Thin Films

Thomas Wildsmith

A thesis submitted for the degree of Doctor of Philosophy

University of Bath

Department of Chemistry

September 2014

COPYRIGHT

Attention is drawn to the fact that copyright of this thesis rests with the author. A copy of this thesis has been supplied on condition that anyone who consults it is understood to recognise that its copyright rests with the author and that they must not copy it or use material from it except as permitted by law or with the consent of the author.

This thesis may be made available for consultation within the University Library and may be photocopied or lent to other libraries for the purposes of consultation.

THOMAS WILDSMTH

Abstract

The work in this thesis describes the attempts to synthesise precursors for the formation of tin oxide thin films.

Chapter 1-Introduction

Chapter 1 is intended to provide a brief background to both tin(II) and tin(IV) oxide thin films and the numerous applications that they can be utilised in. Brief discussions on the different deposition techniques utilised to grow thin films of metal oxide materials is given along with the introduction of the concept and application of chemical vapour deposition. A review of tin oxide precursors presented in the literature is also provided, along with short review of the ligand systems that are investigated further in this thesis.

Chapter 2-Heterocumulene insertions into tin(II) amide bonds

Detailed descriptions of the synthesis, characterisation and precursor evaluation of tin(II) ureate compounds are presented in this chapter. The results of the precursor evaluation were used to select compound **4** for aerosol-assisted chemical vapour deposition studies. The deposited thin films are evaluated using a range of microscopy techniques including scanning electron microscopy, x-ray diffraction analysis and x-ray photoelectron spectroscopy.

Chapter 3- Tin(II) alkoxides

This chapter focuses on the synthesis, characterisation and precursor evaluation of tin(II) alkoxide compounds as potential precursors. Following evaluation three of the tin(II) alkoxide compounds were investigated using aerosol-assisted chemical vapour deposition and the deposited films were evaluated using a range of microscopy techniques.

Chapter 4 - Heterocumulene insertions into tin(II) alkoxide bonds

This chapter centres on the reactivity of tin(II) alkoxides with a range of heterocumulene compounds with the intention of forming a new set of tin oxide chemical vapour deposition precursors. The compounds reported are split into groups according to the type of heterocumulene used in the reaction, and are characterised and evaluated as potential tin

oxide precursors. Deposition studies are also included for compound which exhibited interesting behaviour in the thermogravimetric studies. The deposited films are characterised using a range of microscopy techniques including Raman spectroscopy and energy dispersive X-ray spectroscopy.

Chapter 5 - Conclusions

A brief summary of the work carried out is presented, and conclusions are drawn to compare the different ligand systems utilised in the chemical vapour deposition experiments. A short discussion on potential future investigations is also presented

Chapter 6 - Further work

A discussion about potential research that could be carried out following on from this research.

Declaration

The work described in this thesis was conducted by the author at the University of Bath between October 2010 and October 2013. It represents the author's original and independent work, except where specific reference is made to the contrary. Neither the whole nor part of this thesis has been submitted previously in support of a degree at this or any other university.

Acknowledgments

I would firstly like to thank my supervisor Professor Michael Hill for all the help, encouragement and useful discussions about the work presented within this thesis. I was fortunate to also have the wisdom and guidance of two other academic supervisors with Professor Kieran Molloy providing his wealth of knowledge and experience within the field of tin and materials chemistry and Dr. Andrew Johnson providing the opportunity for numerous discussions and also sorting out the crystals that were investigated by X-ray diffraction - including all of the duds.

Thanks go to the both EPSRC for funding me through the DTC in sustainable chemical technologies and SAFC Hi-Tech who provided financial assistance and advice. In particular I would like Dr. Andrew Kingsley who helped set up the project with SAFC Hi-Tech and Dr. Stephen Richards who helped immensely when at Bath, and again when he moved to SAFC. I would like to highlight my thanks to the DTC for funding several conference trips, I have been very fortunate to attend conferences in France, Greece, Canada and the UK due to their assistance. I would also like to thank the Worshipful Company of Armourers' and Braziers' and the RSC for the travel bursaries I was fortunate to receive.

From a technical viewpoint I would also like to thank Dr. John Lowe for all of his assistance with the NMR spectroscopy - particularly helping me get to the bottom of some rather complex 2D experiments that would have not been possible without his assistance. I would also like to thank Dr. John Mitchel and the rest of the staff at the microscopy analytical suite in physics for training me on the various different machines and tolerating my numerous questions.

I would like to acknowledge all the support and help I received from the 13 other students that formed the inaugural cohort within the DTC - looking back it has been a fun four years that would not have been the same without you guys! Many thanks are also due to the Hill, Molloy and Johnson research groups who have both put up with me and worked alongside me for the past few years. I am particularly grateful for all the useful discussions (and often coffee) with those working on similar projects both past and present and have really valued your input.

Finally I should probably thank Laura, who has nagged at me for the last four years to get things finished, but has also kept me fed and watered and generally looked after me and put up with a ridiculous commute so we could live together (her choice!).

Compound Key

1

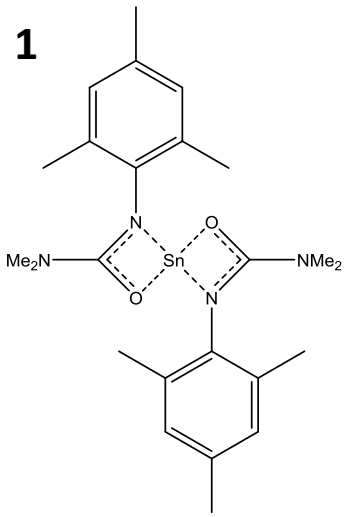

2

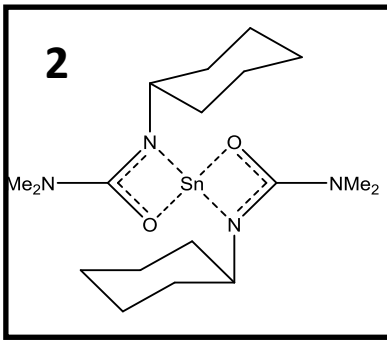

3

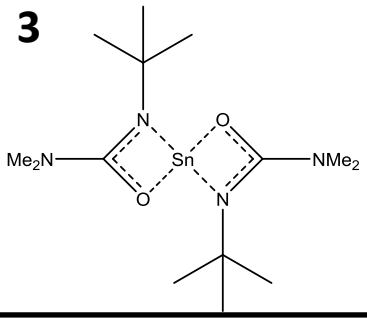

4

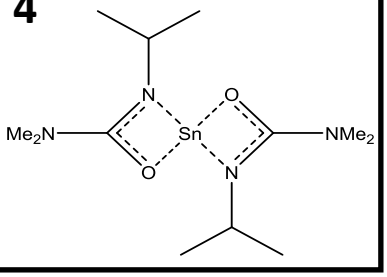

LXXXII

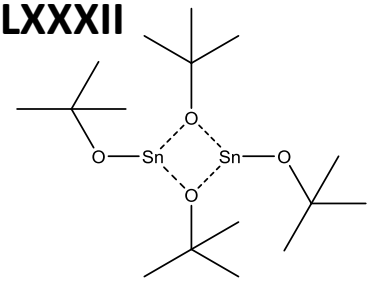

5

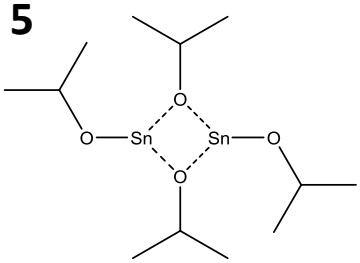

6

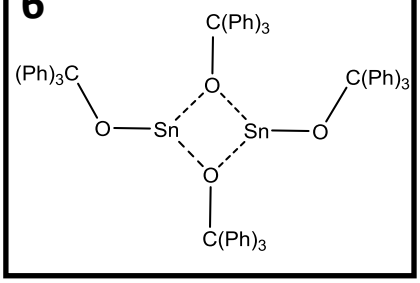

7

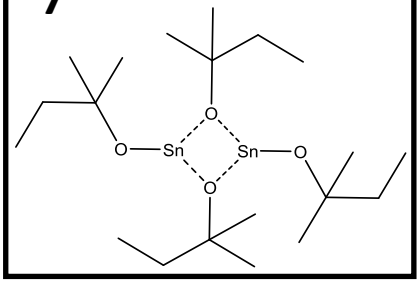

8

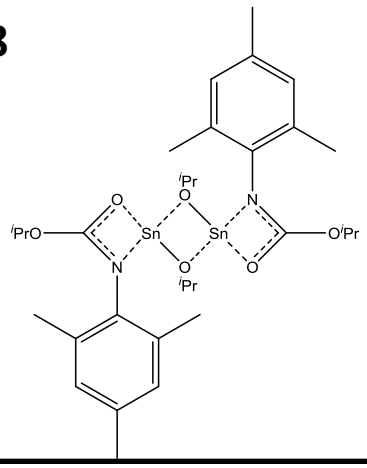

9

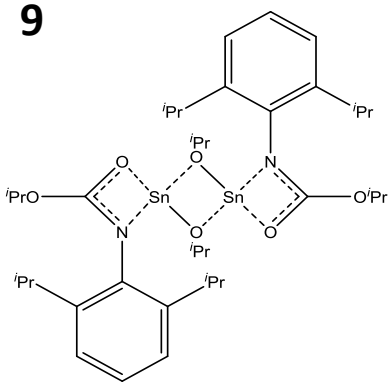

10

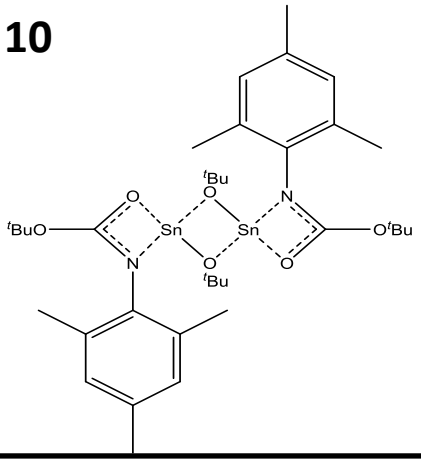

11

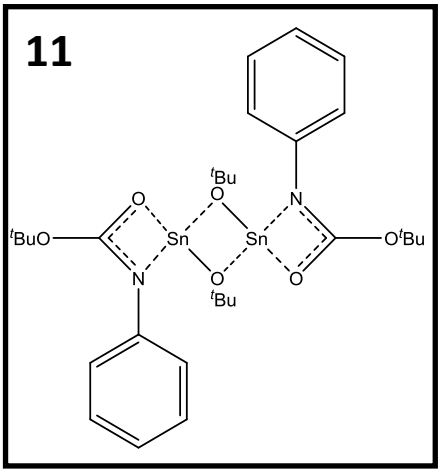

12

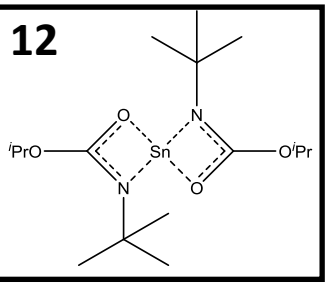

13

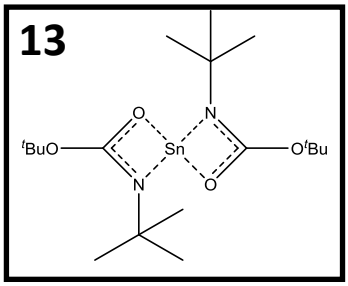

14

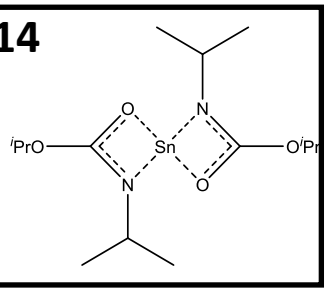

15

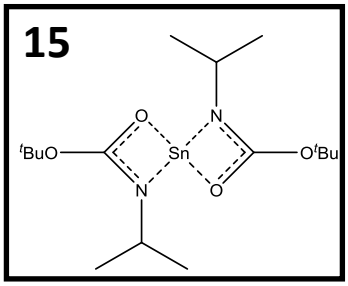

16

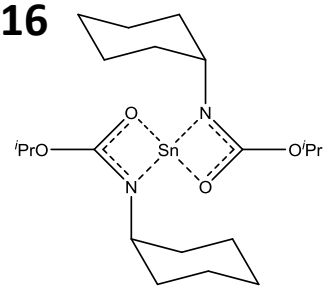
O
N
iPrO
Sn
OiPr
N
O

17

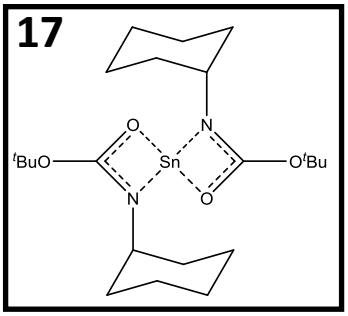
O
N
tBuO
Sn
OtBu
N
O

18

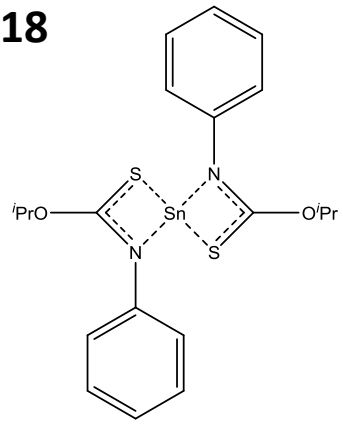
S
N
iPrO
Sn
OiPr
N
S

19

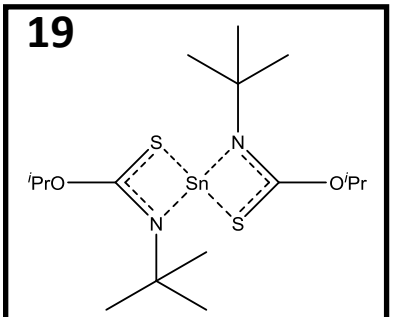
S
N
iPrO
Sn
OiPr
N
S

Abbreviations

α: alpha

Å: Angstrom, 10^{-10} metres

AACVD: Aerosol Assisted Chemical Vapour Deposition

ALD: Atomic Layer Deposition

APCVD: Atmospheric Pressure Chemical Vapour Deposition

ASU: Asymmetric Unit

AFM: Atomic Force Microscopy

β: beta

^{i}Bu: *iso*-butyl, $CH(CH_3)_2CH_3$

^{n}Bu: *n*-butyl, $CH_2CH_2CH_2CH_3$

^{t}Bu: *tertiary*-butyl, $C(CH_3)_3$

C: Celsius (unit of temperature)

cal: calorie (unit of energy)

CB: conduction band

CVD: Chemical Vapour Deposition

Cy: Cyclohexyl

°: Degree

δ: delta, Chemical Shift

d: Doublet

EDS: Electron-Dispersive X-ray Spectroscopy

Et: ethyl, CH_2CH_3

FTO: Fluorine doped tin oxide

ITO: Tin doped indium oxide

IUPAC: International Union of Pure and Applied Chemistry

J: Joule (unit of energy)

K: Kelvin (unit temperature)

LED: Light Emitting Diode

LPCVD: Low Pressure Chemical Vapour Deposition

μ: mu

μm: micro-metre, 10^{-6} metres

m: Multiplet

mbar: millibar, unit of pressure

Me: methyl, CH_3

Mes: mesityl, 2, 4, 6-trimethylphenyl

m.p.: melting point

MOCVD: Metal Organic Chemical Vapour Deposition

mol: mole

Mol: molarity, moles/litre

mmol: millimole

n-type: negative charge carrying semiconductor

nm: Nanometre, 10^{-9} m

NMR: Nuclear Magnetic Resonance

%: Percentage

p-type: positive charge carrying semiconductor

PLD: Pulsed Laser Deposition

PECVD: Plasma Enhanced Chemical Vapour Deposition

^{t}Pentyl: *tertiary*-pentyl, $CH(CH_3)_2CH_2CH_3$

^{i}Pr: *iso*-propyl, $CH(CH_3)_2$

Ph: Phenyl, C_6H_5

ppm: Parts Per Million

PVD: Physical Vapour Deposition

PXRD: Powder X-ray Diffraction

q: Quartet

R_f: fluorinated alkyl group

RF: Radio Frequency

s: Singlet

SEM: Scanning Electron Microscopy

sept: Septet

t: Triplet

TCO: Transparent Conducting Oxide

TGA: Thermogravimetric Analysis

VB: Valence Band

XPS: X-ray Photoelectron Spectroscopy

XRD: X-ray Diffraction

Contents

1. Introduction

Metal oxides are compounds composed of metal atoms and oxygen. Many metals exist in nature as native metal oxide ores; aluminium oxide is a widely abundant example accounting for 15.9% of the earth's crust. The high natural abundance of metal oxides is due to the formation of stable chemical bonds between the electronegative oxygen atoms and the metal. The majority of metals can readily oxidise to metal oxide materials in the presence of oxygen, for example chromium oxidises in air readily forming a protective metal oxide layer. The rate of oxidation can be enhanced by the presence of water, as exhibited by iron which oxidises much more readily in hydrated environments. This enhanced rate of oxidation can be attributed to the formation of hydroxyl groups on the surface.

Metal oxides tend to adopt primarily ionic structures with metal-oxygen-metal crosslinks which in many instances creates an insoluble material in most solvents. Many metal oxide materials are, however, susceptible to attack by acids and bases

The IUPAC suggests using Stock's nomenclature for metal oxides with the compound named metal (n) oxide where n is the oxidation state of the metal, usually expressed in Roman numerals.

The use and application of metal oxide thin films is a long established but still growing market, particularly in the microelectronics industry where metal oxides are used as components in new computer memories, capacitors, transistors and as semiconducting materials. Metal oxide thin films also see widespread use as functional coatings for glass, including as self-cleaning glass systems, for durability enhancement and as low emissivity coatings for energy efficient glass installations.

1.1 Semiconductors

Many metal oxide materials exhibit semiconducting properties which can be exploited in a wide range of micro-electronics applications. A selection of metal oxide semiconductors are shown in Table 1.1.

Table 1.1: Selected semiconductor materials along with current applications and band-gap measurements

Material	Band-gap (eV)	Application	Ref
ZnO	3.27	*n*-type semiconductor, photovoltaics	[1]
TiO_2	3-3.2	*n*-type semiconductor, photocatalyst	[2]
Cu_2O	2.3	*n*-type semiconductor, optics, diodes	[3]
CuO	1.2-1.6	*p*-type semiconductor, photovoltaics	[3]
UO_2	2.1-2.7	Dielectric layer, thermoelectric	[4]
Bi_2O_3	2.7-3.5	*n*-type semiconductor, Optical coatings, optoelectronics	[5]
SnO_2	3.7	*n*-type semiconductor, photovoltaics, glass coatings	[6]
SnO	2.6-3.20	*p*-type semiconductor, TFTs	[7]
In_2O_3	3.6	*n*-type semiconductor,	[8]
NiO	3.4-3.58	*p*-type semiconductor, barrier layer in organic photovoltaic devices.	[9]

Semiconductors are so called because they have both conducting and insulating properties. A conducting material has a very low gap between the valence band (VB) and the conduction bands (CB) which means that little or no energy is required to promote electrons from the valence to the conduction band. Insulators have a much greater energy gap between the valence and conduction bands – high enough for few, if any, electrons to transfer across and so insulating a material. Semiconductors have small energy gaps between the valence and conduction band (Figure 1.1), and when subjected to enough energy will become conducting; this could be thermal energy, electrical energy, or photonic energy. Semi-conductors can be classified on whether they are an electron or hole carrier. Electron carrying systems are referred to as *n*-type semiconductors, while hole carrying systems are denoted as *p*-type semiconductors. Materials with *n*-type character tend to have been doped with electron rich elements, such as fluorine. This creates a surplus of electrons, and also provides a diffusion route for electrons to move through the crystal lattice. The opposite is true for *p*-type oxide materials, where the film is doped with electron deficient elements such

as boron. This creates a deficit of electrons throughout the material, allowing the material to be a hole transporter.

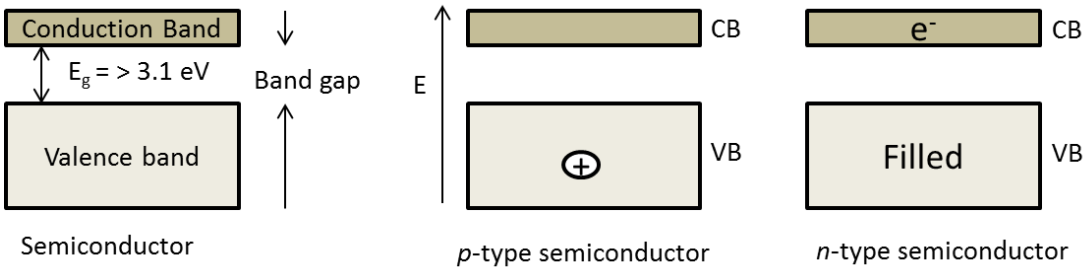

Figure 1.1: Simplified diagram showing how the electronic structures of n and p-type semiconductors differ.

There is already widespread use of *n*-type materials in commercial devices, such as solar cells and touch screen technologies; the common transparent conducting oxides (TCOs) in Tables 1.2 and 1.3 all exhibit *n*-type conductivity. For metal oxides that exhibit p-type conductivity the options are reduced to materials based upon NiO,[10] CuO[3] and SnO.[11] The fundamental reason for a low number of candidates for p-type TCOs with high mobilities is the location of the oxygen 2p levels within the metal oxide. For many metal oxide materials the O2p orbitals generally lie in a lower energy level than the valence band of the metallic atoms.[12–14] If a positive hole is introduced into the system this localises on a single oxygen atom. This localisation results in limited or no migration of holes throughout the crystal lattice. The location of the O2p orbital is due to the ionic nature of metal oxide materials. Introduction of covalency into the metal oxygen bond would result in the difference between O2p and metallic valence band being reduced, potentially reducing the localisation of holes onto individual oxygen atoms. To maintain transparency the metal atom is also required to have a closed electronic configuration to avoid colouration caused by d-d transistions.[13] Therefore the ideal metal cation will have a closed electronic configuration with the uppermost energy level lying close to that of the O2p levels allowing the formation of bonds with some covalency (Figure 1.2).[13]

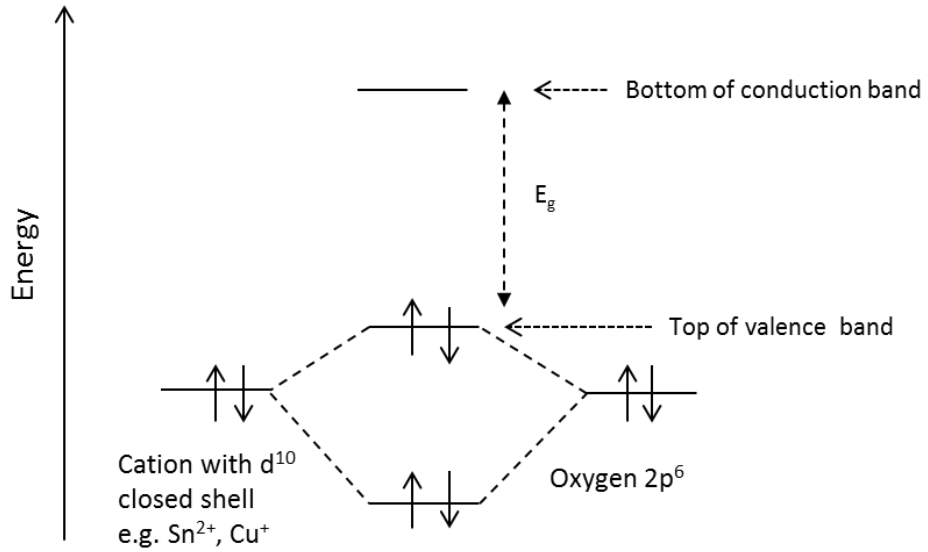

Figure 1.2: Schematic illustration of the bonding between an oxide ion and a closed shell cation

The introduction of $CuAlO_2$ delafossite materials with good *p*-type conductivity (9.5×10^{-1} S cm^{-1}) and visible light optical transparency (80%) by Kawazoe and co-workers demonstrated that this method could result in the formation of good *p*-type conductors.[15] The high mobility was explained by the hybridisation of the Cu^{+} closed shell $3d^{10}$ electrons with the oxygen orbitals and led to the investigation of other copper based delafossite structures including $CuCrO_2$,[16] $SrCu_2O_2$[17,18] and LaCuOS.[19]

1.2 Transparent conducting oxides

A class of metal oxide that has generated wide interest is that of the transparent conducting oxides (TCO). TCOs exhibit a combination of high optical transparency and high electrical conductivity making them an unusual group of materials, particularly as these characteristics are generally thought of as mutually exclusive. There is a wide range of applications for TCO materials, from use in optics and microelectronics through to their application as coatings in architectural glass.[20–22]

1.2.1 Electrical and optical properties

The unique properties observed for TCOs arise from a combination of a sufficiently large energy band gap in excess of 3.1 eV, which prevents absorption of visible light, coupled with a good concentration of electron or hole carriers that have a sufficient range of mobility allowing the conduction of electricity. Carrier concentrations in excess of 10^{19} cm^{-3} and mobilities greater than $1cm^2$ $V^{-1}s^{-1}$ provide sufficient electrical conduction for a TCO material to be viable.[22]

A quantitative comparison of TCOs can be made by measuring the visible absorption coefficient (σ) and the electrical conductivity (α) and the ratio α/σ. A good TCO will have a high electrical conductivity and a low visible light absorption, therefore the greater the α/σ ratio the more effective the TCO will be. Equation 1 shows the relationship between α and σ is related to both the sheet resistance (Rs), the total visible transmission (T) and the total visible reflectance (R).[22]

$$\frac{\alpha}{\sigma} = -\{Rs \ln(T + R)\} - 1 \quad (1)$$

The ratio for some selected TCO materials is shown in Table 1.2. Based on this figure of merit fluorine doped zinc oxide and cadmium stannate are the best TCO materials; while the ratio of indium doped zinc oxide is the lowest. It should be noted that the α/σ ratio is also proportional to the thickness of the film, with the ratio decreasing as the thickness of the film increases. This is due to the increased chance of light scattering by the individual crystal grains situated within the film.[22]

Table 1.2: Some common TCO materials and their α/σ ratio

Material	α/σ ratio value
ZnO:F	7
ZnO:Al	5
Cd_2SnO_4	7
SnO_2:F	3
In_2O_3:Sn	4
ZnO:In	0.2

The most common TCO materials are based on indium oxide In_2O_3, tin oxide SnO_2, and zinc oxide ZnO. Although these materials in un-doped forms all have band gaps in excess of 3.3 eV, high enough for transparency, as well as high carrier concentrations and good mobilities (Table 1.3); it should be noted that these materials are poor electrical conductors versus metals. Copper has a conductivity of 600,000 S cm^{-1}, which is 60 times greater than that of In_2O_3 which is has one of the highest conductivities for a TCO. The theoretical limit of conductivity in TCOs has been predicted to by 25,000 S cm^{-1} by Bellingham *et al*, although the theoretical modelling is always evolving.[23] Doping of these materials has been known to enhance these properties further.

Table 1.3: Electrical characterisation of some common TCOs

Material	Bandgap (eV)	Conductivity (S cm^{-1})	Electron concentration (cm^{-3})	Mobility ($cm^2 V^{-1} s^{-1}$)
In_2O_3	3.75	10000	$>10^{21}$	35
ZnO	3.35	8000	$>10^{21}$	20
SnO_2	3.6	5000	$>10^{20}$	15

Two of the most common TCO materials are indium tin oxide (ITO), predominately an indium based material with a tin concentration of 5-10%,[24] and fluorine doped tin oxide (FTO) which has fluorine doping levels between 1-5%.[25] Selecting a TCO for an application can be determined by a number of different factors, ranging from cost, mechanical hardness, transparency and conductivity. This means that for some applications a single TCO is preferred over the other options, for example, due to the high conductivity of ITO this material is preferred in the solar and display materials, with ITO accounting for 93% of the market, worth $1527 million.[26,27] This is despite ITO being significantly more expensive to make due the scarcity of indium. The crustal abundance of indium is 0.053 ppm compared to 1.7ppm for tin, while the price per kg of indium is over $650, compared to less than $25 for tin metal. As a consequence there is a growing interest in using different TCOs within solar and display applications. FTO is much cheaper to manufacture due to the wider abundance

of tin and production is already established for use in the low emissivity glass market.[22] Other benefits of FTO include a higher thermal stability and a low toxicity. The drawbacks of FTO include a higher deposition temperature, reducing the range of substrates and architectures available for growth. FTO also has a higher resistance to etching which makes patterning FTO for complex electronics architectures more difficult. The rising cost of indium has, however, driven research into the FTO deposition techniques and fabrication in an effort to reduce the costs associated with some of these thin film applications.

1.3 Tin oxides

Tin chemistry is dominated by the dual valency of the metal, with the +2 or +4 oxidation states preferred. Consequently tin oxide chemistry is dictated by these oxidation states with two main oxides, tin(II) oxide, often referred to as stannous oxide and tin(IV) oxide, or stannic oxide. Intermediate phases of Sn_2O_3 and Sn_3O_4 which contain a mixture of Sn(II) and Sn(IV) oxidation states have also been reported.[28] The structural and electronic properties of SnO and SnO_2 are quite different, giving rise to different applications.

1.3.1 SnO_2

SnO_2 is the more stable of the tin oxide materials and exists as the naturally occurring mineral cassiterite. Crystalline tin(IV) oxide displays the rutile structure, with six-coordinate tin atoms bound to three-coordinate oxygen atoms. This structure is adopted by several other metal oxides including TiO_2 and CrO_2.[29] The unit cell of tin(IV) oxide is tetragonal and is found in the $P4_2/mnm$ space group with the lattice constants a=b=4.7374 and c=3.1864 (Figure 1.3).[30]

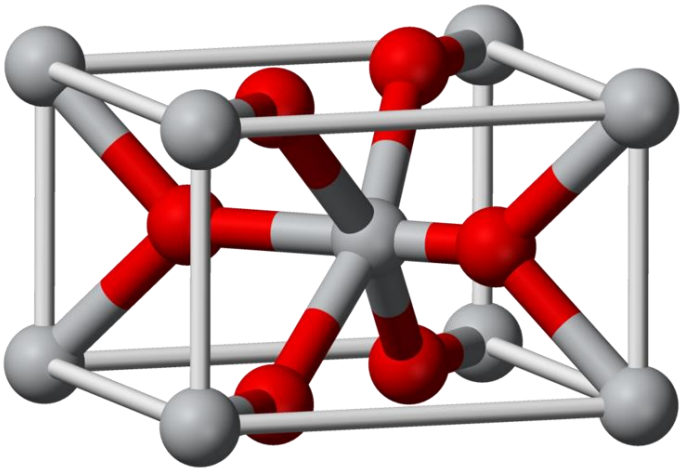

Figure 1.3: Atomic structure of the rutile structure SnO_2. Tin shown in grey, and oxygen in red

This is a highly polar covalent structure with the electron rich oxide character located in the VB, and the metallic character located in the CB. The structure allows the tin ions to adopt a $5s^0$ electron configuration, while the oxide ions take on a $2s^2 2p^6$ configuration resulting in a Fermi level situated at the top of the $2p^6$ level of the oxide.[31]

The presence of intrinsic or extrinsic defects and the introduction of dopants such as fluorine raise the location of the Fermi level much closer to the CB reducing the energy required for electrons to transfer from the VB to the CB and so increasing the electron mobility. Reducing this energy should see a reduction in the transparency of the material. The large energy gap between the ns^0 and the higher energy n*p* shell is thought to aid in maintaining transparency while increasing the electrical conductivity.[31]

1.3.1.1 Applications of SnO_2

SnO_2 has many applications which can be put into three main categories, (1) catalysis, (2) gas sensors and (3) as a transparent conductor.

1.3.1.1.1 Catalysis

While the use of metal oxides such as Al_2O_3 as a support material for transition metal catalysts is common, SnO_2 has been found to exhibit good activity as an oxidation catalyst.[32] These tin dioxide based catalysts have been used in the oxidation of CO with O_2 and NO.[33–40] Catalytic oxidation of CO using granular SnO_2 has been shown to proceed at temperatures below 150°C. The catalyst was made using a sol-gel method (see 1.4.1), and assessed as an oxidation catalyst for CO, using O_2.[40] The catalytic reduction of NO by CO using a SnO_2 catalyst was found to proceed at temperatures in excess of 200 °C, with complete conversion occurring at 360 °C. At low temperatures the catalyst soon became poisoned with CO. On introduction of 1% CrO_2, however, the reaction proceeded at temperatures of 150-220 °C, with no observed poisoning of the catalyst.[36]

Oxidation is believed to follow the Mars-van Krevelen mechanism that is prevalent in many oxide based catalysts.[41] The mechanism requires oxidation of the molecules through consumption of the lattice oxygen of the tin dioxide catalyst. The catalyst is then re-oxidised by gas phase oxidants (Figure 1.4). This is possible due to tin's multiple oxidation states, allowing reduction of the metal from +4 to +2 as lattice oxygen is consumed.[29,41,42] The re-oxidation of the metal centre by atmospheric oxygen allows the process to continue. Studies of the variable oxygen content on SnO_2 surfaces shows that partially reduced surfaces are still stable with varying content of Sn(IV) and Sn(II) ions showing that this reduction and oxidation process is feasible.[29]

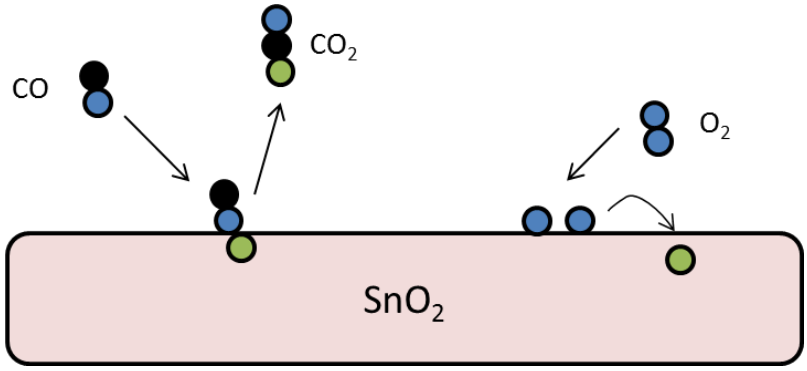

Figure 1.4: Diagram of the Mars-van Krevelen mechanism for the oxidation of CO to CO_2.

1.3.1.1.2 Gas Sensors

Numerous metal oxides exhibit a change in electrical conductivity on introduction of different gases at elevated temperatures. Two of the more common gas sensing materials are ZnO and SnO_2. The gas sensing abilities of metal oxides can be broken down into two different mechanisms, with materials either showing bulk or surface sensitivity.[43] Tin dioxide sensors are known to exhibit surface sensitivity on adsorption of gaseous material. Reducing gases are found to increase the conductivity of the material, while oxidising gases show a reduction in conductivity.[29] The reduction in conductivity brought on by oxidising gases is thought to result from the trapping of charge carriers causing a significant decrease in the electrical conductivity.[43] Charge carriers are trapped as the electrostatic field at the surface causing band bending of the energy bands in the solid. A negative field on the surface, caused by a reducing gas, has the result of an upward bending, resulting in the Fermi level being pushed into the band gap (Figure 1.5). This leads to a reduction in the effective carrier concentration, which is observed by a reduction in conductivity. Sensors based on SnO_2 have been used for the detection of NO_2,[44–46] NO,[45,46] CO,[44] H_2S,[47,48] H_2,[45] ethanol[49] and NH_3.[46]

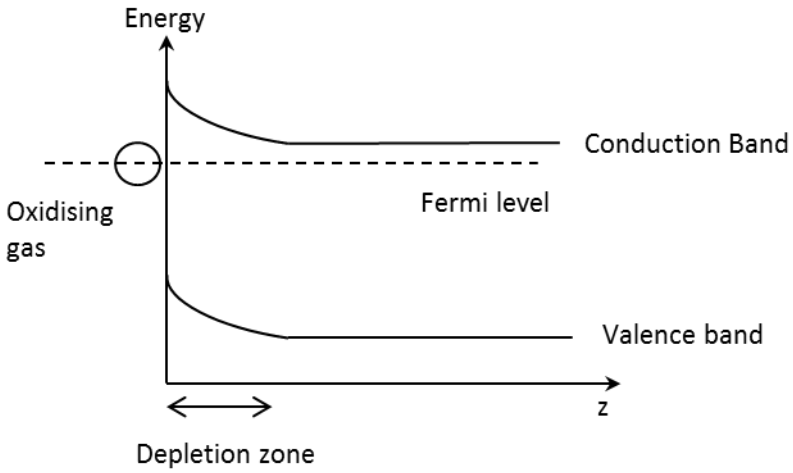

Figure 1.5: Band bending caused by the presence of an oxidising gas

1.3.1.1.3 Low emissivity coatings

By far the biggest application for tin dioxide based materials is the use of FTO as a low emissivity (low-e) coating for more energy efficient glass.[21,22] The market for low-e glass is rapidly expanding, with annual demand for low-e glass in the European Union in 2007 being 60 x 10^6 m^2, and growth projected to reach 100 x 10^6 m^2 in a few years.[50] Energy efficient glass works on the principle that short wavelength radiation enters through the glass where as any long wavelength radiation generated in the room, through the heating of materials inside, is reflected by the glass, therefore reducing the loss of thermal energy outside (Figure 1.6).

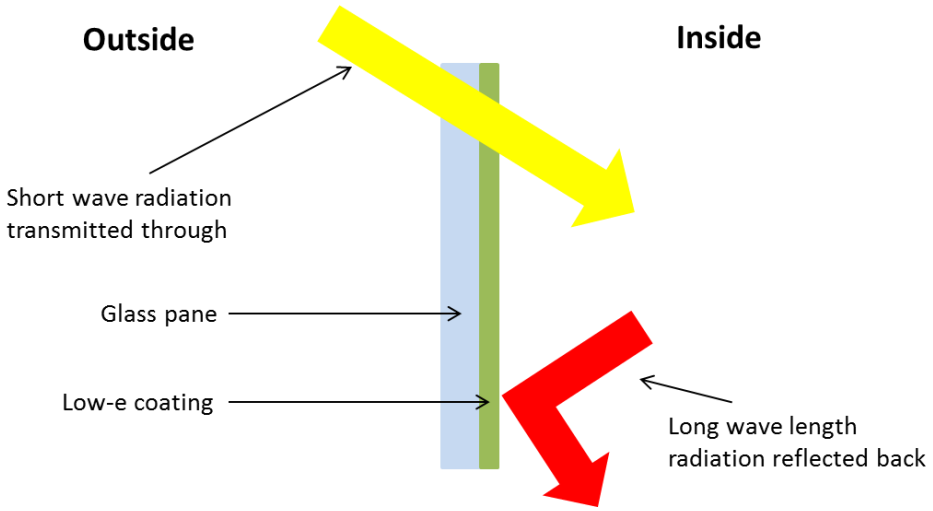

Figure 1.6: Diagram showing how low-e glass coatings are utilised

For an effective low-e coating the material chosen should have good transmission properties in the region of visible light, and then show good reflectance properties in the near infra-red and infra-red regions. For different climates the ideal point at which transmission and reflectance cross over will change. For cooler climates FTO is the low-e coating of choice as it reflects wavelengths of 1500-2000 nm and higher. In a warmer climate greater reflectance may be desired to keep more heat outside of the building, and therefore keep the room cooler. In this latter instance titanium nitride, which reflects light at wavelengths greater than 1000 nm is often used.[22] Figure 1.7 shows the transmission and reflectance spectra for a typical FTO thin film on glass, the transmission drops tails off after 1000nm while the reflectance increases after 1500nm approaching 60% reflection at 2500nm.[51]

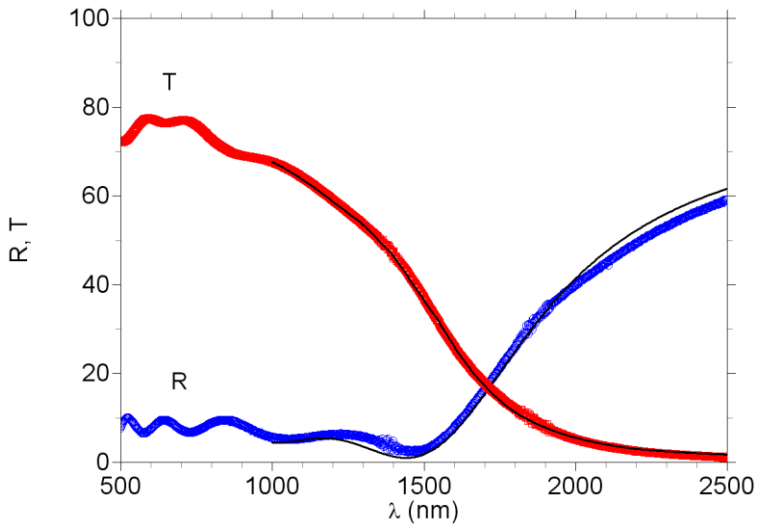

Figure 1.7: Transmission (red) and Reflectance (blue) spectra for FTO - taken from reference[51]

1.3.1.1.4 Transparent electrodes

There are many applications and devices where a transparent electrode is required for efficient operation, including solar cells and electronic displays. As mentioned earlier ITO currently dominates the electronic display market, while other TCO materials such as FTO are responsible for less than 6% of the total market. The dominance of ITO is down to the material having a higher electrical conductivity and a lower chemical resistance, allowing the material to be etched for complex electronic architectures.[22]

Photovoltaics is a rapidly growing area of research and commercialisation. While the original technologies were based on silicon systems, some of the emerging solar cells take advantage of inorganic dye, and alternative inorganic thin films for the generation of electrical current. A simplified diagram of a solar cell is shown in Figure 1.8. Whereby light passes through a glass window coated with an *n*-type TCO material such as ITO or FTO and reaches a photoactive layer. Excitation in the photoactive layer results in the formation of an electron-hole pair, and the TCO acts as the cathode, providing an electron transport route to the rest of the circuit. The anode is generally made of a *p*-type semiconductor material or more commonly a metal, and acts as a hole transporter allowing efficient separation of electron hole pairs and generation of electrical energy.

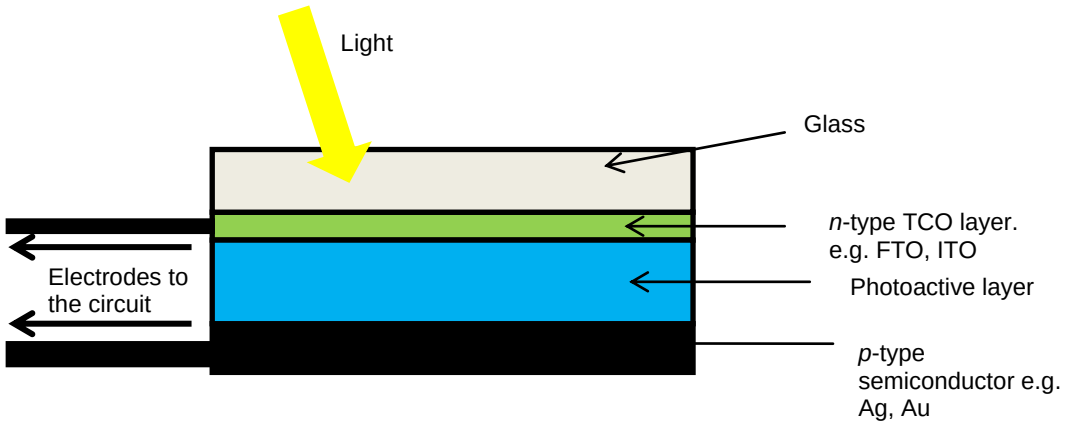

Figure 1.8: Simplified diagram of a thin film solar cell

1.3.2 SnO

The lower Sn(II) oxidation state oxide SnO has recently emerged as a potential *p*-type semiconducting material.[52] The black-brown compound is found to exist as a secondary mineral, romarchite, which occurs as thin soft black crust formed as a weathering product of tin compounds.

Tin monoxide exhibits a litharge structure in the solid state, comparable to the structure of PbO.[53] The unit cell is tetragonal, with the space group symmetry *P*4/*nmm* and the lattice constants are a=b=3.8029 Å and c =4.8382 Å. The structure exhibits a layered effect in the [001] plane with each layer having a $Sn_{1/2}$-O-$Sn_{1/2}$ structure (Figure 1.9) with a Sn-O bond distance of 2.22 Å.[54] The positive 2+ charge on the tin atom is shielded by an electron charge cloud which sits between the tin planes; areas of electron density which arise from the non-bonding $Sn5s^2$ electrons behaviour as a stereochemically active lone pair.[29,55,56] Electron density calculations suggest that the asymmetric nature is due to an antibonding interaction between the Sn5s and O2p orbitals.[57]

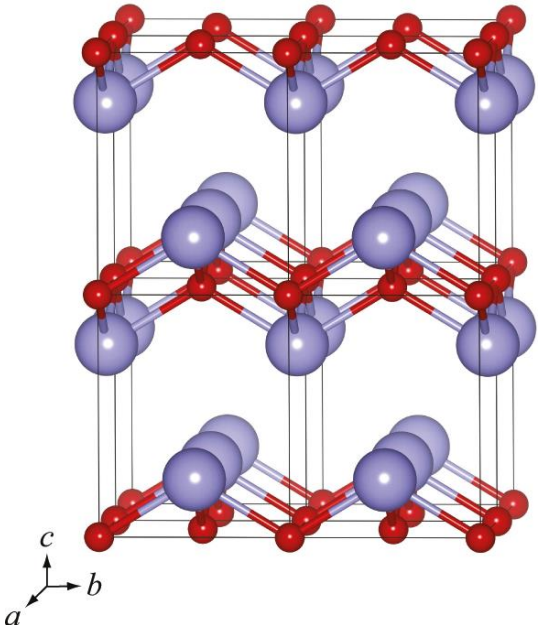

Figure 1.9: Atomic structure of the unit cell of litharge SnO. Tin atoms blue, oxygen atoms red.[57]

There are also reports of a metastable phase of SnO that is red in colour that can be prepared from hydrated tin(II) oxide.[58,59] This red phase of SnO has been synthesised by taking tin(II) chloride dihydrate in concentrated HCl and water and adding H_3PO_4. To this solution

ammonia was added drop-wise until the pH reached 4.9, after several minutes a white hydrous tin(II) oxide precipitated which was converted to red SnO by heating the reaction for five days at 95°C. The pH of the solution on addition of ammonia is observed to be important in the synthesis of red SnO, if the pH is 5 or greater black-brown SnO is formed on heating, and at lower pH values the transformation was much slower, or did not occur.[58] The crystal structure of red SnO was determined through high resolution X-ray powder diffraction experiments. The sample was found to be in the Cmc_2 space group with lattice constants a=5.005 Å, b=5.746 Å, c=11.049 Å. The structure contains double layers of tin and oxygen atoms stacked in the c axis (Figure 1.10). The tin atoms are four-coordinate, but unlike in black SnO, the Sn-O bond lengths are inequivalent ranging from 2.06 - 2.67Å. [58]

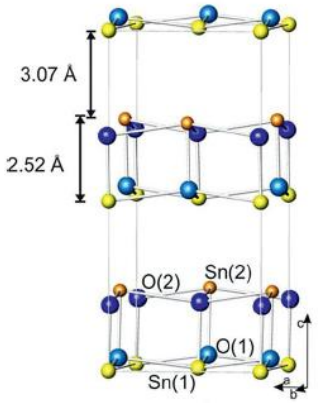

Figure 1.10: Atomic structure of red phase SnO.

Red SnO was found to be stable in air up to 270 °C, and was monitored using high temperature X-ray diffraction methods. Room temperature conversion of red SnO to black SnO can be achieved through mechanical pressure, e.g. grinding, or treatment with a strong alkali. Conversion can also be observed by seeding a solution of red SnO with the black analogue.[58,59]

The conductivity of SnO-based materials has driven the increase in research into the compound. The majority of reports suggest that SnO is a *p*-type semiconductor, and there is data proving this with positive Hall mobility measurements published by several groups.[7,11,60–65] Recently Hosono and co-workers successfully reported *n*-type SnO through doping of the material with antimony at concentrations of 8% or higher. The carrier density and carrier mobilities for SnO and SnO (10% Sb) are similar, although the former is a p-type carrier and the latter a n-type carrier. (2.5 $x10^{17}$ and 2.9$x10^{17}$ cm^{-3} and 2.4 and 2.3 cm^2 V^{-1} s^{-}

[1]). [66] Calculations by Hosono and co-workers, and Piper and co-workers show that the band edge alignment of SnO is comparable to the bipolar $CuInO_2$.[7,66] The bipolar nature of $CuInO_2$ has been explained in terms of having a small fundamental band gap. The band edge alignments are comparable to covalent materials such as Si and GaAs which can also be doped to give *n* or *p* type character.[7]

1.3.2.1 Applications of SnO

Due to the metastable nature of red SnO, the application of SnO has focused on the black morphology. The use of SnO-based materials in applications is a relatively new area compared to many semiconducting metal oxide materials.

1.3.2.1.1 Thin - Film -Transistors

Thin film transistors (TFTs) are used in a host of applications but are best known for their application in liquid crystal displays (LCD). In display applications a TFT acts as a simple on off switch, whereby the speed of the switching is determined by the refresh rate of the LCD, so a 120 Hz display will have a TFT switching speed of 120 changes per second. Figure 1.11 presents a simplified diagram of a TFT architecture. A TFT has three terminals connected to the surrounding circuitry; these are the source, drain and gate. As shown in the image the gate is insulated from the semiconductor by a gate insulator, normally made of a dielectric material.

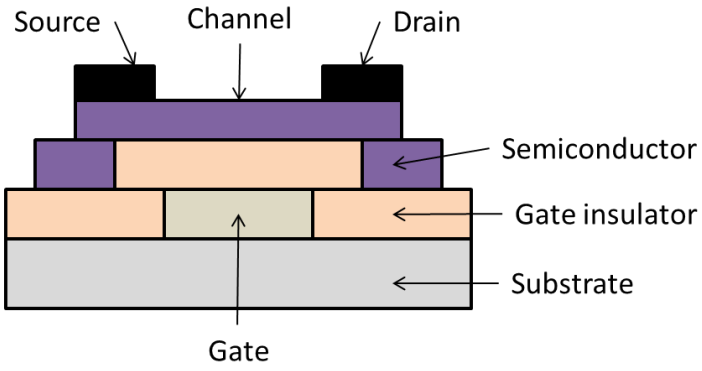

Figure 1.11: Structure of a thin film transistor

For an *n*-channel TFT display a positive charge is applied to the gate in order to switch the device on. The positive charge induces a negative charge on the semiconductor through the dielectric barrier allowing the flow of electrons between the source and drain. When the

positive charge is removed from the gate the flow of electrons is stopped. For a *p*-channel TFT a negative charge is applied to the gate in order to switch the system on.

Although original TFTs were based on CdSe as the semiconducting material this was overtaken by silicon based systems which have the benefit of being doped for *p* or *n* type conductivity. With the recent interest in transparent electronics, and the desire to increase performance of electrical devices TCO materials have been investigated as semiconductor materials, as a consequence of limited *p*-type semiconductors there are few *p*-channel TFT systems based upon metal oxide systems.

Hosono and co-workers identified SnO as a potential *p*-type semiconducting material[11] after unsuccessful attempts to make TFTs using some of the copper delafossite systems[13,15–19] described in Section 1.1. SnO was identified due to its similar electronic configuration to the previously identified copper-based systems; the advantage for SnO is a filled $5s^2$ orbital, which should allow for spatially spread *s* orbitals giving a larger hole mobility. The SnO layer was grown on yttria stabilised zirconia (YSZ) substrates using pulsed laser deposition (PLD - see section 1.4.3). The gate insulator was made of aluminium oxide while the source, drain and gate electrodes were gold/nickel composites (Figure 1.12).

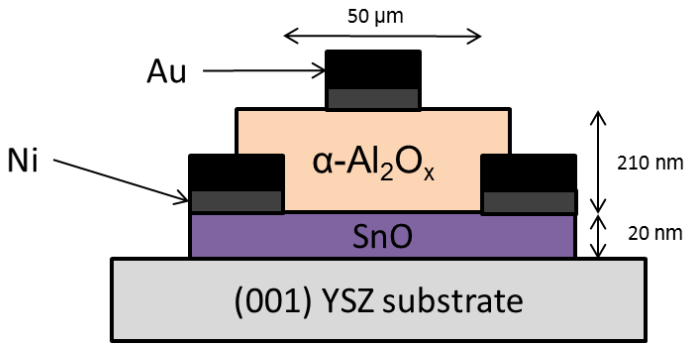

Figure 1.12: Structure of top-gate TFT device made using SnO as the semiconductor

Hosono and co-workers recorded Hall effect measurements confirming the *p*-type nature of SnO thin films. The hole mobilities and densities, 2.4 $cm^2\ V^{-1}\ s^{-1}$ and 2.5 x $10^{17}\ cm^{-3}$ are amongst the highest values obtained for *p*-type oxide materials.[11,65] With the introduction of SnO as a potential *p*-channel TFT material there have been several recent papers describing different methods for preparing SnO thin films, improving the mobilities and improving the TFT performance.[7,62–64,67–69] Alshareef and co-workers currently claim the highest mobilities for SnO thin films with a recorded mobility of 18.71 $cm^2\ V^{-1}\ s^{-1}$.[60]

1.3.3 Disproportionation of SnO

The disproportionation of SnO to tin metal and SnO_2 has been reported to occur when samples are heated in an inert atmosphere. Analysis of the heats of formation for both SnO, and SnO_2 show that this process is thermodynamically viable, with the heat of formation at 298K for SnO_2 measured at ΔH_{298} = -138 cal/mol while SnO is much higher at ΔH_{298} = -68 cal/mol.[29] This disproportionation has been found to occur via the intermediate tin oxides, Sn_2O_3 or Sn_3O_4 (Figure 1.13).

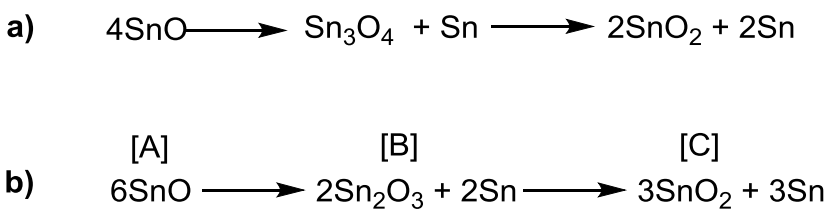

Figure 1.13: Potential thermal disproportionation routes for SnO.

The precise conditions that this takes place over are dependent on the sample preparation and the conditions the sample is subjected to. Giefers and co-workers studied at the thermal decomposition of SnO using both ex-situ and in-situ X-ray power diffraction techniques.[70] They used two commercial samples of SnO, from Chempur and Sigma Aldrich as provided and also grinded samples up to provide a fine powder. The Chempur sample was 100 mesh (0.152 mm sieve size), the Sigma Aldrich samples were <40μm in diameter, analysis of the ground Chempur SnO showed the particles had an average measurement of 1-2μm. The samples were sealed in high vacuum quartz tubes (10^{-5} mbar) and heated for 102 hrs at 275, 300, 350, 450 and 550 °C before X-ray analysis. Analysis was based on decomposition route b in Figure 1.13, with the sum of [A], [B] and [C] giving a total of 100 %. The results are shown in Figure 1.14 (taken from ref [70]) demonstrating shows the variation in disproportionation depending on sample preparation.

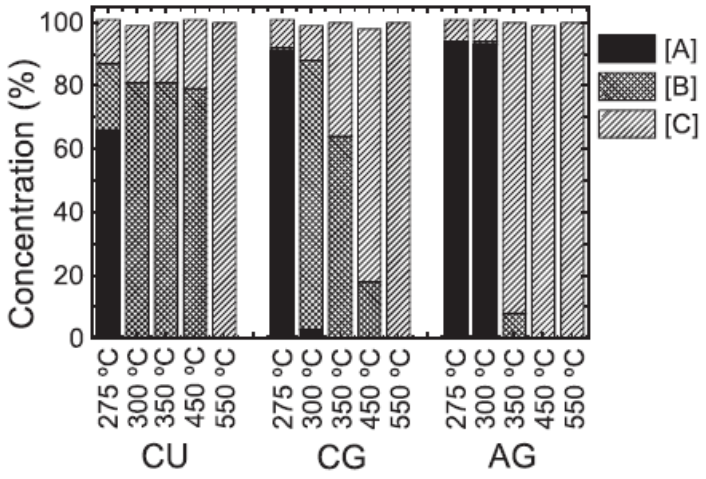

Figure 1.14: Data from ex-situ disproportionation reactions conducted by Giefers and co-workers.[70] [A]= SnO, [B]=1 /3Sn_2O_3 +1/3 Sn, [C] 1/2 SnO_2 + 1/2 Sn after 102h of heating. For sample preparation CU=Chempur, CG=Chempur ground and AG = Aldrich ground.

The temperature of disproportionation is debated by other researchers, Gauzzi and co-workers reported that SnO is converted to the intermediate Sn_3O_4 between 250-525 °C in studies lasting 100 hours.[71] At temperatures above 525 °C SnO_2 and tin metal were observed after 100 hours, although at 630 °C this time is reduced to just one hour. Interestingly in this study they see significant decomposition to tin metal and the oxide intermediate after 1h at 300 °C. Moreno and co-workers monitored the decomposition by Mössbauer spectroscopy at 450 °C, observing the presence of both the intermediate oxide and SnO_2 after four hours of heating.[72] There are also examples of SnO synthesis that incorporates tin metal and SnO_2 which has been attributed to the thermal decomposition of SnO. Hosono and co-workers reported that during the preparation of an antimony doped PLD target tin metal was detected if the target was annealed at temperatures higher than 340 °C in just 7 minutes.[66]

1.4 Thin film fabrication methods

There are several methods for the formation of metal oxide thin films both in crystalline and amorphous phases. Generally the metal oxide layer is formed directly onto a substrate that is suitable for the application, therefore the growth of metal oxides most commonly utilise silicon or, for TCOs, glass or quartz substrates.

1.4.1 Sol-Gel

A sol –gel process requires a suitable metal precursor, for example a metal lakeside, which can be taken and dissolved in a suitable solvent to make a precursor solution. The solution can then be condensed into a gel phase, which can occur as chemical process such as an acid catalysed hydrolysis reaction of the metal alkoxide, or through a thermal evaporation of solvent. Once the material is in a gel form it can be manipulated depending on the morphology required for the final product before it is calcined to give a ceramic film of a metal oxide (Figure 1.15). Calcination occurs at varying temperatures depending on the shape and thickness of the required oxide layer but temperatures are generally around 500 °C.[31]

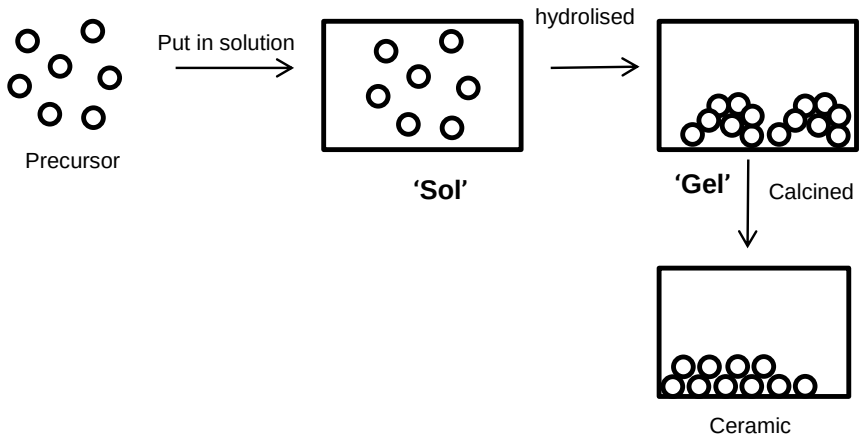

Figure 1.15: Diagram showing the sol-gel route to the formation of ceramics.

1.4.2 Sputtering

Sputtering takes advantage of a phenomenon observed when a surface is bombarded with energetic particles such as accelerated ions. Upon bombardment, surface atoms of the solid are scattered backward due to collisions between the surface atoms. The energetic particles, which are normally inert, thus cause atoms to be ejected. There are several variations on how sputtering can be carried out, one of the most common being cathode sputtering. This system works by coating a cold cathode in an amorphous layer of the target material, e.g. ZnO particles. The target substrate is attached to the anode, and the system is put under vacuum to prevent additional collisions which could deflect the sputtered ions. A sputter gas, such as positive argon ions, is directed in a stream at the cathode, accelerating due to electronic attraction. This bombardment leads to the formation of a film on the substrate at the anode.

1.4.3 Pulsed laser deposition

Pulsed Laser deposition (PLD) is a deposition technique that has a lot in common with sputtering. Instead of bombarding a sample with a stream of ions, the substrate is bombarded with a laser beam at different pulse lengths resulting in the discharge of atoms from the energetic collision. These can then nucleate on a substrate that is positioned parallel to the target. The target is held at 45° so that discharge is directed away from the laser beam. This process occurs in a vacuum to prevent further scattering of discharged atoms, and also reduces the risk of contamination with impurities.

1.5 Chemical vapour deposition

Chemical Vapour Deposition (CVD) is an umbrella phrase to describe many processes that result in the formation of a solid material from the controlled decomposition of a gas phase precursor. The process is industrially relevant for the manufacture of materials in large scale plants. For example, Pilkington Glass uses CVD to deposit layers of TiO_2 and FTO directly on to glass on the float line. This takes advantage of the high temperatures used in the manufacture of glass.

The process of CVD is outlined in Figure 1.16. A vapourised precursor is introduced to the target substrate and in the simplest case is followed by adsorption of the precursor to the substrate. The precursor will then decompose to form the desired material, with any side products removed by the carrier gas or vacuum. The continued growth may occur by either migration of adsorbed precursors to an existing nucleation point (step wise growth that is energetically favoured during physisorption processes) or decomposition to form new islands. There are many variations of CVD, however they all require the entrainment of a precursor into the gas phase, with subsequent controlled decomposition of the precursor on the substrate.[73–75]

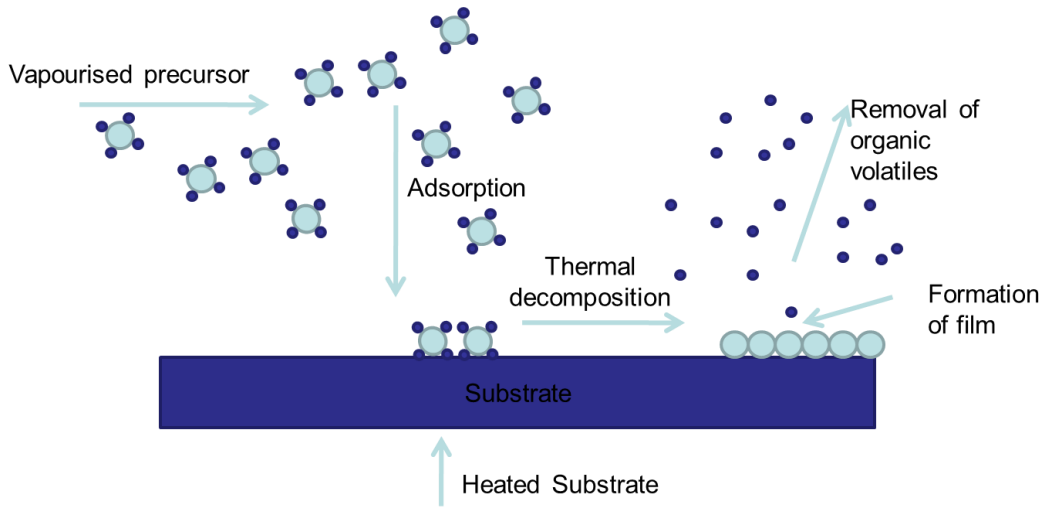

Figure 1.16: Simplified diagram of CVD process showing the main steps.

1.5.1 Vaporisation techniques

Vaporisation of a compound is a crucial aspect of CVD, and there are several common methods for providing gas phase precursors. Some chemical precursors already exist in a gaseous state, or have a suitably low vapour pressure such that passage of a carrier gas through the material enables a controllable quantity of the precursor to be transported to the deposition chamber. In some instances the precursor may require gentle heating to promote appropriate volatility. If the system is run at close to atmospheric pressures, as is desirable for many industrial applications this is known as atmospheric pressure CVD (APCVD). To provide enhanced control of the delivery of liquid or solid precursors to the gas phase the compounds are generally delivered to the system via a bubbler (Figure 1.17).[76,77] The bubbler allows uniform heating of the compound to the desired temperature and for the carrier gas to enter the system in a uniform manner. The carrier gas is generally heated to ensure delivery of the precursor rather than condensing in transit and the flow of the carrier gas is controlled by a mass flow controller. Heating a precursor must be done with care to prevent the decomposition in the bubbler before delivery to the deposition chamber.

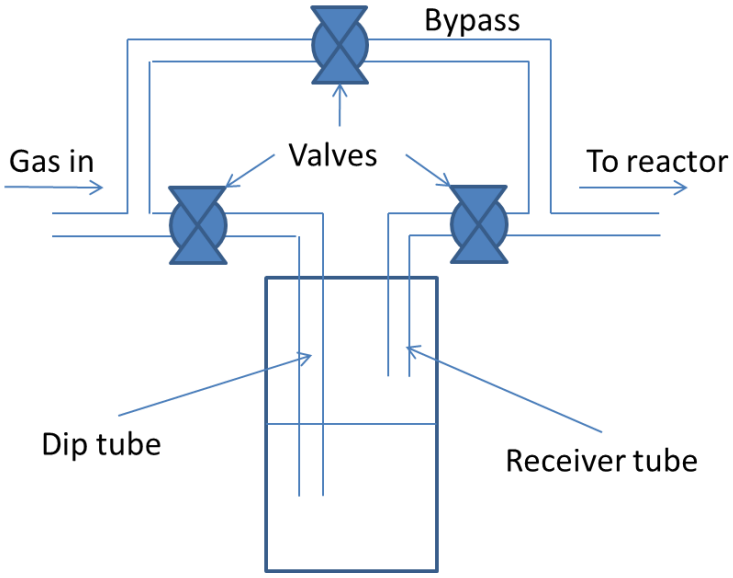

Figure 1.17: Simplified scheme of bubbler system with bypass

If the precursor is not sufficiently volatile to enter the gas phase with gentle heating a vacuum can be introduced to increase the amount of precursor entering the gas phase. This is commonly referred to as low pressure CVD (LPCVD). While the costs of running this on a

commercial scale increase due to the need for a low pressure system, LPCVD is still suitable for deposition in electronics applications. An added benefit of LPCVD is the vacuum removal of by products and possible impurities during deposition. The method of delivery is most commonly the same as that for APCVD with the precursor delivered to the system via a bubbler.

Precursors that show limited or no volatility may be vapourised through the generation of an aerosol; a technique commonly referred to as aerosol assisted CVD (AACVD).[78] For large scale deposition, and to maintain a uniform droplet size over several runs, a compressed gas aerosol can be used. A precursor solution is pumped at high pressure through a narrow nozzle, generating a fine spray of precursor solution, which is carried by the carrier gas to be deposited on the substrate (Figure 1.18). For smaller pilot lab scale depositions the use of an ultrasonic nebuliser may be preferred.[78] This generates a fine mist of a precursor solution that can enter the carrier gas stream. Ultrasonic nebulisers are less accurate at producing a constant droplet size, but will generate a mist of nano and micron sized droplets.[77]

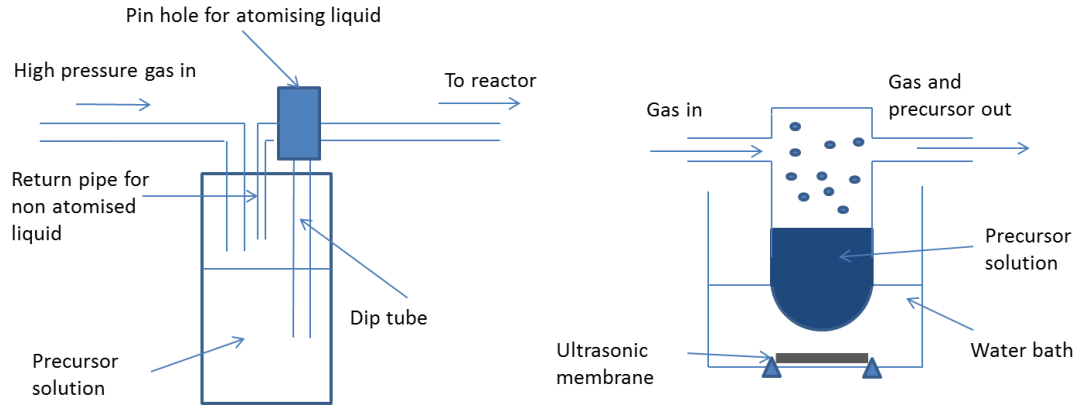

Figure 1.18: a) Simple diagram of high pressure atomiser and b) diagram of ultrasonic nebuliser aerosol system

The choice of solvent is crucial to the deposition process in AACVD as the surface tension and viscosity of the solvent impact the droplet size.[78] Other factors to take into consideration are the solubility of the precursor in the solvent chosen. If the precursor is insufficiently soluble precipitation may occur before reaching the deposition chamber. The reactivity of the solvent at elevated temperatures and how the solvent may affect films grown are also important considerations. For example using oxygen containing solvents could increase the percentage of oxygen in the system – acting as an oxygen source in the deposition.[78] There is

also evidence to suggest that the combustion of alcohols, particularly methanol, can cause a localised increase in surface temperature which can affect film quality.[78]

1.5.2 Deposition

Decomposition of the precursor and the resultant deposition of material are also important steps in CVD.

The decomposition of precursors on the surface is predominately activated by a thermal process, with the substrate heated to the desired temperature to give an even growth. High temperature growth is often required to enable the formation of crystalline materials. This does limit the range of substrates that can be used in CVD to thermally stable materials such as glass, or silicon wafers.

Decomposition of precursors can also be enhanced by using a plasma discharge in the deposition chamber; in a process known as plasma enhanced CVD (PECVD). This technique allows deposition to occur at significantly lower temperatures, with reports of PECVD at room temperature due to the use of electrical energy rather than thermal energy to initiate the reactions. The production of ions and radicals leads to the occurrence of gas-phase and surface reactions, allowing a layer formation of the target material on the substrate. Although low temperatures have been reported, it should be noted that, due to the high energy and temperature of the electrons, the substrate will heat as the particles collide with the surface. While PECVD allows deposition on to less thermally stable materials, the high energy nature of plasma can result in damage to the substrate, or the film grown. It should be noted that this process is also used to clean, or pre-treat substrates before deposition by subjecting the substrate to a short burst of ozone and plasma. Due to the nature of forming plasma there are several parameters that need to be considered before PECVD may be deployed including the radio frequency and power, the pressure and precursor flow rate.[79]

Photo-induced decomposition has also been used in the CVD process– in this case a light source is used to activate the decomposition of the precursor.[80] Due to the inorganic nature of the majority of CVD precursors this is often undertaken with a UV light source and opens up the possibility of low temperature deposition on a range of substrates without the possible substrate damage observed with PECVD.

1.6 Desirable precursor properties

1.6.1 Types of precursor

The majority of CVD target materials are metal based systems; metal precursors can be loosely classified into three different categories. Inorganic precursors contain metal bonds to non-hydrocarbon ligands such as metal halides and nitrates; organometallic compounds which have at least one metal – carbon bond, and metal –organic compounds which have no direct metal-carbon bond but exhibit a metal-hydrocarbon linker such as a metal alkoxide. For the formation of metal oxide thin films, oxygen needs to be incorporated into the growth mechanism. Although this can come from oxygen incorporation in the ligands employed, more often in CVD the oxygen is introduced as a co-reagent. Most commonly this will be in the form of O_2 or H_2O, however, more exotic oxidants have been used including NO, N_2O, H_2O_2 and ozone.[25]

1.6.1.1 Multi-source vs. single source precursors

Many of the films grown using CVD are complex multi-element systems. Multi-source CVD is a common process with the ratio of elements controlled by their relative concentrations in the gas phase. This method is also suitable for the introduction of dopants, for example fluorine for the formation of fluorine doped tin oxide, particularly when the doping level is much lower than stoichiometric. Designing a single source precursor with a high ratio of one element to another would be difficult, and a multisource approach is currently used in most industrial scale operations for the formation of metal oxide thin films.

When synthesising mixed systems such as III/V semiconductors a mixture of MR_3 (M = Al, Ga, In, R= alkyl) and PH_3, or AsH_3 is typically used to form a crystalline layer. These compounds are highly toxic and pyrophoric so have large safety concerns attached to them. The semiconducting properties are also highly sensitive to impurities including carbon. To combat this issue research has been conducted into the design and synthesis of single source precursors which have a controlled decomposition route to the desired material. An example of a single-source precursor is $[^{n}Bu_2GaAs^{t}Bu_2]_2$, which contains a strong covalent bond between gallium and arsenic. In the decomposition of $[^{n}Bu_2GaAs^{t}Bu_2]_2$ the first step is a β-hydrogen elimination step involving Ga and a *n*-butyl group to give a Ga-hydride and *n*-butene. This is followed by formation of Ga and As containing species responsible for film growth (Figure 1.19).

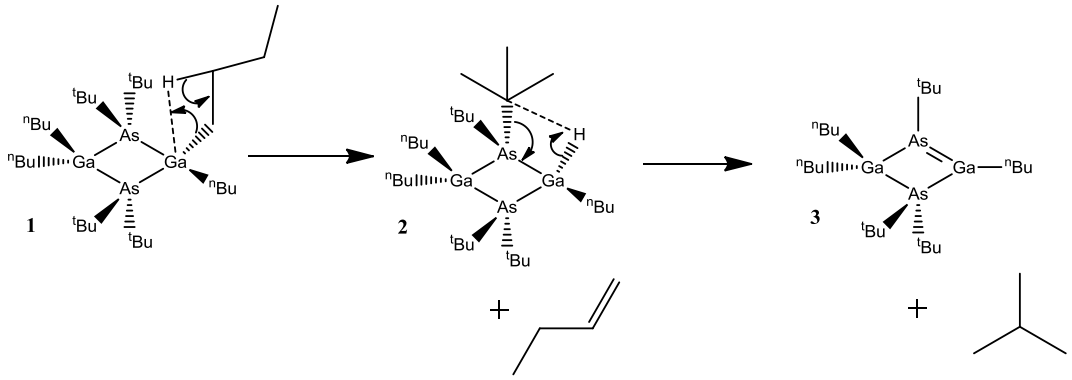

Figure 1.19: Initial decomposition pathway for [^{n}Bu$_2$GaAs^{t}Bu$_2$]$_2$

1.6.2 Volatility

As mentioned earlier, the volatility of a precursor is an important property which should be assessed before deposition studies can be undertaken. Volatile precursors are preferred as they can be used at atmospheric pressure, or under vacuum with limited heating, and therefore do not require a solvent to generate an aerosol. The volatility of a precursor can be determined by measuring the vapour pressure of the compound. The vapour pressure is the pressure exerted by a vapour when in equilibrium with the liquid, solid or both phases. The vapour pressure of a compound can be given by the Clausius-Clapeyron equation which derives the pressure as a function of temperature (T), the latent heat of vaporisation/sublimation (L), the ideal gas constant (R) and a material specific constant C (equation 2). [81]

$$\log_{10} P = -\left(\frac{L}{R}\right)\left(\frac{1}{T}\right) + C \qquad (2)$$

For new compounds the partial pressures are measured at a range of different temperatures to give a plot showing pressure as a function of temperature. This data can be used to calculate L as a plot of $\log_{10}$P against 1/T shows a linear relationship which can be extrapolated to give a figure for L/R and also a figure for C.

Another useful tool for the assessment of precursors is thermo-gravimetric analysis (TGA). A sample of the compound is heated gradually to a desired temperature while the mass is measured; allowing a graph of temperature against weight percentage to be plotted. The final

observed mass can give an indication of the molecular weight of the fully decomposed compound, which can be used to deduce the identity of the material formed. Often TGA analysis can result in final observed masses significantly lower than expected compounds with especially low residual masses suggesting a fully volatilised compound. In such cases the residual mass is attributed to impurities, possibly due to partial oxidation in transferring the sample. The TGA plot can also give information on the thermal decomposition events for a precursor (Figure 1.20).

1.6.3 Thermal stability

The thermal stability of a precursor is also important. While the majority of CVD processes are thermally activated, the decomposition of the precursor needs to occur at or near the substrate. Therefore the decomposition temperature of the precursor should occur in a window that allows for effective transport to the deposition chamber, but be low enough to not cause damage to the substrate. An indication of the thermal stability of a compound can be obtained by TGA. The onset temperature observed in the TGA indicates the temperature of thermal decomposition, or volatilisation, or a combination of both. [76]

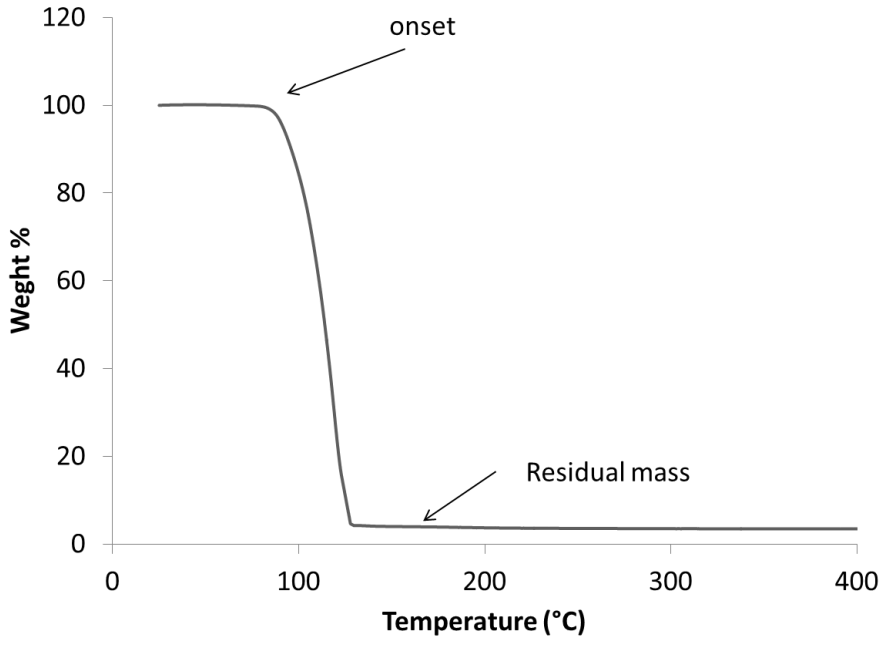

Figure 1.20: Example thermogravimetic analysis plot.

1.7 Precursor design

As discussed above there are several desirable properties that a potential CVD precursor should display. Ideally the precursor should also exhibit a clean decomposition pathway and possess a reasonable shelf life. The introduction of new precursor delivery systems such as aerosol assisted CVD has reduced the volatility requirements; however a volatile precursor will have a wider choice of delivery mechanisms. The target material should also be considered when designing precursors, for example for metal oxide formation use of a compound containing a pre-existing metal-oxygen bond may be beneficial.

The volatility of inorganic and organometallic precursors can be linked to the intermolecular forces such as van der Waals, hydrogen bonding and pi interactions that the precursor is subjected to in the solid or liquid states. Compounds that form dimeric, oligomeric or polymeric systems tend to have a reduced volatility compared to monomeric systems as energy is required to break the intermolecular forces responsible for oligomerisation. [82]

The formation of monomeric precursors can be achieved by saturating the coordination sphere of the metal centre, preventing the formation of bridged systems. For mono-dentate ligands this is especially challenging but may be achieved by using bulky groups which can successfully block coordination sites on the metal. The use of dialkylamide ligands will therefore provide a greater steric demand than the use of alkoxide ligands due to the increased number of substituents bound to the heteroatom (Figure 1.21) and therefore the more coordination sites that are sterically hindered.[82]

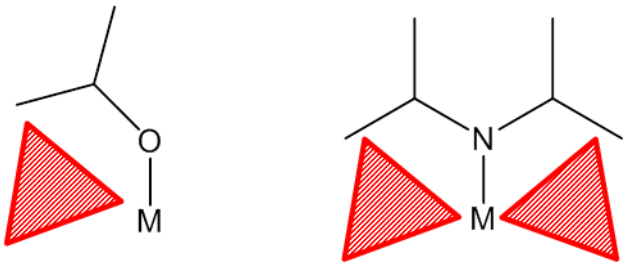

Figure 1.21: Alkoxide and dialkylamide systems showing the effect on access to the coordination sphere, red triangles represent blocked sites

As the number of ionic ligands (n) bound to the metal in a neutral complex is dictated by the oxidation state of the metal for a neutral compound ML_n it is often difficult to form monomeric complexes using monodentate ligands. This can be overcome by the introduction

of neutral donor ligands to satisfy the coordination sphere of the metal centre such as tetramethylethylenediamine or digylme (Figure 1.22).[82]

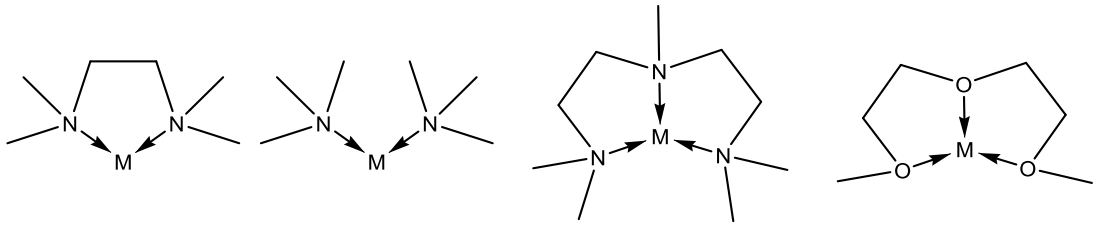

Figure 1.22: Examples of neutral donors that can be used to fill the coordination sphere of a metal centre

The use of chelating ligands to saturate the coordination sphere of the metal centre can also be used to afford a monomeric precursor. Some examples of commonly used chelating ligands for CVD precursors are shown in Figure 1.23. [82]

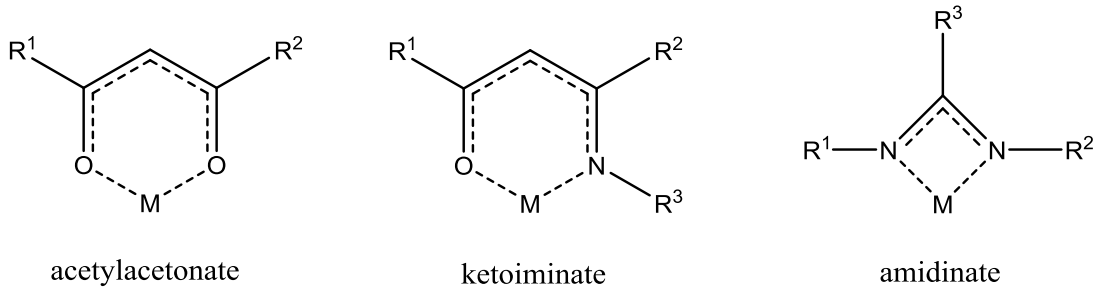

Figure 1.23: Some common multidentate CVD ligand systems

The intermolecular interactions between molecules can also be reduced by exchanging hydrogen atoms for fluorine atoms. This reduces the inter-molecular interactions by increasing the electron concentration on the periphery of the complex, consequently increasing electrostatic repulsions between monomers. The replacement of H with F also decreases intermolecular interactions the F atoms are less susceptible to polarisation and formation of intermolecular bonds. The increase in volatility by introduction of fluorine does however increase the risk of fluorine contamination during thin film formation.

1.7.1 Carbamate, iso-carbamate, carbonate, ureate, guanidinate, amidinate and iso-ureate ligands

This thesis focuses on the development and characterisation of carbamate, iso-carbamate, ureate and carbonate systems as potential precursors for metal oxide materials. Carbamate, iso-carbamate, carbonate and ureate ligands share many characteristics with other ligand systems including amidinate, guanidinate and iso-ureate ligands. These ligand systems have attracted much recent interest due to their potential for facile electronic and steric tuning. These ligands all adapt an XC(Y)Z (X=N, O Y=N, O Z=OR, NR_2) central core which can be modified through variation of the R, R' and R'' groups (Figure 1.24).

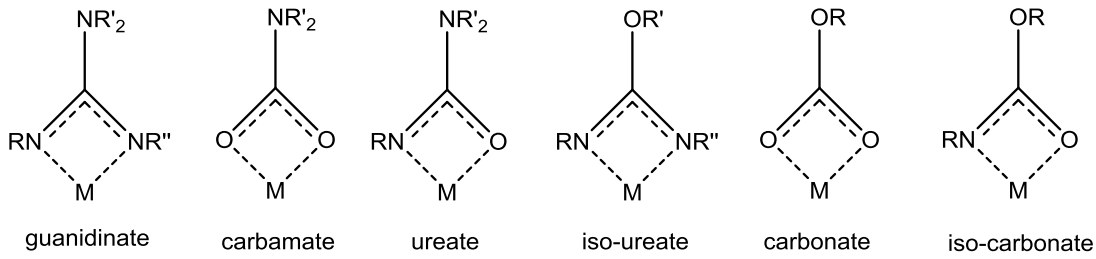

Figure 1.24: Selection of possible O, O', N, O and N, N' chelating ligands that maybe suited to CVD applications

The presence of the NR_2 group for the ureate, guanidinate and carbamate ligands and the OR group of the iso-ureate allows for significant lone pair interaction and delocalisation of electron density from the nitrogen or oxygen atoms into the XCY backbone. This delocalisation allows for the formation of a potential zwitterionic resonance structure as shown in Figure 1.25.

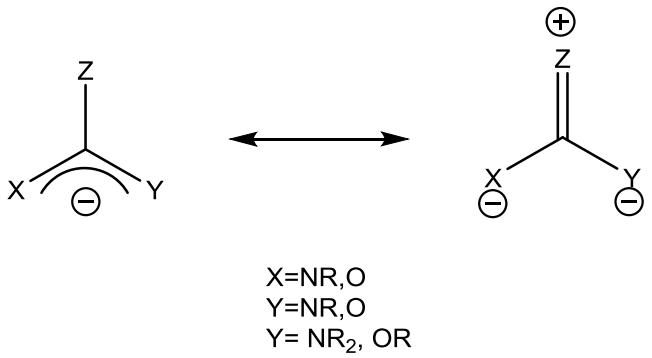

Figure 1.25: Possible resonance structures for carbamate, ureate and guanidinate ligands

The donation of electrons into the backbone of the ligand is dependent on the orientation of the NR_2 or OR moiety which can be affected by the steric demand and electronic character of the R group. For NR_2 this requires a planar sp^2 hybridised geometry that allows for overlap between the nitrogen p orbital and the central sp^2 carbon of the NCY fragment (Figure 1.26). For this geometry to be sterically unhindered the R-groups present on the NR_2 moiety are generally less sterically demanding, allowing the electron donation from the NR_2 to the NCY unit and the overall sigma or pi basicity of the ligand system to be tuned by both the electronic effects of the R groups and the size of these groups.

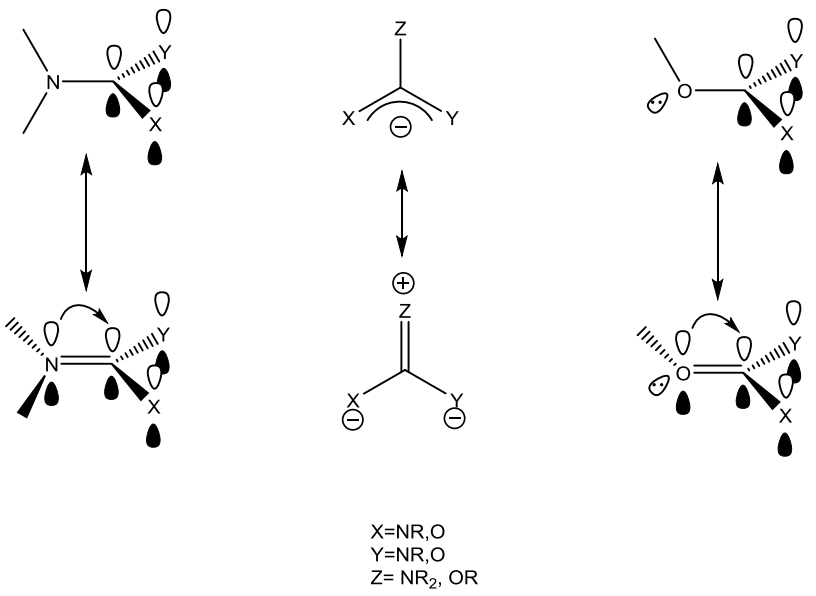

Figure 1.26: Diagram showing how orientation of NRR' or OR group effects delocalisation of electron density.

The steric effect of the alkyl groups in guanidinate ligands has been observed experimentally with zirconium guanidinate complexes containing either $N(SiMe_3)_2$ or NMe_2 groups (Figure 1.27).[83,84] The bulkier guanidinate **I** was published by Richeson and co-workers, the $N(SiMe_3)_2$ group is perpendicular to the NCN backbone resulting in a longer Zr-N bond length than that observed in **II** which has a NMe_2 group co-planar with the NCN backbone (**I** = 2.242(4) Å, **II** = 2.206(3) Å). Compound **II** was published by Arnold and co-workers; the other notable structural difference is a longer C-NR_2 length observed for **I**, at 1.408(6) Å compared to **II** at 1.363(5) Å.

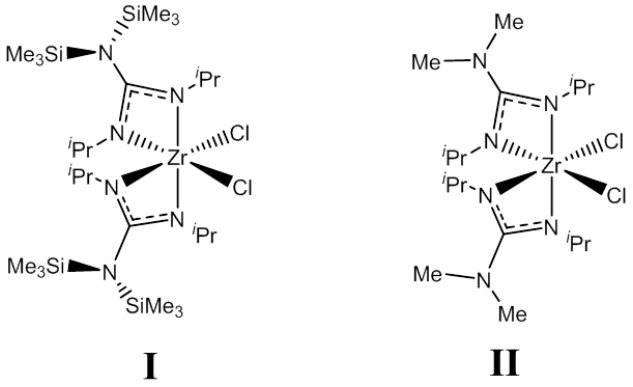

Figure 1.27: Structures of I and II

For electron delocalisation to be favourable between an OR group and the central XCY core orbital overlap is again required. Donation is not possible if the oxygen is sp^3 hybridised as the lone pairs situated on the oxygen will be orientated away from the delocalised XCY core. For the sp^2 hybridised OR group overlap is possible when the group is co-planar with the XCY core (Figure 1.26). Electron donation can also occur if the OR group is sp hybridised, in this instance the C-O-R angle is approximately 180° and so alignment of either of the two p-orbital based lone pairs is possible. Any degree of π bonding will result in the reduction of the C-OR bond length.

Due to the delocalisation of the negative charge across the ligand a variety of different binding modes are available. In Figure 1.28 a selection of these possible binding modes are shown. The coordination of these ligands can be affected by several factors including the size of the alkyl groups attached, the size of the metal centre, the bite angle the ligand may adopt to form a chelate and the size and orientation of other ligands bound to the metal centre.

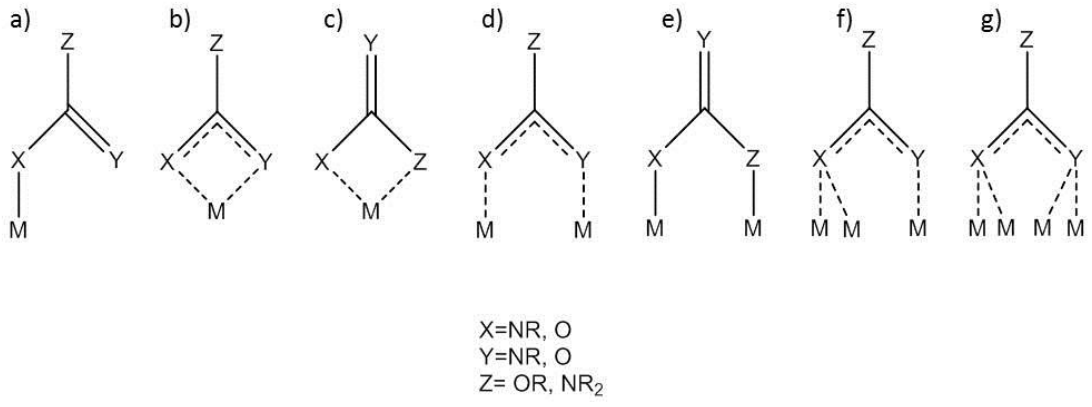

Figure 1.28: Some of the possible binding modes of O, O' N, O and N,N' chelating ligands can adopt

1.7.2 Guanidinate CVD precursors

Guanidinate ligands have been incorporated into CVD precursors recently for metal,[85] metal oxide,[86–89] metal nitride[90–96] and metal carbon-nitride thin films.[97,98] Initial studies into the use of guanidinate ligands to stabilise metal complexes for CVD applications were published by Carmalt and co-workers in 2005 who reported the synthesis and deposition of titanium guanidinate complexes for the formation of titanium nitride thin films (Figure 1.29).[97] The application of guanidinate precursors as metal oxide precursors is restricted to multi-source depositions as the ligand system does not contain any oxygen, therefore depositions carried out to grow metal oxide thin films require an oxygen source introduced. Guanidinate complexes have been utilised for the formation of hafnium oxide, gadolinium oxide and dysprosium oxide, details of the precursors and reaction conditions are presented below.

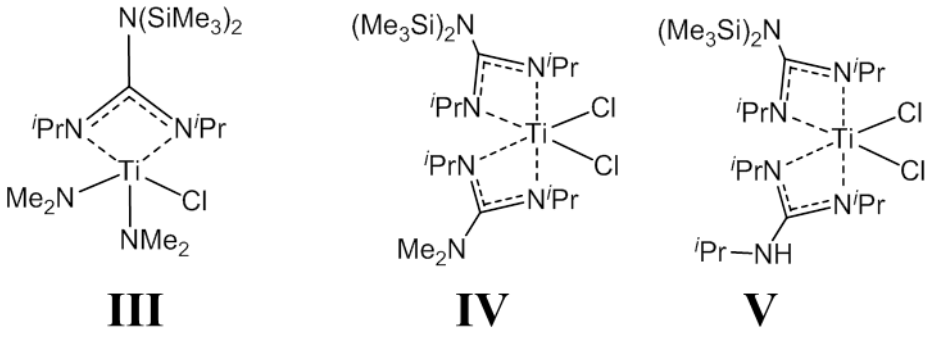

Figure 1.29: Titanium guanidinate complexes used CVD of TiN thin films

1.7.2.1 Hafnium guanidinate precursors for HfO_2

Devi and co-workers reported the use of a hafnium guanidinate complex **VI** for the formation of HfO_2 thin films.[89] The precursor is synthesised by taking $Hf(NEtMe)_4$ in hexanes and adding two equivalents of N,N'-diisopropylcarbodiimide. The complex was isolated through removal of the solvent and purified through recrystallisation from hexane/diethyl ether mixture. The heteroleptic compound consists of two guanidinate ligands bound in a κ^2 arrangement in a *cis* geometry, with two NMeEt groups completing the coordination sphere of the hafnium centre (Figure 1.30). Depositions were carried out using a low pressure CVD reactor configuration with the precursor vaporised through heating to 120 °C and deposited onto silicon substrates heated between 300 °C and 700 °C in the

presence of oxygen. Analysis of the films showed that growth between 300 °C and 500 °C resulted in amorphous material while temperatures of 600 °C and higher resulted in crystalline HfO_2.

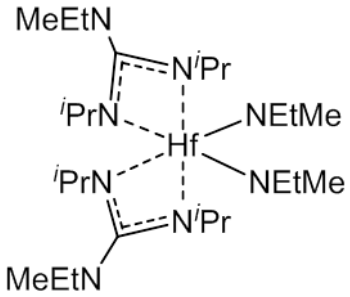

VI

Figure 1.30: Hafnium guanidinate precursor used for HfO_2 deposition

Devi and co-workers also evaluated the dialkyl hafnium guanidinate complex **VII** as a potential precursor for HfO_2 thin films.[87] The precursor was synthesised by taking reacting $HfCl_4$ with two equivalents of the lithiated N, N'-diisopropylguanidinato ligands in hexanes. This resulted in the bis-chloro bis-guanidinato system, which was reacted further with two equivalents of MeLi to afford the dialkyl complex Hafnium guanidinate precursor used for HfO_2 deposition **V**. The heteroleptic compound consists of two guanidinate ligands bound in a κ^2 arrangement in a *cis* geometry with two methyl groups completing the coordination sphere of the hafnium centre (Figure 1.31). Depositions were carried out using a low pressure CVD reactor configuration with the precursor vaporised at 100 °C and deposited onto silicon wafers heated between 300 °C and 700 °C in the presence of oxygen. Analysis of the films showed growth was achieved at temperatures of 300 °C and higher, with crystalline material grown from 500°C and higher. This is 100°C lower than observed for the bis-amido analogue **VI** discussed above.

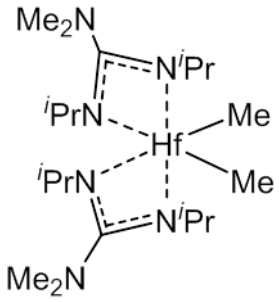

VII

Figure 1.31: Hafnium guanidinate precursor used for HfO_2 deposition

Daniele and co-workers evaluated two hafnium precursors **VI** and **VII** synthesised through the reaction of $Hf(NEt_2)_4$ with one equivalent of an unsymmetrical carbodiimide (Figure 1.32), the precursors were isolated as a liquid.[88] Deposition studies using **VI** and **VII** were carried out using pulsed liquid injection CVD on to silicon substrates heated between 350 °C and 580 °C in the presence of oxygen. Analysis of the films showed amorphous growth at 350 °C for both compounds. For compound **VI** FTIR analysis suggested crystalline growth was achieved at 500 °C, while XRD analysis of films grown with precursor **VII** showed monoclinic crystalline growth at 530 °C, at higher deposition temperatures of 580 °C cubic HfO_2 was also observed.

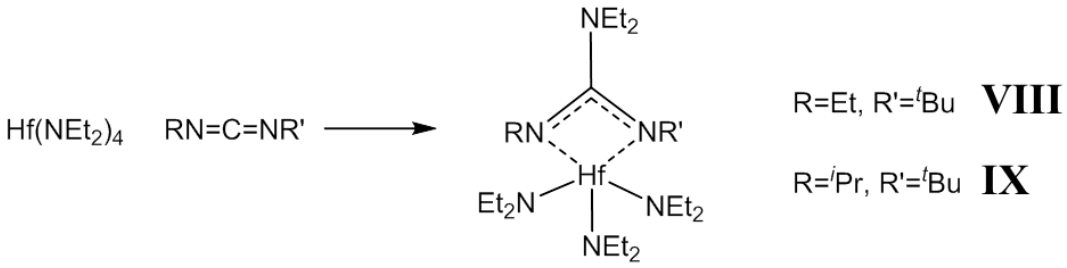

Figure 1.32: Synthetic route to hafnium guanidinates using unsymmetrical isocyanates. Systems were evaluated as HfO_2 precursors.

1.7.2.2 Zirconium guanidinate precursors for ZrO_2

Devi and co-workers also utilised as zirconium guanidinate precursor **X** for the formation of ZrO_2. The precursor was synthesised by reacting two equivalents of N, N'-diisopropylcarbodiimide with one equivalent of $Zr(NMe_2)_4$ in hexanes. The compound was purified by recrystallisation from hexanes at -35°C. The precursor consists of two κ^2 guanidinate ligands bound in a *cis* geometry with two NMe_2 groups completing the coordination sphere of the zirconium centre (Figure 1.33). Deposition studies were carried out using a low pressure CVD apparatus on silicon substrates between 400 °C and 700 °C in the presence of oxygen. Analysis of the films showed ZrO_2 was formed at all temperatures, with low temperature (<500 °C) resulting in amorphous films, while higher temperature depositions had diffraction peaks that matched ZrO_2.

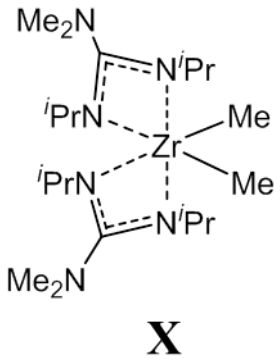

X

Figure 1.33: Zirconium guanidinate complex used for ZrO_2 deposition

1.7.2.3 Lanthanide guanidinate precursors for Ln_2O_3

Rare earth metal oxides have also been deposited using guanidinate based precursors. Devi and co-workers evaluated precursors for both gadolinium oxide and dysprosium oxide using tris guanidinate complexes **XI** and **XII**. The precursors were synthesised by reacting MCl_3 with three equivalents of the lithiated N, N'-diisopropylguanidinato ligand in diethyl ether, before recrystallising in hexanes (**XII**), or diethyl ether (**XI**). The compounds have a near identical structure with three κ^2 guanidinate ligands bound in a distorted trigonal prism geometry around the metal centre (Figure 1.34). Depositions were carried out using a low pressure CVD apparatus with the precursors both vaporised at 120 °C deposited on silicon

and sapphire substrates heated between 300-700 °C. Successful depositions were reported across the temperature window for both Gd_2O_3 and Dy_2O_3, with both materials appearing to be amorphous between 300-400°C before diffraction peaks corresponding to cubic Gd_2O_3 and Dy_2O_3 are observed at 500°C and higher.

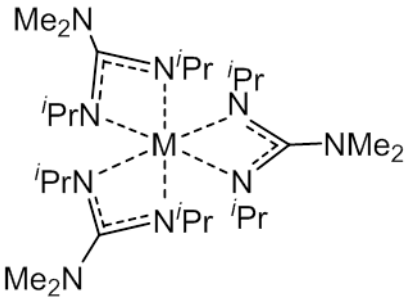

M=Gd **XI**

M=Dy **XII**

Figure 1.34: Gadolinium and dysprosium guanidinate complexes for Gd_2O_3 and Dy_2O_3 depositions

1.7.3 Tin guanidinate complexes

There are no reported tin guanidinate complexes that have been utilised in CVD applications in the literature. Lappert and co-workers reported the first tin (IV) guanidinate complex in 1965 through the reaction of Me_3SnNMe_2 with di-p-tolylcarbodiimide which resulted in a pale yellow oil.[99] Tin(II) guanidinate complexes were not reported until 2006 when Jones and co-workers reported the synthesis of **XIII** (Figure 1.35).[100] The compound was synthesised through the reaction of the lithiated guanidinate with $SnCl_2$ to form the heteroleptic species. Further work by Jones and co-workers has been carried out utilising bulky guanidinate tin complexes to stabilise low valent metal complexes containing metal-metal bonds.[101,102]

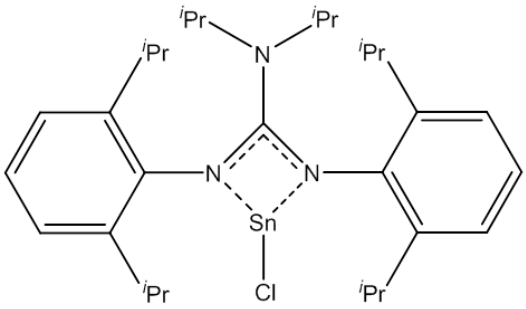

XIII

Figure 1.35: Structure of bulky tin(II) guanidinate compound

Růžička and co-workers reported a selection of homoleptic and heteroleptic tin(II) guanidinate compounds synthesised through the insertion of symmetrical carbodiimide compounds into Sn-N$(SiMe_3)_2$ bonds (Figure 1.36).[103] The heteroleptic systems **XIV**, **XV** and **XVI** formed through 1:1 reaction with $[Sn\{N(SiMe_3)_2\}_2]_2$ and the carbodiimide were formed regardless of the substituent on the carbodiimide in good yield with the ^{119}Sn NMR spectra obtained ranging from δ -87ppm to -127 ppm in C_6D_6. The heteroleptic chloride complexes **XVII**, **XVIII** and **XIX** were also formed regardless of substituent when the carbodiimide is taken in a 1:1 ratio with $(Me_3Si)_2NSnCl$ with the ^{119}Sn NMR spectra showing a downfield shift to δ -30 ppm to -108ppm in C_6D_6. For the formation of the homoleptic bis guanidinate systems only the reaction with di-p-tolylcarbodiimide and the unsymmetrical N-[3-(dimethylamino)propyl]-N′-ethylcarbodiimide gave isolatable

compounds **XX** and **XXI** with upfield $^{119}Sn\{^{1}H\}$ NMR chemical shifts of δ -377 ppm and -432 ppm reported in C_6D_6.

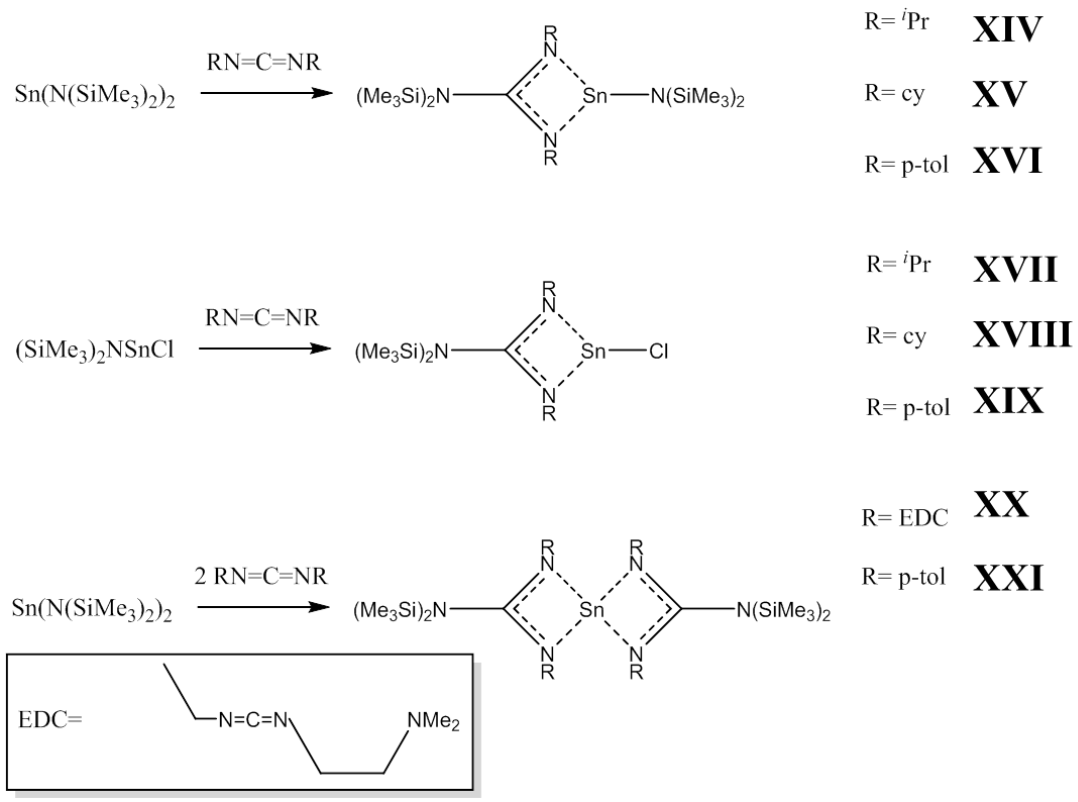

Figure 1.36: Synthesis of tin(II) guanidinate compounds through insertion of carbodiimide into Sn-N(SiMe$_3$)$_2$ bonds

1.7.4 Carbamate CVD precursors

The utilisation of dialkyl N, N' carbamato-type ligand systems for the CVD of metal chalcogenide materials has primarily been used for the deposition of metal sulphide and metal selenide thin films using di-thio and di-seleno carbamate precursors (Figure 1.37).[76] While extensive research has gone into the utilisation of these di-thio and di-seleno carbamate ligands in single-source precursor systems research into the use of di-alkyl carbamate ligands as CVD precursors is limited.

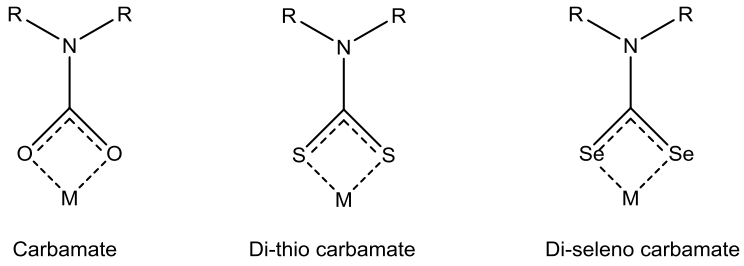

Figure 1.37: Carbamate, di-thio carbamate and di-seleno carbamate structures

1.7.4.1 Magnesium carbamate precursors for MgO

Lamb and co-workers reported the use of a magnesium carbamate system (**XXII**) as a single-source CVD precursor for the formation of MgO.[104] The cluster is readily formed when $Mg(NEt_2)_2$ is stirred in THF with CO_2 bubbled through the mixture.[105] Compound **XXII** consists of six magnesium atoms supported by 12 diethylcarbamate ligands; the solid state structure is shown in Figure 1.38. Deposition studies were carried out using a LPCVD reactor with the precursor vaporised through heating to 120-175°C, while the silicon substrate was heated between 350 and 600°C. Analysis of the deposited films showed crystalline growth at all temperatures. As the substrate temperature was increased the (111) plane increasingly became the dominant orientation, and at temperatures exceeding 450 °C only the major peak corresponding to the (111) plane and a small reference to the (220) were observed.

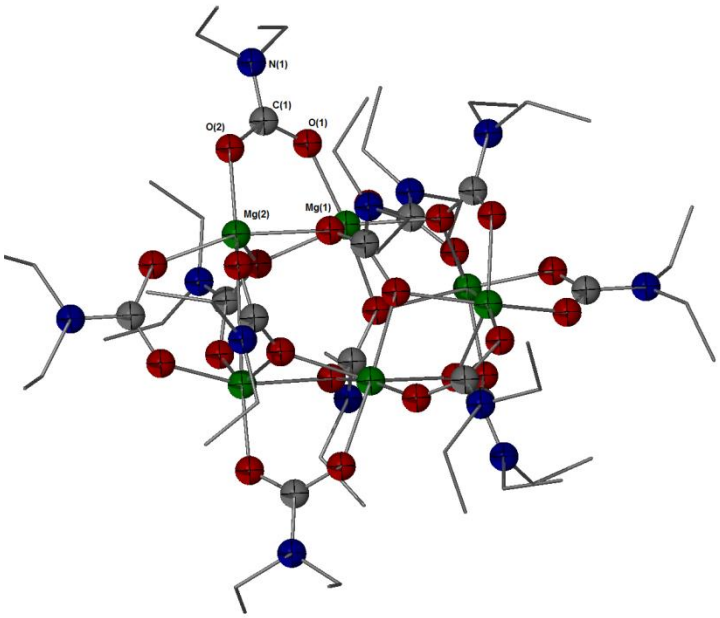

Figure 1.38: Molecular structure of $Mg_6(O_2CNEt_2)_{12}$ (XXII) used in LPCVD experiments to form MgO

1.7.4.2 Zinc carbamate precursors for ZnO

Lamb and co-workers also evaluated a volatile zinc cluster for the LPCVD of zinc oxide.[106] The cluster, **XXIII** was originally reported by Calderazzo and co-workers through reaction of zinc metal and $HNEt_2$ in an autoclave under 50 atm of CO_2.[107] The resulting $Zn_4(O)(CO_2NEt_2)_6$ cluster is formed through the de-oxygenation of CO_2 to form the diethylformamide. The molecular structure of **XXIII** consists of a central oxygen bound to four zinc atoms in a tetrahedral geometry; each zinc is then bound to three bridging carbamate ligands (Figure 1.39). The precursor was evaluated in LPCVD experiments, with the precursor vaporised through heating to 185-195°C. Growth studies were conducted on silicon (111) wafers, heated to 350-450°C. Comparison of the films grown using **XXIII** with ZnO films deposited using RF sputtering show a similar film morphology when analysed in the SEM. Analysis of films grown with **XXIII** had a carbon content below the detectable limit by XPS showing a high film purity, the films also showed significant orientated growth with only the (002) reflection observed in the PXRD spectra. On introduction of water less orientated growth was observed.

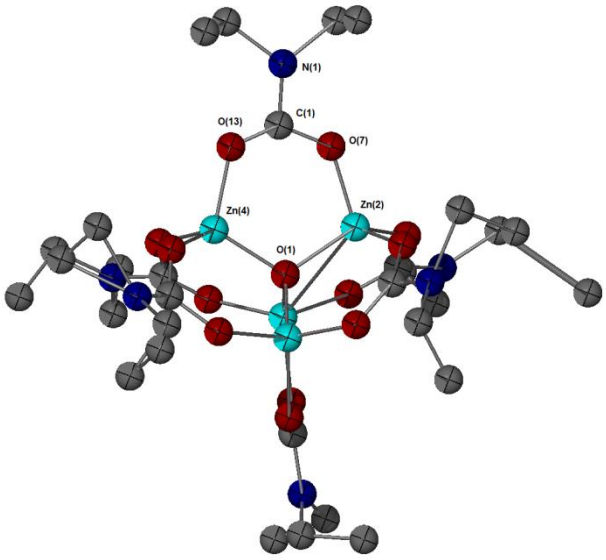

Figure 1.39: Molecular structure of $Zn_4(O)O_2CNEt_2)_6$ (XXIII) used for LPCVD experiments to form ZnO

1.7.4.3 Antimony carbamate precursors for Sb_2O_3

Molloy and co-workers reported a series of antimony carbamate complexes as potential precursors for the formation of antimony oxide, Sb_2O_3.[108] They were formed in an analogous manner to the magnesium complexes with $Sb(NR_2)_3$ taken in solution and CO_2 bubbled through the reaction mixture. The $Sb(O_2CNMe_2)_3$ system **XXIV** was found to be dimeric in the solid state with short intermolecular contacts of 2.769 Å between the Sb of one monomer with the oxygen of a neighbour (Figure 1.40). The molecular structures are thought to be influenced by the lone pair located on the Sb centre which are parallel to each other in this dimer. Precursor **XXIV** was used to grow Sb_2O_3 thin films via LPCVD experiments. The precursor was vaporised by heating to 130 °C, with depositions occurring on a glass substrate at 380 °C. Analysis of the films showed them to be crystalline, although the crystallite size was much smaller than previous Sb_2O_3 growth experiments using $Sb(OBu^n)_3$ (1 μm vs. 1-10 μm).[109]

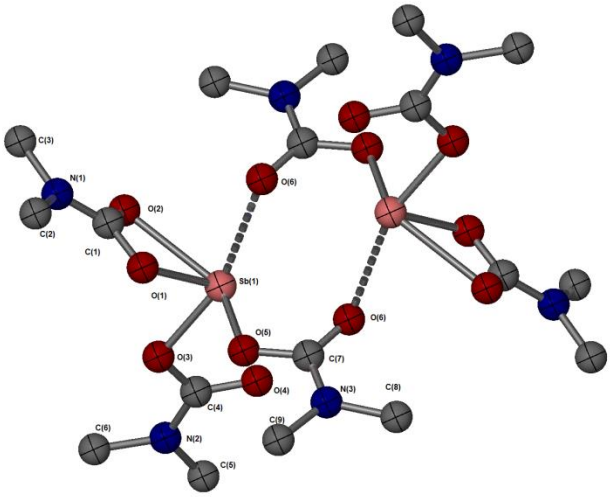

Figure 1.40: Molecular structure of $[Sb(O_2CNMe_2)_3]_2$ (XXIV) used in LPCVD experiments to form Sb_2O_3

1.7.5 Tin(II) carbamates

While the reaction of tin(IV) amides with CO_2 has been investigated by several groups,[108,110,111] the reactivity of tin (II) amides towards related small molecules has received little interest in the literature. The reactivity of heteroleptic tin amide systems such as the bulky β- diketiminiate stabilised tin diisopropylamide **XXV** has been investigated as a catalyst for the polymerisation of lactide.[112] The reactivity of this system has also been investigated with reactive ketones, terminal acetylenes,[113] methyl triflate and methyl iodide.[114] Reactions between **XXV** and heterocumulene compounds are limited to work by Fulton and co-workers who described that reaction of **XXV** and CO_2 resulted in the formation of tin carbamate **XXVI** (Figure 1.41).[114] The compound was analysed by multinuclear NMR spectroscopy. The ^{119}Sn resonance came at δ= -394 ppm, upfield of the parent amide. The ^{13}C NMR spectrum featured a resonance at δ = 161.8ppm which the authors attribute to the carbamate sp^2 carbon. Single crystal X-ray diffraction analysis showed that the carbamate ligand is bound to the metal through the oxygen atom. This contrasts to the analogous lead(II) carbamate where the ligand was observed to bind through the nitrogen. [115]

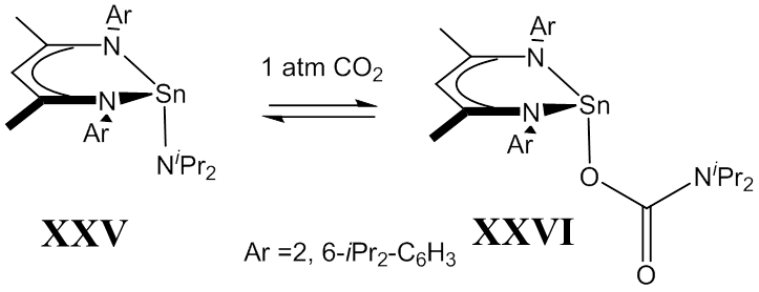

Figure 1.41: Formation of a tin carbamate species XXVI through reaction of tin amide XXV with CO_2

The insertion of CO_2 into homoleptic tin amide complexes has been evaluated for both $[Sn(NMe_2)_2]_2$ and $[Sn\{N(SiMe_3)_2\}_2]_2$ with different results observed depending on the amide investigated and the reaction conditions. The reaction between $[Sn\{N(SiMe_3)_2\}_2]_2$ and CO_2 has evidence of a complex reaction pathway.[116] The insertion of CO_2 is quickly followed by the migration of $SiMe_3$ group on to an oxygen atom and the consequential elimination of a trimethlysilyl isocyanate fragment (Figure 1.42). The 1,3 shift of the $SiMe_3$ group is thought to be facilitated by the bidentate binding of the carbamate to the metal centre which enhances the electrophilic character. This silyl migration is also observed in small quantities when $Ln(N(SiMe_3)_2)_3$ (Ln = Pr, Nd) derivatives are exposed to an atmosphere of CO_2 with 5-10 % of Me_3SiNCO produced.[117] The tin based reaction is further complicated by the reactivity of

Me_3SiNCO with $[Sn\{N(SiMe_3)_2\}_2]_2$, which undergoes an insertion reaction preceded by an additional 1,3 $SiMe_3$ migration and consequent elimination of the $Me_3SiNCNSiMe_3$ carbodiimide .

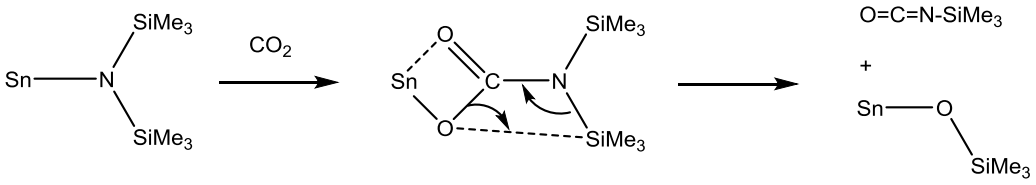

Figure 1.42: Mechanism for the formation of $O=C=NSiMe_3$ through insertion of CO_2 into $Sn(N(SiMe_3)_2$

The reaction between $Sn(NMe)_2$ and CO_2 has recently been investigated by Kemp and co-workers (Figure 1.43).[118] The carbamate **XXVII** was formed by taking $Sn(NMe_2)_2$ in hexanes and bubbling CO_2 through the solution. A white precipitate is formed which could be isolated and re-crystallised from warm toluene. Characterisation of **XXVII** by multinuclear NMR spectroscopy suggested the formation of a simple symmetrical bis-carbamato compound. Analysis of the compound by IR spectroscopy showed multiple vibrations below $1600cm^{-1}$, indicative of a compound containing both bridging and terminal carbamate groups. This was confirmed by single crystal X-ray diffraction studies which revealed a dimeric compound with each tin bound to two bridging carbamate ligands, and one terminal ligand. There is also significant interaction between dimers to form a polymeric chain with an Sn-O distance of 2.8499 (18) Å between neighbouring molecules giving an extended chain-like polymeric network.[118]

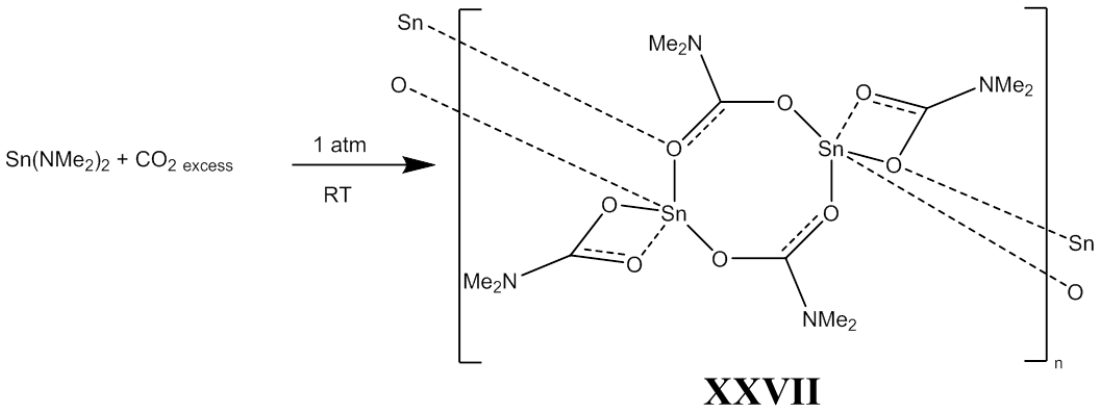

XXVII

Figure 1.43: Synthetic route for the formation of XXVII

Kemp and co-workers have also studied the CO_2 insertion into $Sn(N(SiMe_3)Ar^F)_2$ (Ar^F=3,5 – $(CF_3)C_6H_3$) (**XXVIII**) to evaluate the effect of electron withdrawing groups on the insertion of CO_2 and potential migration of the $SiMe_3$ group.[119] They found that rather than eliminating the expected isocyanate the reaction led to the formation of **XXIX**. The proposed mechanism is shown in Figure 1.44. The process is thought to be initiated by generation of the Ar^FNCO fragment in an analogous fashion to that reported by Sita (Step A). The isocyanate is then thought to insert into another molecule of $Sn(N(SiMe_3)Ar^F)_2$ (B). At this point the reaction is believed to proceed by a re-arrangement to form the ureate (D and E), rather than formation of Sn-$OSiMe_3$ and elimination of a carbodiimide as observed by Sita (C). This mechanism is rationalised by a near 50% yield, in keeping with a further 50% of the starting tin material being consumed and forming $Sn(OSiMe_3)_2$.

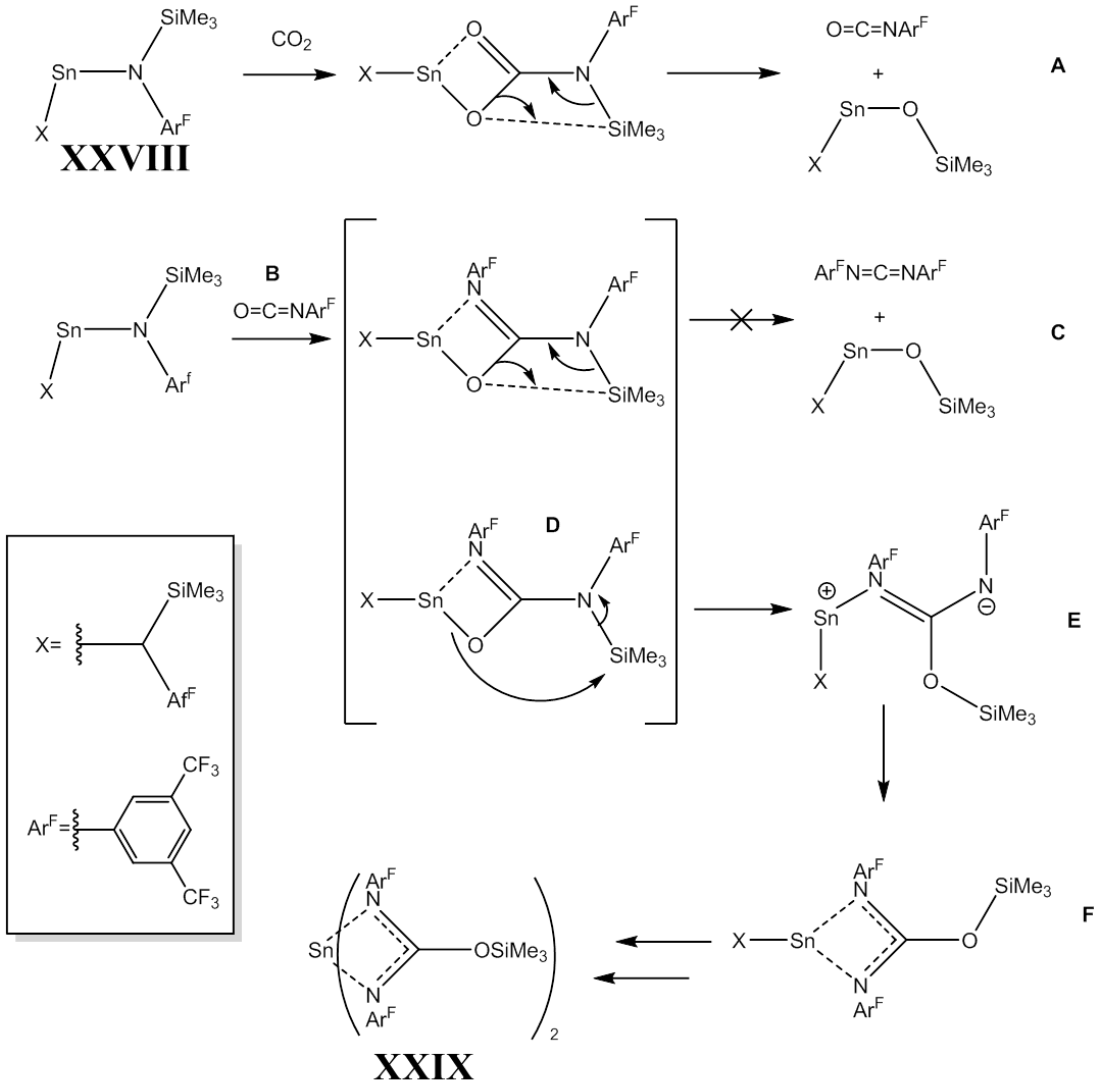

Figure 1.44: Proposed mechanism for the formation of XXVII through the reaction of XXVI with CO_2.

1.7.6 Iso-carbamate CVD precursors

An alternative to carbamate ligands is the iso-carbamate system shown in Figure 1.45. This class of compound is synthesised by insertion of an isocyanate into a metal-alkoxide bond.

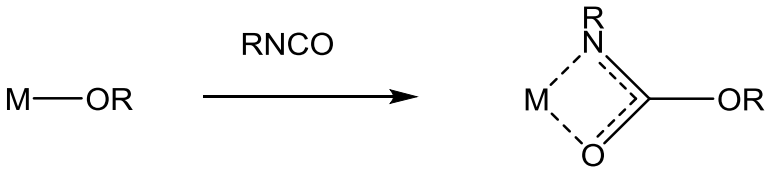

Figure 1.45: Possible synthetic route to metal iso-carbamate compounds

1.7.6.1 Hafnium iso-carbamate precursors for HfO_2

Devi and co-workers reported the synthesis of the hafnium iso-carbamate complex **XXX** as a potential CVD precursor for the formation of HfO_2.[120] The precursor was synthesised by reacting $Hf(O^iPr)_4$ with four equivalents of ^{i}PrNCO. The compound was characterised by single crystal X-ray diffraction studies, with the molecular structure found to exist as a monomer with the hafnium bound to four κ^2-N, O iso-carbamate ligands (Figure 1.46). Compound **XXX** was evaluated using low-pressure CVD apparatus with the precursor vaporised at 100°C and depositions carried out on silicon substrates between 250 °C and 700 °C. Analysis of the deposited films shows crystalline HfO_2 can be achieved at temperatures of 250 °C half the temperature that observed for the hafnium guanidinate complex **VII**.

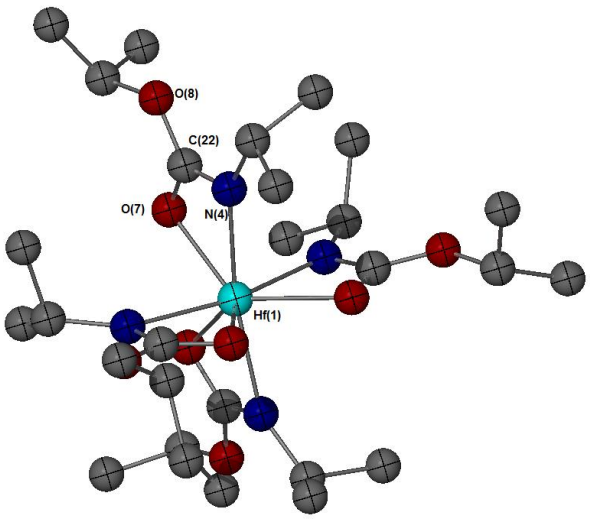

Figure 1.46: Molecular structure of $Hf(N(^iPr)C(O)O^iPr)_4$ (XXX) used in LPCVD experiments to form HfO_2

1.7.7 Tin iso-carbamate compounds

There are no reports in the literature for tin iso-carbamate compounds used as CVD precursors. Davies and co-workers reported the formation of several trialkyltin iso-carbamate compounds formed through the insertion reaction of an isocyanate with a trialkyltin alkoxide compound in 1965, although due to spectroscopic limitations they could not fully ascertain the binding mode of the iso-carbamate ligand.[121] Further research by Davies and co-workers in 1967 examined the reactivity of dibutyltin dimethoxide with phenyl isocyanate and ethyl isocyanate in 1:1 and 1:2 ratios showed the formation of both the mono iso-carbamate and bis-isocarbamate compound.[122] The publication of tin(II) iso-carbamate compounds followed shortly in 1969 by Zuckerman and co-workers.[123] They reported the reaction of tin(II) dimethoxide with two equivalents of phenyl isocyanate, which when hydrolysed yielded methyl N-phenylcarbamate consistent with the reaction forming the homoleptic bis iso-carbamate tin species.

1.7.8 Tri-alkyl ureate CVD precursors

The application of trialkyl ureate ligands as precursors for the CVD of materials is limited to the iso-ureate **XXXI** published by Johnson and co-workers for the deposition of copper metal.[124] The dimeric precursor has two copper atoms bridged by two iso-ureate ligands in a μ_2-(κ^1-N) (κ^1-N') binding fashion with the $\{Cu_2(N_2C)_2\}$ core existing in a planar geometry (Figure 2.15). For delocalisation to occur the sp^2 hybridised oxygen centre would need to lie co-planar to the backbone of the ligand. For compound **XXXI** the OMe moiety lies 72° perpendicular to this plane suggesting no delocalisation onto the OMe group. This is further evidenced by the C-OMe bond length of 1.384(3) Å which suggests single bond character. The precursor was used in LPCVD at temperatures ranging from 225-300 °C, with optimum growth occurring at 225 °C, providing the smoothest films and the lowest contamination of carbon or oxide.

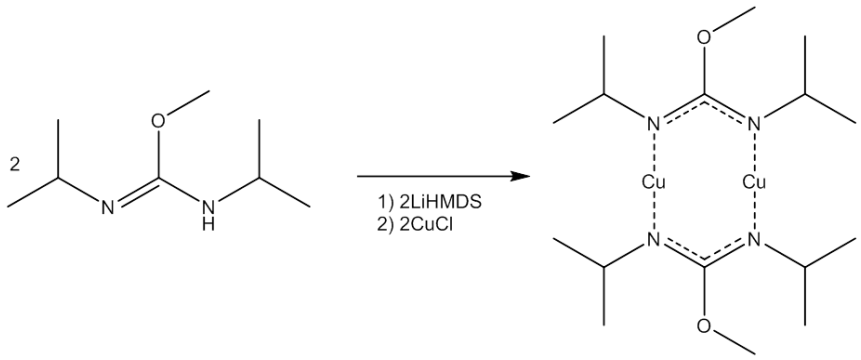

XXXI

Figure 1.47: Synthetic route for the formation of XXXI

1.7.9 Tin (II) ureate complexes

There are no reported tin (II) ureate complexes in the literature. Attempts to synthesise ureates by isocyanate insertion into $[Sn\{N(SiMe_3)_2\}_2]_2$ resulted in similar 1, 3 migration of the $SiMe_3$ group onto the oxygen that was observed by Sita and co-workers when $[Sn\{N(SiMe_3)_2\}_2]_2$ was subjected to an atmosphere of CO_2.[116] In the case of reaction with isocyanates, the unsymmetrical carbodiimide is extruded rather than the isocyanate (Figure 1.48).[125–127]

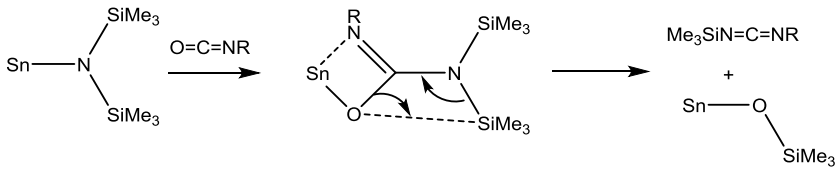

Figure 1.48: Mechanism for formation of carbodiimides through reaction of isocyanate with $[Sn\{N(SiMe_3)_2\}_2]_2$ group.

This methodology was extended further through the synthesis of unsymmetrical bisamides with only one silylated group in the hope that nonsilylated carbodiimides could be synthesised (Figure 1.49).[125] This reaction proceeded as expected with bisamides **XXIX-XXXVI** investigated with a range of isocyanates. Mechanistic studies using the symmetrical bisamide **XXX** centred on the reaction of aryl isocyanates with different electron donating and withdrawing groups. A Hammett plot of the rate of reaction between **XXX** and the isocyanates gave a value of ρ = -0.64. The negative value of ρ indicates that the rate of reaction is facilitated by electron donating groups, and infers that the rate is related to the resultant increase in nucleophilicity of the isocyanate.[126] This data suggests the rate determining step is likely to involve coordination of the heterocumulene to the electron deficient divalent tin centre.[126] This is in slight disagreement with previous claims by Sita and co-workers who postulated that the rate determining step was the breaking up of intermediate mono-insertion dimers that possess tri-coordinate tin(II) centres.[127]

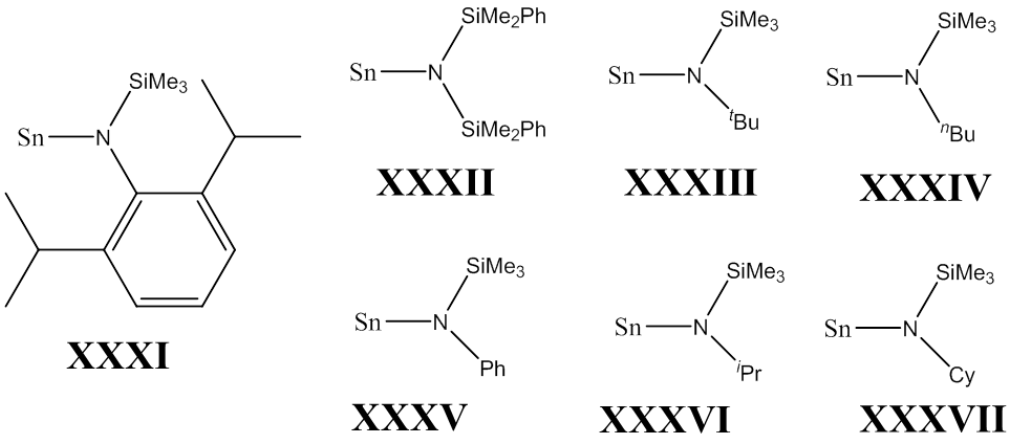

Figure 1.49: The different symmetrical and unsymmetrical tin silyl amides reacted with isocyanates for the formation of unsymmetrical carbodiimides.

1.7.10 Tin Carbonate compounds

There are no reported CVD compounds utilising alkyl carbonate ligands reported in the literature for any metal or metal oxide deposition process. Carbonate compounds are synthesised reacting a metal alkoxide with CO_2 (Figure 1.50).

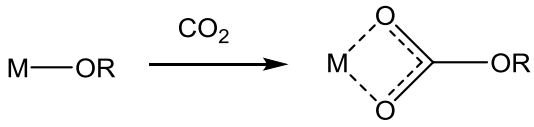

Figure 1.50: Synthetic route to the formation of metal alkyl carbonate compounds

The reactivity of tin alkoxides with CO_2 has been previously studied with a variety of different compounds. Early research by Davies and co-workers investigated the reaction of tributyltin methoxide with CO_2, the resulting compound was found to exist as an oil.[128] This reaction was re-investigated by Blunden and co-workers, who utilised Mössbauer spectroscopy measurements to ascertain that the tin centre had a five-coordinate geometry with the carbonate ligand proposed to bind in an κ^2 O, O' fashion.[129]

In the late 1990's and early 2000's there was an increase in research into tin carbonate complexes through the application of tin catalysts for poly carbonate synthesis. Sakakura and co-workers successfully isolated the tin carbonate species **XXXIX** as part of studies into the catalytic reaction between CO_2 and methanol to form dimethylcarbonate.[130] The catalyst used was dimethyltindimethoxide **XXXVIII**, which was found to exist as a methoxo bridged dimeric compound (Figure 1.51). The authors comment that the carbonate is unstable in

solution at room temperature under nitrogen and readily releases CO_2, and the carbonyl carbon-tin interaction is weak in the solid state analysis (2.822 Å).

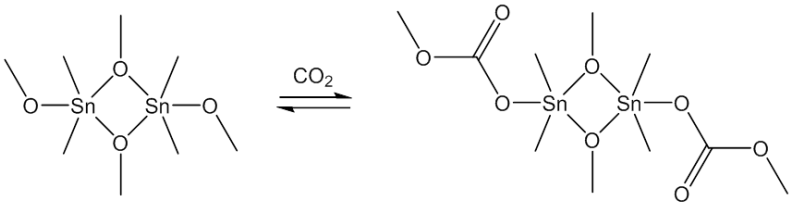

XXXVIII **XXXIX**

Figure 1.51: Synthesis of tin(IV) alkyl carbonate compound through reaction of XXXVIII with CO_2

Ballievet-Tkatchenko and co-workers have also investigated the reactivity of tin-oxygen bond systems to gather information for the catalytic formation of dimethylcarbonate using tin catalysts.[131] Part of the study included investigation into the effect of the alkyl group bound to the oxygen on CO_2 insertion for nBu_3SnOR and $nBu_2Sn(OR)_2$ systems (Figure 1.52). For the mono-alkoxide systems they found that quantitative formation of the carbonate was observed for the alkyl systems with equilibrium reached in 30 minutes for **XLI**, **XLII**, and 18h for **XLII**. The phenoxy system had no observable reaction. For the bis-alkoxide systems only one equivalent of CO_2 reacted with the tin system, even when put under an excess amount of CO_2. The insertion of a second equivalent of CO_2 maybe hindered by steric crowding around the tin centre, or it the reaction maybe less favoured due to the need to break up the alkoxy-bridged dimer that is thought to form.

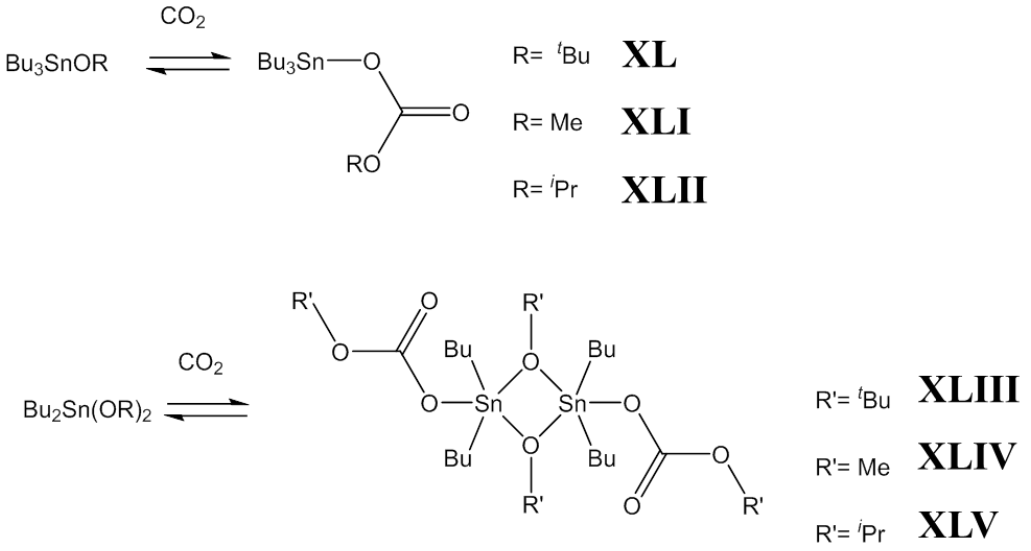

Figure 1.52: Reactions between tin(IV) alkoxide systems and CO_2 carried out by Ballivet-Tkatchenko and co-workers

Fulton and co-workers investigated the reactivity of tin(II) alkoxides with CO_2 using a β-diketonate ligand to satisfy the coordination sphere of the tin centre (Figure 1.53). The reaction with CO_2 was found to be facile with the carbonate species formed and detected in situ via NMR spectroscopic measurements. Isolation of the carbonate compounds was not possible due to the reversible nature of the reaction. This is in contrast to the lead analogue reported by Fulton and co-workers previously, where the lead carbonate was isolated and characterised by single crystal X-ray diffraction studies. Experiments centred on measuring the time taken to reach equilibrium showed that the R group of the alkoxide had a direct influence on the equilibrium of the system. The observations suggested that steric factors were influential with the smaller isopropyl group taking three hours to reach equilibrium, and the bulky tertiary butyl group requiring three days.

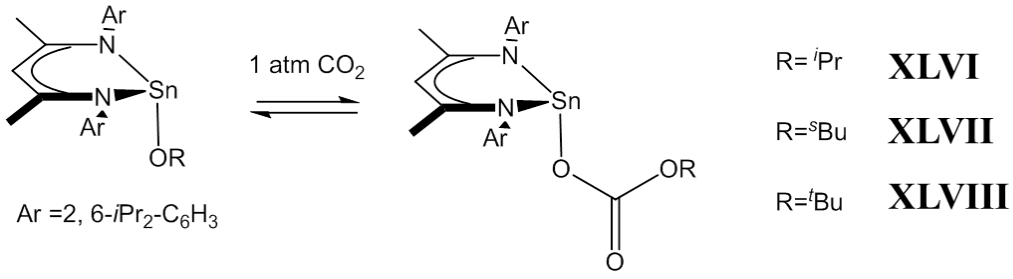

Figure 1.53: The tin(II) alkoxides investigated for reactivity with CO_2 by Fulton and co-workers

1.8 Tin(IV) CVD precursors for SnO_2

It is possible to deposit SnO_2 in CVD processes using many different organometallic, inorganic and metal-organic tin precursors.[25] The deposition process for many tin oxide precursors have been optimised for use with flat glass using on-line coating systems in a continuous method. On-line coatings refer to modifications to the glass which occur when the glass is still hot from the glass making process, this is opposed to off-line coatings which take place when the glass has been cooled and cut. On-line coatings are favoured for mass production of glass based products as they can be added to existing glass manufacturing processes. For example, online CVD coatings are utilised by Pilkington glass NSG in the manufacture of low emissivity glass using an FTO coating, this is marketed as K Glass™. For industrial scale processes a fast, uniform growth rate is required as the glass passes through the system, typically the glass residence time is 1-3 seconds and the target film thickness range from 1-7 μm.[132] For the deposition of tin oxide the most common industrial precursors are tin tetrachloride ($SnCl_4$), dimethyltin dichloride (Me_2SnCl_2) and monobutyltin trichloride (n-$BuSnCl_3$) in conjunction with O_2 and/or H_2O.[132]

The oxidation of $SnCl_4$ to SnO_2 requires both the breaking of tin-chlorine bonds and the formation of tin oxygen bonds in either gas phase or surface reactions. Tin chloride bonds have a high dissociation energy of $\Delta H°$ (298K) = 352.3 kJ mol^{-1} reducing the likelihood of thermal decomposition in the gas phase.[132] Roth and co-workers carried out shock tube measurements on the thermal decomposition of $SnCl_4$; the work indicates that pyrolysis of this precursors is too slow to initiate gas - phase reactions. Experimentally no deposition was found to occur at temperatures up to 923K using 1-3% $SnCl_4$ and 20% O_2 mixtures.[133] At elevated temperatures 950K deposition at rates of 1 Å / minute have been reported and at 1350 K the rate increases to 100Å/ minute.[134] The addition of water to this process significantly increases the rate of deposition, with $SnCl_4$ and water forming SnO_2 at 670K. The increase in deposition through addition of water indicates that a hydrolysis step enhances decomposition, and subsequent formation of tin oxide. The coordination of water to $SnCl_4$ to form species such as $Cl_4Sn(OH_2)_2$ have been proposed.[133,135] The decomposition of these through loss of HCl to generate $Cl_2Sn(OH)_2$ is thermodynamically viable ($\Delta H°$=34.6 kcal mol^{-1}).[133] It is also possible that $SnCl_4$ is hydrolysed on the substrate surface, without prior gas phase reactions. Experimental and theoretical experiments have determined that HCl formation is crucial for the formation of SnO_2 from $SnCl_4$ as this provides a thermodynamic sink to stabilise the chlorine in the system.[133]

For the dissociation of tin-carbon bonds Allendorf and co-workers calculated the Sn-C bond enthalpies for both Me_2SnCl_2 and $nBuSnCl_3$ to be $\Delta H°(298K) = 292.1$ kJ mol^{-1} and 288.3 kJ mol^{-1} respectively.[132] These are lower than the energies calculated for tin-chlorine dissociation ($\Delta H°$ (298K) = 352.3 kJ mol^{-1}) and approximately 100kJ mol^{-1} lower than the C-C bond energy for ethane (380 kJ mol^{-1}).[136] The lower enthalpies for bond dissociation suggest that cleavage of tin-carbon bonds can be thermally activated within a CVD timescale.

This was proven experimentally by Gordon and co-workers who investigated the gas-phase chemistry APCVD of SnO_2 using Me_4Sn and oxygen in the temperature window of 645-752 K.[137] This study, combining kinetic modelling and experimental analysis of the gas phase gave an overall deposition method containing 27 gas phase species and 96 chemical reactions. A summary of the major reaction pathways determined by Gordon and co-workers is presented in Figure 1.54. The study did find that the primary initiation process for the oxidation of Me_4Sn is the cleavage of a tin-carbon bond to produce $Me_3Sn^{\cdot}$ and $CH_3^{\cdot}$ radicals. This initiation, however, was not rate determining, and Gordon and co-workers postulate that the formation of Me_3SnOH and subsequent decomposition and oxidation to be important steps.

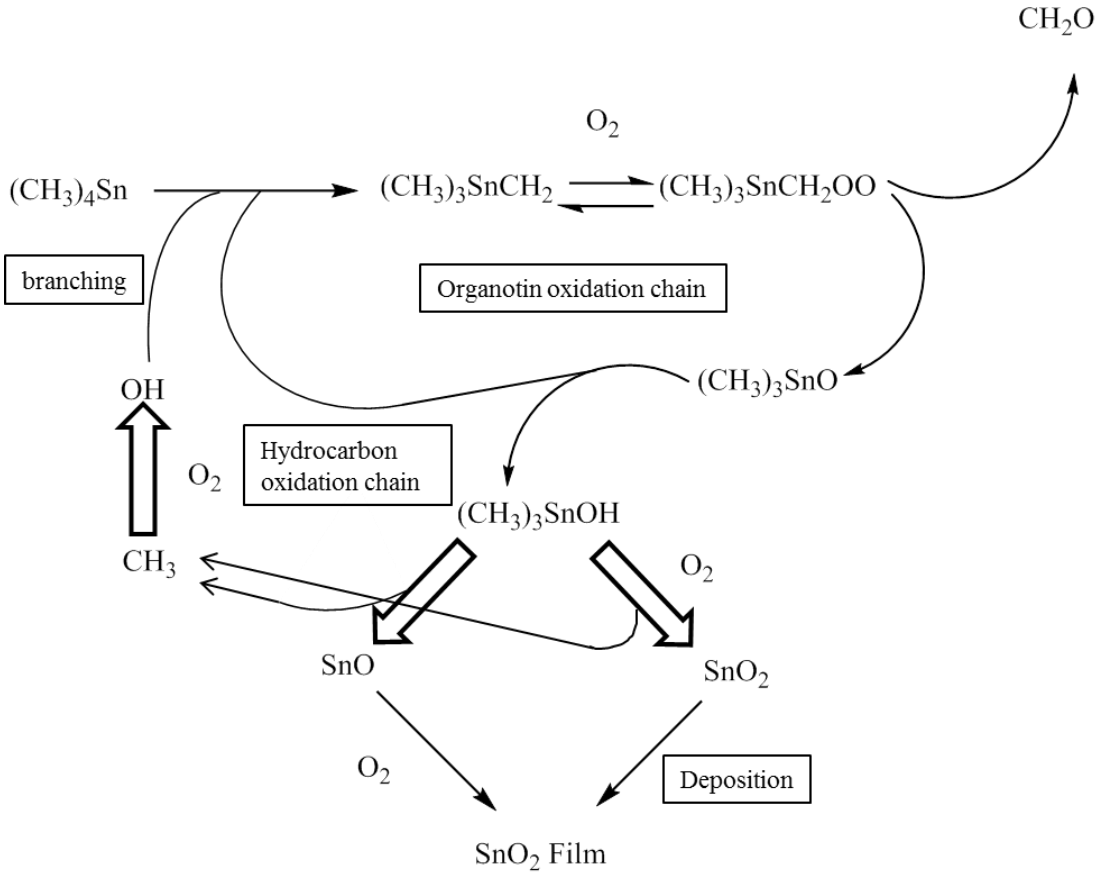

Figure 1.54: Proposed mechanism for formation of SnO_2 using Me_4Sn.[137]

Mechanistic studies of the decomposition of alkyl tin halide complexes such as Me_2SnCl_2 and $nBuSnCl_3$ have also been carried out.[132,138] On evaluation of the gas phase reactions of Me_2SnCl_2 Gordon and co-workers proposed a similar mechanism for deposition to that suggested for Me_4Sn[138] in which deposition is initiated by pyrolysis of Me_2SnCl_2 to generate $MeSnCl_2^{\cdot}$ and $CH_3^{\cdot}$ radicals. Through a series of radical reactions the formation of a hydroxytin intermediate $MeCl_2SnOH$ is postulated to be an important intermediate which decomposes and oxidises to form more radical species in a similar process to that described for Me_4Sn above.[138]

Allendorf and co-workers investigated the reaction kinetics for the decomposition of $nBuSnCl_3$ as a tin oxide precursor.[132] They postulated that the decomposition pathway was influenced by pyrolysis, hydrolysis and surface reactions and the limiting factors were dependent on the reaction conditions. The coordination of two equivalents of water to $nBuSnCl_3$ was calculated to be an exothermic reaction with $\Delta H°(298K) = -62.4$ kJ mol^{-1}; the subsequent elimination of two equivalents of HCl was to form $nBuSnCl(OH)_2$ was also found to be favourable with $\Delta H°(298K) = 129.6$ kJ mol^{-1}. Allendorf and co-workers went on to present five potential models for the deposition of SnO_2 using $nBuSnCl_3$ in a mixture of water and oxygen (Figure 1.55). Models A, B and C assume no gas phase reactions occur and therefore the reactions occur on the substrate surface. For surface reactions to occur at least one reagent needs to adsorb to the surface. For model A $nBuSnCl_3$ adsorbs and then reacts with H_2O and O_2. For model B oxygen adsorbs and decomposes on the surface before reacting with the tin compound and water, and model C is based on the formation of hydroxyl species on the surface which can react with $nBuSnCl_3$ and oxygen. For the two models that assume gas phase reactions can occur (models D and E) only coordination of H_2O with $nBuSnCl_3$ is assumed to occur. Here the pre-bound system can react with oxygen adsorbed to the surface (model D) or the coordinated tin - water compound can adsorb and react with gaseous O_2 (model E). The theoretical models, coupled with experimental data tentatively suggested that the reactive tin species in the deposition of tin oxide involves the gas phase coordination of water to the $nBuSnCl_3$ and subsequent adsorption and reaction with gaseous O_2.

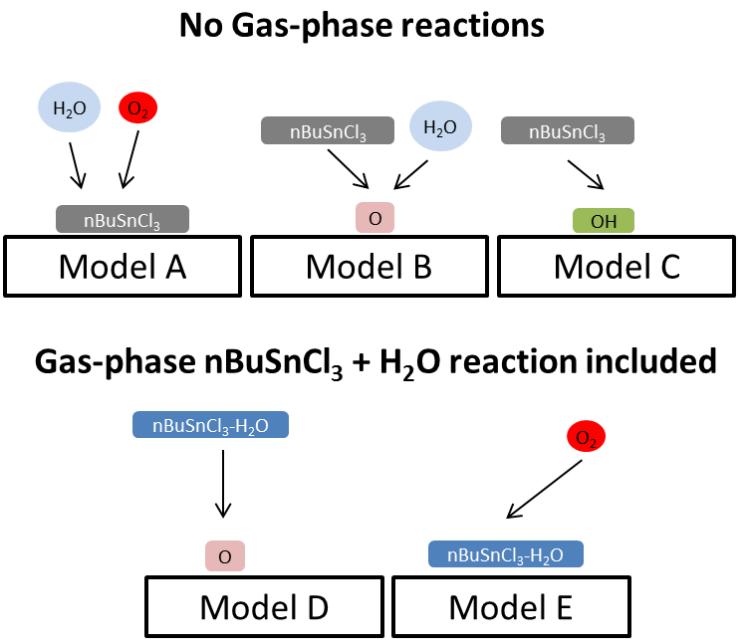

Figure 1.55: Proposed mechanisms for SnO_2 formation using $nBuSnCl_3$ with water and oxygen.[132]

The coordination of two ethylformate molecules to $SnCl_4$ results in the bis-ethylformate adduct **XLVII** (Figure 1.56), which when analysed by single crystal X-ray diffraction has a cis-orientation.[139] Growth studies for APCVD found that deposition was minimal below 320°C; at elevated temperatures of 550-600 °C the growth rate was in excess of 2000 Å per minute. The depositions did not have oxygen or water present in the carrier stream, suggesting that the ethyl formate was the oxygen source for SnO_2 formation. Doping of the film was achieved through addition of triflouroethyl triflouro acetate, with the fluorine source added at a flow of 2mL per hour. Comparison of SnO_2.F films grown at 560 °C with TEC15 glass (produced by NSG) showed slightly higher resistivity (5.9×10^{-4} Ω m^{-1} compared to 4.1×10^{-4} Ω m^{-1}) and lower mobility (27.3 cm^2 V^{-1} s^{-1} compared to 30.1 cm^2 V^{-1} s^{-1}) but overall film properties were in good comparison with industrially produced samples.

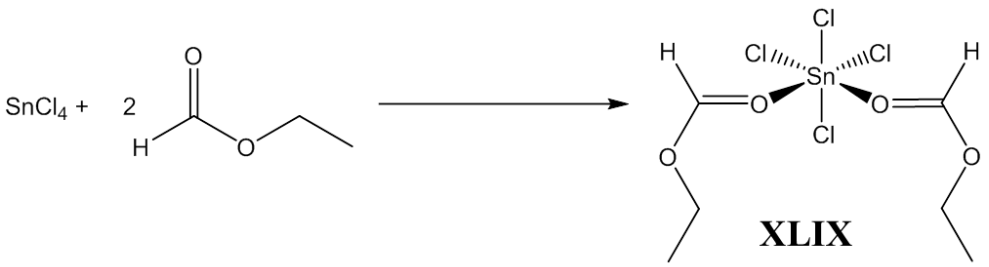

Figure 1.56: Synthetic route to bis-ethyl formate adduct of tin tetrachloride (XLIX)

The use of metal-organic tin(IV) precursors has also been evaluated for SnO_2 deposition. The homoleptic amide $Sn(NMe_2)_4$ was used in APCVD studies with an O_2 co reagent to deposit uniform SnO_2 thin films at temperatures ranging from 250-400°C.[140] Growth rates were found to be increased at elevated temperature and oxygen content. The films were characterised by PXRD, XPS and Rutherford backscattering, and showed good uniformity and low contamination from carbon and nitrogen (<1% carbon, and <0.3% nitrogen).

Replacing alkyl groups with other organic substituents has also been investigated as a route to other potential CVD precursors. Dibutyl tin diacetate (**L**) was evaluated as a potential precursor for APCVD of SnO_2 by Kern and co-workers.[141] Studies showed that deposition could be obtained at 420 °C, with experiments focused on contribution of water alongside oxygen in the rate of deposition and film quality. The rate of deposition was found to be slightly higher in anhydrous conditions (240 Å min^{-1} compared to 210 Å min^{-1}). The properties of films grown in wet conditions were better than those grown anhydrously with the figure of merit (transmission % / sheet resistance) for films grown for 20 minutes in wet conditions being 0.24 and only 0.08 for anhydrous conditions.

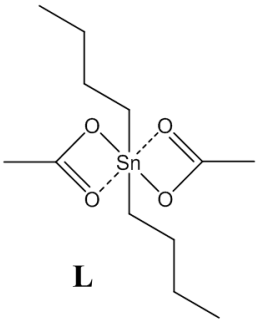

L

Figure 1.57: Structure of $nBu_2Sn(OOCMe)_2$

The deposition of SnO_2 using tin alkoxides has also been investigated. Jones and co-workers initially evaluated $Sn(O^tBu)_4$ as a single-source precursor for SnO_2 deposition in both APCVD and LPCVD systems using glass substrates.[142] Depositions were carried out between 250 and 400 °C, with the sheet resistance decreasing at higher temperatures. The films were generally amorphous, although the LPCVD deposition at 400 °C showed some peaks in the PXRD that corresponded to casserite SnO_2. Analysis using Auger electron spectroscopy showed the tin-oxygen ratio varied between 1.5-1.9, although LPCVD generally showed increased oxygen content. Mathur and co-workers carried out LPCVD experiments using $Sn(O^tBu)_4$ on quartz substrates at 500, 600 and 700 °C.[143] Analysis via PXRD confirmed that samples grown at all three temperatures were SnO_2. The study did find that the substrate temperature had an impact on the surface morphology; 500 and 600 °C saw

needle growth with size increasing with temperature. The sample at 700 °C was much more porous. The films were assessed as gas sensors for carbon monoxide at a range of temperatures. The films were heated and subjected to 15ppm of CO and the resistance was recorded. The sensitivity figure was determined by dividing the resistance in air by the resistance in CO. The films grown at 700 °C showed a sensitivity of 1.35; while those grown at 500 °C showed a negligible response of approximately 1. The difference in response was attributed to the greater surface area of the film grown at 700 °C.

Attempts to deposit SnO_2 in LPCVD conditions by Caulton and co-workers using $Sn(O^iPr)_4$ were unsuccessful with tin metal the major product.[144] The depositions were carried out on glass at 350°C, and film analysis did show some SnO_2 deposition; however analysis of the volatiles collected during the run showed just HO^iPr and acetone present. The authors put SnO_2 deposition down to adventitious water present in the system resulting in hydrolysis and then SnO_2 formation.

1.9 Tin(II) CVD precursors for SnO_2

While tin(II) compounds have also been utilised as CVD precursors for SnO_2, their use requires oxidation of the metal centre during the process. Deposition studies using $SnCl_2$ for APCVD were carried out by Hűmmelgen and co-workers.[145] $SnCl_2$ was introduced to gas phase through reactive evaporation although the conditions used to vaporise the precursor were not reported. The melting point of $SnCl_2$ is 247°C suggesting a high temperature would be required in the evaporating tube. The films were grown using purified air as the co-reagent and carrier gas with substrate temperatures ranging from 400-600°C. The samples were analysed by PXRD which evidenced increased crystallinity as the substrate temperature was increased. There was also an observed increase in optical transparency up to 550 °C and the resistivity of the samples decreased as the substrate temperature was increased to 550 °C. The decrease in transparency and increase in resistivity at 600 °C was explained by the presence of Sn_3O_4 in the PXRD pattern. Further experiments with $SnCl_2$ by Hitchman and co-workers under APCVD conditions showed that $SnCl_2$ was volatilised sufficiently at 340°C to allow gas phase transport to silicon wafer substrates at substrate temperature ranging from 375-575 °C.[146] Similar trends to those reported by Hűmmelgen and co-workers were observed with the resistivity decreasing as the substrate temperature increased.

The di-hydrate of $SnCl_2$ was investigated by Zhou and co-workers as a SnO_2 precursor grown using AACVD. [147] Depositions were carried out using $SnCl_2.2H_2O$ in ethyl alcohol, with a tin concentration of 0.1M, while the solution was volatilised using an ultrasonic atomiser and a N_2 carrier gas was used. Films were grown on alumina substrates at 400°C and then samples were annealed in air for 2h at 600°C. Analysis of the films by PXRD confirmed SnO_2 was grown; the effect of deposition time was studied, increasing depositions led to increased surface roughness, as observed by SEM micrographs. The samples were utilised as gas sensors for H_2S, with the response found to decrease as the deposition time increases; this is expected as the longer deposition time lead to films with smaller surface areas. Maleki and co-workers also used $SnCl_2.2H_2O$ for APCVD, with the precursor heated adjacent to the substrate under a controlled flow of O_2 and N_2 (Figure 1.58).[148] Depositions were carried out on glass, with substrate and precursor temperatures ranging from 300 °C to 550 °C. The crystallinity of the sample increased at higher substrate temperatures and the electrical properties of the films grown also improved as substrate temperature increased although the optical transparency of the films was observed to deteriorate at elevated deposition temperatures.

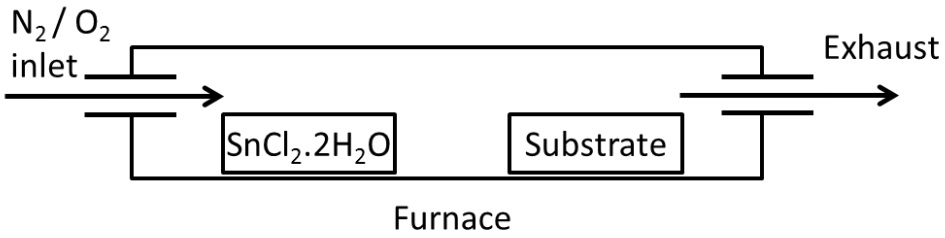

Figure 1.58: Reactor set-up used by Maleki and co-workers for SnO_2 deposition[148]

Maruyama and co-workers investigated the growth of SnO_2 using tin(II) acetylacetonate **LI** (Figure 1.59) in APCVD experiments.[149] The precursor was volatilised through heating at temperatures from 60 to 150°C, with N_2 and air carrier gases. Both glass and quartz substrates were used, with the substrate temperature ranging from 100 to 600 °C. While depositions in inert N_2 yielded no result, addition of H_2O vapour provided SnO thin films, through a hydrolysis reaction and subsequent dehydration. Using air as an oxidant resulted in the deposition of transparent SnO_2 films at substrate temperatures as low as 100 °C and crystalline thin films of SnO_2 were obtained at substrate temperatures above 230 °C. Unlike the depositions observed using $SnCl_2$ the electrical properties stayed quite uniform as the substrate temperature increased, although the growth rate was increased at higher deposition temperatures.

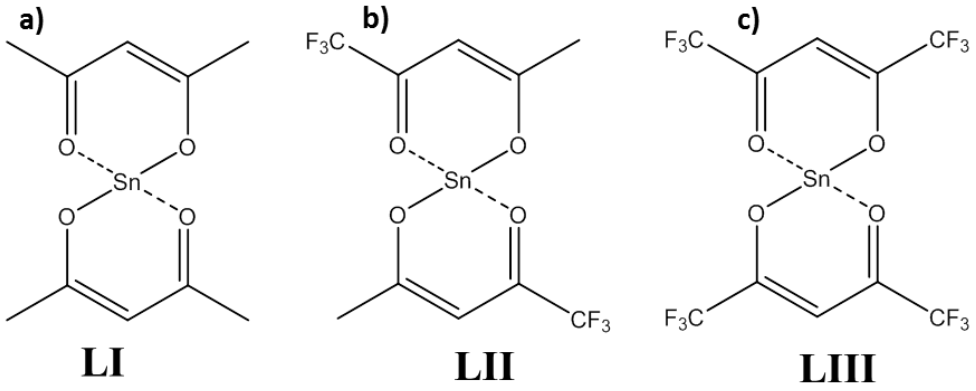

Figure 1.59: Structures of a) Sn(acetylacetonate)$_2$ b) Sn(trifluoroacetylacetonate)$_2$ c) Sn(hexaflouroacetylacetonate)$_2$

The properties of acetylacetonate ligands can be altered through the introduction of fluorine atoms to the methyl groups on the backbone (Figure 1.59). The fluorinated systems **LII** and **LIII** were evaluated alongside **LI** by Chi and co-workers as precursors in the LPCVD of SnO_2.[150] Depositions were carried out on silicon, titanium nitride and Pyrex® glass at

substrate temperatures of 300-600°C. Although in the absence of oxygen depositions resulted in the formation of tin metal **LI**, **LII** and **LIII**, the introduction of oxygen into the system resulted in the formation of polycrystalline SnO_2. For **LIII** this was achieved at temperatures in excess of 400 °C while **LI** and **LII** required temperatures greater than 450 °C. Low temperature experiments resulted in amorphous material, containing 77-81% tin by weight calculated through atomic adsorption spectroscopy, suggesting that SnO_2 had been formed.

Maruyama and co-workers evaluated the deposition of tin(II) acetate **LIV** (Figure 1.60) onto glass substrates between temperatures of 200-500°C. [151] The depositions were carried using APCVD, with the precursor heated to 120°C and carried to the reaction chamber by N_2. The growth rate of the films was found to increase with increasing temperature, while the introduction of oxygen was found to reduce the crystallinity of the films. A later study by Maruyama found that the deposition properties were enhanced by illuminating the sample with light of wavelengths 253.7nm and 184.9nm.[152] This photochemical CVD resulted in a reduction in carbon contamination, an increase in oxygen content in the films and also resulted in a faster deposition rate at lower temperatures. The crystallinity of the films grown was found to decrease on introduction of oxygen into the system, matching the observations for depositions without illumination.[151,152]

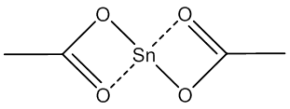

LIV

Figure 1.60: Structure of $Sn(O_2OCMe)_2$

Deposition studies with tin(II) alkoxides have generated a variety of products depending on the alkoxide and the reaction conditions. Caulton and co-workers found that depositions using $Sn(O^iPr)_2$ in LPCVD experiments with no carrier gas resulted in the formation of tin metal at 295°C.[144] The volatile products from the deposition process were trapped and upon analysis were found to contain only acetone and HO^iPr suggesting that no cleavage of the C-O bond required for SnO_2 formation occurred. Boyle and co-workers explored the use of $[Sn(ONep)_2]_\infty$ (Figure 1.61) (**LV**) as a LPCVD precursor for tin oxide.[153] Depositions were carried out on silicon wafers with the precursor vaporised at 130 °C, and the substrate was heated between 315 °C and 500 °C. The films were analysed by PXRD with results showing

a mixed deposition of SnO, Sn_2O_3, SnO_2 and Sn^o. Although the relative ratios of the oxides were not calculated, the authors did note that the tin metal content increased with temperature.

Boyle and co-workers have also evaluated the deposition of partially hydrolysed tin(II) neo-pentoxide compounds as LPCVD precursors for SnO_2. Compound **LVI** was synthesised through addition of 0.4 equivalents of H_2O to form a cage structure with five tin atoms, two bridging oxygen atoms and six neopentoxide groups (Figure 1.61). The precursor was vaporised through heating to 173°C in LPCVD experiments using silicon substrates heated to 330-500°C. As observed with **LV** a mixture of SnO, Sn_2O_3 SnO_2 and tin metal were found in the PXRD analysis. Unlike **LV**, the tin metal content dominated XRD plots at lower temperatures (330-350 °C), with the oxide content steadily increasing until 450 °C; at temperatures exceeding this tin metal was the dominant material.

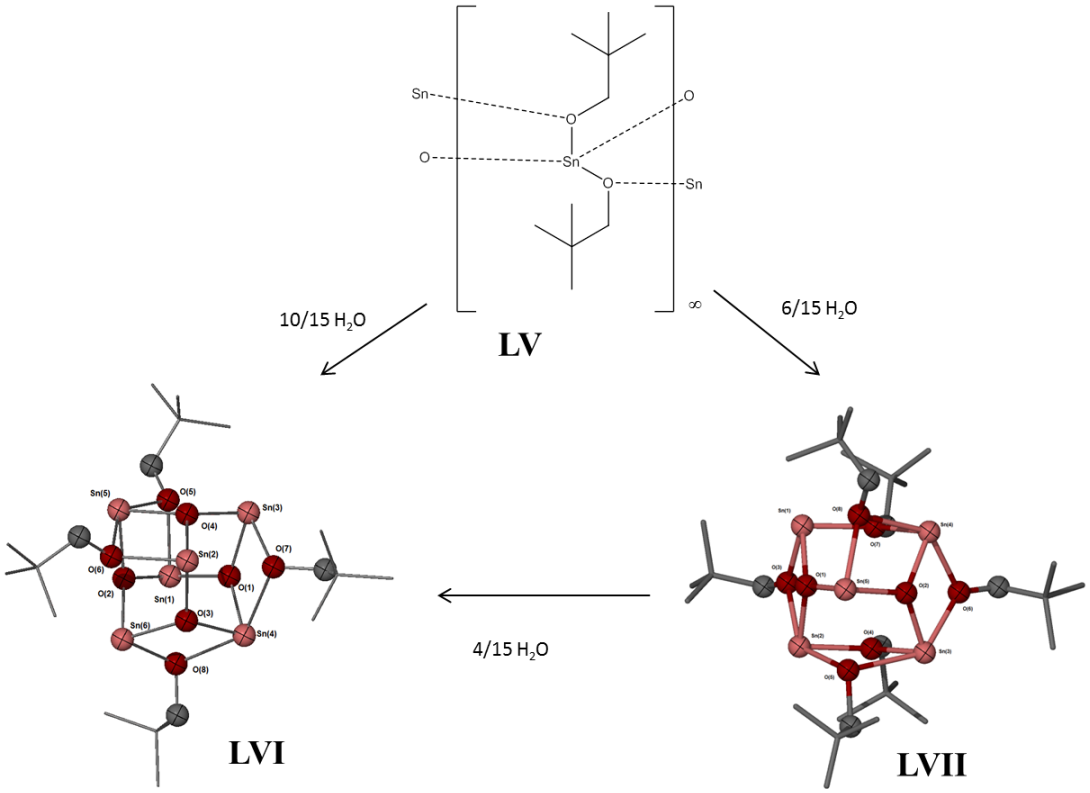

Figure 1.61: Synthetic routes to the formation of tin cluster compounds formed through hydrolysis of Sn(neopentoxide)$_2$[154]

Further hydrolysis of **LVI** through addition of 0.27 equivalents of water resulted in the cage compound **LVII** containing six tin atoms, four bridging oxygen atoms and four bridging neopentoxide groups. Vaporisation of **LVII** occurred at 178 °C in LPCVD experiments with depositions occurring on silicon wafers at 350-440°C. The crystalline content of these films

adopted a similar pattern to that observed with **LVI**; with lower temperature depositions (<350 °C) consisting of tin metal, SnO, SnO_2 and Sn_2O_3, mid-temperature depositions (350-380°C) containing increased metal oxide content, before the tin content increased in concentration at higher temperatures (>380 °C).

Giebelhaus and co-workers introduced a tin(II) β-heteroarylalkenolate system **LVIII** (Figure 1.62) that was utilised in LPCVD experiments for the gold-catalysed growth of SnO_2 nanowires. Depositions were carried out at 800°C using silicon wafers as the substrate, and precursor vaporisation at 95 °C. Depositions under these conditions produced SnO_2 nanowires with no detectable tin metal contamination. [155] While the mechanism for the decomposition is not determined, analysis of the decomposition products resulted in the detection of **LIX**, which gives some indication of how the ligand reacts under heating, however, attempts to detect the elemental carbon that should be generated as part of this process were unsuccessful.

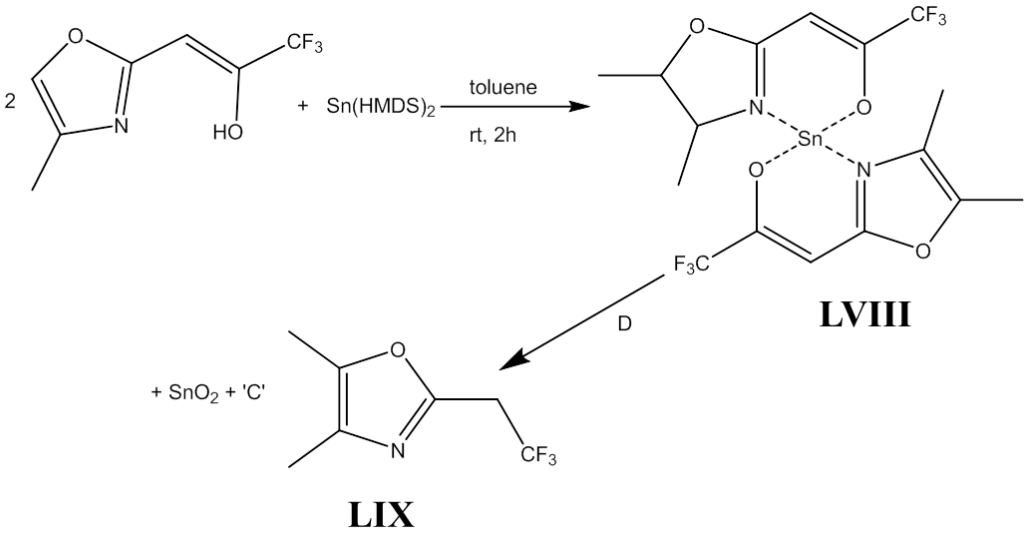

Figure 1.62: Synthetic route for the formation of tin(II) β-heteroarylalkenolate

1.10 Single-source fluorine-doped tin oxide precursors

There is significant interest in the growth of fluorine-doped tin oxide on industrial scales. Many industrial processes utilise the tin precursors presented above, and introduce fluorine through an additional precursor. For fluorine incorporation this can be achieved by using HF,[156] F_2,[157] $NH_4.F$[158] or fluorocarbons.[159] Another approach is to incorporate fluorine into the tin precursor.

Molloy and co-workers investigated fluorinated alkyl tin compounds as single source precursors for the formation of $SnO_2.F$. [160] Theoretically use of a perfluorinated alkyl system such as R_3SnR^F could result in the formation of R_3SnF through a fluorine transfer mechanism. A β-fluoride transfer mechanism (Figure 1.63) is one potential route to this, although the thermolysis and radical formation observed by R_4Sn as discussed earlier is still possible. Five different fluorinated systems were evaluated in the study $Bu_3SnC_4F_9$ **LX**, $Bu_2Sn(C_4F_9)_2$ **LXI**, $BuSn(C_4F_9)_3$ **LXII**, $Bu_3SnC_6F_{13}$ **LXIII** and Et_3SnC_4F **LXIV**. Depositions were carried out by APCVD with the precursors heated to 136 °C, 121 °C, 109 °C, 131 °C and 84 °C respectively. The substrate used for this study was glass with a SiCO blocking layer to prevent sodium migration through the glass into the films, at a substrate temperature of 564 °C (546 °C for **LXIII**). Analysis of the deposited films by energy dispersive spectroscopy (EDS) showed a range of doping levels varying from <0.05-2.02% fluorine. The highest fluorine content was found with compound **LXI**, while the lowest was observed for compound **LXIII**. The shorter fluorinated alkyl chains resulted in greater fluorine inclusion, while the number of fluorinated alkyl chains did not improve the fluorine content with **LX** < **LXI** > **LXII**.

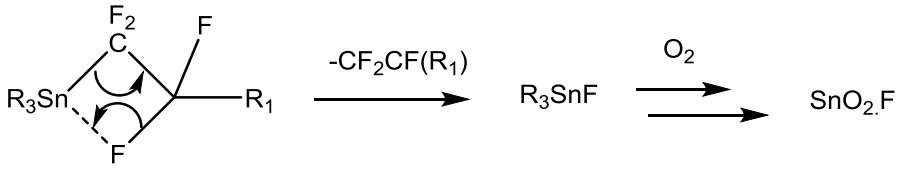

Figure 1.63: Mechanism for β-fluoride transfer to form Sn-F bonds

The use of fluorocarboxylate systems is thought to provide another potential route to R_nSnF precursors generated through decarboxylation in the reaction chamber (Figure 1.64). Maruyama and co-workers evaluated tin(II) bis-trifluoroacetate (**LXV**) as potential single source precursor for formation of FTO using APCVD conditions.[151] The precursor was vaporised through heating to 150 °C and transported to the reactor using a N_2 carrier gas

stream. The films were characterised and the resistivity measurements were found to be lower than depositions using the non-fluorinated analogue. Although the inclusion of oxygen into the system had an effect on the crystallinity promoting growth in the (300) plane, variable oxygen content experiments showed that the inclusion of O_2 did not affect the growth rate.

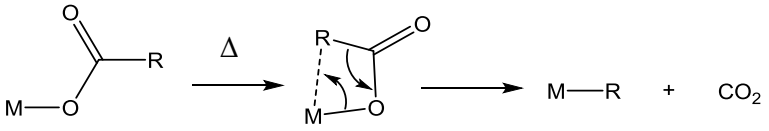

Figure 1.64: Decarboxylation mechanism

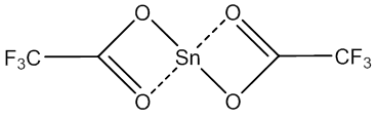

LXV

Figure 1.65: Structure of tin(II) bis fluoroacetate

Hoffman and co-workers evaluated a tin(IV) fluorocarboxylate, $nBu_2Sn(O_2CCF_3)_2$ using APCVD conditions.[161] The precursor was vaporised by heating to 70°C and the carrier gas used was argon mixed with oxygen, with deposition occurring on silicon wafers and glass slide substrates at temperatures of 370-490°C. The analysed films showed a tin:oxygen ratio consistent with SnO_2 measured by Rutherford Backscattering (RBS) and confirmed by XRD patterns consistent with casserite. The fluorine content was found to increase as a function of deposition temperature this resulted in a decrease in resistivity, which is expected with a greater fluorine content.

Studies by Molloy and co-workers of tin(IV) carboxylate precursors **LXVI-LXX** focused on varying the R groups and R_f groups (Figure 1.66).[162] Depositions were carried out using APCVD on SiCO coated glass using a N_2 and O_2 carrier gas system. The precursors were vaporised through heating from 110-150 °C and the substrate was heated to 540-570°C. Analysis of the films showed compound **LXX** gave the highest F content (4.5%) while the other precursors produced F contents of 0.88-1.10%. The optical and electrical properties of **LXX** were not as good, however, with a resistivity of 1.13 x 10^{-3} Ω cm^{-3} compared to 0.43 - 0.54 x 10^{-3} Ω cm^{-3} for the other precursors.[160] The deposition studies showed that the fluorine content was largely consistent throughout suggesting a common β-F decomposition pathway.

This was further confirmed by mass spectral analysis of the gaseous by-products on decomposition of **LXVII**.

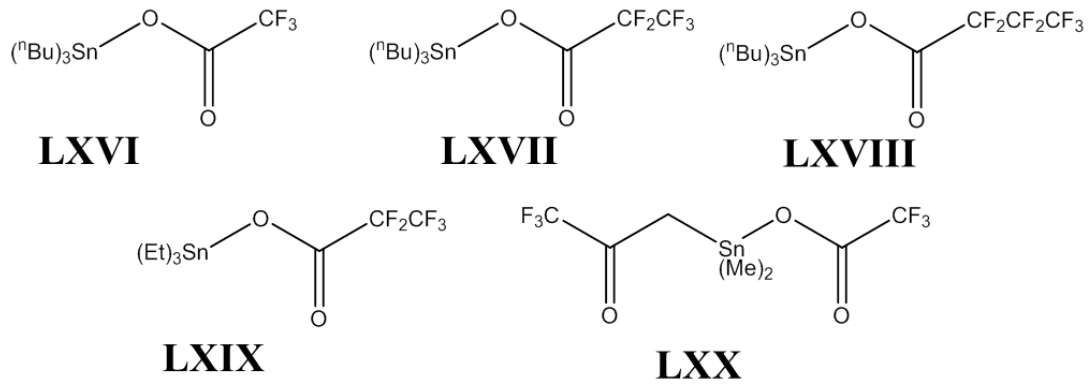

Figure 1.66: Structures of fluorinated carboxylates used in CVD studies

Homoleptic flouro-alkoxides have also been considered as single source precursors for FTO. Hoffman and co-workers assessed $Sn(OCH(CF_3)_2)_4.2HNMe_2$ (**LXXI**) using LPCVD conditions with air present as a source of additional oxygen.[163] Depositions were carried out on glass substrates heated to 200-450°C. When depositions were carried out using dry O_2 deposition was restricted, suggesting that hydrolysis is important. Although XRD analysis of the films showed that they were amorphous, RBS analysis of the tin:oxygen ratio suggested SnO_2 formation with the oxygen content decreasing slowly on increased substrate temperature. The fluorine content varied with no pattern across the substrate temperatures with the maximum being 2.6%, and minimum 0.6%.

Hoffman and co-workers also carried out LPCVD experiments using the fluorinated tin(II) alkoxide $Sn(OCH(CF_3)_2)_2.HNMe_2$ (**LXXII**). The films were deposited on glass substrates at temperatures ranging from 180 -450 °C using an air or water co-reagent. Analysis of the films showed that the tin-oxygen ratio was approximately 1:1 suggesting growth of SnO rather than SnO_2. The fluorine content was much higher, with 0.4-0.1 F:Sn ratios observed. Although the use of dry air or dry oxygen gas resulted in no observable growth, addition of water to the system saw the formation of SnO:F thin films. Hoffman and co-workers postulated that the decomposition method proceeds via a hydrolysis step. The films were observed to delaminate on annealing in air, and turn milky when left out for a period of months, attributed to the slow oxidation to SnO_2 or the disproportionation of the SnO to SnO_2 and tin metal.

Molloy and co-workers also investigated a series of Bu_3SnOR_f systems **LXXIII - LXXVII** as potential single source CVD precursors for the formation of FTO (Figure 1.67).[164] The

precursors were evaluated using APCVD conditions with an N_2/O_2 carrier gas onto SiCO coated glass slides, with the substrates heated to 460-550 °C. While precursor **LXXV** was also investigated in anaerobic growth studies, the film grown in the absence of O_2 was found to have poor adhesion properties and the deposition was powdery. The fluorine content varied across the precursors, attributed to a β-hydride elimination process being more favourable than γ- fluoride elimination for all but **LXVII**, which exhibited a more favourable γ –fluoride elimination step.[164]

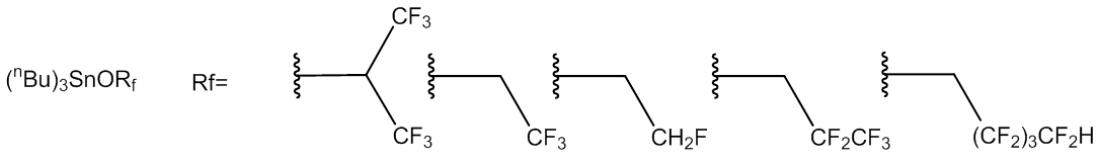

LXXIII LXXIV LXXV LXXVI LXXVII

Figure 1.67: The range of ^{n}Bu$_3$Sn fluoroalkoxide systems evaluated by Molloy and co-workers

1.11 SnO precursors

There are few reports of targeted SnO growth using CVD methods, with the majority of films grown using physical processes such as sputtering and pulsed laser deposition. As previously discussed Maruyama and Hoffman both grew SnO films with tin(II) precursors when water or oxygen were not present.[149,163]

Molloy and co-workers recently published a single source precursor for SnO thin films based on the partial hydrolysis of a tin siloxide complex to form a tin cage compound similar to **LVI** utilised by Boyle and co-workers (Figure 1.36).[165] The cage complex **LXXIX** consists of six tin atoms bound with four oxygen atoms and four bridging siloxide groups. Deposition was carried out under APCVD conditions with the precursor vaporised through liquid injection of a toluene solution of **LXXIX**, with a N_2 carrier gas. Both glass and silicon substrates were utilised, with the substrate temperature varied from 450-550°C. Analysis of the films grown showed SnO formation at 450°C with some tin metal contamination; however at elevated temperatures only tin metal was detected. Depositions were also carried out using the siloxide **LXXVIII** using AACVD. The precursor was vaporised using an electrostatic nebuliser from a toluene solution. Depositions carried out at 450 °C resulted in SnO thin films with no tin metal or other oxide contamination and XRD analysis revealed that, the film has an increased orientation in the (001) and (002) directions.

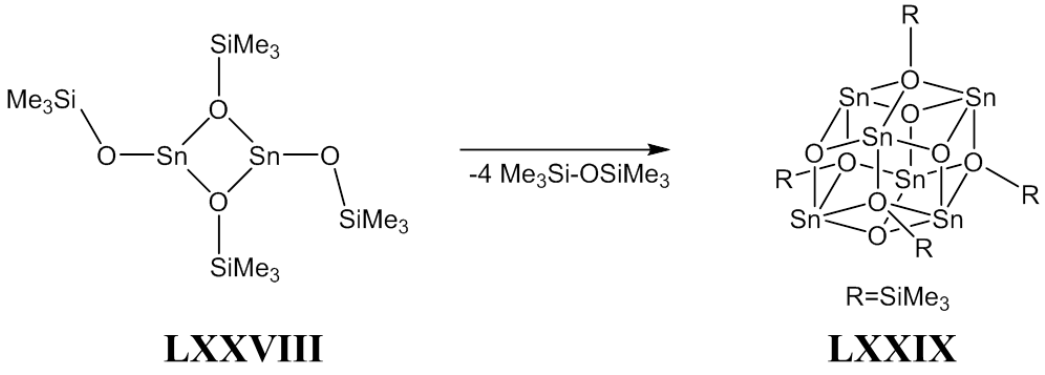

LXXVIII **LXXIX**

Figure 1.68: Synthesis of $Sn_6O_4(OSiMe_3)_4$ cage complex

1.12 Objectives

The general aim of this research project was to design, synthesise and evaluate a range of new single source precursors that could be utilised in chemical vapour deposition of tin oxide thin films.

Precursors for chemical vapour deposition were targeted as CVD allows for large area functionalization at relatively low costs compared to other thin film fabrication methods. One of the primary aims of the project was to develop precursors that could form tin oxide at low temperatures.

The focus of tin(II) precursors is due to the limited examples of tin(II) precursors in the literature, when compared to tin(IV) examples. Using tin(II) systems also allows for the potential formation of SnO or SnO_2 depending on the oxidative nature of the deposition. There are limited examples of SnO CVD precursors, and interest in SnO thin films as potential *p*-type or bipolar semiconducting materials. This could lead to the formation of an all tin heterojunction devices for microelectronic or photovoltaic devices. Tin(II) systems also have the potential for further chemistry, particularly oxidation to tin(IV) systems which could allow for further incorporation of fluorine to form fluorine doped tin oxide.

The initial design rationale was to utilise oxygen containing analogues of metal xanthate and or metal dithiocarbamate systems which have been found to be good low temperature precursors for metal sulphide materials.[74,76,166–171] The general structures of xanthate and dithiocarbamate compounds are shown in Figure 1.69, along with a simplified diagram of the target compounds.

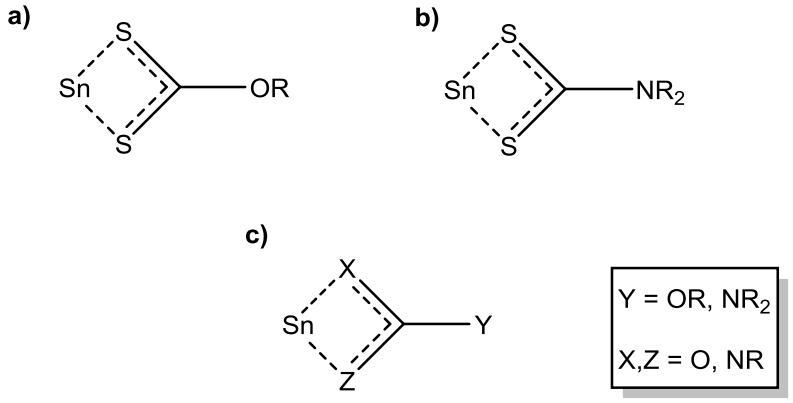

Figure 1.69 : General structure of a) xanthate, b) dithiocarbamate c) potential tin oxide precursors

2. Heterocumulene insertions into tin(II) amide bonds

The reactivity of tin(II) amide compounds with heterocumulene derivatives allows for the formation of many potential products that can be evaluated as precursors for formation of tin oxide thin films via chemical vapour deposition. In this manner oxygen containing heterocumulenes such as organic isocyanates or CO_2 maybe reacted with tin(II) amides to form the respective ureate or carbamate (Figure 2.1).

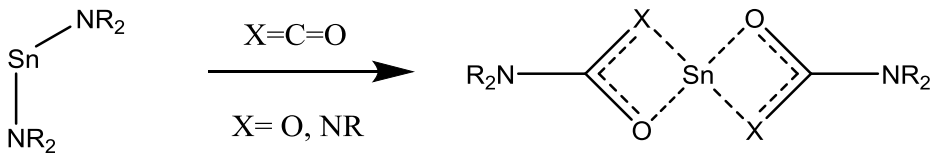

Figure 2.1: General reaction scheme for formation of new tin(II) compounds for use in CVD processes

2.1 Synthesis of metal ureate complexes

There are three potential routes to the formation of metal ureate systems. Protonolysis reactions which take the protonated ligand and a metal starting material containing basic ligands such as amido or alkyl groups have been used for the formation of zirconium ureate complexes for use in catalysis. Alternatively salt metathesis reactions can be utilised in forming metal ureate complexes. Here the protonated ligand is reacted with a strong alkali metal base resulting in the formation of the alkali metal ureate complex. This intermediate can be reacted further through a transmetallation reaction with a metal halide, with formation of the metal ureate and elimination of an alkali metal salt.[172]

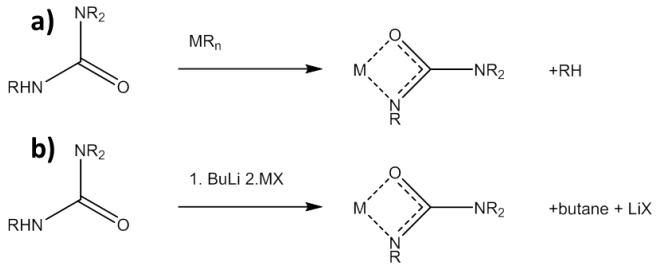

Figure 2.2: Synthesis of metal ureates a) protonolysis, b) salt metathesis

The most commonly utilised method for the formation of metal ureate compounds involves the insertion of an isocyanate into a metal-amide bond. This was the method used for the formation of the first reported metal ureate complexes by Lappert and co-workers, synthesised through the insertion of PhNCO into the M-N bonds of $Ti(NMe_2)_4$, $Zr(NMe_2)_4$ and $Hf(NMe_2)_2$ (Figure 2.3).[173,174]

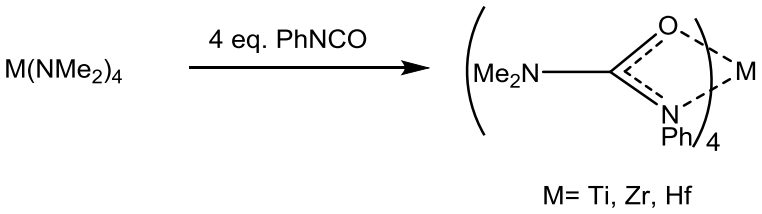

Figure 2.3: Formation of group IV ureates via insertion of phenyl isocyanate into M-NMe_2 bond

2.2 Synthesis of tin(II) ureate systems

For the synthesis of tin(II) ureate systems the insertion of isocyanates into tin nitrogen bonds was explored as the primary synthetic route. As mentioned earlier the choice of dialkyl amido tin is important for the formation of tin(II) ureate systems as the presence of silyl groups bound to the nitrogen can result silicon migration to the oxygen of the isocyanate and expulsion of a carbodiimide and formation of metal siloxide. Experiments therefore centred on the insertion reactivity of $[Sn(NMe_2)_2]_2$ with isocyanates.

The starting tin amide, $[Sn(NMe_2)_2]_2$ was prepared according the literature procedure[175] by slow addition two equivalents of $LiNMe_2$ to a stirred solution of $SnCl_2$ in diethyl ether at -78°C (Figure 2.4). The solution was slowly warmed to room temperature followed by extraction into *n*-hexanes, and purification through crystallisation at -40°C.[176]

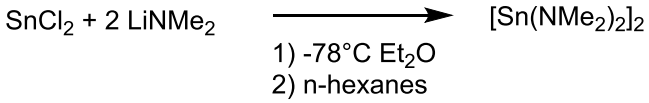

Figure 2.4: Synthetic route to $[Sn(NMe_2)_2]_2$

For the formation of tin (II) bis-ureate systems two equivalents of isocyanate were added to a solution of $[Sn(NMe_2)_2]_2$ in toluene (Figure 2.5). Removal of solvent in vacuo resulted in an off white precipitate. The products, **1**-**3** were further purified through crystallisation from toluene by gentle evaporation of the solvent in an inert atmosphere.

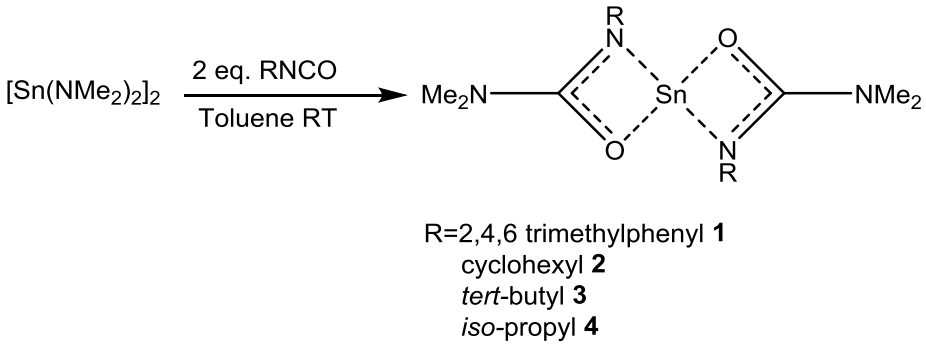

Figure 2.5: Synthetic route to ureate compounds 1-4.

2.2.1 Solution based analysis

The ^{1}H NMR spectrum of the N-mesityl substituted compound **1** in d_8-toluene displayed five singlet resonances at δ=2.17, 2.35, 2.37 ppm corresponding the NMe_2 methyl groups and the ortho and para groups of the trimethylphenyl substituent. A further resonance at δ = 6.75 ppm accounted for the protons on the phenyl group. The $^{13}C\{^{1}H\}$ NMR spectrum of **1** compromised resonances at δ = 19.4 and 20.9 ppm for the para and ortho groups respectively, and a resonance at δ = 36.5 ppm ascribed to the NMe_2 groups. Four resonances in the aromatic region at δ = 128.9, 132.7, 133.9 and 141.1 ppm could be assigned to for the four inequivalent carbons in the phenyl ring and a downfield resonance was observed at δ = 161.4 ppm for the central carbon of the N-C(N)-O back bone of the ureate ligand. The $^{119}Sn\{^{1}H\}$ NMR spectrum displayed a single resonance at δ -353 ppm suggesting a single tin environment. The resonances in the multinuclear NMR spectra were, thus, indicative of a homoleptic system with two ureate ligands bound to a central tin atom.

Compound **2** provided multiple resonances in its ^{1}H NMR spectrum at δ 1.1-1.2, 1.52-1.75 and 1.84-95 ppm corresponding to the CH_2 groups of the cyclohexyl ring. The CH group of the cyclohexyl group resonated at δ 3.45-3.6 ppm and the methyl groups of the NMe_2 appear as a single resonance at δ 2.59 ppm. In the $^{13}C\{^{1}H\}$ NMR spectrum four resonances accounted for the cyclohexyl carbons at δ 26.2, 26.3, 38.6 and 55.3 ppm and a single resonance was observed for the two equivalent NMe_2 carbons at δ 35.6 ppm. The downfield resonance associated with the N-C(N)-O backbone was observed at δ 166.8 ppm. The $^{119}Sn\{^{1}H\}$ NMR spectrum comprised a single resonance at δ -310 ppm, nearly 40 ppm downfield of the resonances observed for compound **1**.

For **3** the ^{1}H NMR spectrum consisted of two resonances δ 1.37 and 2.44 ppm for the ^{t}butyl and NMe_2 groups respectively. The $^{13}C\{^{1}H\}$ NMR spectrum provided resonances at δ = 31.4 and 53.0 ppm for the ^{t}Bu group and a single resonance at δ = 31.4 ppm for the NMe_2 group, while the central carbon of the N-C(N)-O backbone of the ureate ligand appeared as a distinctive feature at δ = 167 ppm, further downfield than that observed for compound **1**. The $^{119}Sn\{^{1}H\}$ NMR for **3** spectrum showed a single resonance at δ = -357 ppm, which is very close to the resonance observed for **1**.

Isolation of compound **4** was unsuccessful; on removal of solvent an orange-brown oil was obtained. The NMR spectra of this compound evidenced the presence of two different environments for the isopropyl groups and the NMe_2 groups and all attempts to crystallise the compound were unsuccessful. The formation of the ureate was confirmed however by

carrying the reaction out in d_8-toluene and monitoring the solution by multinuclear NMR spectroscopy. The ^{1}H NMR for **4** comprised resonances at δ 1.23-1.25 and 3.89-4.01 ppm corresponding to the methyl and methine protons of the ^{i}Pr group and a further resonance at δ 2.57 ppm for the NMe_2 group. The $^{13}C\{^1H\}$ NMR spectrum was also consistent with a homoleptic formulation analogous to those ascribed to compounds **1**-**3** and displayed resonances at δ 25.3, 39.0 and 47.2 ppm assigned to the ^{i}Pr and NMe_2 carbons and a resonance at δ 167.2 ppm assigned to the NC(N)O backbone carbon. The $^{119}Sn\{^1H\}$ NMR spectrum again provided a single resonance at δ -307 ppm which is comparable to that observed for **3** but downfield of compounds **1** and **2**.

The resonances obtained from in-situ monitoring of the reaction allowed the assignment of the major resonances in the isolated material. In the $^{119}Sn\{^1H\}$ NMR spectrum of the isolated material there was a single resonance that corresponded to formation of compound **4**. The ^{1}H NMR spectrum contains resonances assigned to compound **4** alongside resonances for an unidentifiable fragment with a similar chemical make-up. The unidentified resonances have integrals that are half that observed for compound **4** in the spectrum. Attempts to separate compound **4** from the second species were unsuccessful.

Table 2.1 $^{119}Sn\{^1H\}$ and $^{13}C\{^1H\}$ NMR shifts for compounds 1-4

Compound	^{119}Sn NMR shift (ppm)	$^{13}C\{^1H\}$ NMR shift (ppm) Backbone
1	-353	161.4
2	-310	166.9
3	-357	167.0
4	-307	167.2

Table 2.1 provides a comparison of the $^{119}Sn\{^1H\}$ NMR resonances, and the $^{13}C\{^1H\}$ NMR resonance for the N-C(N)-O carbon for compounds **1**, **2**, **3** and **4**. The $^{119}Sn\{^1H\}$ NMR chemical shifts correlate well with those previously reported for homoleptic tin(II) bis-amidinates (δ -255.3 to -397 ppm)[177–180] and bis-guanidinates (δ -377 to -432 ppm)[103], all of which have been identified as unambiguously four-coordinate Sn(II) in solution and maybe interpreted to indicate a similar level of charge donation irrespective of the donor atoms of the two bidentate donor ligands. The resonances are significantly downfield of that reported for the homoleptic *iso*-ureate species **XXIX** which was reported to occur at δ -557ppm.[119] The $^{13}C\{^1H\}$ NMR resonances for the central carbon on the ureate backbone are also similar

to those reported for a range of homoleptic and heteroleptic guanidinates, amidinates, iso-ureates and carbamates with resonances observed between δ 160-170 ppm.

2.2.2 Molecular structures of tin(II) bis-ureate complexes

As discussed earlier ureate ligands may adopt several binding modes when attached to a metal centre. Analysis of the NMR spectra for **1**, **2** and **3** suggested that the isocyanate has inserted into both of the available tin –nitrogen bonds to form a homoleptic tin complex with two equivalent ureate ligands. Compounds **1**, **2** and **3** also displayed a single $^{119}Sn\{^{1}H\}$ resonance suggesting that there is only one tin environment present in the solution phase analysis. The mode of binding (i.e. N, N', N, O or N', O) cannot be elucidated through the NMR spectra alone.

Table 2.2: Crystallographic parameters for compounds 1-3

Compound	**1**	**2**	**3**
Empirical Formula	$C_{24}H_{34}N_4O_2Sn$	$C_{18}H_{34}N_4O_2Sn$	$C_{14}H_{30}N_4O_2Sn$
Crystal System	Triclinic	Monoclinic	Triclinic
Space Group	*P*-1	$P2_1/c$	*P*-1
Cell Constants			
a (Å)	11.1330(5)	8.6700(3)	9.0640(3)
b (Å)	11.2160(5)	9.4020(3)	24.4490(8)
c (Å)	12.4200(4)	12.4160(3)	11.0540(3)
α (°)	100.829(2)	79.878(2)	90
β (°)	105.225(2)	84.751(2)	121.731(2)
γ (°)	117.416(2)	70.462(2)	90
Volume (Å^3)	1228.44(9)	2083.47(11)	938.39(5)
Density (mg/m^3)	1.431	1.458	1.434
Z	2	4	2
Measured reflections	24165	31344	14456
Unique reflections	6579	6083	5596
R_{int}	0.0549	0.0988	0.0340
R_1. w$R_2[I > 2\sigma(I)]$	0.0334, 0.0740	0.0454, 0.0748	0.0228, 0.0539
***R* indices (all data)**	0.0462, 0.0797	0.1202, 0.0935	0.0272, 0.0556

The solid state structures of **1**, **2** and **3** were confirmed by single-crystal X-ray diffraction analysis. A summary of the crystallographic parameters is presented in Table 2.2, and a

selection of bond lengths and angles can be found in Table 2.3. All three compounds were found to exist as monomeric species with the tin in a four-coordinate square based pyramidal geometry, heavily influenced by the stereo-chemically active lone pair at the tin centre. Both compounds **1** and **3** were found to be triclinic when crystallised and shared the same space group, *P*-1; while compound **2** is monoclinic and was found in the space group $P2_1/c$.

The solid state structure of **1** is shown in Figure 2.6. The structure has two ureate ligands orientated in a κ^2 N, O binding motif to tin in a square based pyramidal geometry with the stereochemically active lone pair of the tin situated at the apex. In both cases the nitrogen coordination is provided by the amido N-trimethylphenyl donor rather than the amino NMe_2 component. The ligands are positioned in a transoid configuration so that the bulky 2, 4, 6-trimethylphenyl groups are located on opposite sides of the molecule. This transoid configuration is expected due to the bulky nature of the ligand, with this configuration being less sterically congested than any alternative cisoid orientation. The bonds between the tin centre and the ligand are slightly longer for the Sn(1)-N(11) than the Sn(1)-N(21) (2.2209(19) Å and 2.1985(18) Å respectively), and notably this is not compensated by the Sn(1)-O(11) and Sn(1)-O(21) distances (2.3374(17) Å and 2.2763(16) Å respectively) meaning that one ureate ligand is slightly closer to the tin than the other. The Sn-N bonds are comparable to those reported for homoleptic and heteroleptic amidinates and guanidinates which vary from 2.2-2.4 Å depending on the identity of the N-substituents. The stereo-active lone pair located on the tin centre has a significant impact on the geometry of the compound with the angle subtended by the two O-C-N planes measured at 106°.

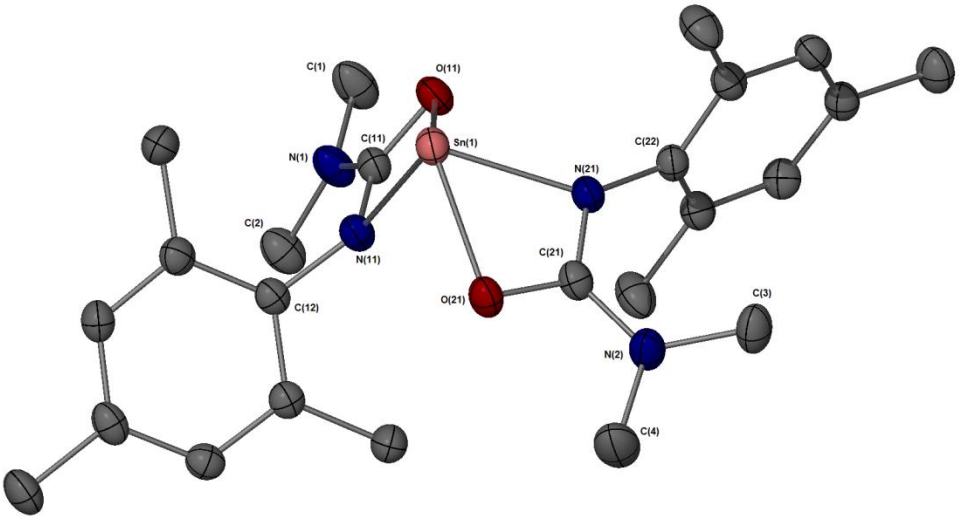

Figure 2.6: Molecular structure of Sn(N(mesityl)C(O)NMe$_2$)$_2$ (1). Ellipsoids shown at 50% probability, hydrogen atoms omitted for clarity

As mentioned previously, for delocalisation of the negative charge to occur between the NMe_2 group and the NCO core of the ureate ligand the sp^2 nitrogen of the NMe_2 group should be co-planar to the NCO core. The plane of the NMe_2 group is close to co-planar with the NCO back bone for both ureate ligands (Figure 2.7 a, b). The dihedral angles measured for O(21)-C(21)-N(2)-C(4) and N(21)-C(21)-N(2)-C(3) are 9.3° and 20.7° indicating that the C(3) methyl group is further out of the plane than the C(4). In comparison the dihedral angles for N(11)-C(11)-N(1)-C(1) and O(11)-C(11)-N(1)-C(2) are 4.0° and 13.6° meaning that the methyl group closest to the oxygen is this time further out of the plane. This is a feature of many small NR_2 groups on metal ureate complexes in the literature.[83,181]

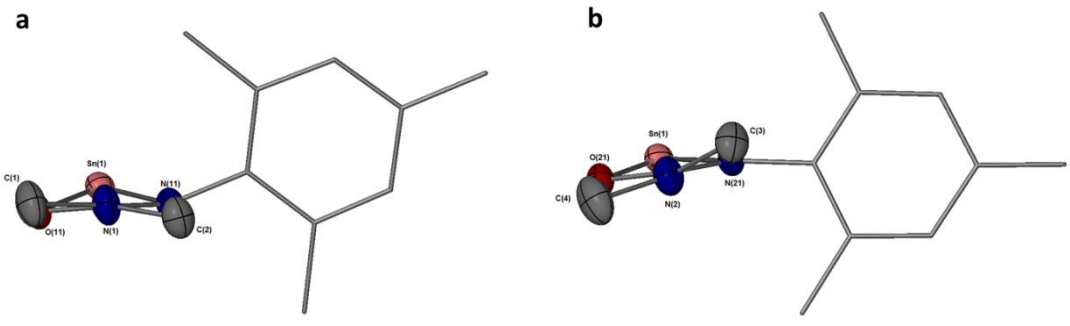

Figure 2.7: Molecular structures of Sn(N(mesityl)C(O)NMe$_2$)$_2$ (1) in the tin-ureate plane show the distortion of the NMe$_2$ groups

Compound **2** has a similar structure and comprises two ureate ligands bound in an overall square pyramidal geometry to the metal with the stereochemically active lone pair located at the apex. The ligands again bind in a κ^2 N, O fashion and the cyclohexyl groups situated transoid to each other (Figure 2.8). In both cases the nitrogen coordination is provided by the amido N-cyclohexyl donor rather than the amino NMe_2 component. One ureate ligand is again more strongly bound to the Sn(II) centre with the Sn(1)-N(11) and Sn(1)-N(21) bond lengths of 2.186(3) Å and 2.176(3) Å while the Sn(1)-O(11) and Sn(1)-O(21) bond lengths are 2.364(2) Å and 2.295(2) Å respectively. The N-Sn bond lengths are approximately 0.02 Å shorter than those observed in compound **1**, which is compensated by the Sn-O bond lengths being approximately 0.02 Å longer, an observation which may be ascribed to the differing steric demands of the cyclohexyl and mesityl substituents. The angle observed between the two ligands is more obtuse than that observed for compound **1** with an angle of 114° observed between the two NCO planes in compound **2**.

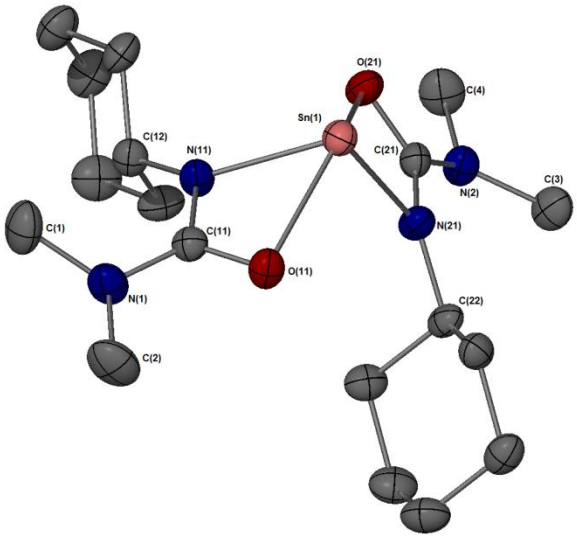

Figure 2.8: Molecular structure of $Sn(N(cyclohexyl)C(O)NMe_2)_2$ (2). Ellipsoids shown at 50% probability, hydrogen atoms omitted for clarity

As observed with **1**, the NMe_2 groups of compound **2** are not quite co-planar with the O-C-N core of the ureate ligands. For compound **2** this is more pronounced with dihedral angles of 5.3° and 35.1° for O(21)-C(21)-N(2)-C(4) and N(21)-C(21)-N(2)-C(3) and 8.5° and 39.2° for O(11)-C(11)-N(1)-C(2) and N(11)-C(11)-N(1)-C(1) (Figure 2.9). These angles are larger than those observed with compound **1**; as a consequence the C(11)-N(1) and C(21)-N(2) bond lengths for **2** are 0.02 Å longer than found in **1**. The C-NMe_2 bond length can be used

as indication of the delocalisation of the negative charge onto the NMe_2 groups, elongation of this bond is indicative of a reduction in delocalisation.

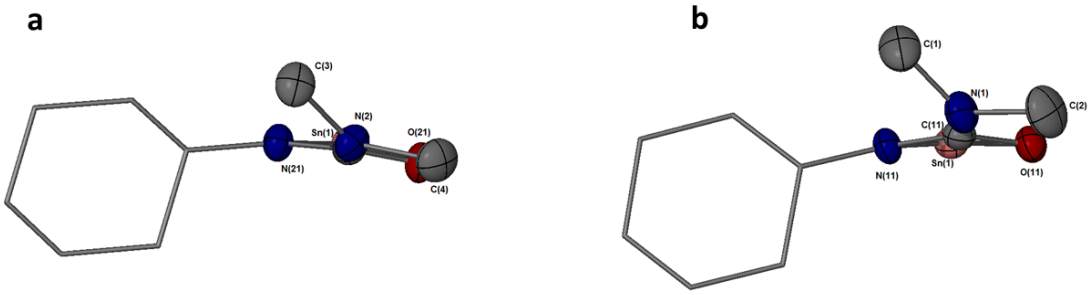

Figure 2.9: Molecular structures of $Sn(N(cyclohexyl)C(O)NMe_2)_2$ (2) in the tin-ureate plane show the distortion of the NMe_2 groups

The solid state structure for compound **3** provided different coordination geometry of the tin atom compared to **1** and **2** with different anisobidenticity of the two ligands. Rather than two κ^2 N, O bound ureate ligands, **3** has one κ^2 N, O and one κ^2 N, N' bound ureate (Figure 2.10). The two ^{t}butyl groups are also located with a cisoid relationship with respect to the basal plane of the distorted square pyramidal coordination geometry. Consequently that the majority of the ligands' bulk is located on the same side of the compound with the ureate ligands twisted somewhat to accommodate resulting in the C=O group being pushed towards the NMe_2 group of the rotated ureate ligand.

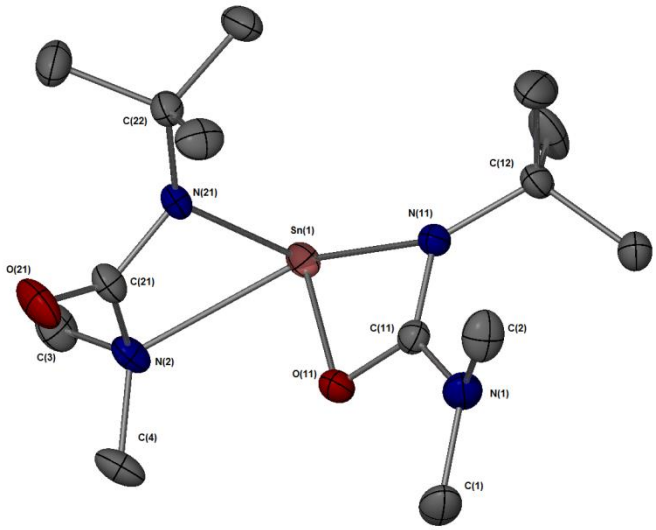

Figure 2.10: Molecular structure of $Sn(N(^tButyl)C(O)NMe_2)_2$ (3). Ellipsoids shown at 50% probability, hydrogen atoms omitted for clarity

For the κ^2 N, O bound ureate the Sn(1)-O(11) bond length is significantly shorter than those observed in **1** and **2** at 2.1688(11) Å (c.f. 2.3374(17) Å and 2.364(2) Å for **1**, and **2**). The shortening of the Sn(1)-O(11) bond is compensated by elongation of the Sn(1)-N(11) bond to 2.3151(13) Å (c.f. 2.2209(19) Å and 2.186(3) Å for **1** and **2**). For the κ^2 N, N' bound ureate the Sn(1)-N(21) bond is similar to that found for **2** at 2.1715(13) Å (for **2** Sn(1)-N(21) is 2.176(3) Å). The Sn(1) - N(2) bond is 2.4839(13) Å which is weakest Sn-N interaction measured for the three ureate compounds at over 0.26 Å longer than the Sn(1)-N(11) bond measured for **1** and over 0.3 Å longer than the Sn(1)-N(21) bond measured for **2**. As a consequence of this different ligand orientation the C(21)-O(21) bond is much shorter measuring 1.220(2) Å, suggesting significant double bond character. The angle between the ureate ligands is more acute than that observed for compounds **1** and **2** (106° and 114° respectively) with the angle between the ligands measuring 92° for compound **3**.

For the κ^2 N, O bound ureate the NMe_2 unit displays similar characteristics to those observed by **1**, and **2** with the C-N-C plane of the NMe_2 groups twisted from the N-C-O plane (Figure 2.11). The N(11)-C(11)-N(1)-C(2) and O(11)-C(11)-N(1)-C(1) dihedral angles measure 45.4° and 11.8° respectively, larger than those observed for **2** albeit the C(11)-N(1) bond length is found to be the same as that measured for **2** at 1.369 (4) Å.

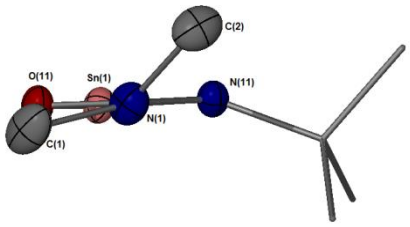

Figure 2.11: Molecular structure of 3 in the tin-ureate plane show the distortion of the NMe_2 groups

Table 2.3: Selected bond lengths and angles for compounds 1, 2 and 3

Selected bond lengths (Å)				Selected bond angles (°)			
	1	**2**	**3**		**1**	**2**	**3**
Sn(1)-N(21)	2.1985(18)	2.176(3)	2.1715(13)	**N(21)-Sn(1)-N(11)**	100.62(7)	100.47(10)	94.47(5)
Sn(1)-N(11)	2.2209(19)	2.186(3)	2.3151(13)	**N(21)-Sn(1)-O(21)**	59.02(6)	59.05(9)	-
Sn(1)-O(21)	2.2763(16)	2.295(2)		**N(11)-Sn(1)-O(21)**	85.46(6)	90.89(9)	-
Sn(1)-O(11)	2.3374(17)	2.364(2)	2.1688(11)	**N(21)-Sn(1)-O(11)**	87.07(7)	93.08(9)	-
Sn(1)-N(2)			2.4839(13)	**N(11)-Sn(1)-O(11)**	57.96(6)	57.93(8)	59.15(4)
N(1)-C(11)	1.358(3)	1.369(4)	1.369(2)	**O(21)-Sn(1)-O(11)**	125.19(6)	135.10(8)	-
N(1)-C(2)	1.452(3)	1.459(4)	1.457(3)	**O(11)-Sn(1)-N(2)**	-	-	76.27(4)
N(1)-C(1)	1.454(3)	1.465(4)	1.464(2)	**N(21)-Sn(1)-N(2)**	-	-	57.90(5)
N(2)-C(21)	1.353(3)	1.368(4)	1.482(2)	**N(11)-Sn(1)-N(2)**	-	-	127.90(4)
N(2)-C(4)	1.454(3)	1.468(4)	1.472(2)	**C(11)-O(11)-Sn(1)**	91.10(14)	88.98(18)	96.33(9)
N(2)-C(3)	1.456(3)	1.451(5)	1.472(2)	**C(21)-N(21)-Sn(1)**	127.41(15)	94.9(2)	104.19(10)
N(11)-C(11)	1.338(3)	1.328(4)	1.3202(19)	**C(21)-O(21)-Sn(1)**	91.98(13)	90.55(17)	-
N(11)-C(12)	1.424(3)	1.460(4)	1.487(2)	**O(11)-C(11)-N(11)**	114.9(2)	115.7(3)	115.16(13)
N(21)-C(21)	1.331(3)	1.326(4)	1.3318(19)	**C(11)-N(11)-Sn(1)**	94.85(14)	95.7(2)	89.35(9)
N(21)-C(22)	1.423(3)	1.463(4)	1.478(2)	**O(21)-C(21)-N(21)**	114.6(2)	114.9(3)	131.57(16)
O(11)-C(11)	1.284(3)	1.280(4)	1.3058(19)	**N(21)-C(21)-N(2)**	-	-	107.42(13)
O(21)-C(21)	1.289(3)	1.290(4)	1.220(2)	**C(21)-N(2)-Sn(1)**	-	-	86.42(8)

There is only one previous example of a κ^2 N, N' bound ureate ligand in the literature. This was reported by Ruiz and co-workers for the platinum complex **LXXV** (Figure 2.12).[182] The compound was synthesised through reaction of $[nBu_4]_2[\{Pt(C_6F_5)_2(\mu\text{-}OH)\}_2]$ with two equivalents of iPr_2NH in the presence of PhNCO. The bond lengths for the N-C(O)-N core are similar to those observed for **3** and **LXXX**. For the C-O bonds, **LXXX** measures 1.212(10) Å, while for **3** C(21)-O(21) is 1.220(2) Å. For the N-C bonds there is a longer bond in **LXXX** for the R_2N - C bond. This is mirrored in **3** with the measurements being 1.505(11) Å and 1.482(2) Å respectively. The shorter bond comes between the NR moiety and the central carbon, with **LXXX** measuring 1.313(11) Å compared to **3** at 1.3318(19) Å.

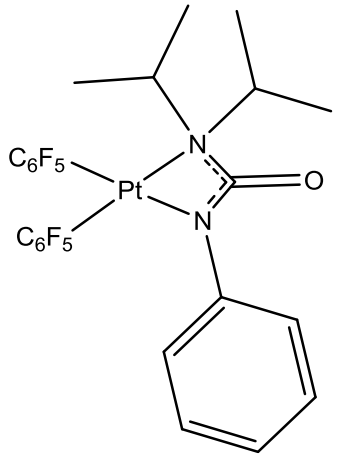

Figure 2.12: Molecular structure of platinum ureate complex LXXX.

2.2.3 Solution based analysis of ligand rotation in compound 3

As mentioned earlier, the NMR spectra for **3** suggested a single ureate environment when recorded at room temperature. Variable temperature ^{1}H NMR studies focusing on the *tert*-butyl resonance at 1.45ppm of compound **3** were therefore undertaken in order to determine whether both the κ^2-N,O and κ^2-N,N' binding modes were present in solution. As the temperature was reduced from 298K to 238K the resonance broadened before splitting into two distinct resonances at 208K (Figure 2.13).

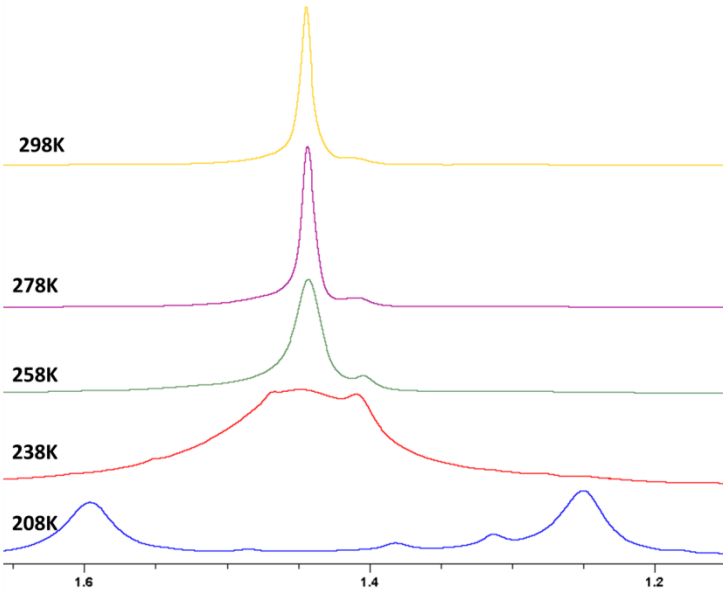

Figure 2.13: Variable temperature ^{1}H NMR spectra focusing on the ^{t}butyl resonance for compound 3.

The low temperature separation of these peaks suggests a facile intramolecular exchange between the κ^2-N,O and κ^2-N,N' coordination modes. By taking the temperature of coalescence (T_c) and the maximum peak to peak separation ($\Delta\nu$), which was observed at 200K a value of ΔG for this exchange was obtained using equation 3. The observed coalescence temperature of 234K and a maximum peak to peak separation of 142Hz result in a value of $\Delta G \cong 46$kJ mol^{-1} an indication that solution exchange between the two differing anisobidentate coordination is a facile low energy process. This is comparable to the energies calculated by Barroso-Flores and co-workers for three organotin xanthate compounds; they found that the Gibbs free energy for rotation between κ^2-S,O and κ^2-S,S for $RR'Sn(SC(S)OMe)_2$ (R=R'=Me, R=Me R'=Ph, R=R'=Ph) was 43.4 -55.2 kJ mol^{-1}.[183]

$$\Delta G \cong RT_c\left[23 + \ln\left(\frac{T_c}{\Delta\upsilon}\right)\right] \quad (3)$$

2.3 Evaluation of compounds 1-3 as potential CVD precursors

2.3.1 Thermogravimetric analysis of compounds 1-3

As mentioned in section 1.5.3, one of the primary methods of assessing the suitability of a potential precursor is to analyse its thermal stability and decomposition pathway by means of thermogravimetric analysis. Samples for TGA were prepared for compounds **1** and **3** and sent to SAFC Hi-Tech as part of a collaboration. The results from the TGAs for **1** and **3** are shown in Figures 2.14 and 2.15, with the first derivative also shown. The derivative gives an indication of the number of steps in the decomposition process. The TGA for **1** shows complex decomposition pathway from 110 °C through to 400 °C where the weight percentage begins to level off, however mass loss is still recorded up to 550 °C when the run finished. The residual mass of 38% does not correspond to SnO_2 (residual mass of 28.9% expected and no sensible product can be attributed to this mass, suggesting that the residue is a mixture of decomposition products. The derivative shows at least nine different mass loss events during the course of the decomposition. The multiple mass loss events and broad decomposition temperature window suggest that this is not a suitable CVD precursor.

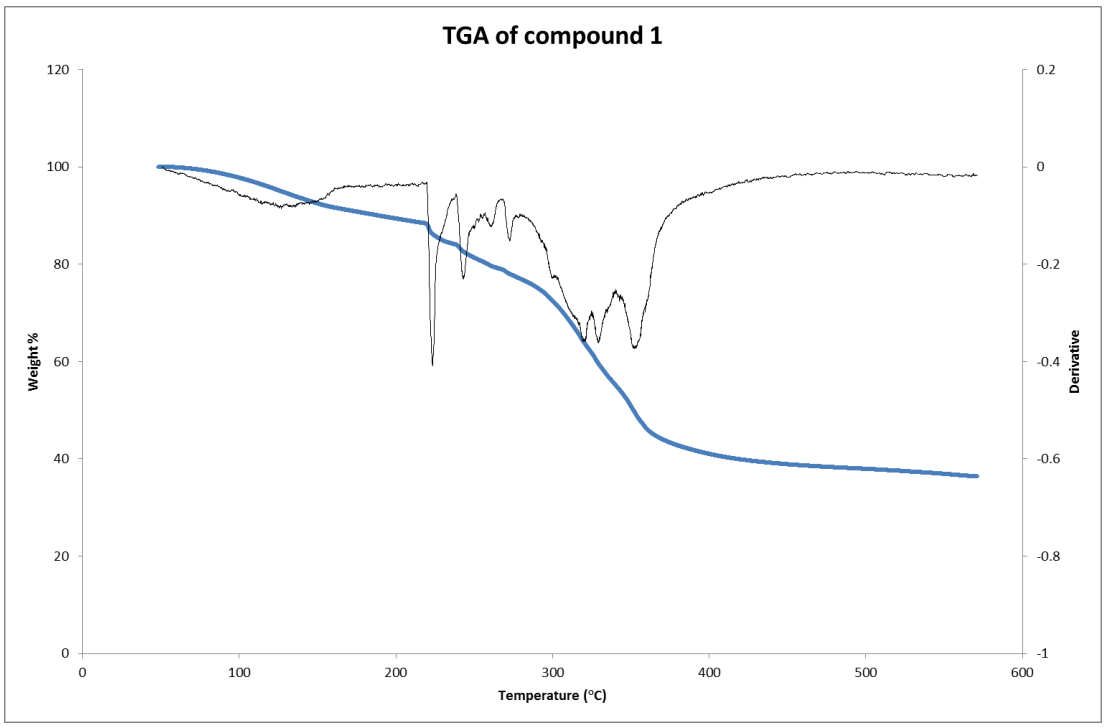

Figure 2.14: TGA data for compound 1.

The TGA data for compound **2** shows a mass loss onset at 180°C which has a minor plateau at 50% mass and 240°C (Figure 2.15). A second mass loss event takes the percentage mass down to 30% with decomposition finishing at approximately 450°C. The residual mass of 30% is close to the calculated percentage mass of SnO (29.46%) indicating that the decomposition product could be SnO. The decomposition process is much cleaner than that observed for compound **1** with only two mass loss events observed.

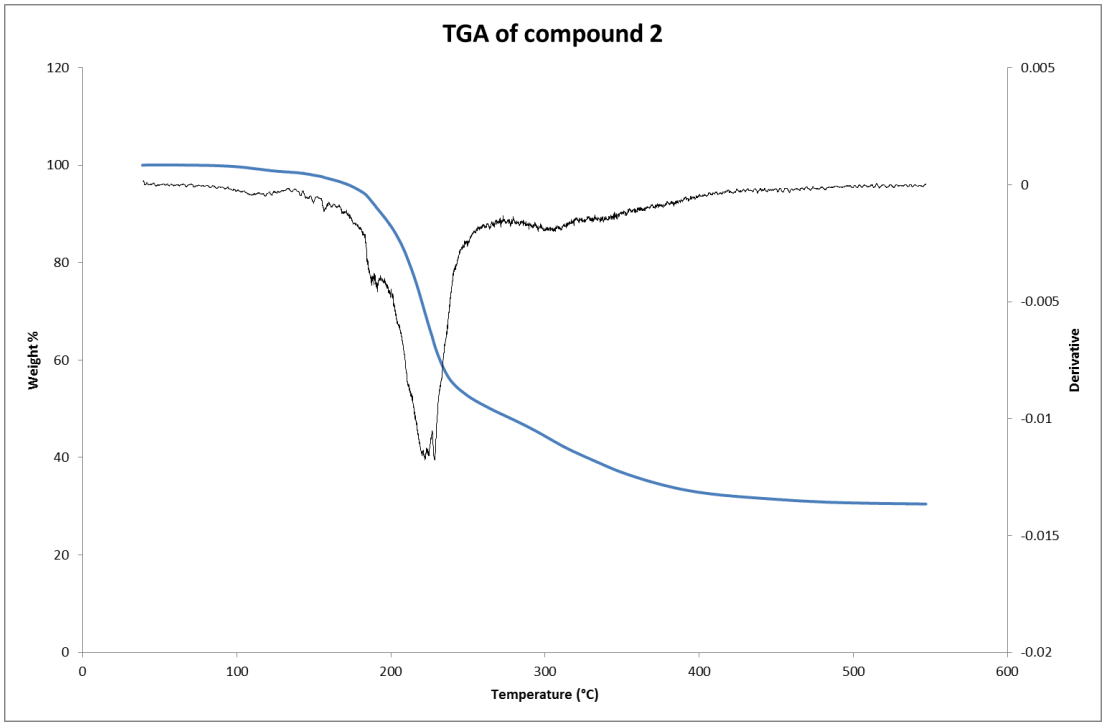

Figure 2.15: TGA for compound 2

In contrast the TGA of **3** shows a single mass loss event with the onset occurring at 90 °C and finishing at 180 °C with a residual mass of 6% (Figure 2.16). The residual mass is significantly lower than the percentage mass expected for tin metal (29.5%), this is indicative of the precursor having some appreciable volatility.

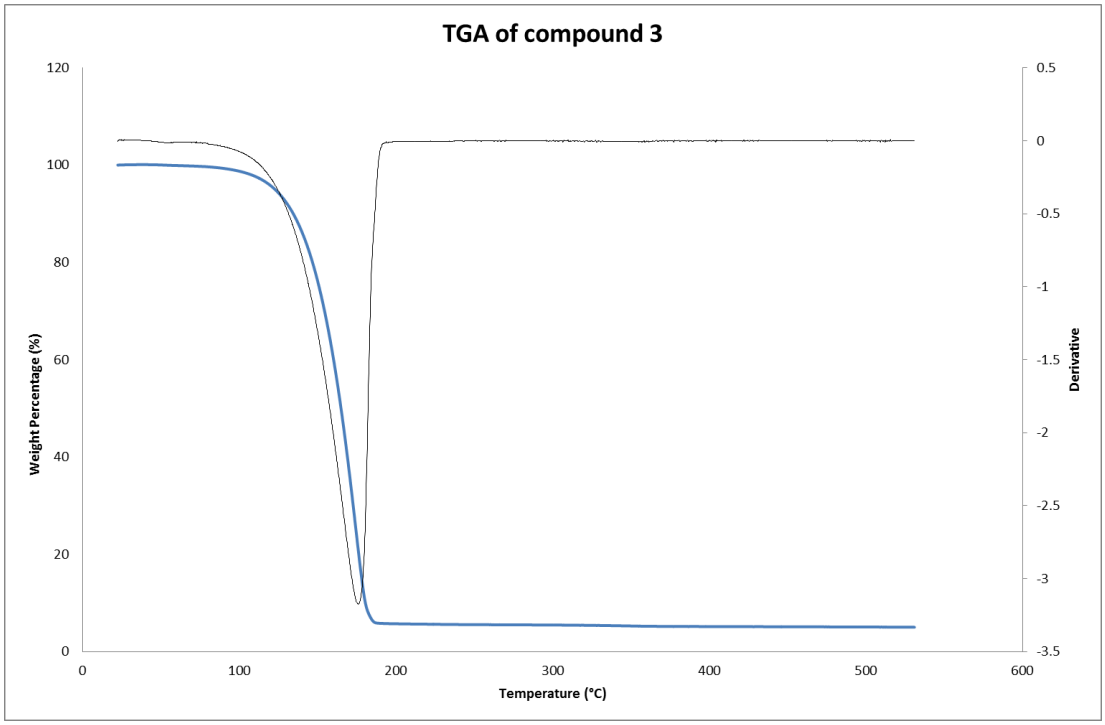

Figure 2.16: TGA data for compound 3

Compound **3** was also sent for vapour pressure analysis - see Appendix 2 for further information.

2.4 AACVD deposition using tin(II) bis-ureate

The thermal analysis used for the evaluation of compound **3** indicated that it could be a suitable low temperature single-source precursor for SnO_x thin films. To ensure sufficient mass transfer to the substrate it was decided that aerosol-assisted chemical vapour deposition would be the best method for initial deposition experiments.

2.4.1 AACVD reactors

Two types of AACVD reactor were used for deposition studies using **3**. A commercial reactor produced by Electro Gas Systems (EGS) and a custom built apparatus. The EGS CVD reactor is designed to conduct atmospheric pressure, low pressure or aerosol assisted CVD. The apparatus consists of a cold wall quartz reactor with the substrate mounted on a graphite block (Figure 2.17 and 2.18). Substrate heating was achieved using an infrared heating lamp, with the temperature controlled by a platinum thermocouple positioned inside the graphite block. Gas lines were heated using heating tape controlled with platinum thermocouples. The nitrogen gas flow was controlled using an electronic mass flow controller. The precursor was dissolved in a suitable solvent at a target concentration of 0.1M and introduced into the carrier gas flow through the use of a Pifco Health ultrasonic humidifier device.

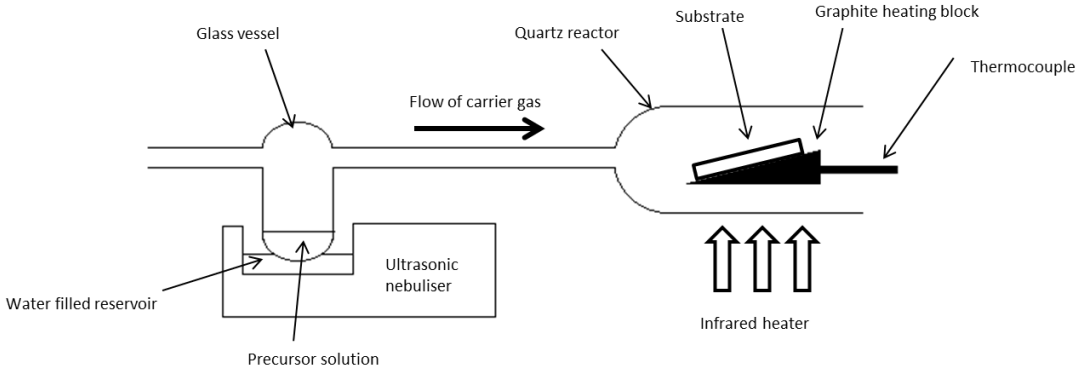

Figure 2.17: Schematic of Electro Gas Systems CVD apparatus with Pifco nebuliser for AACVD

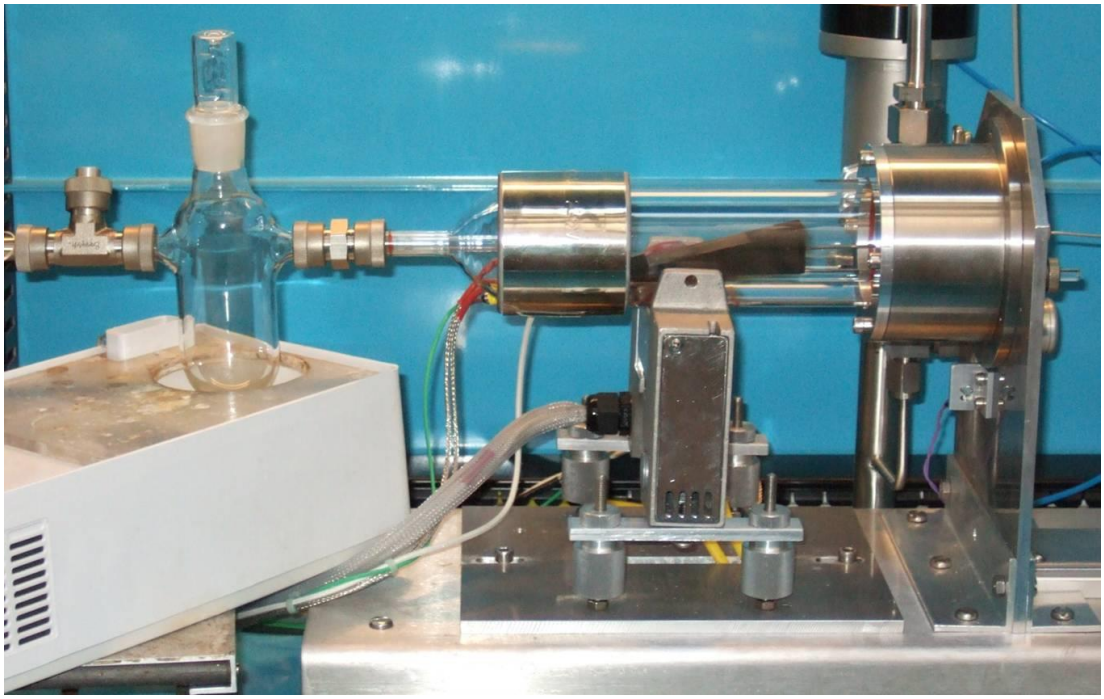

Figure 2.18: Photograph of EGS apparatus set up for AACVD experiments

The custom built AACVD apparatus consists of a hot-walled quartz reactor situated inside a tube furnace (Figure 2.19 and 2.20). The precursor solution is vaporised using a TSI aerosol generator 3076 with an argon carrier gas at 20 psi used to generate a mist by driving the solution through a platinum pin hole.

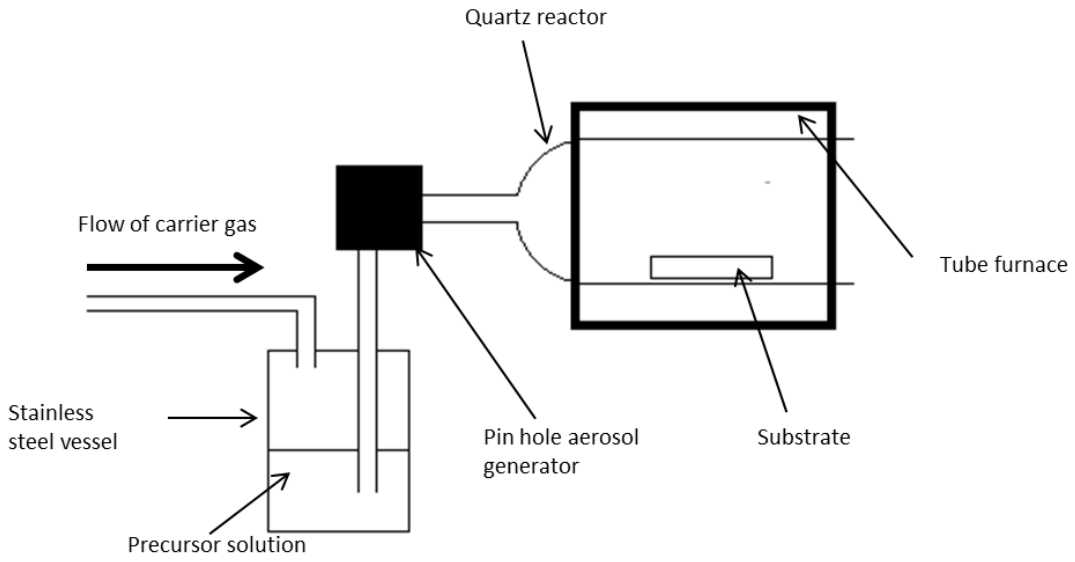

Figure 2.19: Schematic of custom built hot-walled CVD reactor using TSI aerosol generator

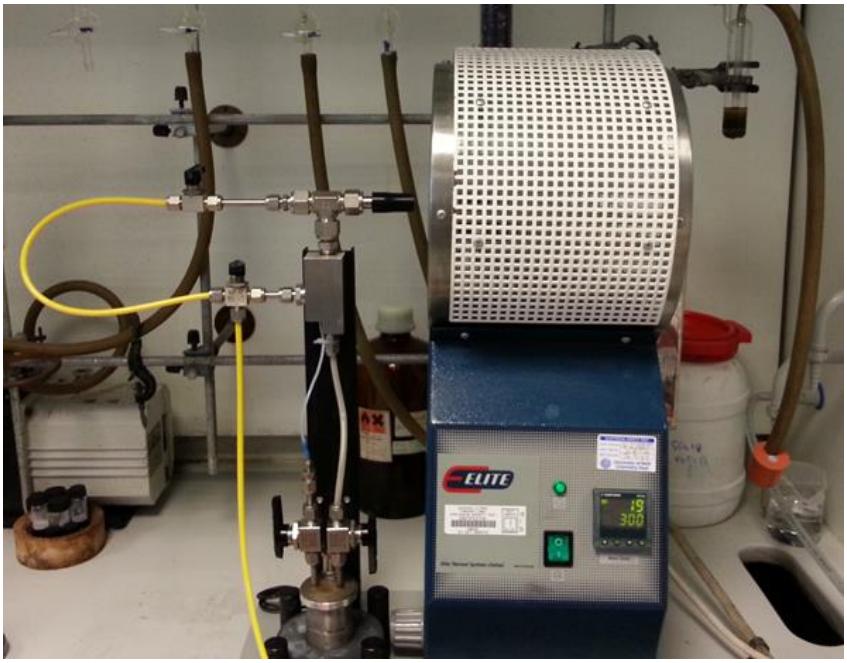

Figure 2.20: Photograph of the custom made hot-walled AACVD reactor system utilising the TSI aerosol generator

Initial depositions using **3** were carried out using the EGS CVD apparatus. Depositions were carried out using a solution of **3** in toluene at a concentration of 0.1M with depositions attempted on glass microscope slides and silicon wafer substrates at temperatures ranging from 250 °C to 350 °C. General deposition parameters are shown in Table 2.4. The deposited films had a yellow-brown hue, which was more pronounced at elevated substrate temperatures, while samples grown on glass showed strong adherence and minimal haze. Similar coloured thin films have been reported by Wu and co-workers, and Piper and co-workers for thin films of SnO.[7,68]

Depositions carried out using the TSI atomiser with a solution of **3** in toluene at the same concentration resulted in powdery depositions at temperatures ranging from 250-400°C. The powdery nature was attributed to gas phase reactions occurring in the hot walled reactor, whereas powdery films were not obtained using the cold walled reactor. Reduction of the precursor concentration from 0.1M to 0.01M rectified this problem and resulted in uniform growth of thin films on glass, silicon wafer and gold substrates with a yellow-brown coloured deposition again observed. The samples showed minimal haze and a strong adherence to the substrate.

Table 2.4: Deposition parameters for AACVD experiments carried out with 3.

Variable	Value	
Apparatus	EGS	TSI
Precursor concentration	0.1M	0.01-0.05M
Substrate Temperature	250-350°C	250-350°C
Substrate	Glass, silicon wafer	Glass, silicon wafer, gold
Carrier Gas Flow Rate (Ar)	0.9-1.5 L/min	3.0 L/min
Gas Flow Temperature	100°C	-
Deposition time	20-60 minutes	30-120 minutes

2.4.2 Raman spectroscopy

To ascertain which tin phases were present in the deposited thin films grown using **3**, Raman spectroscopy was utilised. The Raman spectrum of a sample grown on a silicon wafer using the TSI delivery system is shown in Figure 2.21. The two observed vibrations at 109 cm^{-1} and 209 cm^{-1} correspond to the B_{1g} and A_{1g} modes in SnO, while the vibration at 521 cm^{-1} is the silicon signal from the substrate, which can be used to calibrate the Raman spectrum.[184] SnO_2 has several Raman active vibrations however these all have larger wavenumbers for example, the A_{1g} vibration is reported at 638 cm^{-1} and the E_g vibration is found at 476 cm^{-1}.[29,185] The oxidation of SnO has been monitored using Raman spectroscopy with two resonances at 145, and 171 cm^{-1} observed during the oxidation process, these have been attributed to the Sn_2O_3 and Sn_3O_4 phases.[184]

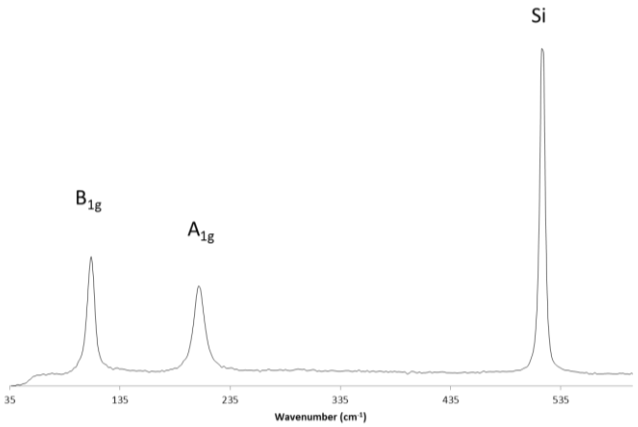

Figure 2.21: Raman spectrum of film grown on silicon at 340 using TSI apparatus. Spectra acquired using 532nm laser

The Raman spectra for films deposited from **3** on glass at different substrate temperatures using the EGS apparatus are shown in Figure 2.22. At elevated substrate temperatures of 350 °C and 325 °C the Raman vibrations are strong for both B_{1g} and A_{1g} modes. As the deposition temperature decreases to 300 °C and 275 °C there are still clear vibrations for both modes. At 250°C the B_{1g} vibration is still visible; however the A_{1g} vibration is no longer observed. The Raman data does suggest however that SnO is being deposited at substrate temperatures of 250 °C, while depositions at 350°C show no sign of disproportionation to tin metal and SnO_2 in the Raman spectra.

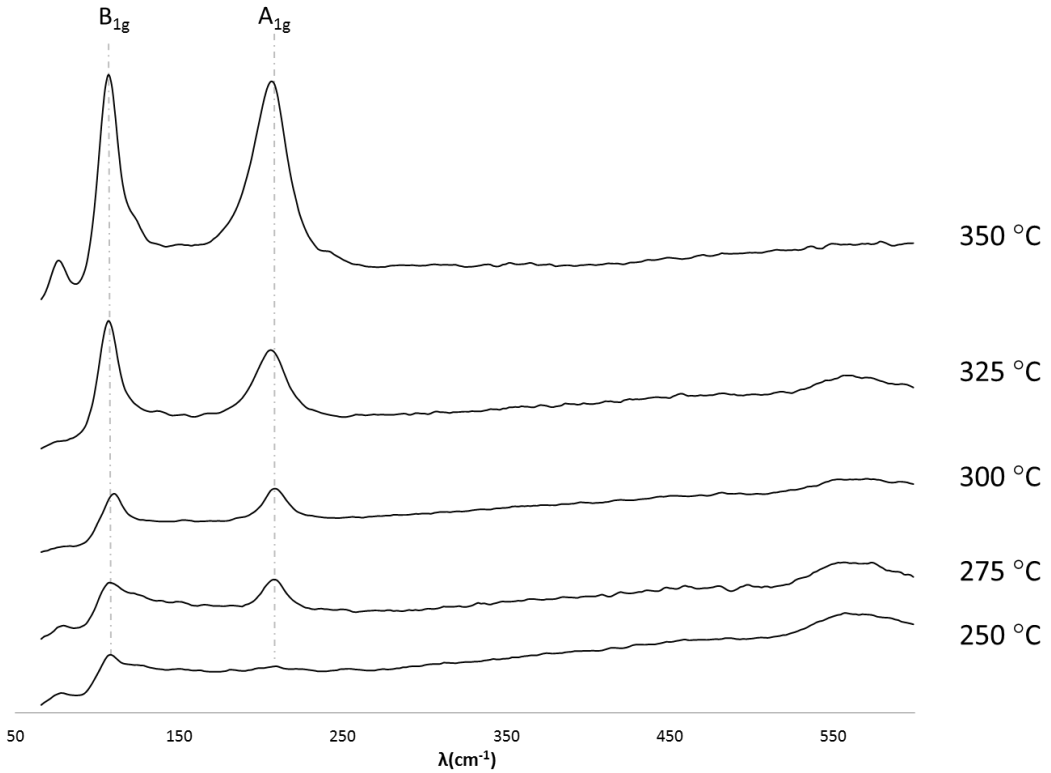

Figure 2.22: Raman Spectra taken of samples grown on glass using EGS apparatus at varying temperatures. Spectra acquired using 532nm laser.

2.4.3 Scanning electron microscopy

Evaluation of the surface morphology of thin films grown with **3** was carried out using scanning electron microscopy (SEM). Samples grown on glass at 250 °C and 275 °C were found to charge significantly in the SEM suggesting an insulating, or poorly conducting material was present on the surface. Analysis of samples grown at 300 °C, 325 °C and 350 °C was obtainable; Figure 2.23 shows a micrograph of a film grown on glass at 350 °C using

the EGS apparatus. The SEM micrograph shows a uniform coverage of the surface comprised of un-orientated disk like particles. The particles appear to vary in size with individual particles measuring less than 10nm across in some sections, although they tend to be approximately 30-50nm wide in many sections.

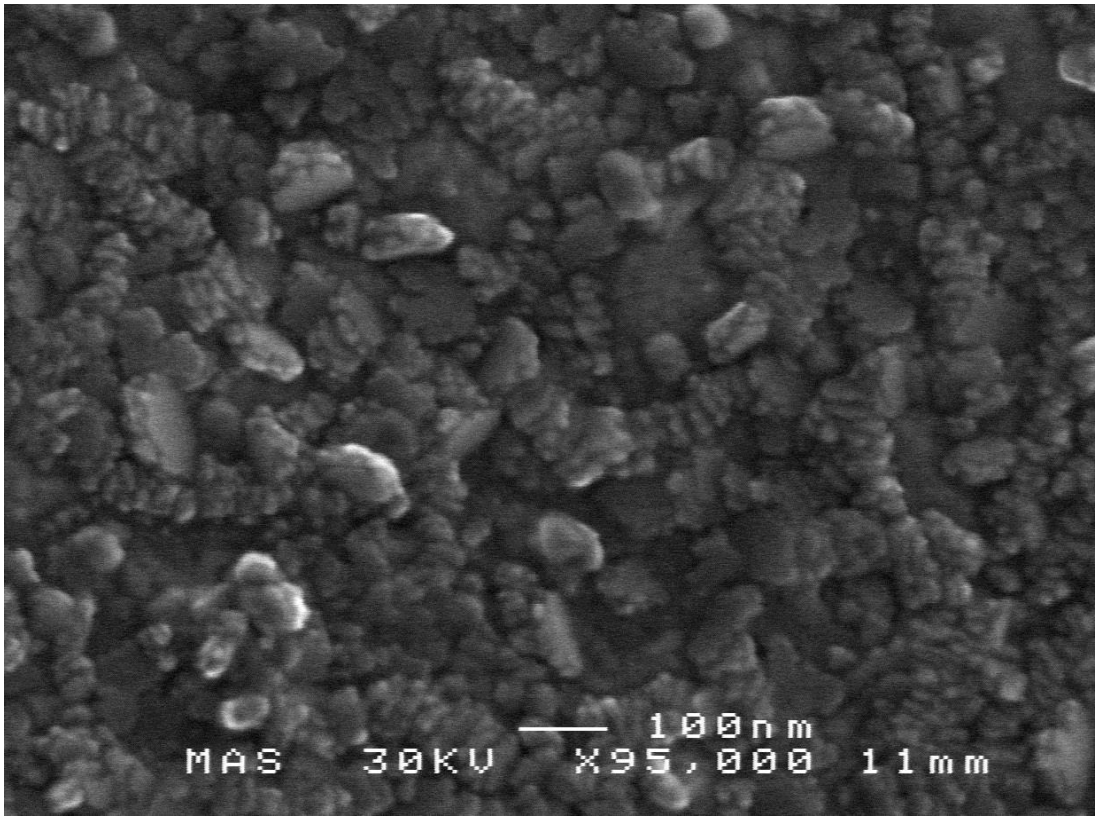

Figure 2.23: SEM micrograph of thin film grown on glass at 300 °C using the EGS apparatus

When the substrate temperature was increased to 325 °C the particles take on more uniform shape and size, as shown in Figure 2.24. The surface coverage is once again uniform with no observable pin-holes or defects in the surface observed. The majority of uniform particles are again disk shaped and randomly orientated throughout the sample and are less than 30nm wide and vary from 40-140nm in width. At points the plates appear stacked together to give a tiled effect, potentially showing orientated growth on previously deposited crystals.

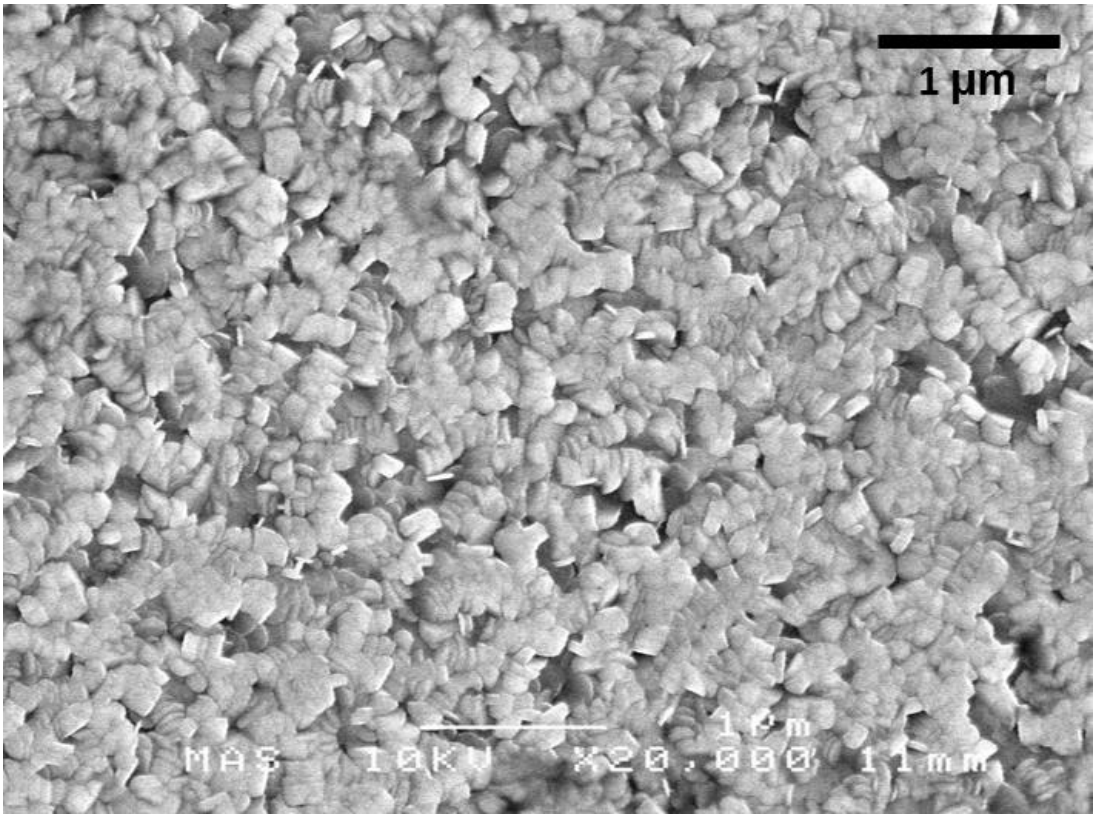

Figure 2.24: SEM micrograph of thin film grown on glass at 325 °C using the EGS apparatus

Increasing the substrate temperature to 350°C results in much larger particle sizes observed in the SEM micrograph (Figure 2.25). The particles again show a uniform coverage with no observable pin-holes or defects on the surface. The particles are randomly orientated across the sample, with particle sizes much larger than observed at lower substrate temperatures. The particles are plate shaped, ranging in size from 140-300+ nm, with thicknesses of 50-75 nm. The surface morphology of these films is comparable to those published by Okamura and co-workers who grew SnO thin films using a solution processing technique.[61]

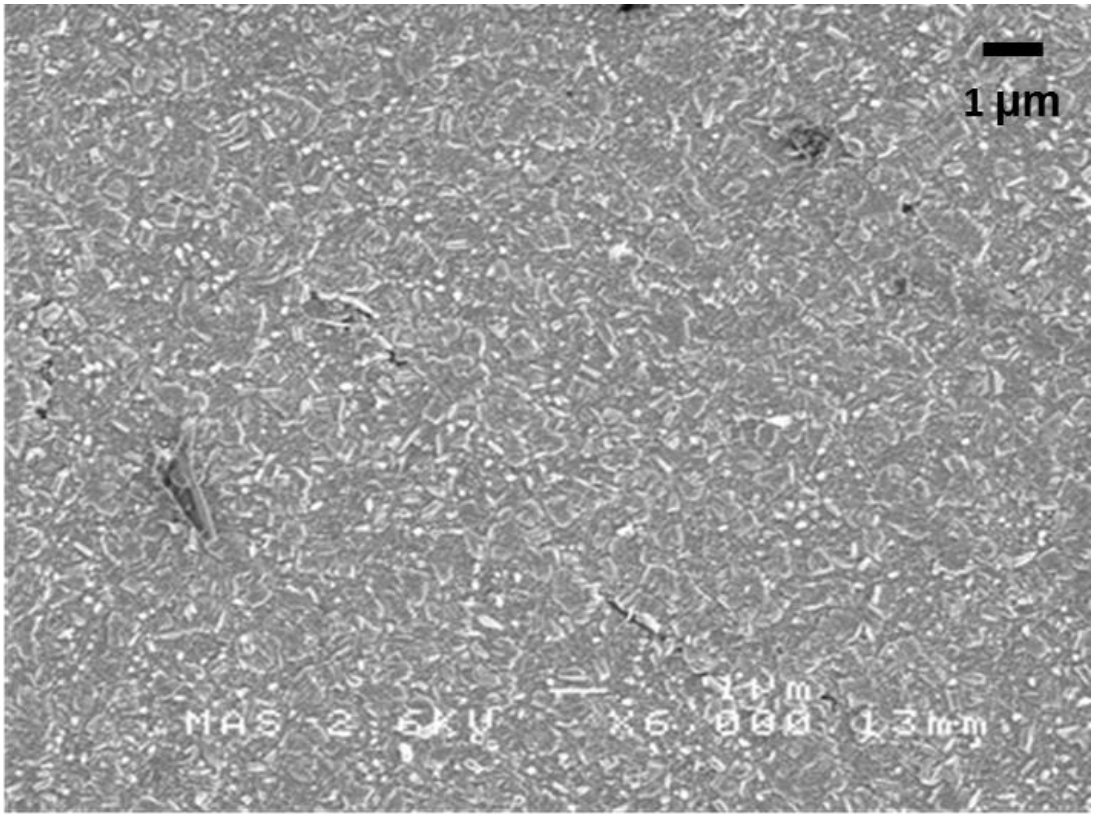

Figure 2.25: SEM micrograph of thin film grown on glass at 350 °C using the EGS apparatus

The surface morphology changed when depositions were carried out using the TSI apparatus, with the particles becoming smaller and more spherical. Figure 2.26 shows a SEM micrograph of films deposited from **3** at 350 °C. The film coverage is continuous with uniform particles with some evidence of coalescence of the particles. The film morphology is more in keeping with the orientated growth observed by Molloy and co-workers with liquid injection CVD of cubane **LXXIV** (Section 1.9).[165]

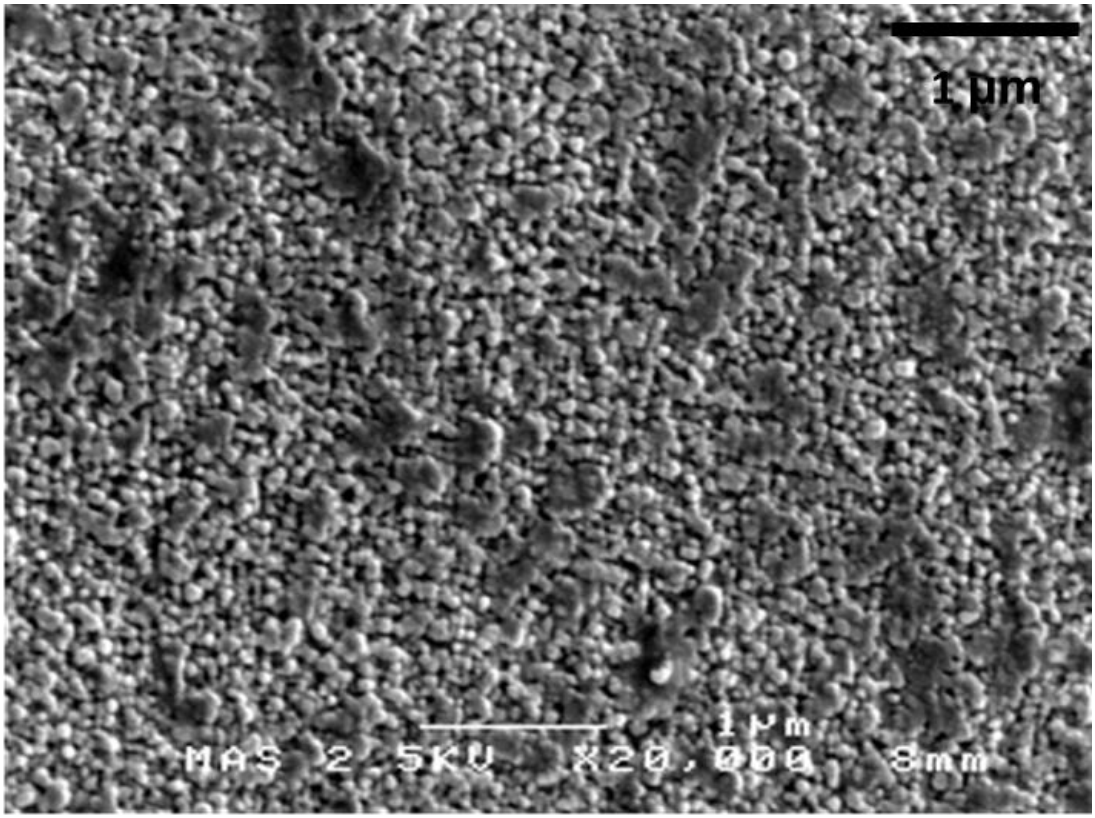

Figure 2.26: SEM micrograph of thin film grown on glass at 350 °C using the TSI apparatus

The morphology of films grown on silicon differed from those grown on glass. The particles are again plate-like, with no evidence for orientated growth observed, however the surface coverage is much less continuous with 200nm flakes scattered across the surface (Figure 2.27 a, b, c), with smaller particles also present underneath the flakes. The cross-section SEM micrograph (Figure 2.27 d) highlights the random orientation and thin plate particle shapes. The cross section provides more evidence that a film has been deposited with the plate particles scattered across the surface. Kim and co-workers reported the formation of highly uniform nano-diskettes when attempting to grow SnO films on SiN_x/Si substrates.[186]

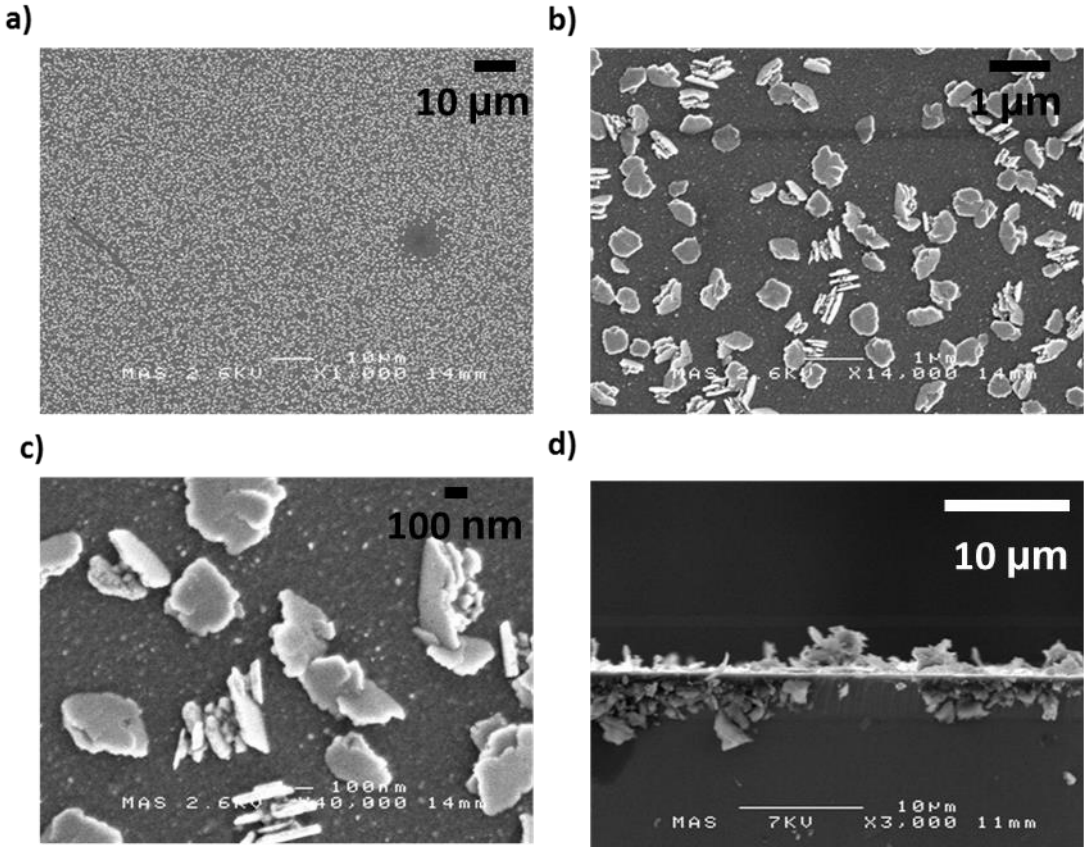

Figure 2.27: SEM micrographs of films grown on silicon at 340 °C using the TSI apparatus. a-c) increasing magnification, d) cross section analysis

Depositions were also carried out on a gold substrate. The gold layer was approximately 10nm thick and deposited by sputtering onto an adhesive layer of chromium on glass. The CVD depositions were carried out using the TSI apparatus at 340 °C with the resulting depositions providing a mixture of particles on the surface with a combination of plate like particles and more spherical objects growing on the surface (Figure 2.28). Cross section SEM (Figure 2.28 d) showed a rough surface with several large features.

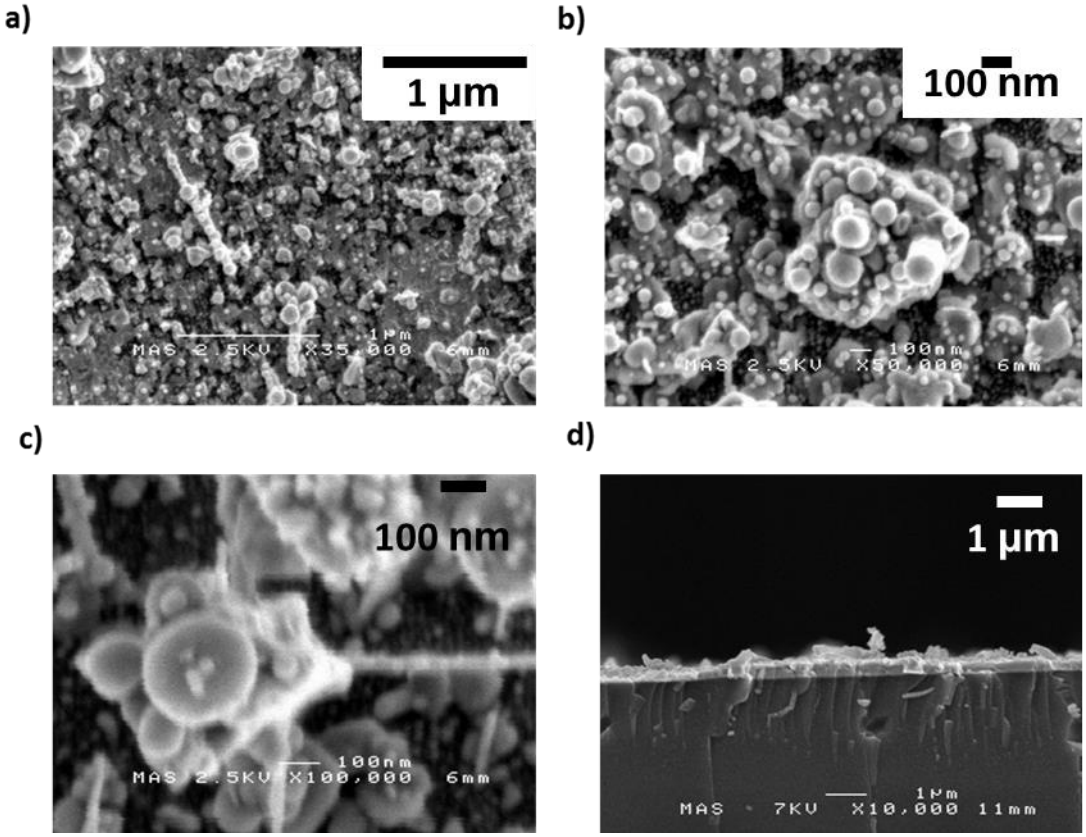

Figure 2.28: SEM micrographs of films grown on gold substrate at 350 °C using the TSI apparatus, a-c) increasing magnification d) cross section analysis

2.4.4 Atomic force microscopy

Another technique for evaluating the surface morphology of deposited films is to use atomic force microscopy (AFM). Data collected through AFM can be used to evaluate the roughness of films grown as well as measure particle size and observe particle shape. The data presented was obtained using an AFM in contact mode. Figure 2.29 shows AFM micrographs for samples grown on glass using **3** at 325 °C and 350 °C. The AFM data show that the films have a regular particle size throughout the sample, the roughness of the samples decreases as the deposition temperature increases, with the sample grown at 325 °C having an RMS of 21.6 nm and the sample grown at 350 °C possessing an RMS of 14.2 nm. The particle sizes were observed to be larger at higher substrate temperatures in the SEM suggesting that the growth is affected by the substrate temperature. Larger particles would be expected to give a lower RMS as there are fewer fractures on the surface.

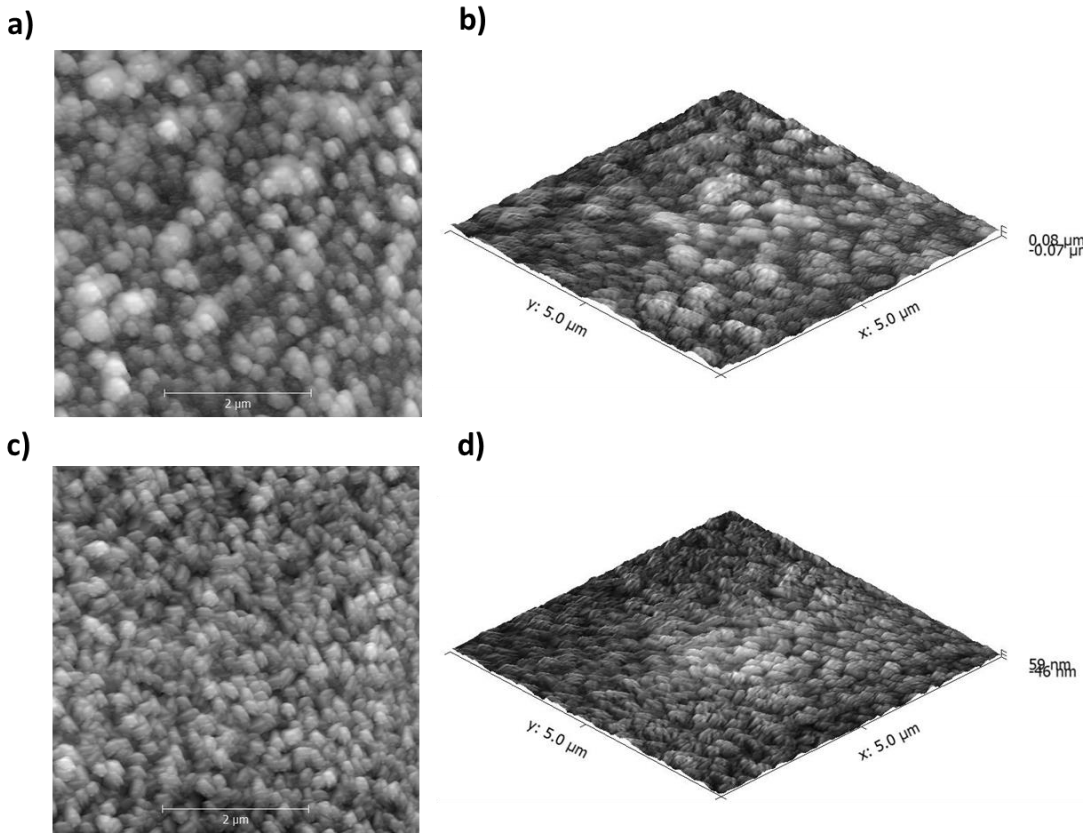

Figure 2.29: AFM micrographs of SnO thin films on glass grown using the EGS apparatus. a-b) substrate temperature of 325°C, c-d) substrate temperature of 350°C

Analysis of an AFM micrograph for a smaller surface area allows more precise analysis of the particles formed through the CVD process. In Figure 2.30 a) the AFM micrograph is taken from a 1μm x 1μm area grown at 325 °C on glass. The image shows the larger plate like particles, measuring approximately 80-100 nm in size have smaller nodules on the surface. These could be nucleation points on the surface, or indicate surface oxidation to SnO_2. The high magnification highlights the random orientation of the particles on the surface. Further reduction of the area analysed to 500 nm x 500 nm increases the resolution on the surface nodules observed on the larger particles (Figure 2.30 b)). The growth of secondary particles on the surface of the larger plates is similar to the features observed in the SEM for the growth of **3** on the gold substrate using the TSI apparatus (Figure 2.28).

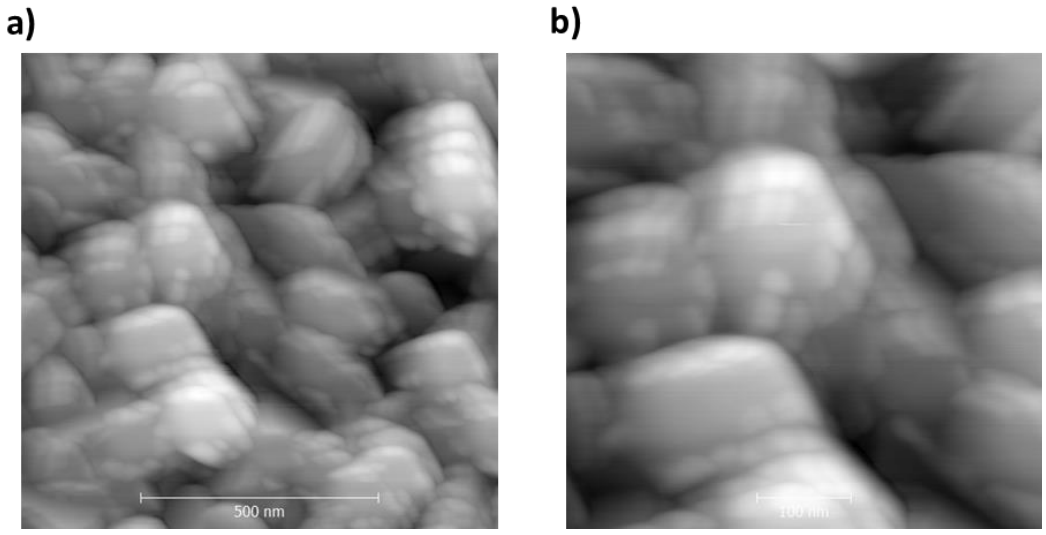

Figure 2.30: AFM micrographs of SnO thin films on glass grown at 325 using the EGS apparatus a) 1 μm by 1 μm area, b) 500 nm by 500 nm.

Analysis of the AFM micrographs shows that depositions using the TSI apparatus had a similar particle size and morphology to films grown using the EGS equipment (Figure 2.31). The roughness calculated for films grown at 350 °C on glass differed slightly, with the RMS for the EGS-deposited film measured at 17.9 nm, while the TSI deposition had an RMS of 21.7nm. The rougher film is expected given the difference observed in the SEM when looking at these samples (Figures 2.25 and 2.26). The morphology shown by the AFM micrographs is comparable to those published by Cao and co-workers for films grown at 600°C on silicon by electron beam evaporation.[62,187]

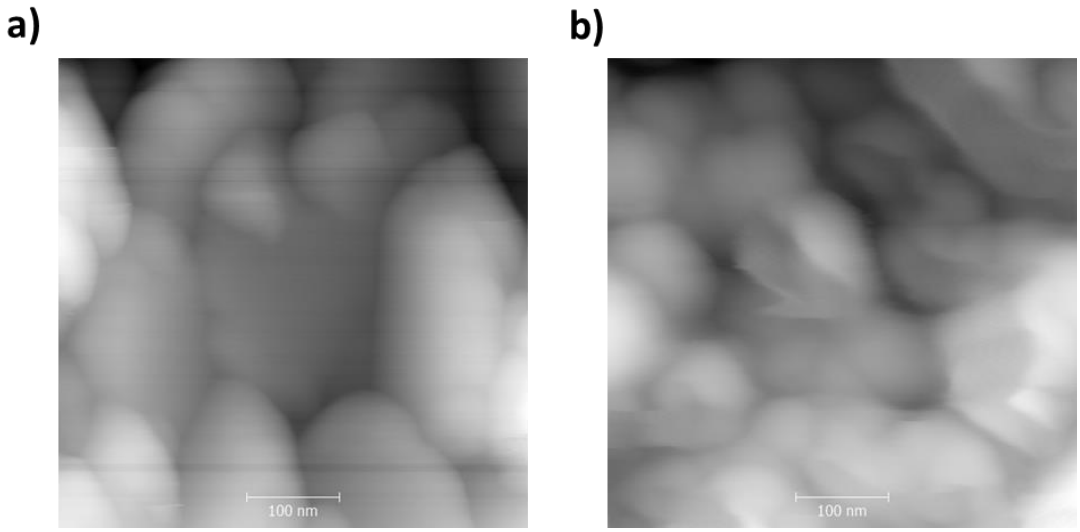

Figure 2.31: AFM micrographs of SnO thin films grown at 350 °C on glass a) using EGS apparatus b) using TSI apparatus

2.4.5 Energy dispersive spectroscopy

Energy Dispersive Spectroscopy (EDS) is an analytical tool used within SEM to detect elements and elemental concentrations within a sample. The tool relies on the emission of X-rays from the sample, with the energy of the X-ray quantum emitted characteristic of the atomic number from which it is derived. Measurement of the energy of the X-rays emitted, therefore, allows elemental composition to be determined. The emission of X-rays during SEM analysis is a consequence of hole generation in the inner shell of an atomic core, whereby the hole is subsequently filled from an outer shell. Due to the energy difference between the core and outer shell electrons the superfluous energy is emitted as an X-ray quantum (Figure 2.32).

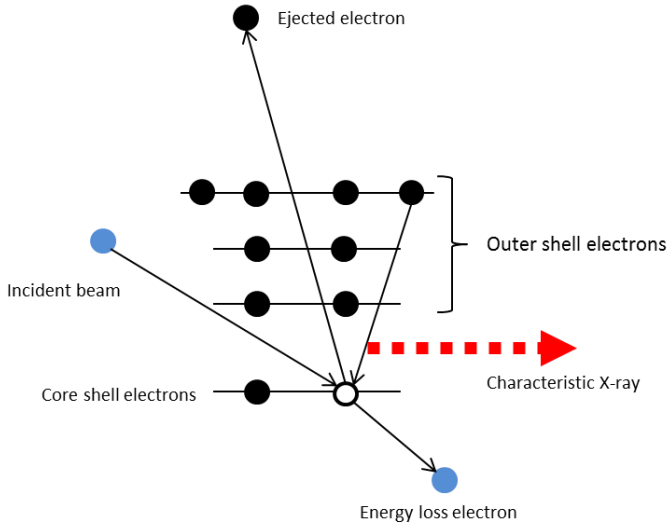

Figure 2.32: Schematic showing X-ray emission due to electron beam interaction, the basis of EDS.

While EDS can be used to determine both qualitative and quantitative data about the elemental make up of a material a high energy electron beam current is often required which increases the sample size and depth. Due to the large zone of inclusion quantitative data could not be obtained as the substrates used all have a native oxide layer or contain significant oxygen. A typical EDS spectrum for a film grown from **3** on silicon is shown in Figure 2.33; as expected the silicon peak dominates the spectra with small peaks for tin and oxygen present. The low intensity of the tin and oxygen peaks could be due to the poor surface coverage observed in the SEM images.

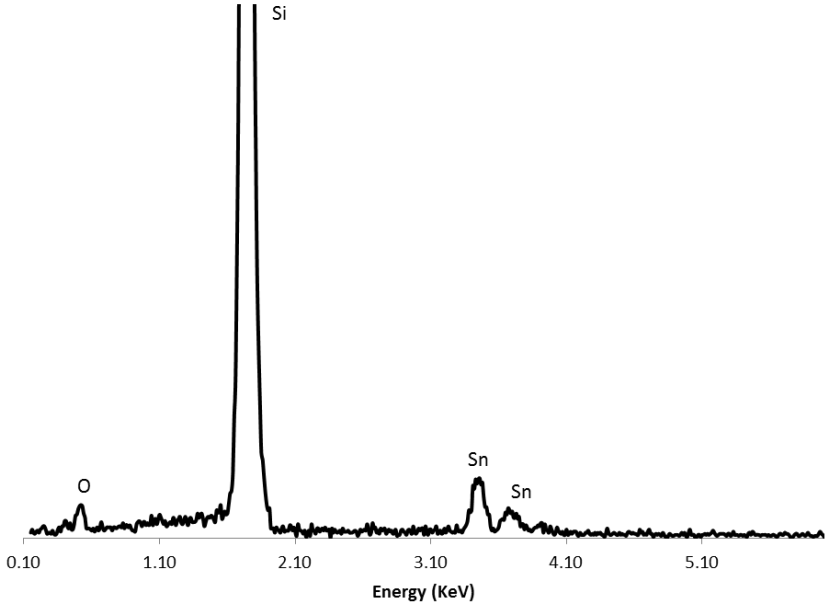

Figure 2.33: EDS spectrum taken of SnO on silicon grown at 325 °C on the EGS apparatus

Stronger tin and oxygen signals could be obtained from films grown on glass substrates using compound **3**. The EDS spectrum for a film grown at 350 °C using the EGS apparatus is shown in Figure 2.34. The intensity of the tin and oxygen peaks are much greater than those observed on silicon substrates. The EDS also contains peaks referenced to calcium, magnesium, and aluminium which are all components of the glass microscope slide.

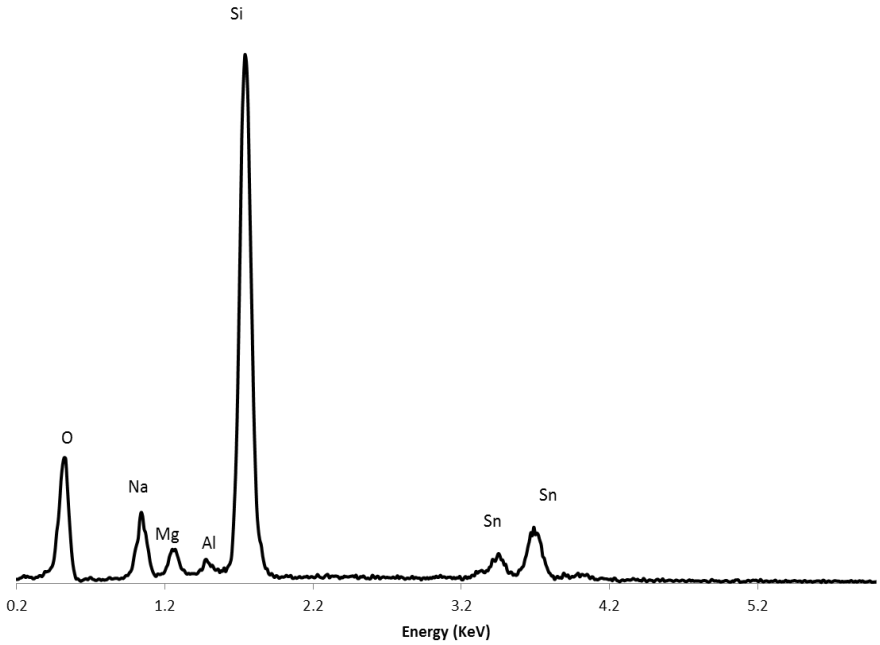

Figure 2.34: EDS spectrum for SnO on glass grown at 350 °C using the EGS apparatus

Depositions using either apparatus sometimes showed carbon and nitrogen contamination, the depositions carried out using the TSI kit showed a higher carbon and nitrogen content. The increase in carbon and nitrogen content, coupled with a different surface morphology observed in the SEM micrographs could be caused by a different decomposition mechanism. The TSI apparatus utilises a hot walled reactor, while the EGS CVD kit has a cold-walled reactor, which could result in different decomposition mechanisms. The cold walled reactor is more likely have surface, or near surface based decompositions, while the hot walled reactor can result in more rapid gas phase heating of the precursor and could result in more gas phase decompositions. This could also explain the required reduction in concentration when operating the hot walled reactor, as at higher concentrations powdery films were deposited, which can be another indicator of gas phase reactions.

2.4.6 X-ray diffraction analysis

Samples were analysed using X-ray diffraction to ascertain the crystallinity of the films, and gather information about potential preferential growth. Analysis by XRD of films grown at on glass at different substrate temperatures using **3** on the EGS apparatus is shown in Figure 2.35. The materials grown have crystalline phases at substrate temperatures in excess of 300°C, with the diffraction peaks matching tetragonal SnO (*P*4/*nmm*) (powder diffraction file (PDF) #85-0712). The powder patterns show no evidence of tin metal (PDF #19-1365) or SnO_2 (PDF #41-1445) present in the films deposited, even at elevated temperatures. As discussed in Section 1.3.3, disproportionation of SnO to tin metal and SnO_2 has been well documented and for thin film fabrication Hosono and co-workers found that tin metal contamination occurred at substrate temperatures higher than 340 °C in as little as seven minutes.[63] The powder patterns observed from deposition with **3** show good agreement with the diffraction pattern reported for SnO powder with the major diffraction lines being the (101) and (110) planes. Previously reported thin films of SnO have showed some preferential growth with Molloy and co-workers finding that cubane **LXXIX** had strong diffraction lines in the (001) and (002) planes.[165] Kim and co-workers also found that orientated growth for SnO was found on SiO_2/Si wafers (001) with the diffraction maxima of the (001), (002) and the (202) planes increasing in intensity when grown by chemical vapour transport deposition methods.[188] For solution processed SnO growth Okamura and co-workers also saw an orientated growth of SnO on SiO_2/Si wafers (001) with the (001) and (002) diffraction lines appearing to be stronger when annealed at 450 °C.[61]

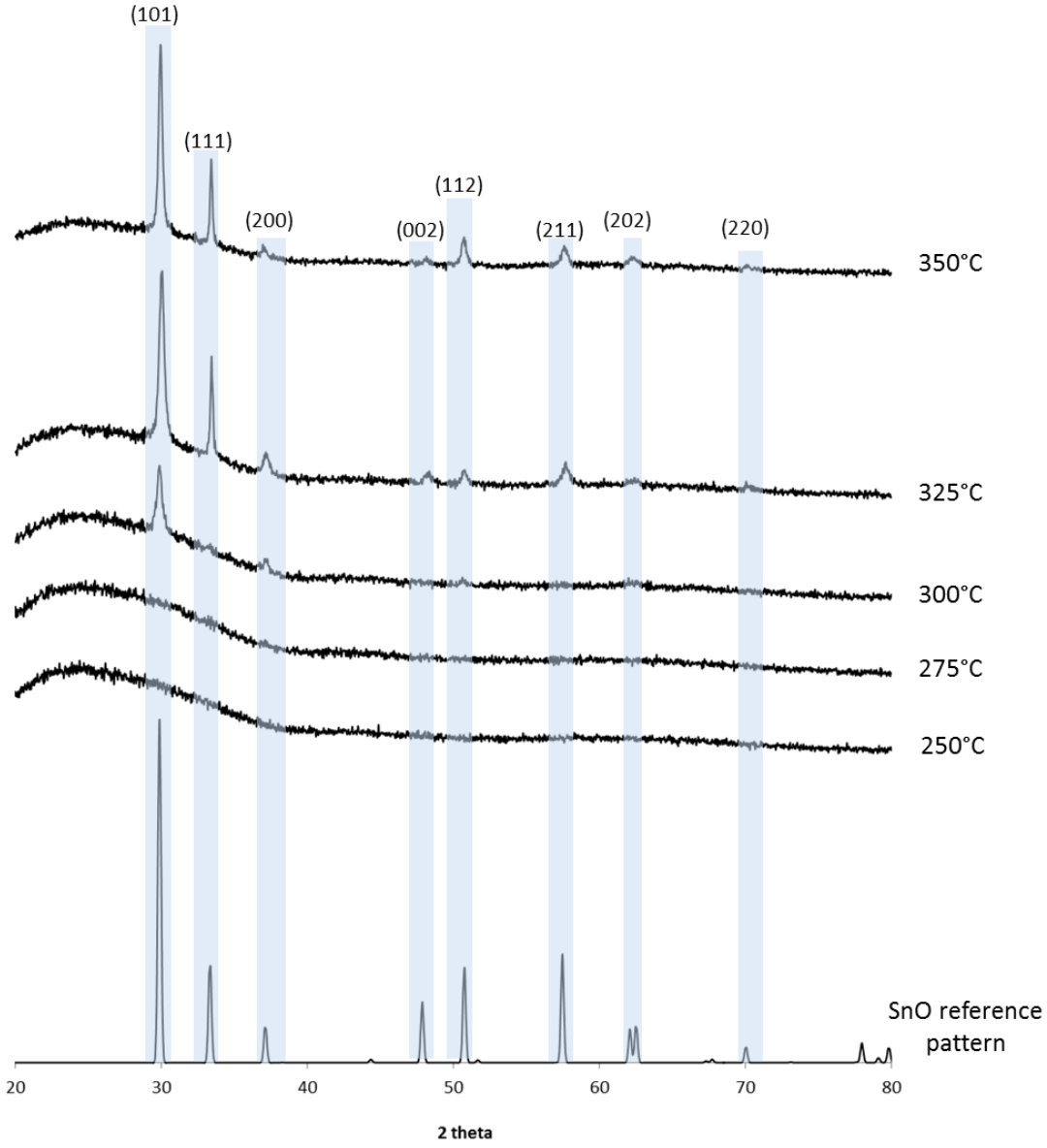

Figure 2.35: X-ray diffraction patterns for thin films grown using compound 3 on glass using the EGS apparatus at varying temperature. A SnO reference pattern is shown taken from ref.[189]

Variation of deposition temperature had a clear effect on the crystallinity of the films, with depositions at 275 °C and 250 °C either being microcrystalline or amorphous with no diffraction lines apparent. Diffraction lines were observed at 300 °C with a strong diffraction line corresponding to the (101) reflection of SnO and a minor diffraction line in the (200) reflection. At 325 °C and 350 °C the (101) and (111) planes have the strongest intensity with several other diffraction lines also present suggesting un-orientated growth. This is in agreement with the Raman spectra taken at different deposition temperatures, which showed much stronger vibrations at elevated substrate temperatures. In comparison the Raman

spectra showed SnO was present at 275 °C and 250 °C where diffraction lines are not observed, therefore amorphous or microcrystalline growth is expected to occur at these temperatures.

The Scherrer equation can be used to calculate the average crystallite sizes based on the width of diffraction peaks at half the maximum height.[190] The Scherrer equation correlates the width of a peak to the crystallite size, with a sharp thin peak corresponding to a larger crystallite than a broad peak. Equation 4 requires the use of a dimensionless shape factor (*K*) which can vary depending on the shape of the crystallites, this has a typical value of 0.9. The X-ray wavelength (λ) is used in nm, and β is the full width at half maximum (FWHM) of the peak and is measured in radians. The final term is the Bragg angle θ of the diffraction peak analysed.

$$crystallite\ size = \frac{\kappa\lambda}{\beta \cos\theta} \qquad (4)$$

It should be noted that the Scherrer equation can only be used as an approximation of crystallite size and gives the lower limit of the crystal size. Analysis of the (101) peak using the Scherrer equation suggested a crystallite size of 41 nm for films grown at 300 °C and 325 °C, while at 350 °C the size increased to 55 nm.[1] The values estimated are similar to those reported by Cao and co-workers (55nm) and Okamura and co-workers (40-55nm).[61,187]

The CVD apparatus used for deposition does have an apparent impact on the growth mechanism of the SnO thin films. Films deposited using **3** using the EGS system and the TSI aerosol generator at substrate temperatures of 350 °C were analysed by XRD (Figure 2.36). The TSI based system (red) produced a different orientation of SnO with the (001) and (200) reflections being much more prominent than in the EGS generated sample (black) which matches the pattern for powdered SnO. These observations are in keeping with the analysis of the SEM and EDS spectra which suggest a different mechanism for SnO formation which is dependent on the apparatus used.

[1] These measurements do not take into account any line broadening as a result of the instrumentation.

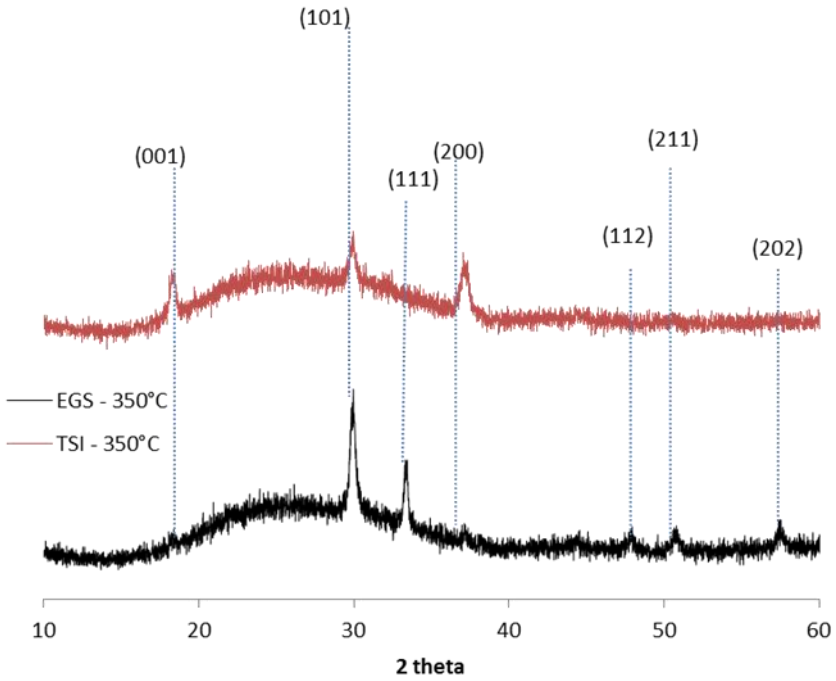

Figure 2.36: XRD patterns for SnO grown on glass at 350 °C using both the TSI and EGS apparatus illustrating the preferred orientation found in the TSI apparatus

2.4.7 X-ray photoelectron spectroscopy analysis

Due to the thin nature of the films grown, accurate elemental composition of the deposited films can be difficult to obtain. X-ray photoelectron spectroscopy (XPS) is a technique that can measure elemental composition that is highly surface sensitive, probing no more than 5-10 nm under the surface of the sample. Unlike EDS which measures the energy of X-rays emitted from a sample as a consequence of electron loss, XPS measures the energy of electrons emitted from a sample upon irradiation with XX-rays. The emission of electrons results in a high surface sensitivity with electrons unlikely to be ejected from depths greater than 10 nm. The energy of the electrons emitted can be defined in terms of the binding energy of the electronic states of the atoms, and so XPS can provide information not only in relation to the identity of the elements present but also their oxidation states and chemical environments.

Differentiation between oxidation states for tin is difficult due to small differences in the binding energies observed. Commonly tin oxidation state and concentration values are determined by the 3d 5/2 locations; for tin these vary from 485.0 eV to 486.7 eV covering tin metal through to SnO_2.[29,191] Distinguishing between the three different oxidation states and

chemical environments is challenging due to the close proximity of the reference values for the tin valence states. To accurately discriminate between the oxidation states lengthy calibration procedures must be undertaken. Previously spectral calibration has been achieved through measurement of the energy difference between the O 1s and Sn 3d lines; however the change in tin oxidation state is thought to affect the position of the O 1s line reducing the accuracy of this technique. Analysis of the Sn 4d lines is also ineffective as the difference between Sn^{4+} and Sn^{2+} is reported to be only 0.7eV.[191] The most effective method of determining the oxidation state of tin present in the XPS spectra is, thus, achieved through analysis of the valence band region. In the valence band the energy difference between SnO and SnO_2 is 3.5 eV, significantly greater than the difference between the spectral lines in the Sn 3d and Sn 4d locations.[191] Sample XPS spectra of the VB region for SnO and SnO_2 are shown in Figure 2.37.

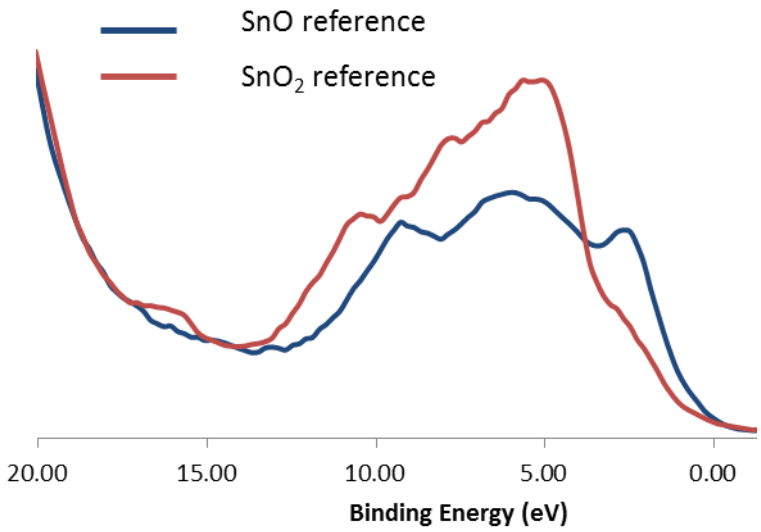

Figure 2.37: Reference valence band XPS spectra for SnO and SnO_2 (taken from Thermoscientific software)

Samples prepared using **3** were sent to the UK's National EPSRC XPS Users' Service (NEXUS) facility based at the University of Newcastle for analysis. As noted earlier XPS is a surface analysis technique; initial surveys for all samples had lines in locations for silicon regardless of substrate indicating that film thickness was therefore below 10 nm or the films were non-continuous with pinholes or defects that meant the substrate was also detected. Given that the SEM micrographs of the material show a plate like formation on the surface it is more likely that this is due to pin holes or surface defects; the presence of defects meant that quantitative data on the atomic composition of the materials grown could not be used to

determine the tin-oxygen ratios. Analysis was conducted on samples grown on glass and silicon grown using both the EGS and TSI apparatus. Selected atomic percentages are shown in in Table 2.5 for survey scans before and after a 20 second etch using an argon ion mill. Carbon contamination was observed on the surface of the films, and although the atomic percentage of carbon is reduced upon etching there is still significant carbon content particularly on the samples grown using the TSI apparatus. As expected with surface contamination the oxygen and tin atomic percentages increased after etching, although due to substrate interaction the tin - oxygen ratio did not reach 1:1 expected for SnO.

Table 2.5: Atomic percentages measured by XPS before and after etching for samples on glass and silicon

	Atomic %							
Sample	EGS 350 Glass		TSI 350 Glass		EGS 325 Silicon		TSI 340 Silicon	
Etch time	0	20s	0	20s	0	20s	0	20s
O 1s	36.94	48.17	26.2	32.39	35.1	46.65	31.82	32.86
C 1s	39.12	14.8	58.55	33.73	40.8	5.42	34.15	18.93
Sn 3d	10.83	25.72	5.32	22.72	7.72	33.6	8.26	17.12

Analysis of the valence band region for all samples before etching showed a strong degree of SnO_2 character (Figure 2.38a), surface oxidation of SnO to SnO_2 has been observed previously in XPS analysis of SnO thin films.[191] Scans of a sample grown using the EGS kit grown on glass at 350 °C after etching, however, clearly evidence SnO as the main feature observed in the valence band region, providing confirmation that SnO thin films have been grown (Figure 2.38b).

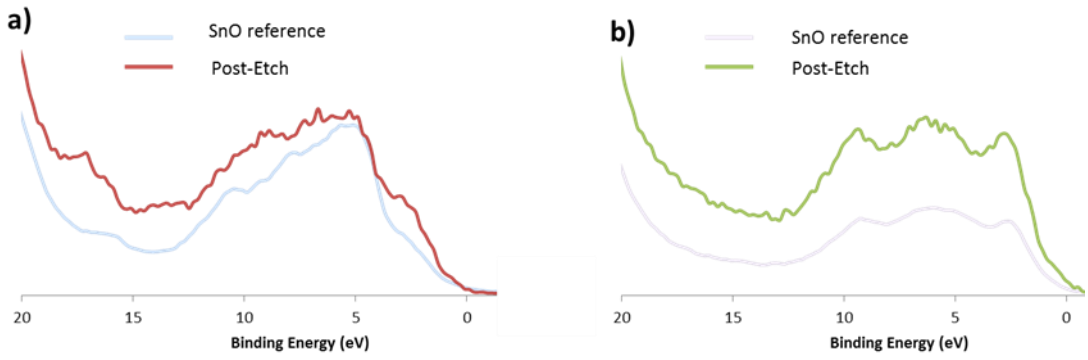

Figure 2.38: XPS analysis of valence band for SnO sample grown on glass at 350 °C using EGS apparatus, a)before etch b) after etch

Traditionally XPS analysis of tin species focuses on the Sn 3d location. For comparison spectral data was obtained for the Sn 3d region pre and post etches. Figure 2.39a shows the

pre etch spectra for a film grown using the TSI apparatus on silicon wafer at 340 °C. The two peaks show some asymmetry due to the presence of Sn^{2+} and Sn^{4+} atoms in the material as a consequence of surface oxidation. Upon etching the peaks show a distinct shoulder at lower binding energies (Figure 2.39b). This shoulder is indicative of tin metal present in the sample; it is proposed that this observation is most likely a consequence of the highly energetic etching process, rather than SnO disproportionation during deposition, and has been observed previously by Themlin and co-workers when using argon ion milling to etch the surface SnO_2 from SnO samples.[191]

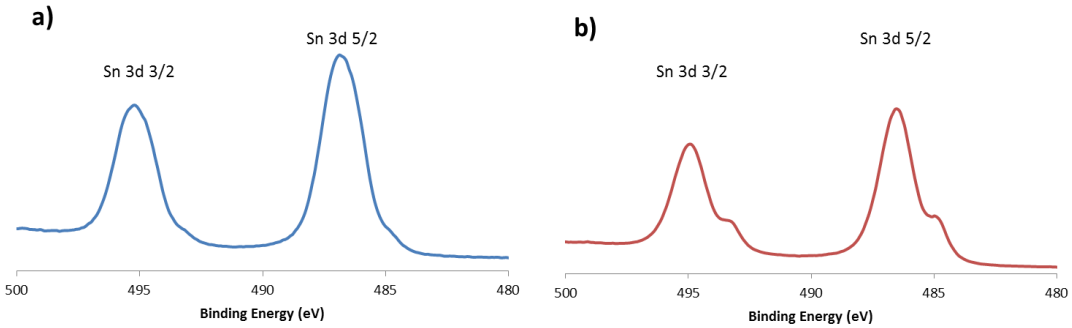

Figure 2.39: XPS spectra of Sn 3d location of a SnO sample grown on silicon at 340 °C using the TSI apparatus a) before etching b) after etching

2.4.8 Electrical characterisation of thin films

In an effort to provide electrical data to confirm the *p*-type conductivity expected of SnO thin films some electrical characterisation was attempted. Efforts to obtain Hall mobility data for the films were unsuccessful due to the high resistance of the thin films grown. Films grown at 350 °C on glass using the TSI apparatus had a resistance of 30-60 MΩ, two orders of magnitude higher than the upper limit for Hall measurements to be conducted.

In conjunction with Professor Laurie Peter and Dr Anna Sudlow flashing LED experiments were conducted to assess the photo activity of the films and their potential to exhibit *n* or *p*-type conductivity. The experiment works by measuring the photo-response of a material when subjected to high intensity light from a LED. Flashing LED experiments were conducted on SnO films grown on gold substrates. An example of the data generated is shown in Figure 2.41. While the photo-response was low for the films, there is some indication of *p*-type conductivity. The data in Figure 2.40 shows the response to a long flash of blue light followed by a short pause. On illumination there is a decrease in measured current, this is indicative of a *p*-type material. The increase in current observed when the light is turned off is thought to be a result of charge recombination.

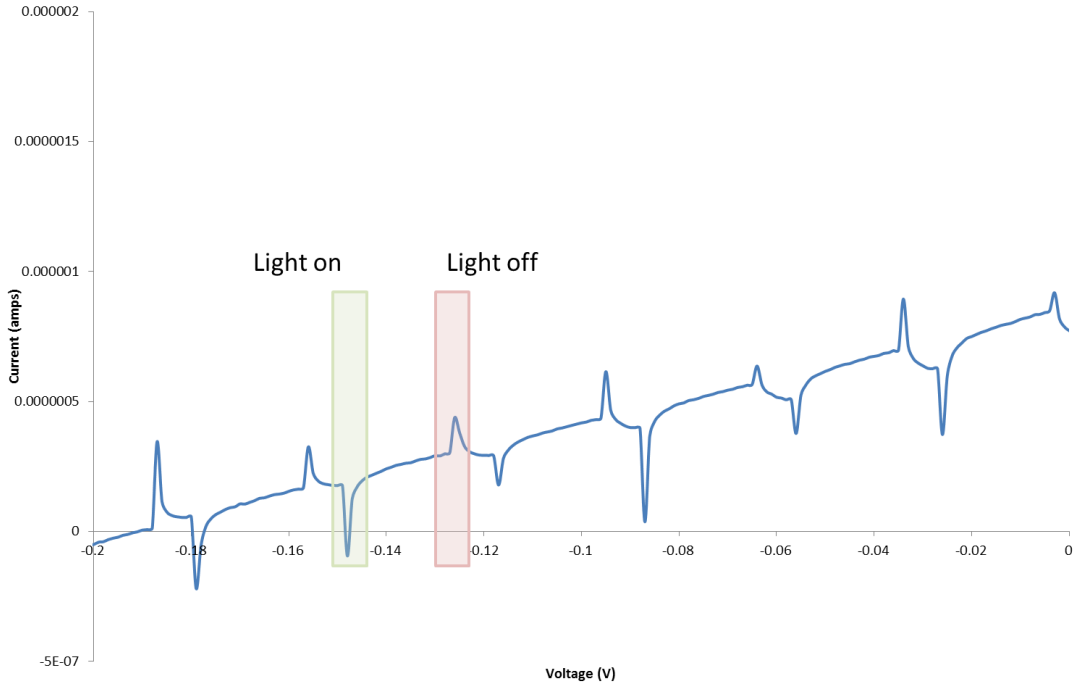

Figure 2.40: Data from flashing LED experiments showing small p-type photo response. Carried out using blue LED.

2.5 Conclusions

The insertion reaction of organic isocyanates with $[Sn(NMe_2)_2]_2$ has resulted in the formation of tin(II) bis- ureate compounds **1-4**; these are the first reported ureate compounds of tin(II) and have been characterised using solution and solid state methods. All four bis-ureate systems exhibited $^{119}Sn\{^1H\}$ NMR resonances between -307 and -357 ppm which is in agreement with the $^{119}Sn\{^1H\}$ NMR resonances observed for tin(II) bis-amidinates (-255 to -397 ppm)[177–180] and tin (II) bis-guanidinates (-377 to -432 ppm)[103] in the literature. The structural similarities between the tin(II) ureates **1-3** and literature examples of tin(II) amidinates and guanidinates was confirmed further through single crystal X-ray diffraction analysis which showed that in the solid state compounds **1-3** existed as monomeric species with a centrally bound four-coordinate tin in a distorted square based pyramidal geometry. For compounds **1** and **2** the ureate ligands both adopted a κ^2 N, O binding motif around the tin centre with the bulkier N substituents in a transoid orientation through the molecule. In comparison compound **3** was found to have one ligand located in the same κ^2 N, O orientation, while the second ligand was found to have rotated resulting in a κ^2 N, N' binding motif with the bulkier N-^{t}Bu groups located on the same side of the molecule in a cisoid relationship resulting in a greater torsional twist within the compound. Variable temperature ^1H NMR experiments allowed the energy barrier for rotation to be calculated as $\Delta G \approx 46$ kJ mol^{-1} which is comparable to organo-tin xanthate compounds studied by Barroso-Flores.[183]

Compounds **1-3** were assessed as potential CVD precursors for the low temperature deposition of tin oxide thin films through thermogravimetric analysis. The bulky aromatic groups situated on the ureate ligand for compound **1** resulted in the compound being unsuitable for further studies as the precursor had a long multistep decomposition pathway with a residual mass much higher than SnO_2. Compound **2** showed much greater promise, with a two-step decomposition over a 200 °C window resulting in a residual mass close to that calculated for SnO; however compound **3** exhibited a much cleaner decomposition with an onset at 90 °C and a residual mass at 180 °C of less than 6% suggesting a good degree of volatility. The sharp, single step decomposition of **3** closely resembles the ideal decomposition pathways for CVD precursors detailed in the literature and was therefore taken forward for deposition studies.[73]

Aerosol assisted CVD using the tin bisureate complex **3** resulted in the exclusive growth of SnO thin films on glass, silicon and gold substrates. Previously the formation of SnO thin films has been carried out using physical vapour deposition methods, such as sputtering limiting the substrates that can be utilised, and often occurring with tin metal and SnO_2 contamination due to disproportionation of the SnO thin films.[11,63] Only three CVD based depositions of SnO have been reported previously through the work of Maruyama, Hoffman and Molloy.[149,161,165] Depositions using compound **3** were carried out between 250 °C and 350 °C using the cold walled EGS reactor system - analysis of the films by Raman spectroscopy showed the presence of SnO, with no detectable presence of SnO_2 or tin metal. The presence of SnO was confirmed for depositions between 300 °C and 350 °C using X-ray diffraction measurements. The patterns showed an un-orientated growth with diffraction lines present for many of the different Miller indices this is comparable to the pattern reported by Maruyama;[149] the depositions carried out by Molloy and co-workers using **LXXXI** showed significantly more orientation with the (001) and (002) reflections having strong reflections.[165] The deposition temperature for films grown using **3** was significantly lower with crystalline films observed at 300 °C the same temperature reported by Maruyama,[149] with Molloy and co-workers requiring substrate temperatures of 450 °C to produce SnO thin films, further to this depositions at 500 °C resulted in the formation of tin metal.[165]

Depositions using the hot walled CVD reactor resulted in more orientated growth, with the (101) and (111) indices having a much greater intensity - this is a different orientation to the growth observed by Molloy and co-workers.[165] Deposition using the hot-walled reactor did result in a higher carbon contamination; this coupled with the more orientated growth indicates that the decomposition pathway of compound **3** may change depending on the heating regime it is subjected to during the deposition process.

Unfortunately due to the quality of the films grown in these preliminary studies a full electrical characterisation of the samples was not obtained, however initial tests did show that the SnO films had p-type semiconductor characteristics which are in keeping with recent publications on SnO material.

In conclusion this chapter has shown that a new type of CVD precursor based on metal ureate compounds can be utilised in AA-CVD depositions for the exclusive formation of metal oxide thin films with low levels of contamination. Furthermore deposition studies using the tin(II) bisureate compound **3** result in the exclusive formation of SnO; this has been verified through Raman spectroscopy, XRD and XPS showing no detectable signs of

oxidation of the tin centre to the thermodynamically favoured tin(IV) oxide. The analysis of the films by XPS clearly shows the presence of SnO in the valence band region with minimal SnO_2 character, the small amount present can be attributed to surface oxidation and is not present after etching of the surface. This suggests that the decomposition route proceeds under kinetic control and could be utilised for the formation of other low oxidation metal oxide thin films.

3. Stannous alkoxides

Tin(II) alkoxide compounds have been utilised as sol-gel and CVD precursors for the formation of tin oxide thin films as discussed in section 1.8. Depositions have mainly focused on atmospheric pressure and low pressure CVD systems with no reports in the literature of aerosol assisted CVD using tin alkoxides. While homoleptic tin(II) alkoxides have previously been reported, there is scope for the development of new systems as potential CVD precursors.

3.1 Previously reported stannous alkoxides

There are several reported synthetic routes for the formation of homoleptic tin(II) alkoxide compounds. Amberger and co-workers reported that the reaction of $SnBr_2$ with two equivalents of NaOMe in absolute methanol resulted in the formation of the $[Sn(OMe)_2]_\infty$ which showed poor solubility in a range of solvents.[192] The resultant white compound was found to be readily hydrolysed, however, and has been used as a reactive source of tin(II) for the formation of several compounds.[123,193–198] The formation of both $[Sn(OMe)_2]_\infty$ and $Sn(OEt)_2$ through the reaction of $SnCl_2$ with the relevant alcohol and Me_3N in non-aqueous solvents has also been reported by Morrison and co-workers (Figure 3.1).[199] The $Sn(OEt)_2$ was found to be poorly soluble in a range of solvents, and exhibited a similar reactivity to that of $[Sn(OMe)_2]_\infty$. A third route to $[Sn(OMe_2]_\infty$ by Harrison and co-workers employed dicyclopentadienyltin and two equivalents of methanol in a protonolysis reaction eliminating cyclopentadiene.[200]

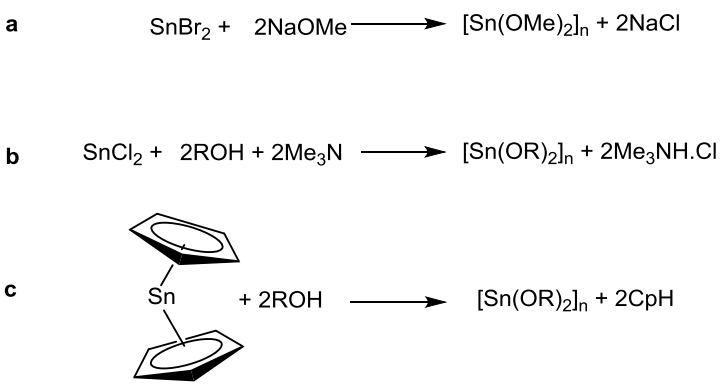

Figure 3.1: Synthetic routes to $[Sn(OR)_2]n$ from the literature. Carried out under anaerobic conditions

A more common route to the formation of tin(II) alkoxide complexes is the protonolysis of a tin(II) di-amide with two equivalents of an alcohol to yield the alkoxide and two equivalents of the corresponding amine (Figure 3.2). The choice of tin(II) amide has been limited to $[Sn\{N(SiMe_3)_2\}_2]_2$ and $[Sn(NMe_2)_2]_2$ in the literature.

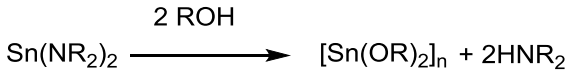

Figure 3.2: Protonolysis reaction between tin(II) amide and an alcohol to form tin(II) alkoxide compounds

`

Caulton and co-workers utilised the protonolysis reaction to synthesis $Sn(O^iPr)_2$ by taking $[Sn\{N(SiMe_3)_2\}_2]_2$ and two equivalents of HO^iPr in Et_2O. The compound was purified further through sublimation at 120 °C and 10^{-2} torr.[144] While a synthetic route and initial deposition studies of $Sn(O^iPr)_2$ were presented, no characterisation data was presented.

Hoffman and co-workers reported the synthesis of a similar compound by reacting $[Sn\{N(SiMe_3)_2\}_2]_2$ with two equivalents of the fluorinated alcohol $HOCH(CF_3)_2$ to form compound **LXXXI**. The homoleptic alkoxide was isolated and purified through recrystallisation although crystals suitable for X-ray diffraction were not grown. Addition of an equivalent of pyridine or dimethylamine as a donor ligand allowed the isolation of X-ray quality crystals which when analysed show a monomeric three-coordinate tin compound (Figure 3.3).[201]

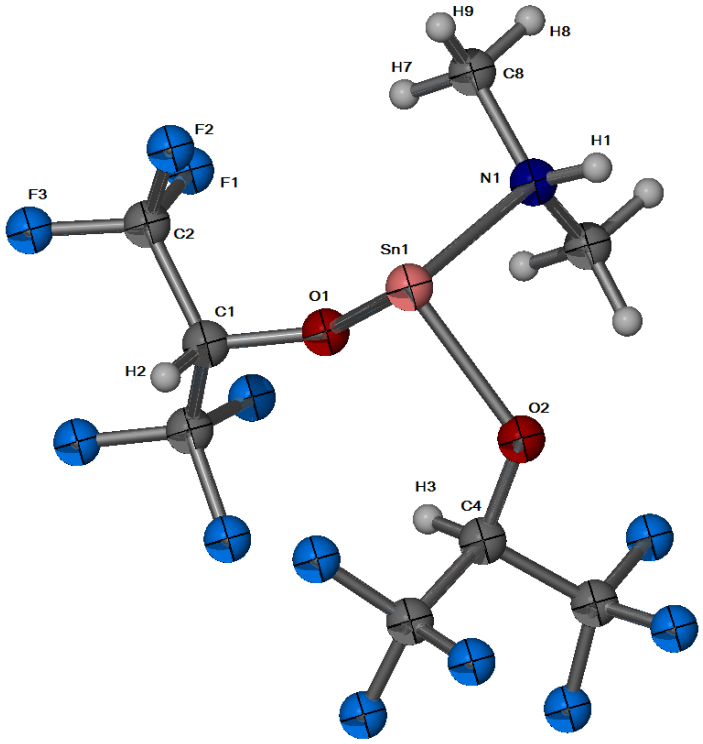

Figure 3.3: Molecular structure of (LXXXI). Ellipsoids shown at 30% probability.

Veith and co-workers have reported the synthesis of the dimeric $[Sn(O^tBu)_2]_2$ (**LXXXII**) through the protonolysis reaction between $[Sn\{N(SiMe_3)_2\}_2]_2$ two equivalents of HO^tBu in *n*-hexanes.[202] Further characterisation was provided by Lappert and co-workers who published $^{119}Sn\{^1H\}$ NMR spectroscopic data, with a resonance reported at δ = -94 ppm, and carried out gas phase electron diffraction experiments which showed the compound was

dimeric in the gas phase.[203] This was verified in the solid state by Veith and co-workers who obtained solid-state X-ray crystallography data.[204] The dimeric compound has two terminal and two bridging alkoxide ligands (Figure 3.4). The terminal ligands are *transoid* to each other in both the gas phase and single crystal diffraction patterns with the terminal ligands at roughly 90° to the Sn_2O_2 plane. [203,204]

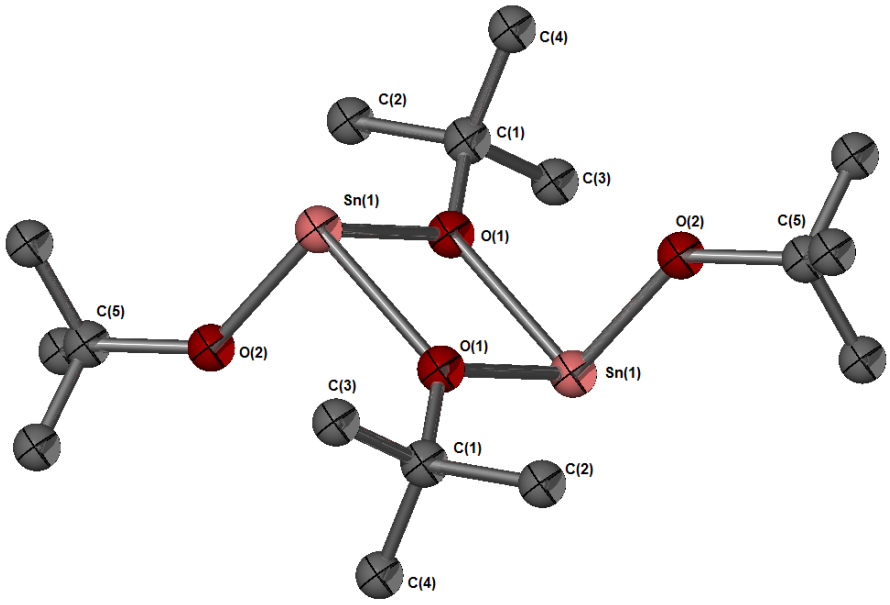

Figure 3.4: Molecular structure of LXXXII. Ellipsoids set at 30% probability, hydrogen's omitted for clarity.

Boyle and co-workers reported the synthesis of $[Sn(OCH_2CMe)_3]_\infty$ (**LXXXIII**) by reacting $[Sn(NMe_2)_2]_2$ with four equivalents of neo-pentanol in hexanes; further purification by recrystallisation from THF resulted in crystals suitable for X-ray analysis which revealed a polymeric crystal structure with four-coordinate tin centres bridged by neopentoxide ligands (Figure 3.5). [154] While solid-state $^{119}Sn\{^1H\}$ NMR spectroscopy yielded a single resonance at δ = -219 ppm, solution-based NMR analysis provided a single broad resonance at δ = -197 ppm in d_8 THF at 25°C although the solubility is poor. Increasing the temperature to 45°C resulted in three resonances at δ = -394, -361 and -197 ppm. The assignment of these resonances was complicated by the poor solubility and the dynamic nature of the compound in solution; with the polymer thought to be broken down into shorter chains leading to terminal and bridging tin centres.

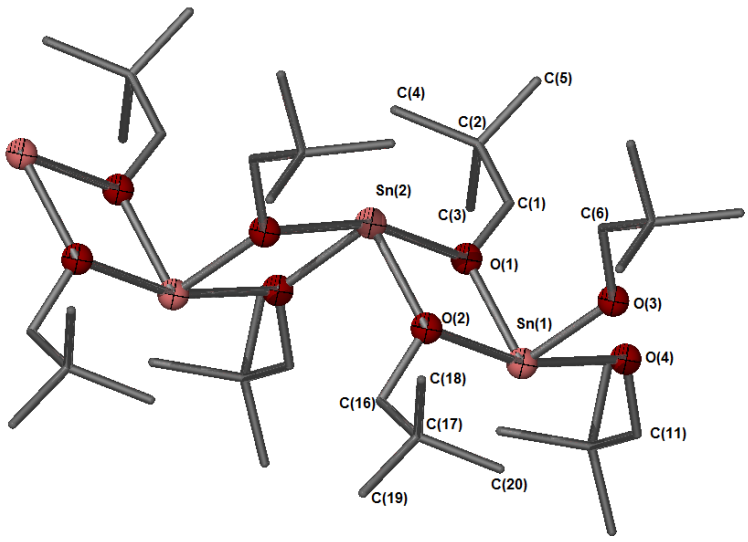

Figure 3.5: Molecular structure of LXXXIII showing the propagation of the 1-dimensional polymeric chain. Ellipsoids shown at 30% probability, hydrogen atoms omitted for clarity

Veith and co-workers reported the synthesis of $[Sn(OC(C_4H_3S)_3)_2]_2$ (**LXXXIV**) be reacting $[Sn\{N(SiMe_3)_2\}_2]_2$ and two equivalents of tris-thienylcarbinol.[205] The reaction was carried out in toluene and THF, with a dimeric species similar to **LXXXII** isolated and characterised by X-ray diffraction analysis. Independent of solvent the dimeric compound is crystallised with two solvent molecules in the lattice and was shown to comprise two bridging and two terminal alkoxide ligands. In this case the terminal alkoxides occupied a *cisoid* orientation with respect to the Sn_2O_2 core of the dimer across the dimer (Figure 3.6 a) rather than the *transoid* geometry observed for **LXXXII**. When THF is used as the solvent, it was possible to isolate the monomer as the three-coordinate THF adduct (**LXXXV**) (Figure 3.6 b) co-crystallised with the dimeric compound. The $^{119}Sn\{^1H\}$ NMR spectra for the dimeric and monomeric species were recorded in $CDCl_3$ with resonances observed at δ= -237 ppm for the dimer and δ= -245 ppm for the monomer.

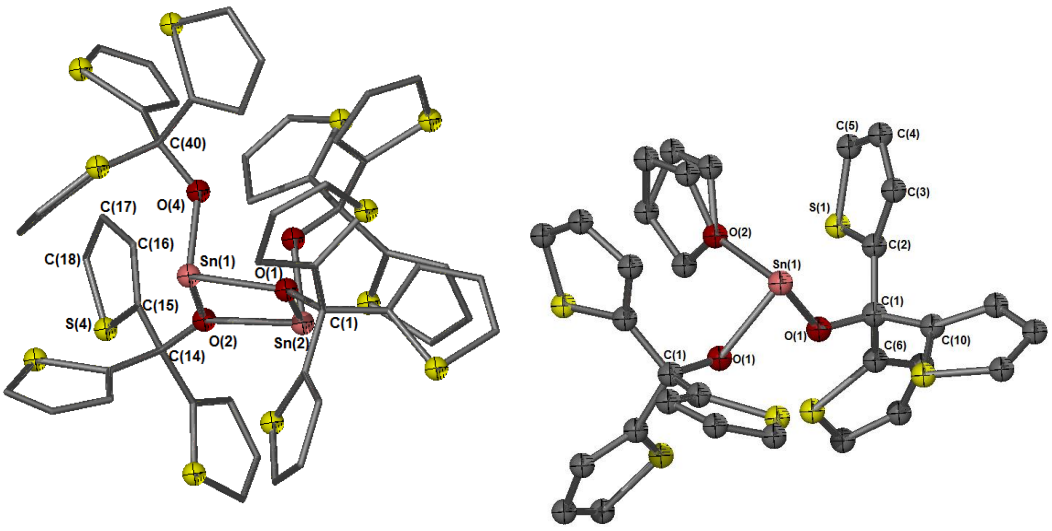

Figure 3.6: Molecular structure of a) LXXXIV. b) LXXXV. Ellipsoids shown at 30% probability, hydrogen atoms omitted for clarity.

Monomeric tin(II) alkoxides have also been synthesised through the use more sterically demanding alkoxide ligands. Lappert and co-workers reported the monomeric $Sn(OC(^tBu)_3)_2$ (**LXXXVI**) through reaction of $[Sn\{N(SiMe_3)_2\}_2]_2$ with two equivalents of $HOC(^tBu)_3$.[203] The reaction is slow, with the compound taking two weeks to form compared to less than five minutes for **LXXXII**. The monomeric nature of the compound was confirmed through X-ray diffraction analysis, investigation of the compound by $^{119}Sn\{^1H\}$ NMR showed a resonance at δ = -163ppm. Other bulky monomeric systems have been reported by the groups of Lappert,[206] Power,[207] Dickie[208], Boyle[209] and Watkin[210] using di-substituted aryl groups. The tin(II) aryloxide **LXXXVII** reported by Power was synthesised through a salt metathesis route, taking two equivalents of lithium aryloxide with $SnCl_2$. The structure of **LXXXVII** is shown in Figure 3.7, and shows a single resonance at -287.7ppm in the ^{119}Sn NMR spectrum, which is upfield of the monomeric two coordinate tin alkoxide reported by Lappert.

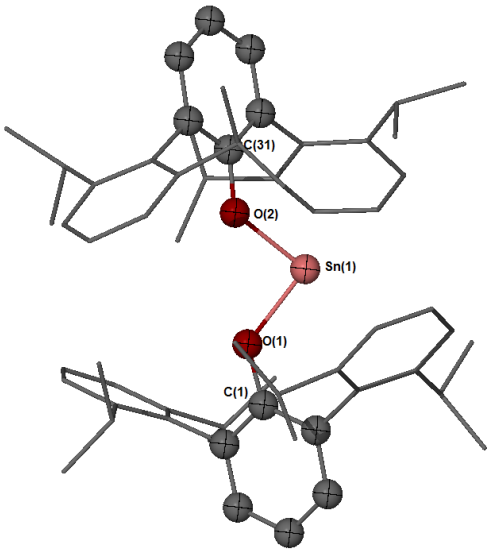

Figure 3.7: Molecular structure of LXXXVII reported by Power and co-workers.

3.2 Results and discussion

3.2.1 Synthesis of tin(II) alkoxides

A protonolysis reaction of tin(II) amides with the two equivalents of the relevant alcohol was chosen as the preferred synthetic route for the formation of tin(II) alkoxides. The synthesis of $[Sn\{N(SiMe_3)_2\}_2]_2$ and $[Sn(NMe_2)_2]_2$ are both carried out by salt metathesis routes as depicted in Figure 3.8.

The synthesis of $[Sn\{N(SiMe_3)_2\}_2]_2$ was carried out through slow addition of two equivalents of $LiNSiMe_3$ in Et_2O to a stirred solution of $SnCl_2$ in Et_2O at 0°C. A white precipitate was observed to form and the reaction mixture turned orange.[211,212] Extraction into hexanes and filtration and removal of the solvent *in vacuo* resulted in a viscous orange oil which was be purified further by vacuum distillation (109-110°C, 0.75 Torr). The purified product crystallises on cooling. The synthesis of $[Sn(NMe_2)_2]_2$ is described in Section 2.5.

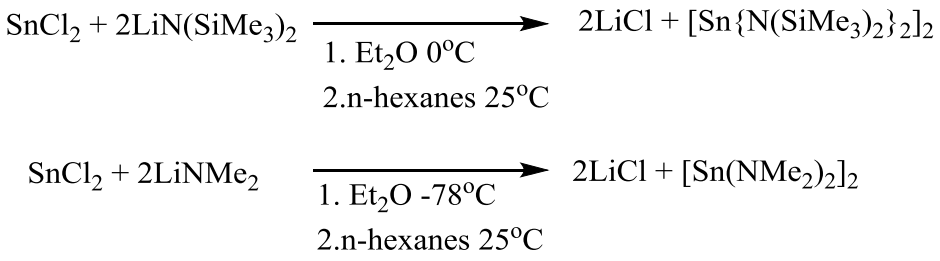

Figure 3.8: Reaction scheme for formation of $[Sn\{N(SiMe_3)_2\}_2]_2$ and $[Sn(NMe_2)_2]_2$

The homoleptic tin(II) alkoxides **5-7** were formed through the protonolysis reaction illustrated in Figure 3.9. The reaction of $[Sn\{N(SiMe_3)_2\}_2]_2$ or $[Sn(NMe_2)_2]_2$ with two equivalents of an alcohol results the displacement of the amide with an alkoxide, with proton transfer giving the tin alkoxide system and the free amine. Isolation of the tin compound was then achieved through removal of the amine *in vacuo* to give the crude alkoxide (Figure 3.9). Further purification of **5** and **6** was achieved through recrystallisation of the crude alkoxides; with **5** crystallised from hexanes at -40°C and **5** crystallised at room temperature from THF. Although compound **6** was isolated as an oil and all attempts to purify by recrystallisation were unsuccessful, elemental analysis indicated that the compound was pure (Found: C 40.88% H 7.56%; Expected: C 40.99% H 7.57%).

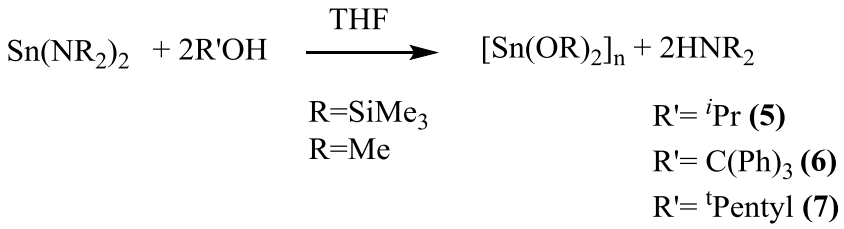

Figure 3.9: Reaction scheme for the synthesis of tin alkoxides

3.2.2 Solution based analysis

The ^{1}H NMR spectrum of **5** in d_8-toluene displayed two resonances, a doublet at δ 1.29-1.31ppm ($^{3}J_{H-H}$ = 6.4Hz) assigned to the methyl groups of the isopropoxide substituents and a septet δ 4.51-4.63 ppm ($^{3}J_{H-H}$ = 6.4Hz) assigned to the methylene proton. Similarly in the $^{13}C\{^{1}H\}$ NMR resonances were observed at δ 28.4 ppm for the CH_3 groups and 65.9 ppm for the -C(H)CH_3 carbon. The $^{119}Sn\{^{1}H\}$ NMR spectrum contained a single resonance at δ -220 ppm which was considerably more shielded in comparison to that observed by Lappert and co-workers for the **LXXXII** system at δ -94 ppm.[203] A solid state $^{119}Sn\{^{1}H\}$ resonance of δ -219 ppm has previously been reported for **LXXXIII**, while solution based $^{119}Sn\{^{1}H\}$ NMR spectroscopy resulted in a resonance of δ -197 ppm at room temperature in d_8-THF.[154] The ^{119}Sn chemical shift gives some indication of the co-ordination number for the tin centre, although as with other NMR active nuclei the electronic effects of the ligand also have a bearing on the relative shielding observed. The chemical shift observed for **5** is consistent with the resonance observed for the four co-ordinate tin system reported for **LXXXIII** which has been identified as a polymeric compound in the solid state.

Compound **6** showed poor solubility in the majority of solvents and NMR spectroscopy could only be carried out using d_8-THF. Resonances in the ^{1}H NMR spectrum showed a broad multiplet for the aromatic groups at δ 7-7.74 ppm. The $^{13}C\{^{1}H\}$ NMR spectrum contained four weak resonances at δ 127.3, 128.2, 129.0 and 149.0 ppm consistent with the aromatic nature of the carbons within the compound. Analysis of the $^{119}Sn\{^{1}H\}$ NMR spectrum shows a single resonance at δ - 67 ppm for **6**. This is considerably deshielded when compared to the structurally similar **LXXXIV** and **LXXXV** compounds reported by Veith and co-workers, who reported ^{119}Sn chemical shifts of δ -244.5 ppm and -236.5ppm for the monomeric and dimeric compounds respectively.[205] The resonance observed for **6**, while slightly downfield, is closer the region reported for the three-coordinate tin geometry found in **LXXXII** at δ -94 ppm.[203]

Compound **7** showed good solubility in a range of different solvents allowing solution characterisation by ^{1}H, $^{13}C\{^{1}H\}$ and $^{119}Sn\{^{1}H\}$ NMR spectroscopy in d_8-toluene. Resonances in the ^{1}H NMR spectrum were observed with a triplet at δ 0.99-1.04 ppm (J_{H-H} = 7.5Hz) attributed to the -$CH_2C\underline{H}_3$ protons, a singlet at δ 1.36 ppm attributed to the -$C(C\underline{H}_3)_2$ protons and an apparent quartet δ 1.57-1.68 ppm (J_{H-H} = 7.5Hz) attributed to the -$C\underline{H}_2CH_3$ protons. The $^{13}C\{^{1}H\}$ NMR spectrum displayed chemical shifts at δ 28.6 ppm and 31.8 ppm attributed to the -CH_3 groups, δ 33.8 attributed to the -$\underline{C}H_2CH_3$ carbon and δ 73.2 ppm attributed to the -$\underline{C}(CH_3)_2Et$ carbon. The $^{119}Sn\{^{1}H\}$ NMR spectrum contained a single peak at δ -99 ppm, comparable to the peak observed by Lappert and co-workers for the similar **LXXXII** which was measured at δ 94 ppm.[203]

Table 3.1: ^{119}Sn NMR chemical shifts for tin (II) alkoxide compounds

Compound	^{119}Sn NMR Shift	Coordination number of Sn	Nuclearity
LXXXI	-162.9 [201]	3	Monomer
LXXXII	-94 [203]	3	Dimer
LXXXIII	-197 [154]	4	Polymer
LXXXIV	-236.5 [205]	3	Dimer
LXXXV	-244.5 [205]	3	Monomer
5	-220		
6	-67		
7	-99		

Table 3.1 displays a selection of tin(II) alkoxide compounds along with the reported ^{119}Sn NMR shifts, the coordination number of the tin and nuclearity of the samples. The range of ^{119}Sn resonances available for compounds with the same coordination number and nuclearity make direct interpretation of the coordination of the compound based solely on ^{119}Sn NMR experiments difficult. For example the monomeric systems **LXXXI** and **LXXXII** both contain two-coordinate tin centres, yet the ^{119}Sn NMR shifts differ by more than 120 ppm. This difference must therefore be attributed to the different electronic contributions of the ligands and the electronic effect on the tin centre should therefore be considered when comparing ^{119}Sn NMR chemical shifts. For this reason it is sensible to compare **5** and **7** to the literature shifts for **LXXXII** and **LXXXIII**. This comparison would suggest that the molecular structure of **5** in solution is more comparable to that of **LXXXIII,** existing as a four-coordinate tin alkoxide polymer. Compound **7** may therefore be expected to exist as a three-coordinate dimeric system analogous to **LXXXII**. Consideration of the ligand structure would suggest that compound **6** is directly comparable to the dimeric **LXXXIV**, however the

tin chemical shifts differ by over 150 ppm. These observations suggest that an assignment of the molecular structure by analysis of the ^{119}Sn NMR chemical shift is less than straightforward.

3.2.3 Molecular structures of tin(II) alkoxides

The solid state structures for compounds **5** and **6** were confirmed by single-crystal X-ray diffraction analysis. A summary of the crystallographic parameters are presented in Table 3.2, and a selection of bond lengths and angles can be found in Table 3.3.

Table 3.2:Crystallographic parameters for compounds 5 and 6

Compound	**5**	**6**
Empirical Formula	$C_6 H_{14} O_2 Sn$	$C_{84} H_{76} O_4 Sn_2$
Crystal System	Monoclinic	Monoclinic
Space Group	$P2_1/a$	$P2_1/c$
Cell Constants		
a (Å)	6.27700(10)	12.49000(10)
b (Å)	7.7700(2)	13.0510(2)
c (Å)	17.6900(4)	40.6560(5)
α (°)	90	90
β (°)	99.3090(10)	92.1630(10)
γ (°)	90	90
Volume (Å^3)	851.42(3)	6622.49(14)
Density (mg/m^3)	1.848	1.423
Z	4	4
Measured reflections	10186	88285
Unique reflections	2260	15167
R_{int}	0.0812	0.0721
R_1. w$R_2[I > 2\sigma(I)]$	0.0299, 0.0722	0.0403, 0.0743
***R* indices (all data)**	0.0345, 0.0750	0.0626, 0.0808

The solid state structure of compound **5** is shown in Figure 3.10. The elucidated structure is polymeric in nature with four-coordinate tin centres bridged by alkoxide units. This structure is consistent with the comparison of the ^{119}Sn NMR chemical shift observed with literature values and the structure of **5** is thus analogous to **LXXXIII** reported by Boyle and co-workers with the Sn_2O_2 planes orientated approximately 90° to each other.[154]

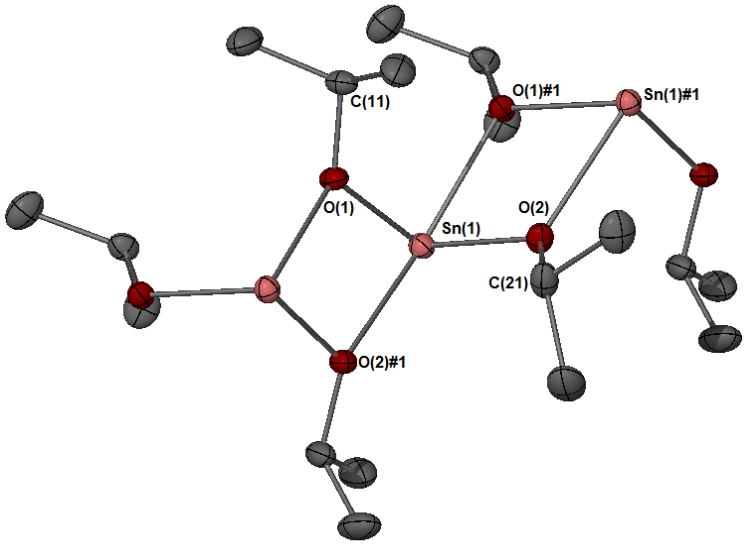

Figure 3.10: Crystal structure of $[Sn(O^iPr)_2]_\infty$. Ellipsoids shown at 50% probability, hydrogen atoms omitted for clarity.

The Sn(1)-O(1) and Sn(1)-O(2) bond lengths of 2.1156(19) and 2.108(2) Å respectively are comparable to those reported by Boyle for $[Sn(ONeo)_2]_\infty$ at 2.114(3) and 2.122(3) Å. The Sn(1)-O(1)#1 and Sn(1)-O(2)#1 bonds are 0.25-0.3 Å longer at 2.3554(18) and 2.4302(19) Å and are attributed as the weaker, formally intermolecular bonds (Table 3.3). This trend is matched in the structure for **LXXXIII** with bonds of 2.403(3) and 2.374(3) Å reported. The tin-oxygen core of the structure has a zig-zag pattern that is also observed by Boyle and co-workers. This is influenced by the stereochemically active lone pair situated on tin atoms in the Sn(II) oxidation state which results in near 90° angles (O(2)-Sn(1)-O(1) 93.70(7)°) between the bridging alkoxides in the plane of the tin atoms.

The solid state structure of compound **6** is shown in Figure 3.11. The compound was found to exist in the solid state as a dimeric species with three-coordinate tin atoms binding to one terminal alkoxide group and two bridging alkoxide groups in a similar fashion to that observed in the literature for dimeric compounds **LXXXIV** and **LXXXII**. The terminal alkoxide ligands are found to be in a *cisoid* orientation with respect to the plane of the Sn_2O_2 dimeric core, this is also observed with **LXXXIV**. This comparable geometry may be most straightforwardly ascribed to the similar steric constraints of the bulky tris-aromatic alkoxide ligands.[205]

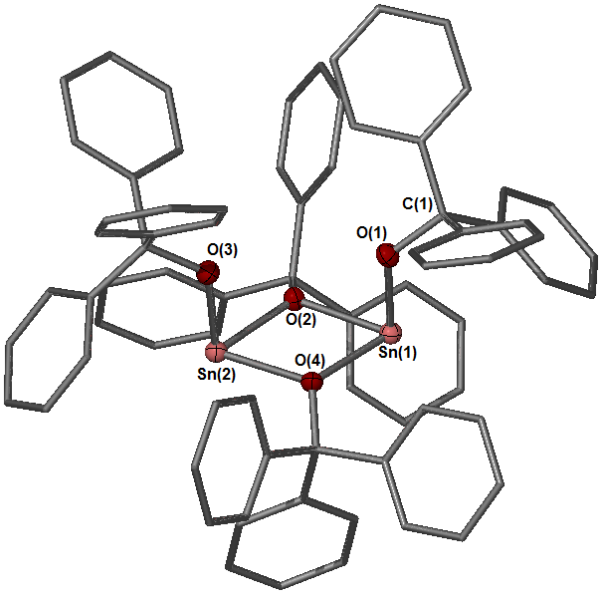

Figure 3.11: Crystal structure of $[Sn(OC(Ph)_3)_2]_2$. Ellipsoids shown at 60% probability, hydrogen atoms omitted for clarity

Apart from the cisiod geometry the solid state structure of **6** shows a close similarity to previously reported dimeric tin alkoxides. The structure of **6** shows a tin – terminal alkoxide bond distance of 2.049(2) and 2.045(2) Å, while the structure of **LXXXIV** has terminal Sn-O distances of 2.053(2) and 2.062(2) Å respectively (Table 3.3). These are also in agreement with the structure of **LXXXII** which displayed terminal Sn-O distances of 2.010(5) and 2.010(2) Å.[204] Although the bridging alkoxide-tin bonds are longer for **6** with distances of 2.1854(19) -2.2324(19) Å, this is in keeping with **LXXXIV** and **LXXXII** which provided distances of 2.182(2)-2.243(2) Å and 2.127(5) -2.165(5) Å respectively. The terminal O_{bridge}-Sn-$O_{terminal}$ angles for **2** are close to right angles ranging from 88.62(8) to 91.02(8)°. This is a consequence of the stereochemically active lone pair on the tin centre and similar angles were again observed in **LXXXIV** and **LXXXII** with angles of 85.4(1)-93.8(1)° and 90.5(2)-93.2(1)° respectively.[204,205]

Table 3.3: Selected bond lengths and angles for compounds 5 and 6

Selected bond lengths (Å)			**Selected bond angles (°)**		
	1	**2**		**1**	**2**
Sn(1)-O(2)	2.108(2)	2.2324(19)	**O(1)-Sn(1)-O(4)**	-	88.62(8)
Sn(1)-O(1)	2.1156(19)	2.049(2)	**O(1)-Sn(1)-O(2)**	93.70(9)	90.02(8)
Sn(1)-O(1)#1	2.3554(18)	-	**O(4)-Sn(1)-O(2)**	-	73.76(7)
Sn(1)-O(2)#2	2.4362(19)	-	**O(3)-Sn(2)-O(2)**	-	90.27(8)
Sn(1)-O(4)	-	2.1854(19)	**O(3)-Sn(2)-O(4)**	-	91.02(8)
Sn(2)-O(3)	-	2.045(2)	**O(2)-Sn(2)-O(4)**	-	74.07(7)
Sn(2)-O(2)	-	2.1890(19)	**O(1)-Sn(1)-O(1)#1**	93.33(6)	-
Sn(2)-O(4)	-	2.2135(19)	**O(2)-Sn(1)-O(2)#2**	94.29(6)	-
O(1)-Sn(1)#2	2.3554(18)	-	**O(1)-Sn(1)-O(2)#2**	70.50(7)	-
O(2)-Sn(1)#1	2.4362(19)	-	**O(1)#1-Sn(1)-O(2)#2**	158.63(8)	-
O(2)-C(21)	1.437(3)	-	**Sn(1)-O(1)-Sn(1)#2**	109.73(7)	-
O(1)-C(1)		1.422(3)	**C(1)-O(1)-Sn(1)**	-	125.28(17)
O(4)-C(4)	-	1.447(3)	**C(4)-O(4)-Sn(1)**	-	124.50(16)
O(3)-C(3)	-	1.426(3)	**C(4)-O(4)-Sn(2)**	-	117.46(16)
O(2)-C(2)	-	1.464(3)	**Sn(1)-O(4)-Sn(2)**	-	106.43(8)
O(1)-C(11)	1.440(3)	-	**C(3)-O(3)-Sn(2)**	-	125.01(18)
			C(2)-O(2)-Sn(2)	-	126.95(16)
			C(2)-O(2)-Sn(1)	-	119.47(16)
			Sn(2)-O(2)-Sn(1)	-	105.65(8)
			C(11)-O(1)-Sn(1)	124.84(16)	-
			C(11)-O(1)-Sn(1)#2	120.98(16)	-
			Sn(1)-O(1)-Sn(1)#2	109.73(7)	-
			C(21)-O(2)-Sn(1)	123.19(17)	-
			C(21)-O(2)-Sn(1)#1	125.20(18)	-
			Sn(1)-O(2)-Sn(1)#1	107.05(8)	-

3.3 Evaluation of tin(II) alkoxide precursors

3.3.1 Thermogravimetric analysis of tin(II) alkoxides

Samples of **LXXXII**, **5** and **7** were prepared and provided to SAFC Hi-Tech for analysis by TGA. Compound **6** was excluded from the TGA analysis due to the high molecular weight and large number of aromatic groups present making it unsuitable for CVD applications. The samples were analysed from 30°C to 550°C under nitrogen at a ramp rate of 5°C/minute. The results are shown in Figures 3.12-14, with the first derivative also displayed. The TGA of **LXXXII** revealed a clean decomposition process (Figure 3.12) with a slow onset observed from 60 °C which becomes increasingly sharper with the fastest rate of mass loss observed at 185 °C. There is a second much smaller event in the derivative at 240 °C, at which point the residual mass is below 2% which is significantly lower than the residual mass for tin metal (45%) indicative of the precursor having some appreciable volatility.

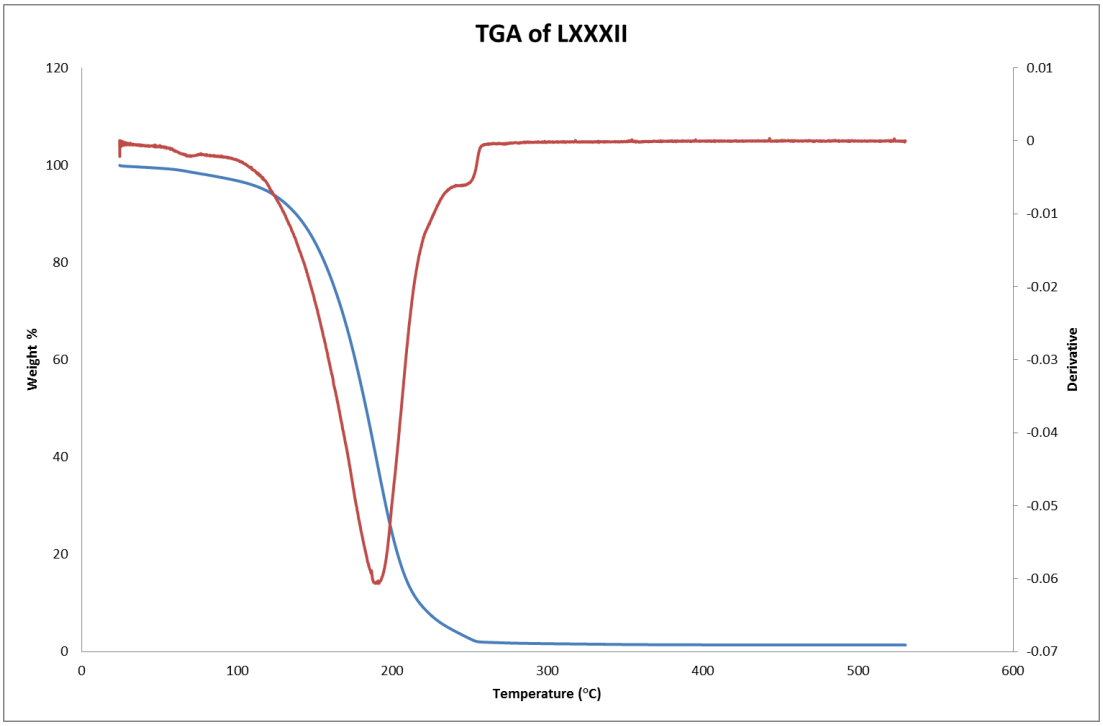

Figure 3.12: TGA of LXXXII

The TGA of **5** displayed a similar decomposition profile with the onset occurring at 125 °C. The profile flattens briefly at 215 °C giving a mass of 22% before decreasing until a residual mass of 2% is obtained at 265 °C (Figure 3.13). In this case, the residual mass expected for

tin metal is 50%, much higher than the mass of 22% found after the first step in the thermal analysis again suggesting that the compound exhibits some volatility.

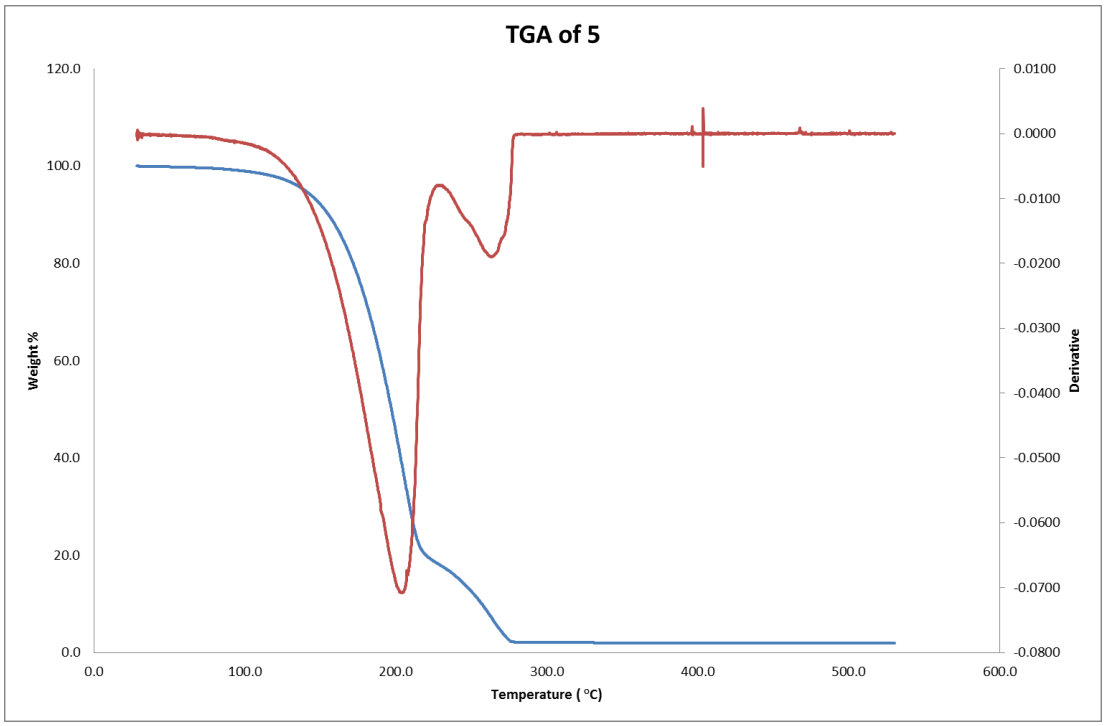

Figure 3.13: TGA of 5

The TGA of **7** has a similar decomposition profile with the onset occurring at 130 °C. The profile flattens briefly at 235 °C giving a mass of 20% before decreasing until a residual mass of 5% is obtained at 295 °C (Figure 3.14). The residual mass expected for tin metal is 50%, much higher than the mass of 20% found after the first step in the thermal analysis suggesting that the compound exhibits some volatility.

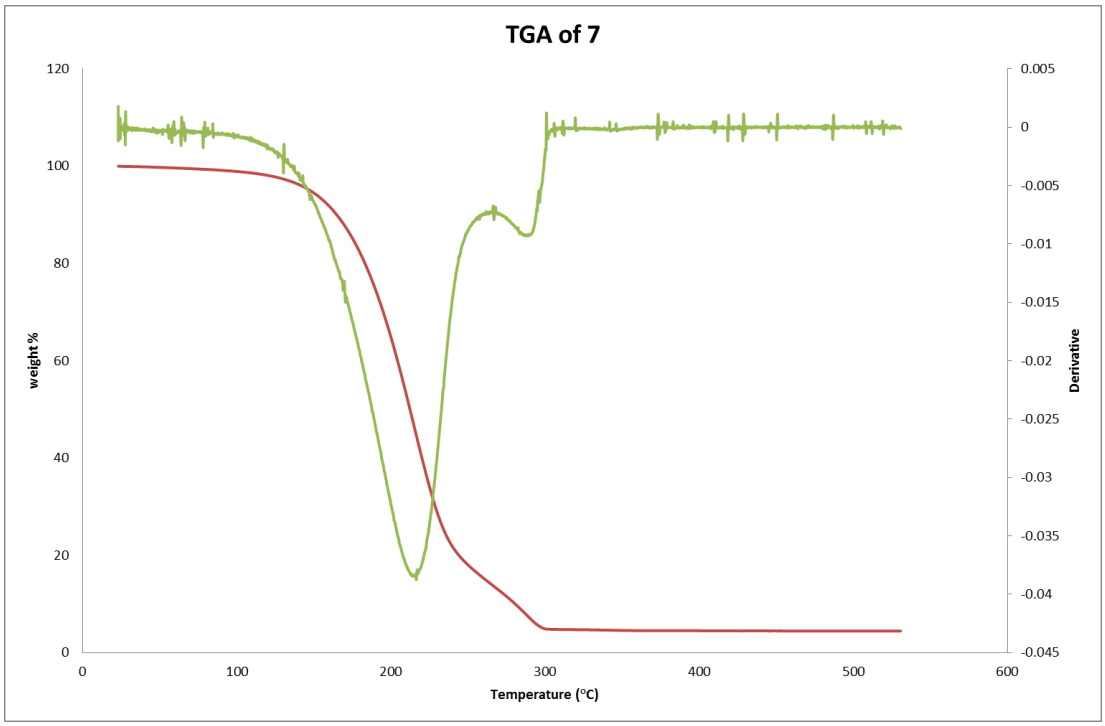

Figure 3.14: TGA of compound 7

Comparison of the three TGA curves on the same graph highlights how similar the profiles for the three alkoxides are (Figure 3.15). All three compounds exhibit similar initial mass loss events and lose mass as a function of temperature at a similar rate. Compounds **4** and **6** have secondary mass loss events at around 20%. As mentioned earlier this is below the residual mass expected for tin metal. The residual masses for three compounds are also similar, with **LXXXII** and **4** having nearly identical residual masses of 1.5 and 2% respectively, while the **6** is slightly higher at 5% all indicative of the compounds exhibiting some volatility.

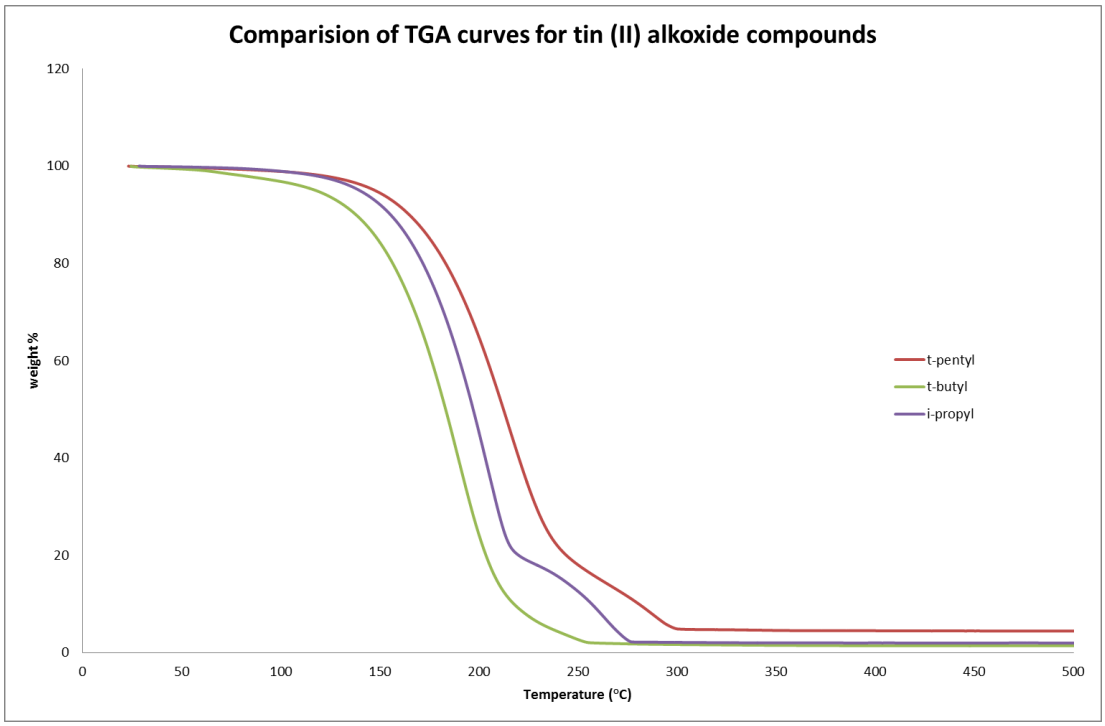

Figure 3.15: Comparison of TGA curves for compounds LXXXII, 5 and 7

Compounds **LXXXII**, **5** and **7** were also subjected to vapour pressure analysis by SAFC Hitech- see Appendix 2 for information.

3.4 AACVD experiments using tin(II) alkoxides

A survey of the literature showed that while tin(II) alkoxides have previously been utilised as tin oxide CVD precursors there are no reports of AACVD experiments; as a consequence depositions were carried out using AACVD conditions on the custom built hot walled CVD reactor with the TSI generator (details in section 2.4.1).

Table 3.4: Deposition parameters for AACVD experiments using precursors LXXXII, 5 and 7

Precursor	**LXXXII**	**5**	**7**
Precursor concentration	0.03M toluene	0.03M toluene	0.03M toluene
Substrate	Glass slide	Glass slide	Glass slide
Substrate temperature	300-450 °C	250-400 °C	250-400 °C
Carrier gas flow rate	3.0 L/min	3.0 L/min	3.0 L/min
Deposition time	30-60 minutes	30 minutes	30 minutes

Depositions carried out using **LXXXII** showed no growth at 300 °C, and limited growth at 350 °C. Films grown at 400 °C and 450 °C were visually much thicker and had a dark brown hue, with some sections looking metallic.

Depositions carried out using **5** at 250 °C had a light brown hue while increasing the deposition temperature to 300 °C resulted in stronger brown coloration. The film had increased haze however and comprised of powdery material. Increasing the deposition temperature to 350 °C worsened the haze and increased the powdery nature of the film surface while further depositions at 400 °C were also hazy and powdery with some metallic looking patches.

The depositions carried out using **7** showed uniform film growth with a yellow-brown hue from 250-350 °C with the film colour becoming increasingly brown as the temperature was raised. At the elevated deposition temperature of 400 °C the films began to become patchy with increased haze and areas of powdery deposition.

The yellow-brown colour observed for the films grown using **LXXXII**, **5** and **7** was similar to that observed for the films deposited using the tin(II) ureate compound **3** (Section 2.4.1). This would suggest that the films grown were predominately tin monoxide. The metallic appearance of films grown using **LXXXII** and **4** may indicate that tin metal has also been deposited in the process.

3.4.1 Raman spectroscopy

Raman spectroscopy was utilised to ascertain which tin phases were present in the films deposited using **LXXXII**, **4** and **7**. For films grown using **LXXXII** between 350 °C and 450 °C the Raman spectra contained two vibrations present at 109 and 209 cm^{-1} (Figure 3.16) consistent with those observed for films grown using **3** in Section 2.4.2 and corresponding to the B_{1g} and A_{1g} modes observed in SnO. The film grown at 300 °C showed no Raman active modes; consistent with the observation of no visual film growth at this temperature.

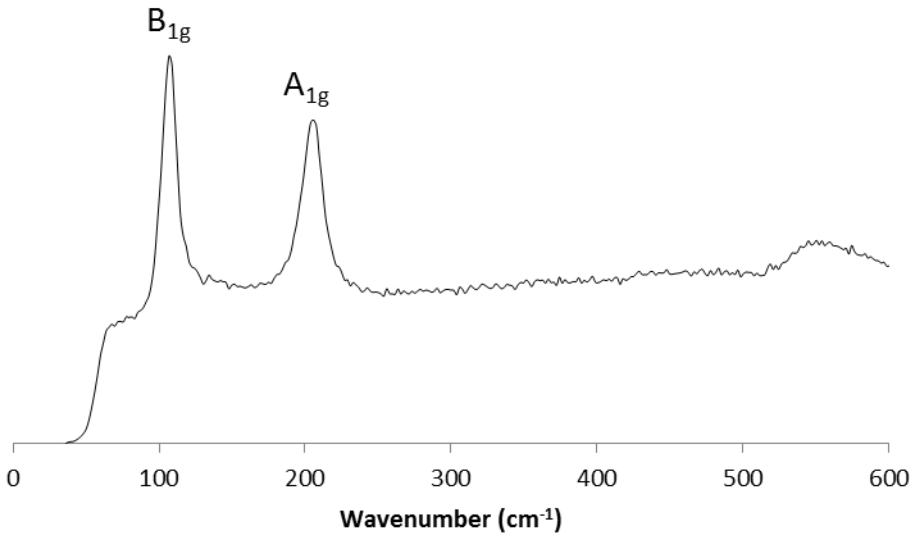

Figure 3.16: Raman spectrum for SnO film grown at 350°C on glass using LXXXII

The Raman spectrum for a sample grown on glass using **5** at 400 °C is shown in Figure 3.18 and is again indicative of single phase SnO deposition. Although the deposition at 250 °C showed no Raman active vibrations, the yellow coloration suggested some deposition which could be too thin to be detectable. Depositions at 300 °C and 350 °C had Raman spectra comparable to that shown in Figure 3.17 with limited change in intensity of the observed vibrations. In comparison the depositions carried out using **3** showed a correlation between increased deposition temperature and increased intensity (Section 2.4.2).

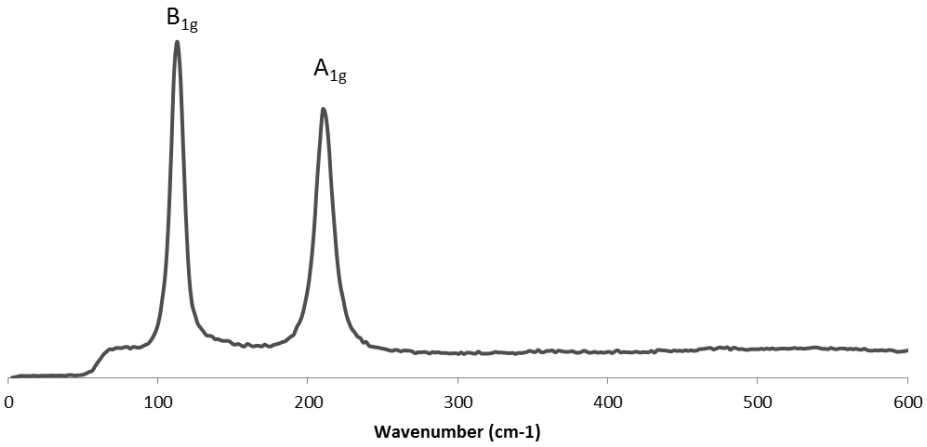

Figure 3.17: Raman spectrum of SnO sample grown at 400 °C on glass using compound 5

While the Raman spectra for films deposited using **7** exhibited the same A_{1g} and B_{1g} vibrations at deposition temperatures from 250-400 °C (Figure 3.18), the intensity of the different vibration modes differed from those observed with depositions carried out with **5**. The A_{1g} mode was stronger in intensity throughout the depositions; however at lower temperatures the B_{1g} mode is weak. This is in contrast to depositions carried out using **3** where at lower temperatures the A_{1g} mode was found to be the weakest.

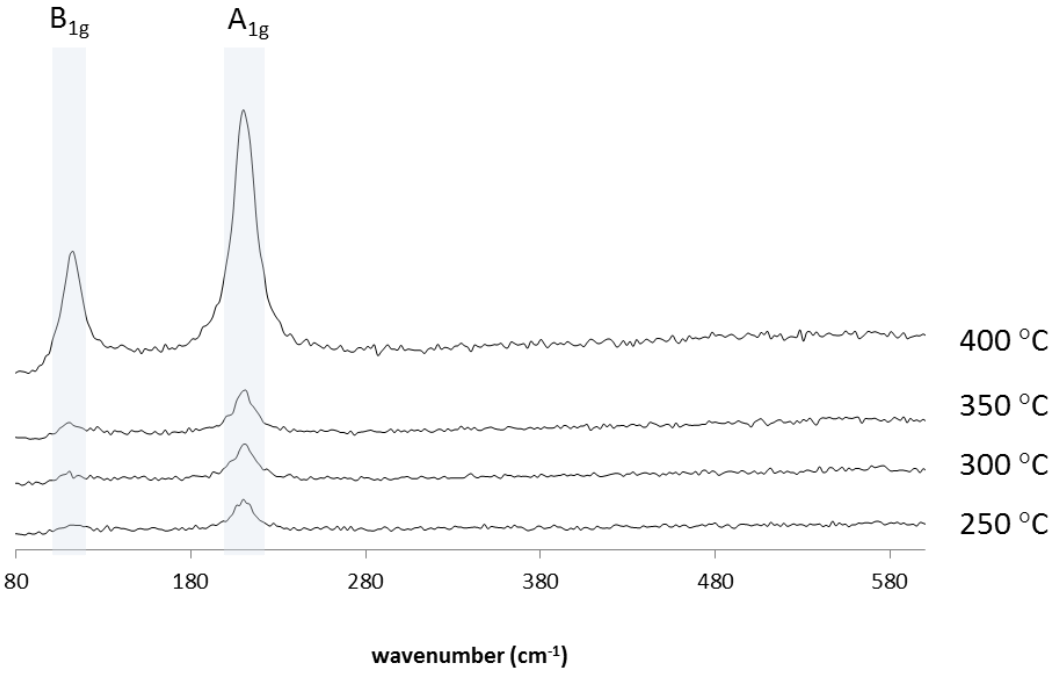

Figure 3.18: Raman spectra of SnO grown at varying deposition temperature on glass using 7

3.4.2 Scanning electron microscopy

Evaluation of the surface morphology of the thin films was carried out using scanning electron microscopy (SEM) for samples grown using **LXXXII** and **5**, samples grown using **7** proved to have poor conductivity and therefore were not analysed. The discontinuous surface of a film deposited 400 °C using **LXXXII** is shown in Figure 3.19. The material deposited had a unique morphology; rather than a continuous film, 1-3 μm long cuboids were observed. The cuboid microstructures were observed to be made up of 100-150 nm spherical particles, giving the overall appearance of nano-rice krispy cakes.

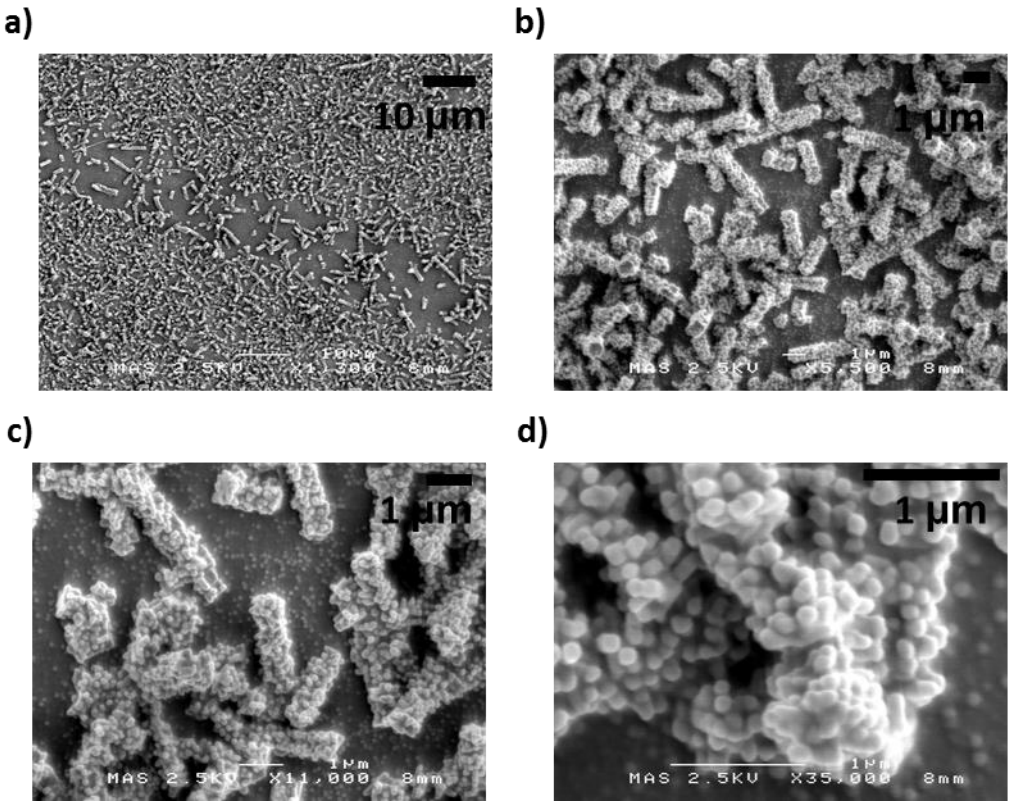

Figure 3.19: SEM micrographs of an SnO sample grown at 400°C on glass using LXXXVII with increasing magnification

Figure 3.20 shows micrographs of a film deposited using **5** at 350°C. The low magnification image shows a uniform film covered with a secondary material that has a different morphology (Figure 3.20 a). Increasing the magnification shows the underlying film has a similar morphology to that reported for depositions carried out using **3** in the same TSI aerosol reactor (Section 2.4.3, Figure 2.26). The surface material does not have a similar morphology to anything deposited previously but could be the result of gas phase reactions resulting in particulate build up on the surface.

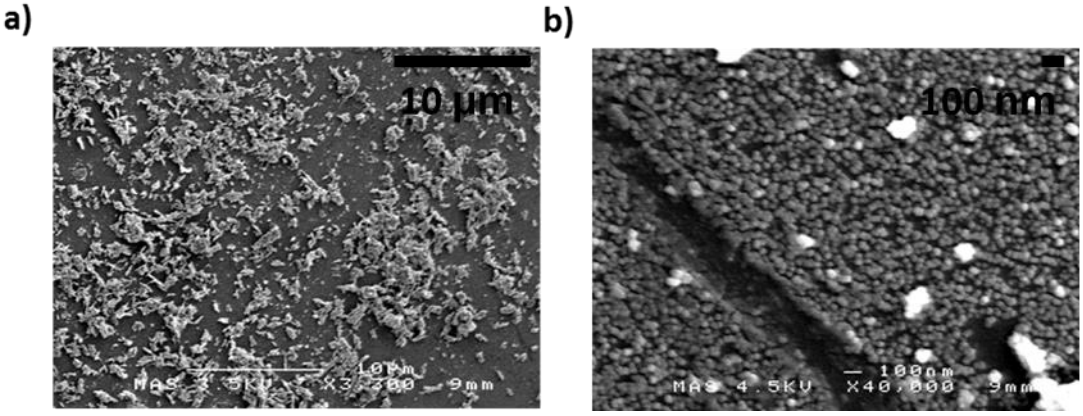

Figure 3.20: SEM micrographs of SnO sample grown at 350 °C on glass using 5 increasing in magnification

3.4.3 Energy dispersive spectroscopy

Depositions carried out using **5**, **7** and **LXXXII** were also analysed using energy dispersive spectroscopy (EDS) to determine the elemental composition of the films grown. As all depositions were carried out on glass microscope slides this was used as a qualitative analysis to determine the presence of tin, and also to gather information on potential film contaminants. The EDS spectra for **5**, **7** and **LXXXII** contained peaks corresponding to tin and oxygen as expected alongside additional peaks for silicon, magnesium and potassium, all components in glass (Figure 3.24). There was no detected carbon or nitrogen contamination for films deposited using all three precursors.

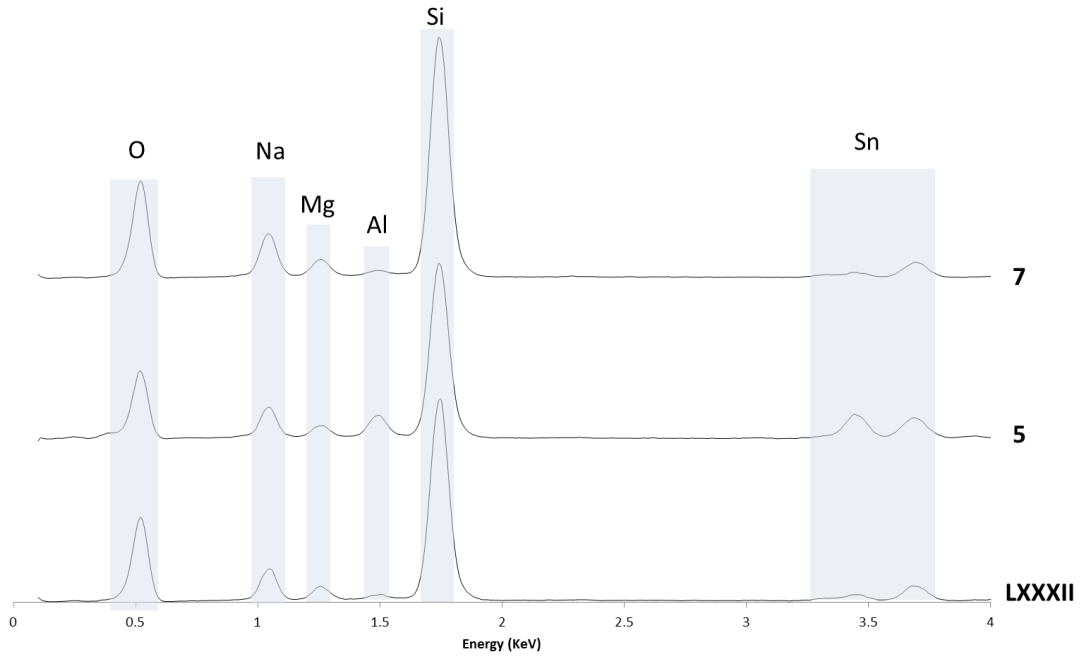

Figure 3.21: EDS spectra of samples grown on glass using LXXXII at 400 °C, 5 at 350 °C and 7 at 375 °C

3.4.4 X-ray diffraction analysis

Samples were analysed using c-ray diffraction to ascertain the crystallinity of the films, and gather information about potential preferential growth. Analysis by XRD of films grown on glass at different substrate temperatures using **LXXXII** is shown in Figure 3.22. The materials grown have crystalline phases at substrate temperatures in excess of 400 °C, with the diffraction peaks matching tetragonal SnO (*P*4/*mmm*). The XRD patterns show no evidence of SnO_2 or tin metal present in the deposited films and have a random orientation as observed with depositions carried out with compound **3** (Section 2.4.6) with the main diffraction lines being provided by the (101) and (111) planes. While the deposition carried out at 350 °C provided no diffraction maxima, the Raman spectrum at the temperature displays vibrations corresponding to SnO growth suggesting that at lower temperatures growth results in microcrystalline or amorphous material.

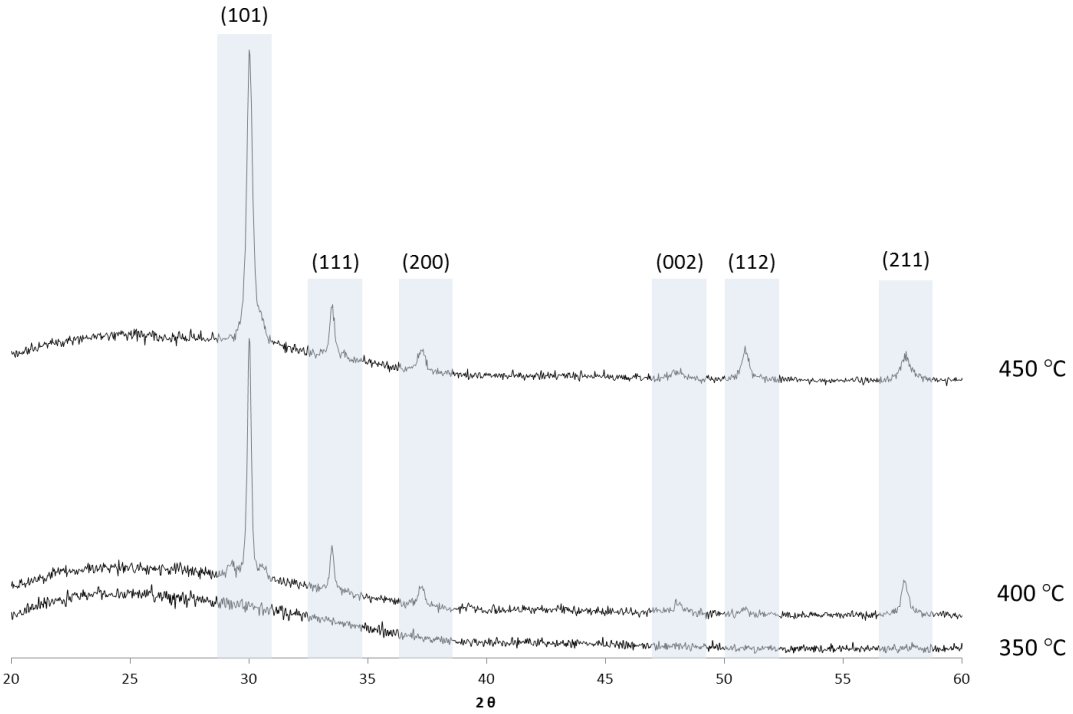

Figure 3.22: XRD patterns for samples grown on glass at varying deposition temperatures using LXXXII

Analysis by XRD of films grown using **5** on glass at different substrate temperatures is shown in Figure 3.23. The material grown shows crystalline phases at 300-400°C which again correspond to SnO as the sole crystalline material present. This is in agreement with the Raman spectra collected for these thin films. The films grown using **5** show greater degree of orientation than those deposited using **LXXXII** and **3** with the main diffraction lines corresponding to the (111), (200) and (112) planes. The substrate temperature does not seem to have a significant influence on the intensity of the diffraction peaks although the deposition at 400 °C has the strongest intensities.

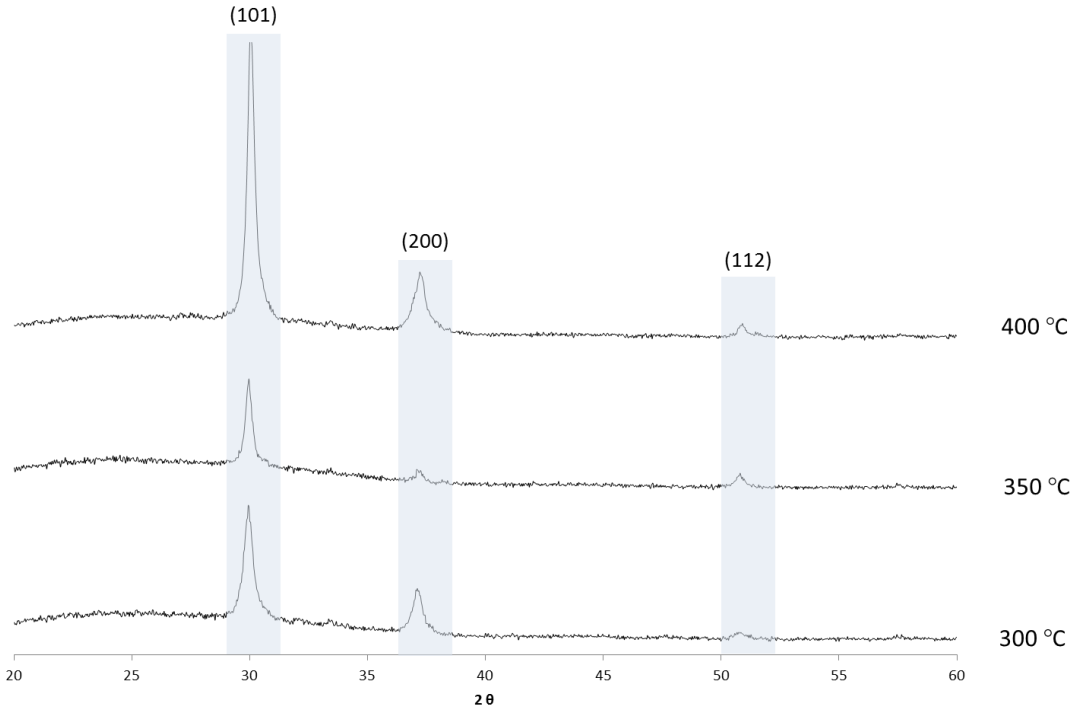

Figure 3.23:XRD patterns for samples grown on glass at varying deposition temperatures using 5

Depositions carried out using **7** showed orientated growth comparable to that observed with depositions carried out using **3** in the TSI reactor (Section 2.4.6) with the (001) and (200) diffraction lines having the greatest intensity (Figure 2.36). The impact of substrate temperature on the intensity of the diffraction peaks was negligible. The pattern shown in Figure 3.24 is from a film grown at 400 °C, at temperatures below this the (101) diffraction line was not observed at all.

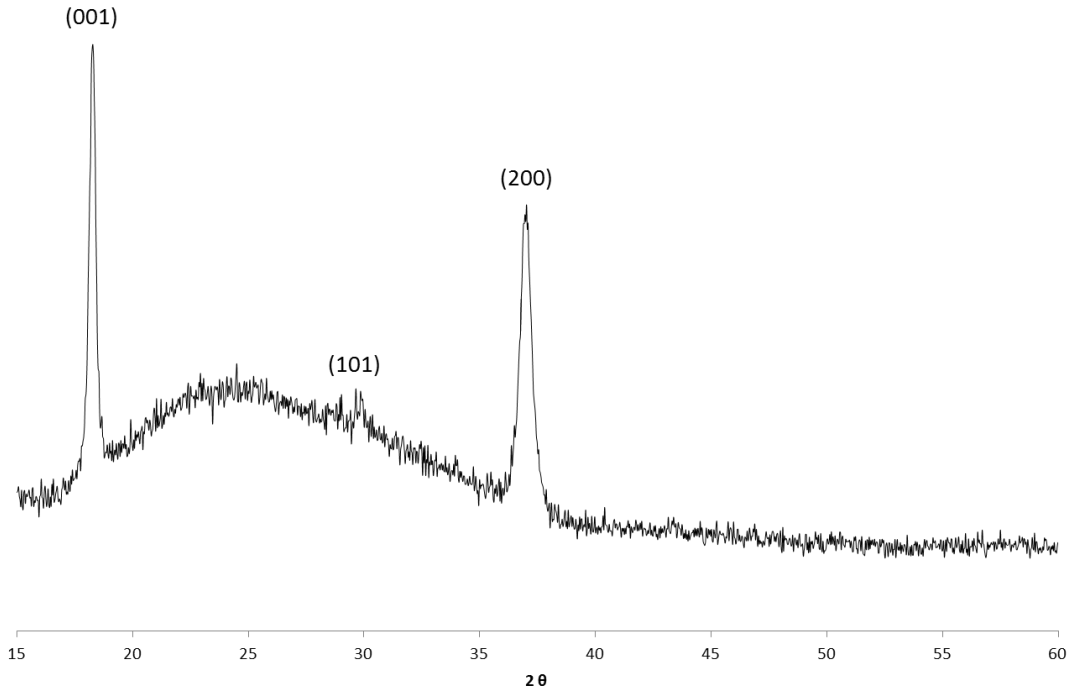

Figure 3.24: XRD pattern for SnO sample grown at 400 °C on glass using 7

The diffraction patterns for films grown using **5**, **7** and **LXXXII** were also assessed using the Scherrer equation to determine the crystallite size resulting from the depositions. This data is summarised in Table 3.5. For samples grown using **LXXXII** the crystallite size was found to decrease as the substrate temperature was increased with the calculated size dropping from 44 nm to 31 nm as the deposition temperature was raised from 400 °C to 450 °C. This was not observed with SnO growth using compound **3**. The crystallite size for films grown using **5** ranged from 22 nm to 31 nm, with the largest particle size observed for the growth at 350 °C and the particle size reducing to 23 nm at 400 °C. For films grown using compound **7** the crystallite size increased from 18 nm at 300°C to 23 nm at 350°C and 400°C, showing limited change in the particle size at different deposition temperatures.

Table 3.5: Calculated crystallite size based on XRD patterns using Scherrer equation

Precursor	Substrate temperature (°C)	Diffraction plane	Calculated crystallite size (nm)
LXXXII	400	(101)	44
LXXXII	450	(101)	31
5	300	(101)	22
5	350	(101)	31
5	400	(101)	23
7	300	(001)	18
6	350	(001)	23
6	400	(001)	23

3.5 Conclusions

The formation of tin(II) alkoxides have previously been reported by several different researchers including Hoffman, Lappert, Boyle and Veith. The work presented in this chapter shows the synthesis and characterisation of three tin(II) alkoxides. Compounds **5**, **6** and **7** were characterised using a combination of solution and solid state techniques. The three compounds were found to have $^{119}Sn\{^{1}H\}$ NMR shifts that corresponded closely to literature compounds which had comparable molecular structures; this was confirmed through the structural determination of compound **5** and compound **6** through X-ray diffraction analysis. Compound **5** has previously been reported by Caulton and co-workers however they provided limited characterisation of the tin(II) alkoxide, preferring to focus on the formation of mixed tin(II)-tin(IV) alkoxide precursors. Structural determination of **5** showed that the compound existed as a polymeric structure very similar to **LXXXIII** reported by Boyle; the tin(II) environment was confirmed by comparable $^{119}Sn\{^{1}H\}$ NMR spectra with compound **5** having a single resonance at -220 ppm, slightly upfield of **LXXXIII** which was reported at -197 ppm. In comparison compound **6** was found to exist as a dimer when analysed by X-ray diffraction with two bridging and two terminal alkoxide groups. The $^{119}Sn\{^{1}H\}$ NMR for **6** was downfield of all reported tin(II) alkoxides at -67 ppm; the previously reported **LXXXII** having the closest shift at -94 ppm also exists as a dimer and therefore the change in chemical shift can be attributed to the electron donating nature of the trisphenyl methoxide groups bound to the tin in **6**. Compound **7** also contained a $^{119}Sn\{^{1}H\}$ NMR shift that was close to **LXXXII**, with a resonance of -99ppm observed, due to the structural similarities of the alkoxide group and the closely matching NMR resonances compound **7** is thought to also exist as a dimer, however structural elucidation was not successful due to the liquid nature of the material.

Evaluation of compounds **5**, **7** and **LXXXII** as potential CVD precursors was carried out by TGA with all three compounds decomposing between 60 °C and 300 °C to give residual masses well below that expected for tin metal suggesting some volatility. The three compounds were separated by approximately 50 °C at the onset with **LXXXII** beginning to lose mass at 60 °C and finishing at 250 °C, the next lowest was **5**, starting at 125 °C and finishing at 265 °C, while **7** began to lose mass at 130 °C before finishing at 295 °C. All three alkoxides evaluated had larger decomposition window than that observed for **3** which exhibited a sharp decrease between 90 °C and 180 °C; furthermore compounds **5**, **7** and **LXXXII** all exhibited a small shoulder in the TGA towards the end of the analysis most

noticeable when the derivative is plotted which suggests that the decomposition pathway involves a second step at elevated temperatures.

Aerosol-assisted CVD using the tin(II) alkoxide compounds **5**, **7** and **LXXXII** resulted in the exclusive growth of SnO thin films on glass substrates. The deposition temperature was found to be affected by the identity of the precursor, with **LXXXII** showing growth at temperatures in excess of 350 °C. Growth was also observed with **5** at temperatures exceeding 300 °C and depositions using **7** resulted in growth at temperatures above 250 °C. This is the reverse of the expected deposition temperature windows based on the TGA analysis - with **LXXXII** having the lowest temperature window and **7** having the highest. For compound **7** the TGA suggests that decomposition is not complete until 295 °C and therefore depositions at 250 °C are much lower than expected.

The morphology of the samples was found to vary depending on the precursor. Depositions carried out using **LXXXII** resulted in the formation of micron sized cuboid particles comprised of smaller spherical units. The depositions carried out using **5** resulted in an initial layer comparable to that observed with depositions carried out using **3** on the same apparatus (Section 2.4.3), however a secondary deposition with a different morphology was observed in the SEM. The morphology of **7** was not studied due to poor conductivity resulting in charging in the SEM. The crystallinity and orientation of the samples was also found to differ depending on the precursor utilised. Depositions using **LXXXII** resulted in unorientated growth that was indexed to SnO at temperatures of 400 °C and 450 °C, whereas depositions at 350 °C resulted in amorphous films confirmed as SnO by Raman spectroscopy. Depositions using **5** showed some orientated growth with intense diffraction lines in the (101), (200) and (112) planes indexed to SnO at deposition temperatures of 300-400 °C. Growth utilising precursor **7** resulted in orientated growth in the (001) and (200) diffraction planes at 300 - 400 °C, comparable to the diffraction patterns observed by Molloy and co-workers using cubane **LXXXII**.[165] SnO growth was also confirmed at 250 °C through analysis using Raman spectroscopy showing comparable low temperature deposition to that observed with **3**.

In conclusion, the work presented in this chapter has shown that AA-CVD of tin(II) alkoxides **LXXXII**, **5** and **7** results in the formation of SnO thin films between 250°C and 450 °C depending on the alkoxide utilised, with the films characterised by Raman spectroscopy and XRD. It has also been shown that the orientation of the SnO thin films can be controlled through the use of different alkoxide groups, with preferred orientation observed for both compounds **5** and **7**. The unique morphology of depositions using

LXXXII which results in micro-rods made of microspheres of SnO results in an un-orientated crystalline growth.

4. Heterocumulene insertions into tin(II) alkoxide bonds

The reactivity of tin(II) alkoxides with heterocumulene derivatives allows for the formation of many potential derivatives that can be evaluated as precursors for the formation of tin oxide thin films via chemical vapour deposition. The utilisation of metal carbonate compounds as CVD precursors has not been described in the literature and, while the reactivity of tin(IV) and tin(II) alkoxides compounds has been explored previously, they have been restricted to heteroleptic systems (see Section 1.5). Alternatively the use of metal iso-carbamate compounds in CVD applications is limited to the work by Devi and co-workers who successfully deposited HfO_2 at 250°C with **XXX**, half the temperature of existing HfO_2 precursors.[120] This chapter focuses on the synthesis and characterisation of tin(II) carbonate and iso-carbamate compounds as potential CVD precursors through the insertion reactions of CO_2 and organic isocyanates into tin alkoxide bonds (Figure 4.1).

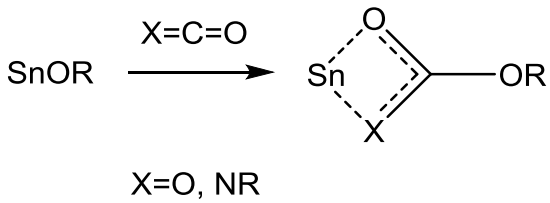

Figure 4.1: General synthetic route to carbonate and iso-carbamate compounds

4.1 Synthesis of tin(II) carbonate systems

The initial aim was to form a range of different homoleptic tin(II) bis carbonate complexes, through the reaction of tin(II) alkoxides with an excess of CO_2, and assess them as potential tin oxide precursors (Figure 4.2). Initial reactions were carried out by taking tin(II) alkoxides **5**, 6, **7** and **LXXXII** and dissolving in toluene under argon. The headspace of the Schlenk tube was then evacuated and the toluene degassed to remove excess argon before the sample was subjected to 1atm of CO_2 whilst stirring was continued. The headspace was then briefly evacuated and backfilled with CO_2 a further three times in an attempt to saturate the solution with CO_2 and replenish any CO_2 consumed in the reaction. Following this procedure samples were placed in a -30°C freezer in an attempt to isolate crystals suitable for X-ray diffraction analysis. The reaction between **LXXXII** and CO_2 did produce a crystalline product, however this quickly decomposed, and visibly evolved gas when removed from a CO_2 atmosphere. Attempts to isolate the products when **5**, **6** and **7** were reacted with CO_2 resulted in the parent alkoxide being isolated.

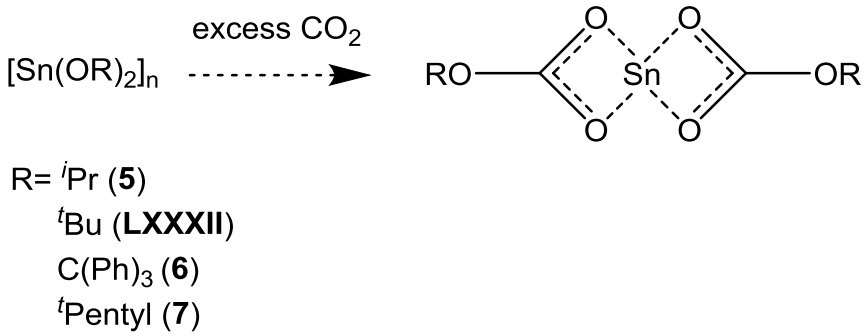

Figure 4.2: Proposed reaction to form tin(II) carbonate species.

To allow a more comprehensive analysis of the formation of tin(II) carbonate complexes, rather than the qualitative observations of gas evolution, the reactions of **5**, **6**, **7** and **LXXXII** with CO_2 were carried out in sealed Youngs tap NMR tubes. This allowed the carbonate compounds to be analysed in situ using multinuclear NMR spectroscopy. The formation of tin(II) carbonate species can be most clearly observed in the ^{13}C NMR spectra through the appearance of a characteristic resonance observed at δ 155-165 ppm corresponding to the quaternary carbon bound to three oxygen atoms.

The reaction of compound **5** with CO_2 was monitored by multinuclear NMR spectroscopy. The sample was pressurised with CO_2 until free CO_2 was detected in the $^{13}C\{^1H\}$ NMR spectrum with a resonance at δ 125 ppm observed in toluene. Analysis of the $^{13}C\{^1H\}$ NMR spectrum showed the presence of two different environments for the alkyl carbons with resonances observed at δ 70.4 and 67.1 ppm for the ^{i}Pr methine carbons and δ 28.1 and 22.7 ppm for the methyl carbons. The presence of two environments was confirmed in the ^1H NMR spectrum, which displayed two doublet resonances at δ 1.15-1.19 and 1.23-1.27 ppm and two septet signals at δ 4.51 and 4.85 ppm. As free CO_2 was detected in the $^{13}C\{^1H\}$ NMR specrum the sample was judged to be saturated with CO_2 with the establishment of an equilibrium between the stannous carbonate and parent alkoxide **5**.

To investigate this apparent equilibrium process 2D ^1H-^1H Exchange Spectroscopy (EXSY) NMR experiment was recorded using the 'noesygpph' (2D homonuclear correlation via dipolar coupling) pulse sequence from the Bruker pulse program library. The recorded spectra contained resonances that could be assigned to both the carbonate and alkoxide protons with exchange cross peaks observed on an NMR timescale (Figure 4.3). This confirmed the reversible nature of the reaction and highlighted the highly facile nature of the reaction.

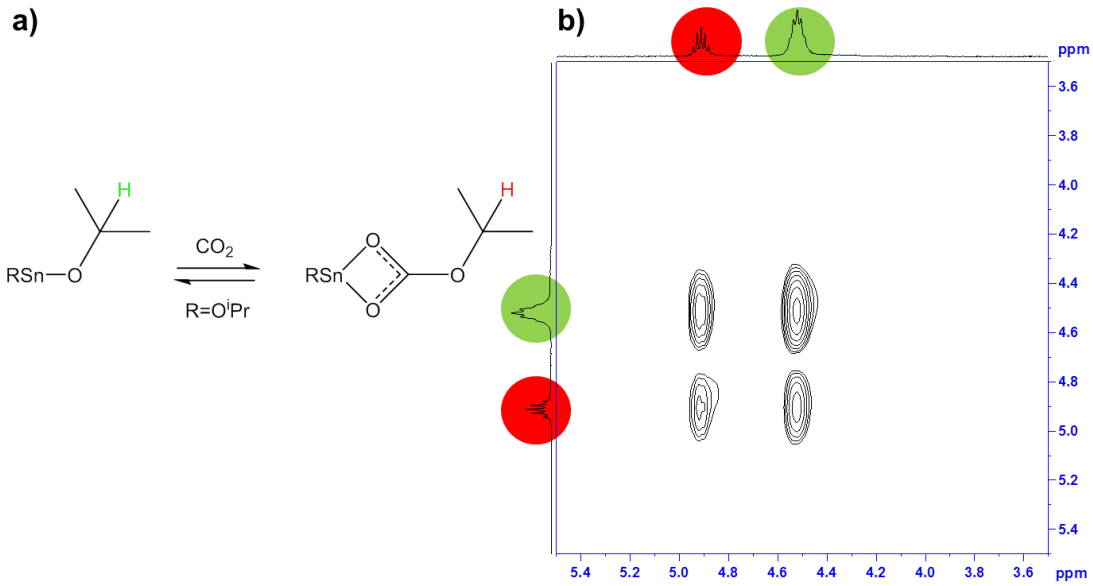

Figure 4.3: a) Colour coded reaction scheme for reaction of 5 with CO_2 b) 2D EXSY NMR of methine resonances for reaction between 5 and CO_2 showing exchange.

By utilising 1D EXSY NMR experiments it was possible to obtain kinetic data for the equilibrium between the tin(II) carbonate and the parent alkoxide **5** using a method adapted

from Nikonov and co-workers.[213] A series of 1D NMR experiments utilising the 'selnopg'(1D NOESY using selective refocusing with a shaped pulse) pulse sequence from the Bruker library were conducted. The 'selnopg' NMR sequence selectively irradiates part of the spectra – one of the resonances observed to be in exchange – with a series of 90 ° and selective 180 ° pulses. This is followed by a second 90° pulse after a short pause, referred to as the mixing time. The initial selective irradiation causes the irradiated peak to be inverted, but as the peaks are in exchange a secondary resonance should appear and the initially irradiated resonance will decrease in size. The rate of exchange, *k*, can be determined by plotting the intensity of the new resonance (normalised against the intensity of the original peak) against the mixing time (Figure 4.4). A series of 1D EXSY experiments were conducted using this pulse sequence with the mixing time and temperature varied. In Table 4.1 the values calculated for *k* are shown alongside the temperature for the individual experiments.

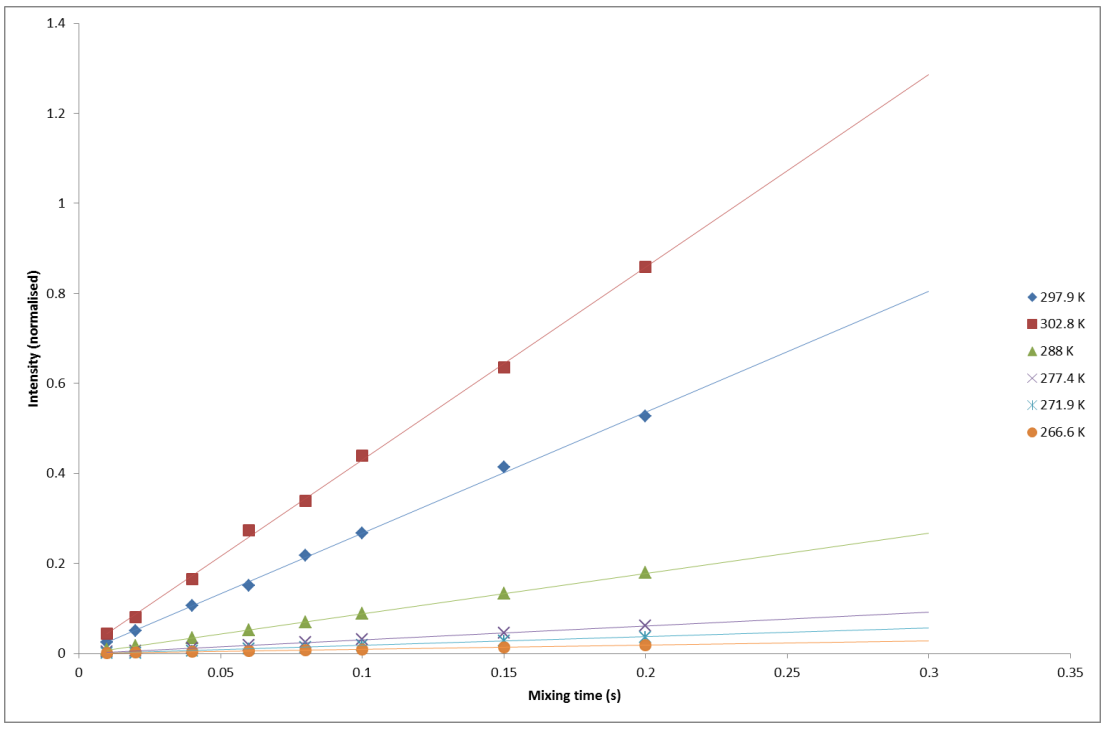

Figure 4.4: Plot of mixing time and normalised intensity data from 1D EXSY experiments at a variety of temperatures

Table 4.1: Rate constants for equilibrium between 5 and CO_2 and different temperatures

Temperature (K)	*k* (s^{-1})
302.8	4.2867
297.9	2.6885
288	0.8975
277.4	0.3062
271.9	0.1829
266.6	0.0942

Repetition of this experiment at several different temperatures allows the rate data to be employed to determine $\Delta H^{\neq}$ and $\Delta S^{\neq}$, the enthalpy and entropy of activation, using an Eyring plot (ln(*k*/T) against 1/T - Figure 4.5). For the reaction **5** with CO_2 $\Delta H^{\neq}$ was calculated to be 67.99 ± 0.57 kJ mol^{-1}, while $\Delta S^{\neq}$ was found to be -7.37 ± 2.45 J mol^{-1} K^{-1}. For comparison Fulton and co-workers were able to calculate $\Delta H°$ and $\Delta S°$ for the equilibrium reaction between CO_2 and BDISnO^{t}Bu to form **XLVIII**. They calculated $\Delta H°$ to be -138 kcal mol^{-1} (-57.7 kJ mol^{-1}) which is approximately 10kJ mol^{-1} lower than $\Delta H^{\neq}$ for **5** with CO_2. For $\Delta S°$ Fulton and co-workers calculated a value of -39.6 cal mol^{-1} K^{-1} (-165 J mol^{-1} K^{-1}), this is nearly 150 J mol^{-1} K^{-1} lower than observed for **5** with CO_2.[214]

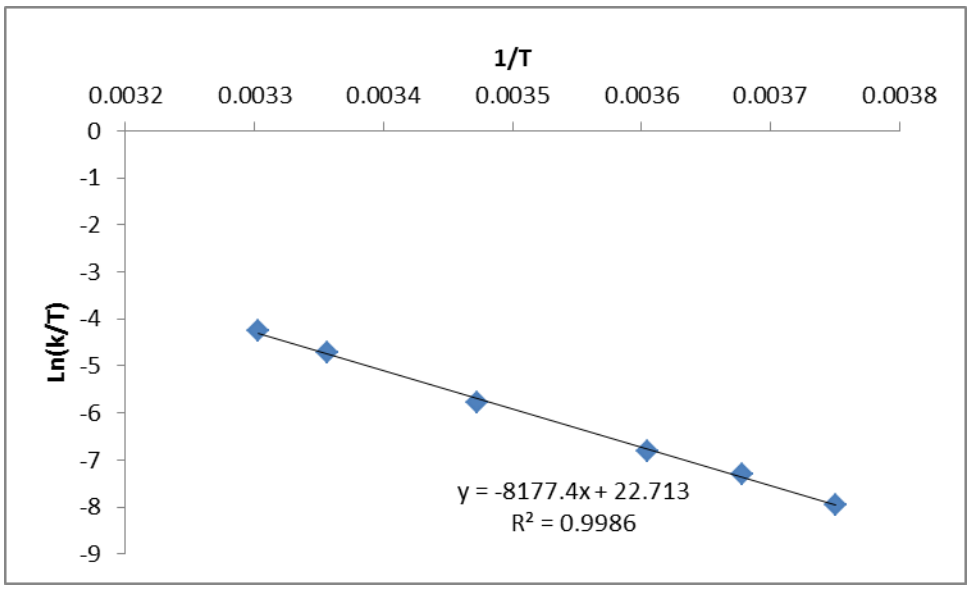

Figure 4.5: Eyring plot for reaction between 5 and CO_2 to determine $\Delta H^{\neq}$ and $\Delta S^{\neq}$.

The rate data collected using the SELNOPG NMR experiments can also be used to determine the activation energy for the reaction between CO_2 and **5** by using an Arrhenius plot (Ln(*k*) against 1/T - Figure 4.6). The gradient of the plot can be used to calculate the activation energy (E_A) as the gradient is equal to $-E_A/R$, the ideal gas constant (8.314 J mol^{-1} K^{-1}), resulting an activation energy of 70.34 ± 10 kJ mol^{-1}.

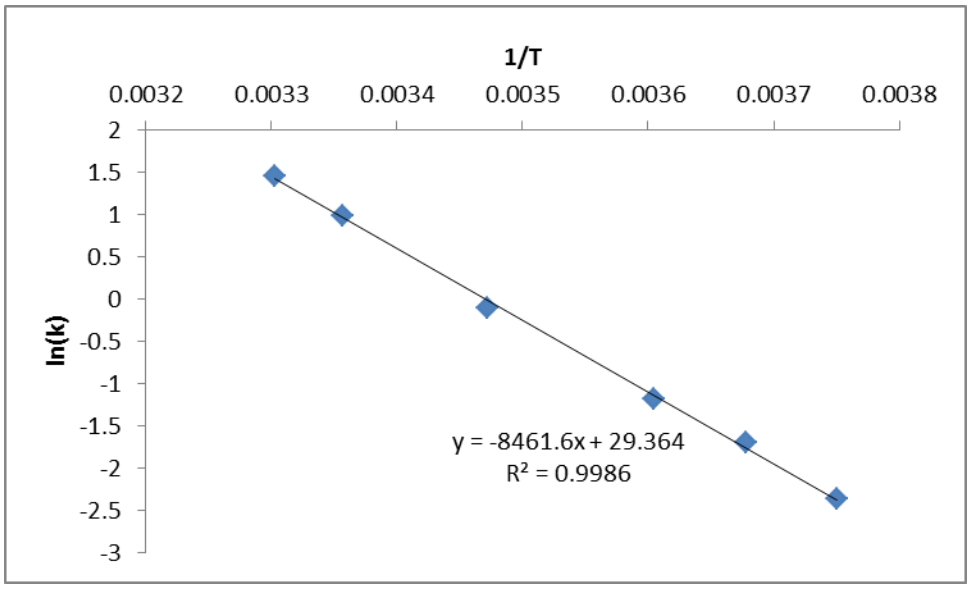

Figure 4.6: Arrhenius plot for reaction between 5 and CO_2 used to determine the activation energy.

Attempts to run comparable 2D EXSY and SELNOPG experiments for the reaction between **7** or **LXXXII** with CO_2 were unsuccessful due to the resonances in the ^{1}H NMR attributed to the carbonate, and the alkoxide having chemical shifts that were too similar. The ^{1}H NMR and $^{13}C\{^1H\}$ NMR spectra did, however, evidence the presence of both alkoxide and carbonate peaks. For the reaction of **LXXXII** with CO_2 the ^{1}H NMR spectrum comprised resonances at δ 1.27 and 1.42 ppm, while the $^{13}C\{^1H\}$ NMR spectrum had resonances at δ 34.7, 33.6, 73.6, 74.6 and 157.9 ppm. For the reaction of **7** with CO_2 the ^{1}H NMR spectrum was complicated by a combination of the overlap of the carbonate and free alkoxide peaks and restricted rotation within the ^{t}Pentyl group. The $^{13}C\{^1H\}$ NMR spectrum provided more information with broad peaks observed at δ 75.5, 40.5 and 32.7 ppm along with sharper resonances at δ 10.1 and 157.7 ppm.

The observed reversible reactivity between tin(II) alkoxides and CO_2 was subsequently confirmed by Fulton and co-worker who described analogous reactivity for heteroleptic β-diketimito-supported tin(II) alkoxide compounds with CO_2 in early 2011, shortly after the

initiation of this investigation.[214] As discussed in Section 1.5, Fulton and co-workers attempted to gather kinetic data on the reversible insertion of CO_2 with tin(II) alkoxide compounds. They concluded that the steric bulk of the alkoxide had an effect on the rate of insertion, with smaller R groups reaching equilibrium faster. Calculations carried out by Fulton and co-workers suggested that the larger alkyl groups resulted in more stable alkoxide compounds, resulting in higher energy transition states for the formation of the carbonate. As we were unable to determine any kinetic information for the reaction of CO_2 alkoxides other than **5** with the EXSY NMR technique we are unable to provide meaningful comparison of our results to these calculations.

In Table 4.2 the ^{119}Sn chemical shifts for the reactions between **5**, **7** and **LXXXII** and CO_2 are shown alongside the resonance observed for the parent alkoxide. The resonances assigned to the carbonate carbon atom in the $^{13}C\{^1H\}$ NMR are also shown as evidence of carbonate formation.

Table 4.2: Multinuclear NMR data for reaction of tin(II) alkoxides with CO_2

Alkoxide + CO_2	**$^{13}C\{^1H\}$ NMR peak**	**$^{119}Sn\{^1H\}$ NMR peak**	**Parent alkoxide $^{119}Sn\{^1H\}$ NMR shift**
5	161.6	-368	-219
LXXXII	157.9	-92	-92
7	157.7	-99	-99

For the reaction of **5** with CO_2 the $^{119}Sn\{^1H\}$ NMR chemical shift was found to resonate upfield of the parent alkoxide at -368 ppm. This is consistent with the $^{119}Sn\{^1H\}$ NMR shifts reported by Fulton and co-workers for the formation of heteroleptic tin(II) carbonate species with the Sn(II) centre of the carbonate resonating upfield of the heteroleptic tin(II) alkoxides. In contrast the $^{119}Sn\{^1H\}$ NMR chemical shifts for the reaction between **7** and CO_2 and **LXXXII** with CO_2 showed limited change from the parent alkoxide. The molecular structure of **5** is known to be polymeric, with the tin centre in a four-coordinate geometry. Insertion of CO_2 could thus result in deaggregation of the polymer into monomeric, or dimeric units with the carbonate ligands adopting a κ^2, O, O' binding geometry which would result in a gross change in the coordination number around the tin(II) centre. Based on NMR spectroscopy **7** is expected to have a dimeric structure that closely resembles **LXXXII**, the tin centres of which are found to be in a three-coordinate geometry. The insertion of CO_2 to form a carbonate could result in limited change in the coordination geometry if the carbonate adopts

a κ^1-O binding mode through insertion into the terminal O^{t}Bu groups, as observed with the tin(IV) compound **XXXIX** (Section 1.7.10) by Sakakura and co-workers.[130] The tin geometry and binding environment are only slightly affected resulting in limited change in the chemical shift. As discussed efforts to isolate the carbonate complexes were unsuccessful due to the facile reversibility of this reaction, therefore the coordination state of the tin(II) centre can only be postulated.

4.2 Synthesis of tin(II) iso-carbamate compounds

For the synthesis of tin(II) iso-carbamate compounds the insertion reaction of isocyanates with **5** and **LXXXII** was explored as the primary synthetic route. The synthesis and characterisation of the tin(II) alkoxides is discussed in chapter 3. Initial reactions centred on the insertion of aryl isocyanates. While these are likely to be poor CVD precursors, it was considered that the potential greater crystallinity of the resultant compounds would allow for proof of reactivity before expanding the substrate scope.

4.2.1 Aryl isocyanate insertion into tin(II) alkoxide compounds

For the formation of tin(II) iso-carbamates, two equivalents of the relevant aryl -isocyanate are added to a tin(II) alkoxide in toluene (Figure 4.7). Removal of solvent *in vacuo* resulted in an off white precipitate. The products, **8-11** were further purified through crystallisation from toluene by slow evaporation of the solvent in an inert atmosphere.

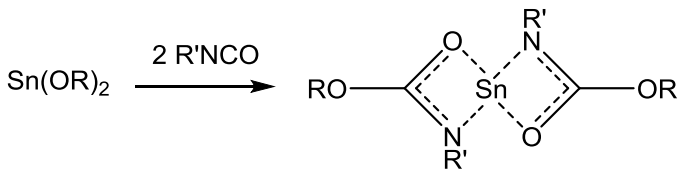

R=^{i}Pr R'=2, 4, 6-trimethylphenyl **8**

R=^{i}Pr R'=2 ,6-diisopropylphenyl **9**

R=^{t}Bu R'= 2, 4, 6-trimethylphenyl **10**

R=^{t}Bu R'= phenyl **11**

Figure 4.7: Insertion reactions of tin(II) alkoxides with aryl isocyanates.

4.2.1.1 Solution based analysis of the iso-carbamate compounds 8-11

When **5** was reacted with mesityl-isocyanate the resulting N-mesityl substituted compound **8** exhibited five resonances in the ^{1}H NMR spectrum with a doublet at δ 0.99-1.01 ppm ($^{3}J_{H-H}$ = 6.0 Hz) corresponding to the methyl groups of the alkoxide isopropyl group, and a singlet at δ 2.12 ppm assigned to the *ortho* and *para* methyl groups of the trimethylphenyl substituent. Two septet resonances at δ 4.19-4.3 ppm and δ 4.96-5.08 ppm (both $^{3}J_{H-H}$ = 6.0

Hz) assigned to the methine protons and a singlet at δ 6.98 ppm corresponded to the aromatic protons. The integrals of these resonances suggest that there are two ^{i}Pr environments for every mesityl substituent. This observation, coupled with the two septet resonances for the methine protons of the ^{i}Pr groups, suggests that the reaction has actually occurred in a 1:1 ratio to produce a heteroleptic complex with a single *iso*-carbamate ligand and one alkoxide ligand bound to the tin centre (Figure 4.8).

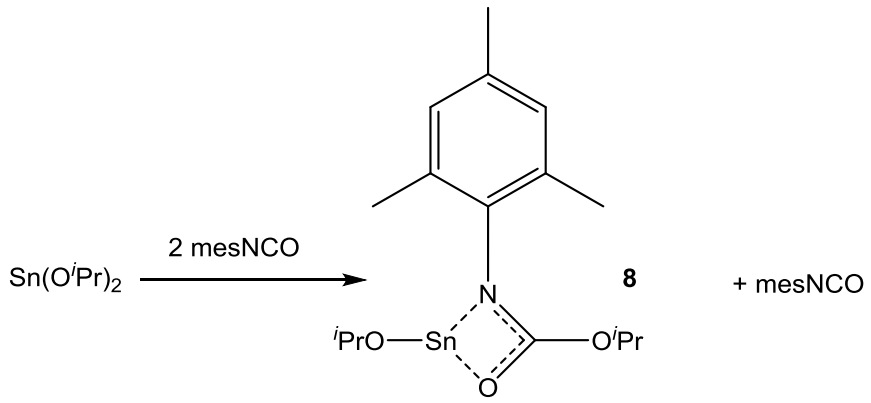

Figure 4.8: Revised reaction between 5 and mesityl isocyanate based on NMR analysis.

The overlapping of the methyl protons for the iso-propoxide was also observed for the corresponding carbon atoms in the $^{13}C\{^{1}H\}$ NMR spectrum with four resonances observed at δ 20-22.7 ppm that can be attributed to the methyl groups of the ^{i}Pr group and the *para* and *ortho* groups of the mesityl substituent. Two resonances observed at 69.0 and 69.1 ppm were assigned to the two methine environments of the *iso*-carbamate and alkoxide ^{i}Pr groups. Further downfield four resonances at 129.7-139.7 ppm corresponding to the aromatic carbons of the trimethylphenyl group could be observed and a resonance at 161.9 ppm could be attributed to the N-C(O)O backbone carbon. Compound **8** exhibited a single resonance in the $^{119}Sn\{^{1}H\}$ NMR spectrum at -315 ppm which is close to the resonances observed for the tin(II) bis ureate compounds **1** and **4** described in Chapter 2.

The formation of a mono-insertion product was also found to be preferred when **5** was reacted with two equivalents of 2, 6-diisopropylphenyl isocyanate to form compound **9** (Figure 4.9). The ^{1}H NMR spectra for **9** showed the heteroleptic nature of the compound in a clearer fashion with four doublet resonances observed, two for the ^{i}Pr substituents on the aryl group at δ 1.30-1.32 and δ 1.35-1.37 ppm (both $^{3}J_{H-H}$ = 6.8Hz), and two for the alkoxide and iso-carbamate isopropyl groups at δ 1.02-1.04 ppm and δ 1.05-1.07 ppm respectively. Although only three methine resonances were observed, the multiplet at δ 3.58-3.71 ppm integrated for two protons suggesting of the signals arising from the *iso*-carbamate and

alkoxide groups. Further septet resonances were observed at δ 4.2-4.32 ppm and δ 4.94-5.07 ppm for the ^{i}Pr methine groups bound to the aryl substituent, while a multiplet at 6.95-7.15 ppm was assigned to the aromatic protons.

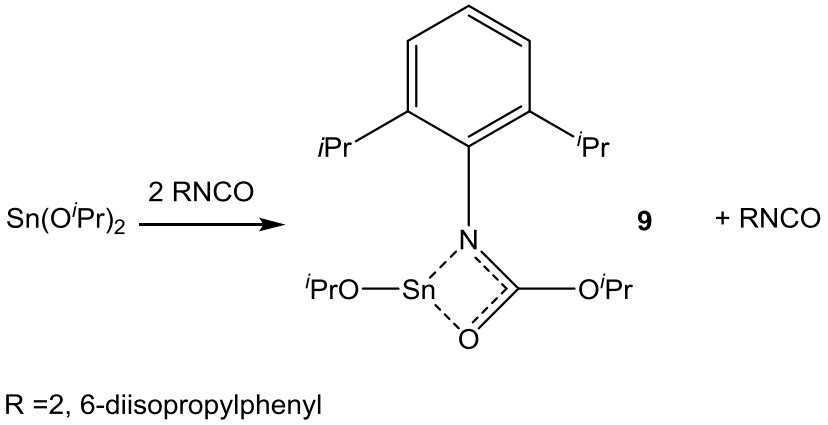

Figure 4.9: Revised reaction between 5 and diisopropylphenyl isocyanate based on NMR analysis.

In the $^{13}C\{^{1}H\}$ NMR spectrum there were four resonances corresponding to ^{i}Pr methyl groups at δ 22.6-29.4 ppm for the alkoxide, iso-carbamate and aryl substituents. Two resonances at δ 69.1-69.7 ppm assigned to the methine carbons suggested some overlap for both the aryl substituents and the alkoxide and *iso*-carbamate ^{i}Pr groups. A further four resonances for the aromatic carbons were observed at δ 123.7-145.5 ppm while the NC(O)O backbone carbon provided a low field resonance at δ 162.4 ppm. Compound **9** exhibited a single resonance in its $^{119}Sn\{^{1}H\}$ NMR spectrum at δ -347 ppm upfield of the resonance observed for **8** and comparable to the resonances observed for the tin(II) ureate compounds **2** and **3** described in Chapter 2.

Assignment of the room temperature ^{1}H NMR spectrum for **10**, the product of the reaction between **LXXXII** and mesityl isocyanate, was complicated by apparent restricted rotation of the bulky aromatic substituent resulting in multiple resonances. Upon heating the sample to 348K the peaks coalesced, however, allowing the spectrum to be interpreted. The spectrum suggested that mono-insertion had again occurred, with singlet resonances at δ 1.60 and 1.63 ppm corresponding to the ^{t}Bu groups for the alkoxide and *iso*-carbamate ligands respectively. A further three singlet resonances for the methyl groups of the mesityl substituent were observed at δ 2.46, 2.51 and 2.56 ppm, while the aromatic protons are attributed to a resonance at δ 7.04 ppm. The $^{13}C\{^{1}H\}$ NMR contained resonances at δ 29.1 and 32.5 ppm attributed to the ^{t}Bu group of the *iso*-carbamate and the *tertiary*-butoxide ligands respectively. The quaternary carbon atoms were observed as resonances at δ 76.9 and 79.8 ppm, the latter attributed to the alkoxide, while four signals at δ 129.0-140.9 ppm were

assigned to the aromatic carbons. A further resonance at 162.0 ppm confirmed the formation of the iso-carbamate system as this was attributed to the NC(O)O backbone carbon. The $^{119}Sn\{^{1}H\}$ NMR spectrum consisted of a single resonance at δ -317 ppm which is close to that reported for **8** (δ -315 ppm); which only differs in containing ^{i}Pr group rather than ^{t}Bu residues.

Compound **11** was found to have limited solubility in any solvents precluding solution based analysis, however elemental analysis confirmed that mono-insertion had again occurred (Expected C 46.91%, H 6.04%, N 3.65%. Found: C 46.80%,H 6.12%,N 3.73%).

4.2.1.2 Molecular structures of tin(II) iso-carbamates

Solution based analysis of compounds **8 - 11** indicated that the reactions proceed in a 1:1 ratio of tin(II) alkoxide and aryl isocyanate even when an excess of isocyanate is added to the reaction resulting in a heteroleptic tin(II) compound. Definitive confirmation of the coordination mode of the *iso*-carbamate ligand may not be elucidated through multinuclear NMR spectroscopy. The solid state structures of compounds **8-11** were confirmed by single-crystal X-ray diffraction analysis the results of which are illustrated in Figures 4.10-4.13. A summary of the crystallographic parameters is presented in Table 4.3 and a selection of bond lengths and angles can be found in Table 4.4. Compound **8** was found to be triclinic in the *P*-1 space group, while compounds **9- 11** were monoclinic with **9** and **10** in the $P2_1/n$ space group and **11** $P2_1/a$ space groups respectively.

Table 4.3: Crystallographic parameters for compounds 8-11

Compound	**8**	**9**	**10**	**11**
Empirical Formula	$C_{16}H_{25}N_2O_3Sn$	$C_{38}H_{62}N_2O_6Sn_2$	$C_{18}H_{29}N_2O_3Sn$	$C_{30}H_{46}N_2O_6Sn_2$
Crystal System	Triclinic	Monoclinic	Monoclinic	Monoclinic
Space Group	*P*-1	$P2_1/n$	$P2_1/n$	$P2_1/a$
Cell Constants				
a (Å)	8.42200(10)	19.49400(10)	10.18900(10)	9.3670(2)
b (Å)	10.9410(2)	10.26900(10)	14.4250(3)	15.0140(4)
c (Å)	11.0120(2)	22.9660(2)	13.7210(3)	12.4220(3)
α (°)	69.0610(10)	90	90	90
β (°)	89.1360(10)	113.90(1)	101.8320(10)	107.959(2)
γ (°)	72.0890(10)	90	90	90
Volume (Å^3)	896.61(3)	4203.18(6)	1973.81(6)	1661.86(7)
Density (mg/m^3)	1.474	1.391	1.434	1.535
Z	2	4	4	2
Measured reflections	16958	71452	35591	31170
Unique reflections	5444	12751	5420	3789
R_{int}	0.0459	0.0402	0.0323	0.0445
R_1. w$R_2[I > 2\sigma(I)]$	0.0265, 0.0626	0.0235, 0.0577	0.0241, 0.0562	0.0257, 0.0624
***R* indices (all data)**	0.0328, 0.0653	0.0270, 0.0602	0.0311, 0.0593	0.0319, 0.0663

The structures of compounds **8-11** were all found to be dimeric with two tin(II) centres bridged by two alkoxide groups. Each tin centre is also bound to a κ^2 O, N iso-carbamate ligand (Figures 4.10 and 4.11). The nitrogen coordination is provided by the amido-NR donor, while oxygen coordination is provided through the carbonyl oxygen. The tin(II) centres occupy a distorted square-based pyramidal geometry with the stereochemically active lone pair located at the apex of the pyramid. The distortion from ideality is mainly a consequence of the *iso*-carbamate groups in which the amido-N substituent are twisted away from the bridging alkoxides. The compounds have a *transoid* configuration with respect to the orientation of the tin(II) lone pairs across the dimeric molecule. The N-substituents of the *iso*-carbamate ligands are thus also located on opposite sides to minimise steric interactions.

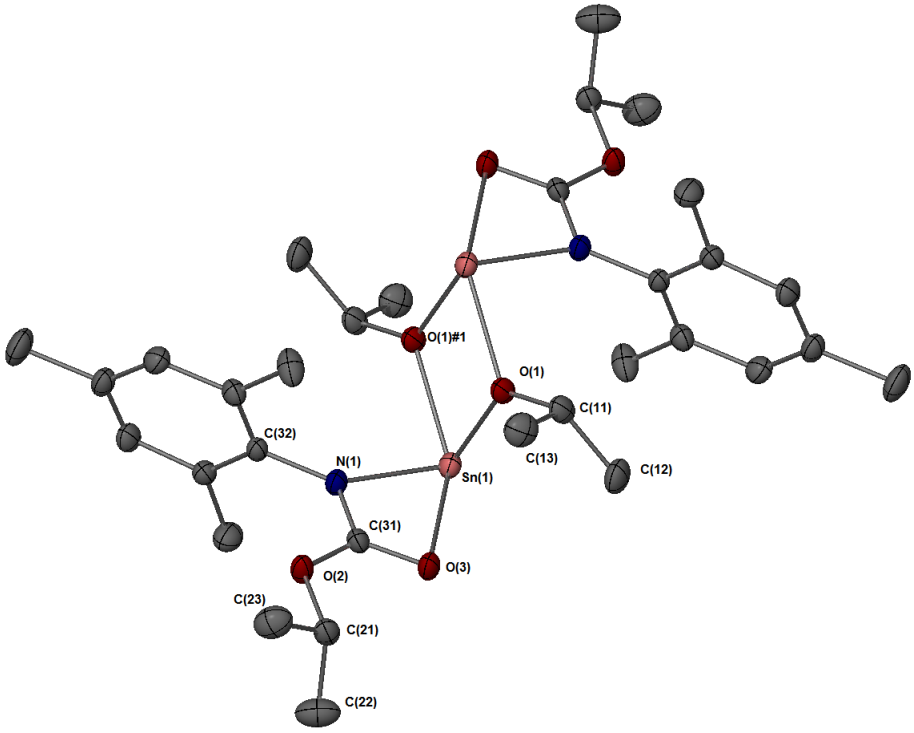

Figure 4.10: Crystal structure of compound 8. Ellipsoids shown at 50% probability, hydrogen atoms omitted for clarity.

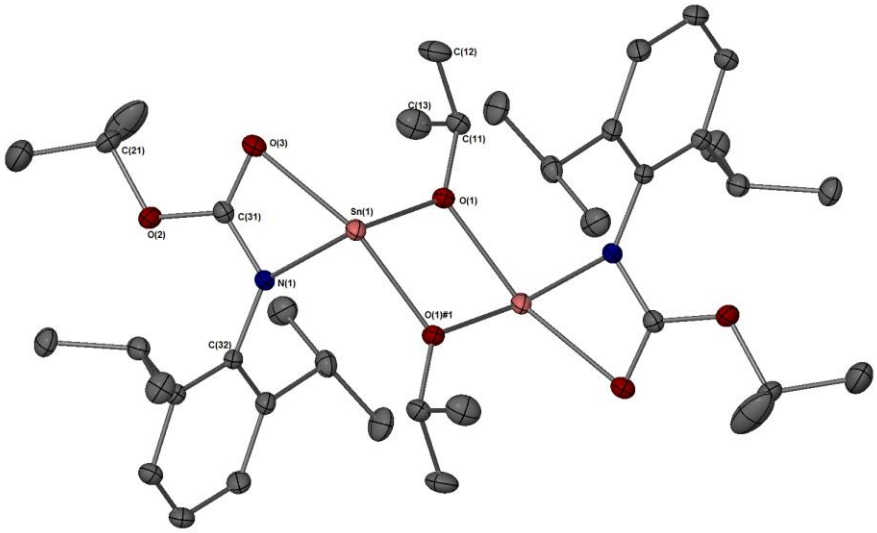

Figure 4.11: Crystal structure of compound 9. Ellipsoids shown at 50% probability, hydrogen atoms omitted for clarity.

The orientation of the OR group at the back of the *iso*-carbamate ligand is of interest as this can be indicative of the electron delocalisation from the N-C-O backbone into the OR moiety. As discussed in Section 1.5.1, the orientation of the OR group and hybridisation of the oxygen atom can determine the potential for delocalisation of electrons. For a sp^2 hybridised oxygen atom, delocalisation is favoured when the OR group is co-planar with the N-C-O backbone as this allows favourable orbital overlap. For all four compounds the OR group is orientated co-planar to the N-C-O backbone with the maximum deviation of 4° measured for compound **11**. The delocalisation is reflected for all three compounds with the C(31)-O(2) bond length which measures 1.349-1.3468 Å this is 0.1Å shorter than the C(21)-O(2) bond which measures 1.465-1.488 Å.

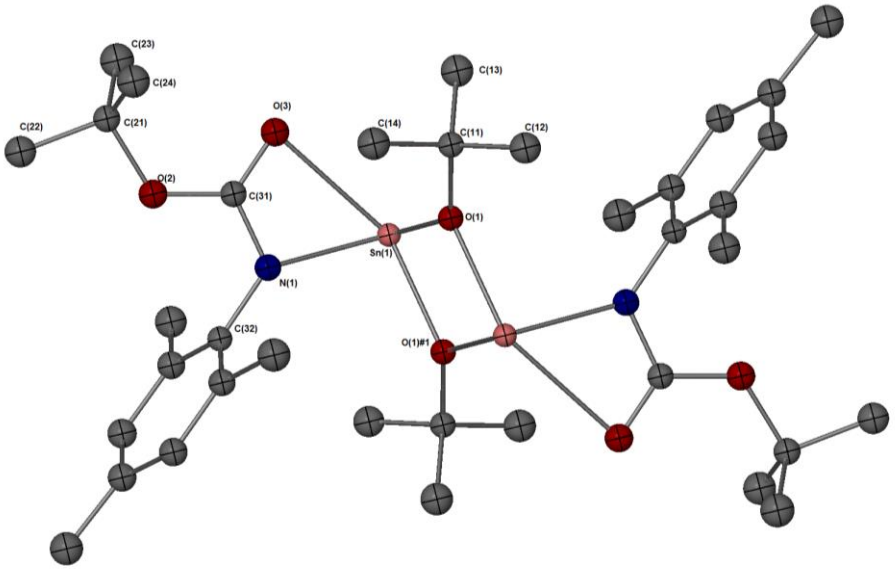

Figure 4.12: Crystal structure of compound 10. Ellipsoids shown at 50% probability, hydrogen atoms omitted for clarity.

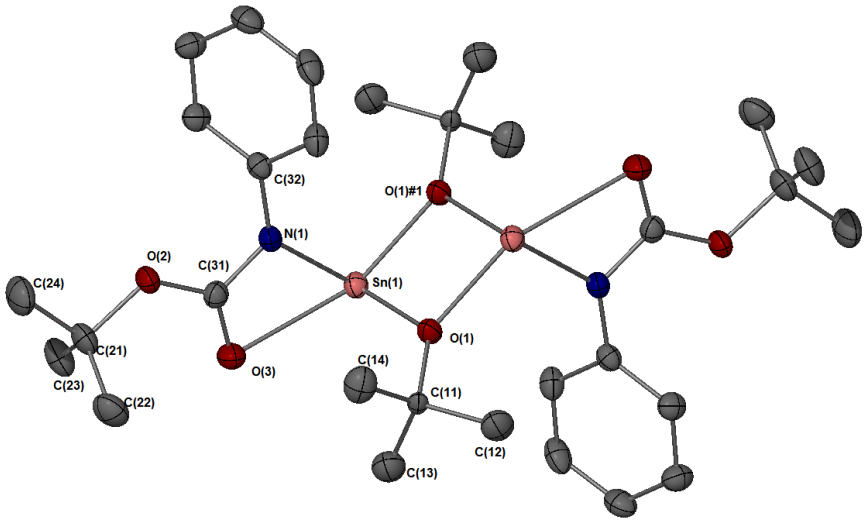

Figure 4.13: Crystal structure of compound 11. Ellipsoids shown at 50% probability, hydrogen atoms omitted for clarity.

The *iso*-carbamate ligands are bound to the tin(II) centres more strongly through the nitrogen with the Sn(1)-N(1) bond lengths ranging from 2.1839(13)-2.2035(10) Å, shorter than the Sn(1)-O(3) bond lengths which vary from 2.5074(11) Å to 2.613(1) Å. The Sn(1)-O(3) bond length is found to be longer for compounds **10** and **11**, this can be attributed to the increased steric bulk on the bridging alkoxide groups which may push the carbonyl oxygen of the iso-carbamate away from the tin(II) centre.

Table 4.4: Selected bond lengths and bond angles for compounds 8-11

Selected bond lengths (Å)				
	8	**9**	**10**	**11**
Sn(1)-O(1)	2.1293(14)	2.1202(10)	2.1372(10)	2.1406(14)
Sn(1)-O(1)#1	2.2085(13)	2.1925(10)	2.2028(10)	2.2023(16)
Sn(1)-N(1)	2.1839(15)	2.2035(12)	2.2035(13)	2.1925(19)
Sn(1)-O(3)	2.5328(14)	2.5074(11)	2.613(1)	2.582(2)
O(1)-C(11)	1.444(2)	1.4479(17)	1.468(4)	1.488(2)
N(1)-C(31)	1.237(2)	1.3301(17)	1.338(4)	1.343(3)
N(1)-C(32)	1.428(2)	1.4287(17)	1.4336(19)	1.419(3)
O(2)-C(31)	1.343(2)	1.3439(17)	1.3468(17)	1.339(3)
O(2)-C(21)	1.465(2)	1.4690(17)	1.4711(17)	1.488(3)
O(3)-C(31)	1.253(2)	1.2570(17)	1.246(2)	1.244(3)
	Selected bond angles (°)			
	8	**9**	**10**	**11**
O(1)-Sn(1)-N(1)	95.49(6)	97.24(4)	98.59(5)	94.14(6)
O(1)-Sn(1)-O(1)#1	70.99(5)	71.34(4)	72.20(4)	73.26(6)
N(1)-Sn(1)-O(1)#1	87.89(5)	89.29(4)	93.49(4)	90.97(6)
O(1)-Sn(1)-O(3)	85.82(5)	88.59(4)	92.37(4)	93.61(6)
N(1)-Sn(1)-O(3)	55.90(5)	56.09(4)	54.62(4)	55.00(6)
O(1)#1-Sn(1)-O(3)	135.15(5)	137.90(4)	142.81(4)	144.19(6)
C(11)-O(1)-Sn(1)	129.99(12)	131.74(9)	127.07(9)	127.8(1)
C(31)-N(1)-C(32)	123.15(15)	123.92(12)	119.97(2)	124.3(1)
C(31)-N(1)-Sn(1)	99.16(11)	97.49(9)	100.2(1)	100.1(1)
C(31)-O(2)-C(21)	117.36(14)	116.71(11)	122.3(1)	121.0(2)
C(31)-O(3)-Sn(1)	85.18(11)	85.64(8)	83.86(9)	84.9(1)
O(3)-C(31)-N(1)	119.75(17)	119.14(13)	120.3(1)	119.2(2)
Sn(1)-O(1)-Sn(1)#1	109.01(5)	108.66(4)	107.91(1)	106.74(7)

4.2.1.3 Evaluation of compounds as potential CVD precursors

Samples of compounds **8** and **9** were prepared and provided to SAFC Hi-Tech for analysis by TGA. The results are shown in Figures 4.14 and 4.15, with the first derivative also shown. The TGA for **8** shows an extended multistep decomposition process with an onset temperature of 195 °C but which does not reach completion before 570 °C. The first step in the decomposition process occurs from 195 to 270 °C and accounts for 25% of the mass of the compound, although efforts to determine the decomposition products at this stage were unsuccessful. A second decomposition step from 290-350 °C accounting for 35% is followed by a slow decomposition up to the end of the experiment resulting in a residual mass of 31% recorded. The residual mass calculated for SnO is 33.8%, while tin metal is 29.8%. In comparison the TGA of the parent alkoxide **5 (**Section 3.3.1 Figure 3.12) exhibits a much sharper decomposition with a major step from 130 to 235 °C followed by a smaller decomposition from 240 to 295 °C resulting in a residual mass of 5%. Based on the TGA data presented the parent alkoxide **5** would therefore be a more suitable tin oxide precursor.

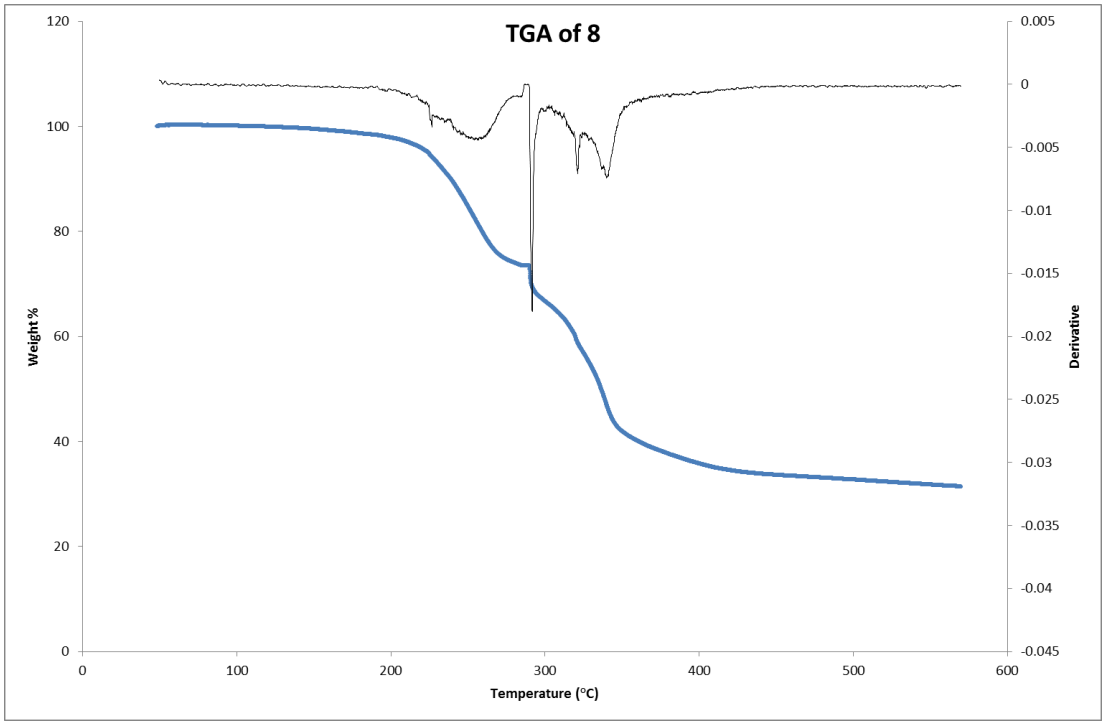

Figure 4.14: TGA of compound 8

The TGA for **9** also displayed a long multistep decomposition process with a slow onset occurring between 50 °C to 180 °C accounting for a 6% mass loss. A sharper decomposition was observed between 190 °C and 240 °C accounting for a further 12 % mass loss before a

large mass loss event between 280 °C and 480 °C corresponding to 50 % of the initial mass of compound **9**. The residual mass at the end of the decomposition process was 29.4% which is slightly below the expected mass for SnO at 30.5% and well above that for tin metal at 26.91% suggesting that the decomposition product is more likely to be SnO. Attempts to calculate the decomposition products at each step along the TGA were unsuccessful although the slow onset observed may be due to evaporation of residual solvent from the synthesis of compound **9**. As commented with compound **8** the TGA curve for the parent alkoxide **5** shows decomposition or volatisation over a much smaller temperature window, and at lower temperatures and would therefore be expected to display more favourable characteristics as a precursor.

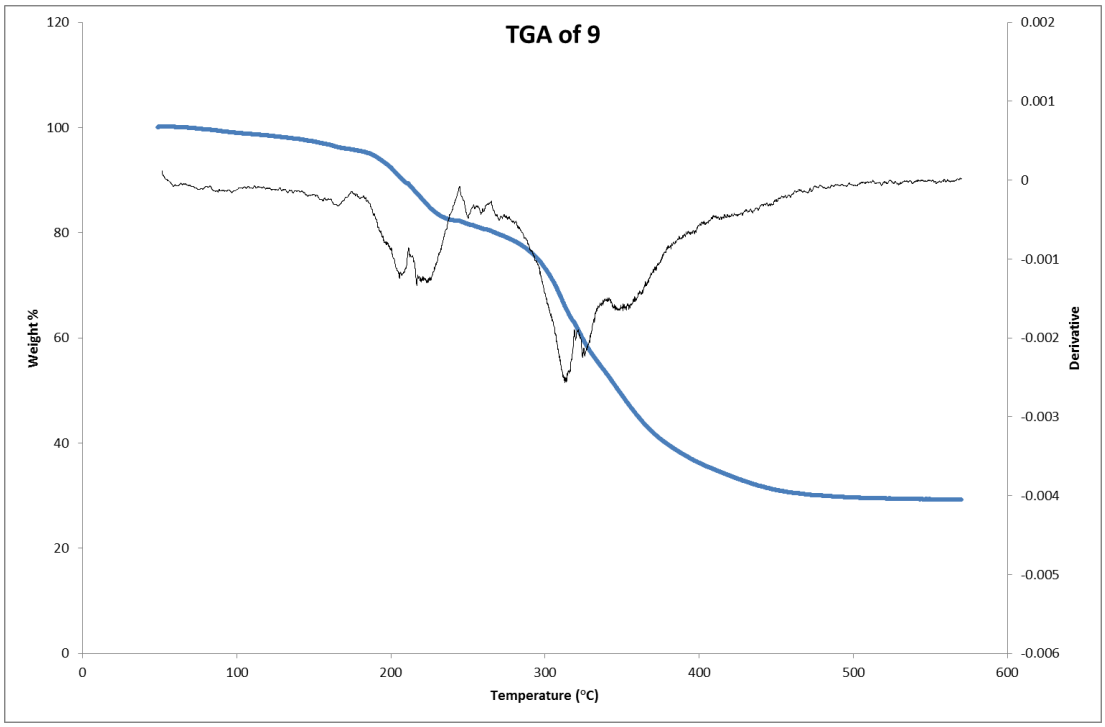

Figure 4.15: TGA of compound 9

Although the residual masses for both **8** and **9** indicated that SnO could be the favoured decomposition product, the elevated temperatures required for full decomposition, and the broad decomposition profiles suggest that these precursors are not suitable for further study. Based upon the analysis of the TGA curves therefore, compounds **8** and **9** were not taken further and used for CVD experiments.

4.2.2 Alkyl isocyanate insertion into tin(II) alkoxide compounds

The reaction of tin(II) alkoxides with alkyl isocyanates was also investigated as the formation of alkyl *iso*-carbamate compounds are more likely to provide suitable CVD precursors for tin oxide deposition. The tin(II) *iso*-carbamate compounds were synthesised through the addition of two equivalents of alkyl isocyanate to a tin(II) alkoxide in toluene (Figure 4.16). Removal of solvent *in vacuo* resulted in white precipitates. The products, **14-17** were further purified through crystallisation from toluene (**15** was recrystallized from hexanes) by slow evaporation of the solvent in an inert atmosphere.

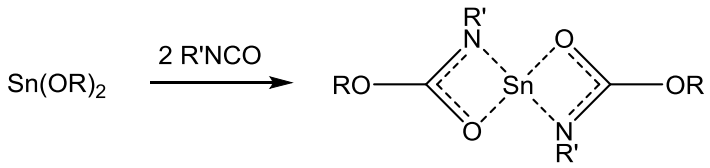

R= ^{i}Pr R'=^{t}Bu **12**

R=^{t}Bu R'=^{t}Bu **13**

R= ^{i}Pr R'= ^{i}Pr **14**

R=^{t}Bu R'=^{i}Pr **15**

R= ^{i}Pr R'=cyclohexyl **16**

R=^{t}Bu R'=cyclohexyl **17**

Figure 4.16: Reactions between tin(II) alkoxides and alkyl isocyanates

4.2.2.1 Reversible reaction between tBuNCO and tin(II) alkoxides

Initial attempts to isolate compounds **12** and **13** were unsuccessful, with the parent alkoxide being recovered with no evidence of the insertion of the ^{t}Bu isocyanate. The reaction between **5** and ^{t}Bu isocyanate to form **12** was, thus, carried out in d_8-toluene and monitored *in situ* using multinuclear NMR spectroscopy. Analysis of the ^{1}H NMR spectrum provided evidence that the insertion was occurring although with resonances associated with the alkoxide were still apparent at δ 1.34-1.35 and 4.56 ppm. Additional signals evidencing the formation of the target *iso*-carbamate ligand could also be observed at δ 1.11-1.13, 1.41 and 4.94-5.02 ppm. The presence of unreacted ^{t}Bu isocyanate was also detected through the observation of a singlet resonance at δ 0.92 ppm. The 119Sn{1H} NMR spectrum contained

a single resonance at δ -360 ppm, this is up-field of the resonances observed for compounds **8-10** which varied from δ -315 to -347 ppm. In order to determine whether the reaction was occurring in a 1:1 ratio as observed with the aryl isocyanates to form compounds **8-11** the reaction was repeated in a 1:1 ratio. The resulting ^{1}H NMR spectrum showed a mixture of free and inserted ^{t}Bu isocyanate to be present in the reaction solution. Based on the data gathered for CO_2 insertion into tin(II) alkoxides it was postulated that the reaction was again reversible with the establishment of an insertion/de-insertion equilibrium process. This was verified through analysis of a 2D EXSY NMR experiment that clearly showed exchange between the two different ^{t}Bu resonances of the inserted and un-inserted N-^{t}Bu components (Figure 4.17).

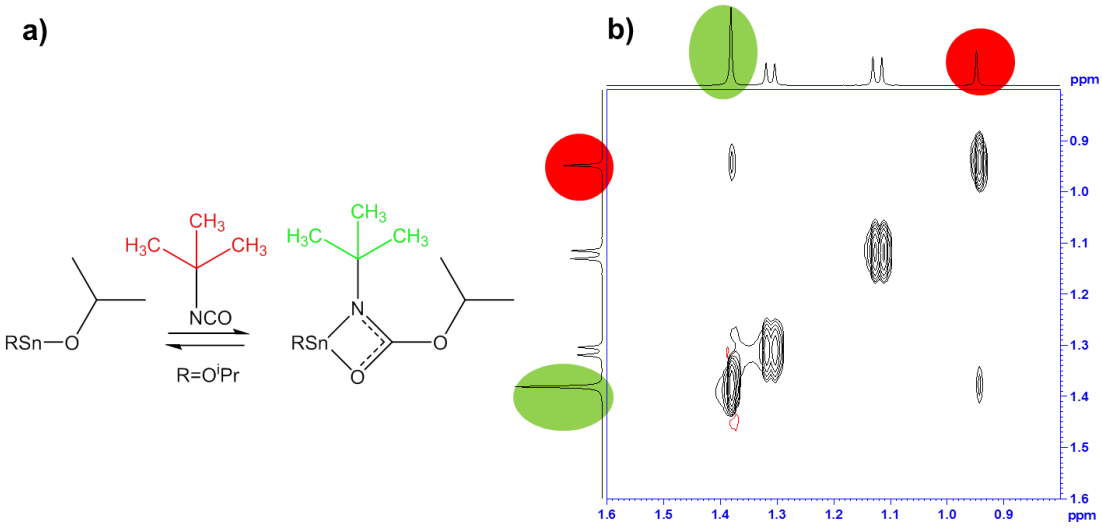

Figure 4.17: a) Colour coded reaction scheme between 5 and ^{t}Bu isocyanate b) 2D EXSY NMR spectrum of reaction between 5 and ^{t}Bu isocyanate showing the exchange between the free ^{t}Bu isocyanate and the *iso*-carbamate ^{t}Bu group.

The reaction between **LXXXII** and ^{t}Bu isocyanate to form compound **13** was also found to be reversible; the initial reaction mixture was analysed in situ using multinuclear NMR spectroscopy. The ^{1}H NMR spectrum contained singlet resonances at δ 0.98 ppm and 1.35 ppm corresponding to the free isocyanate and parent alkoxide **LXXXII** respectively. The iso-carbamate resonances were observed at δ 1.41 and 1.43 ppm. The 119Sn{1H} NMR spectrum contained a single resonance at δ -377 ppm, this is slightly up-field of the resonance observed for compound **12** (-360 ppm). The reaction to form compound **13** was probed using 2D EXSY NMR experiments; this confirmed a dynamic exchange process. A series of 1D EXSY NMR experiments were, thus, conducted using the same procedure detailed for the reaction with CO_2 in Section 4.1 to enable the acquisition of comparable

kinetic data for the reaction between the two alkoxides and ^{t}Bu isocyanate. The data used to determine the rate constants and different temperatures is shown for **12** and **13** in Figures 4.16 and 4.17, with the deduced rate constants shown in Table 4.5.

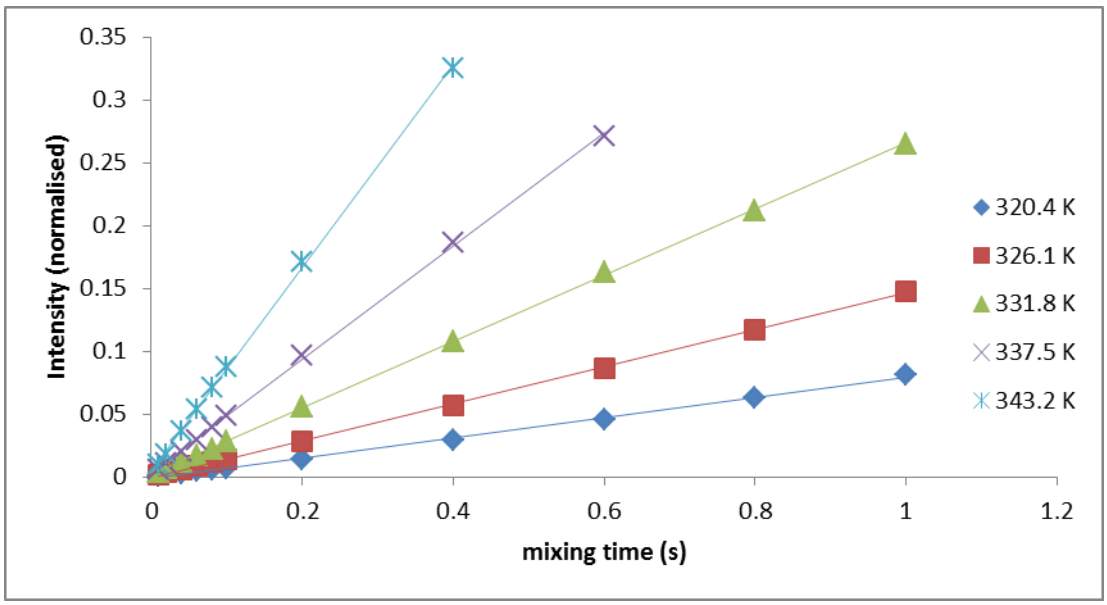

Figure 4.18: Plot of mixing time and normalised intensity for the reaction between 5 and ^{t}Bu isocyanate

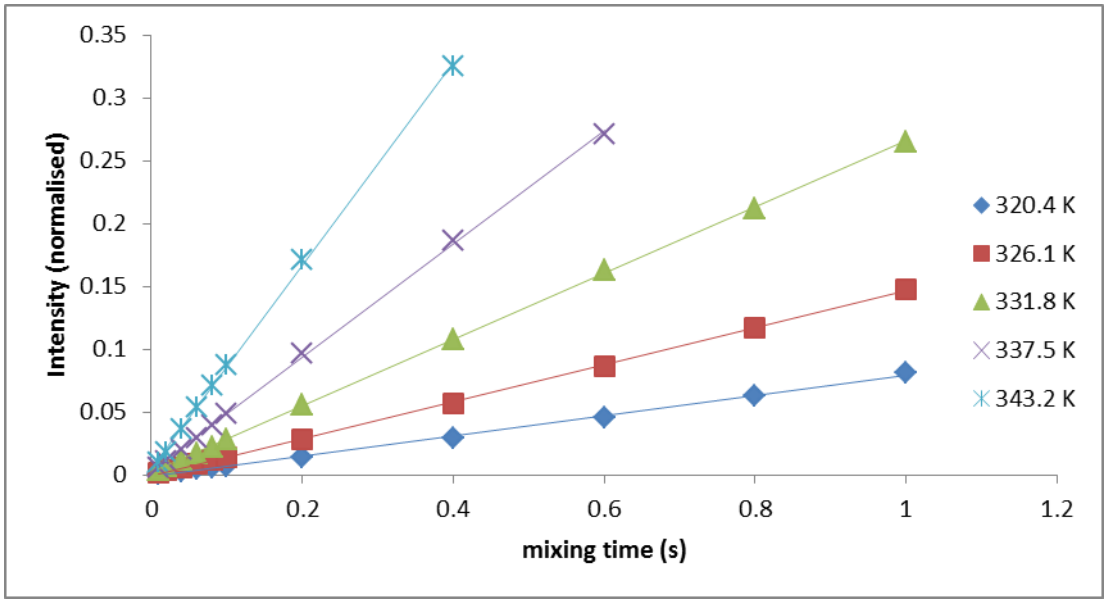

Figure 4.19: Plot of mixing time and normalised intensity for the reaction between LXXXII and ^{t}Bu isocyanate.

Table 4.5: Table of equilibrium rate constants at different temperatures for the reaction between ^{t}Bu isocyanate with 5 and LXXXII

5 + ^{t}BuNCO (12)		**LXXXII + ^{t}BuNCO (13)**	
Temperature (K)	k (s^{-1})	Temperature (K)	k (s^{-1})
320.4	0.0802	328.5	0.0516
326.1	0.1469	333.6	0.0659
331.8	0.2645	338.8	0.0785
337.5	0.4523	343.9	0.0935
343.2	0.8089	349.1	0.1074

The rate constants at different temperatures were used to determine the activation energy, $\Delta H^{\neq}$ and $\Delta S^{\neq}$ for the insertion reaction between **5** and **LXXXII** with ^{t}Bu isocyanate, these values are shown in Table 4.6. The activation energy is significantly lower for the reaction between ^{t}BuNCO and **LXXXII** at only 33.71 kJ mol^{-1} compared to 92.18 kJ mol^{-1} for the analogous reaction with **5**. The high activation energy observed for the reaction with **5** could be due to the polymeric nature of the alkoxide, which would require de-aggregation in order for the insertion reaction to occur. Based on the structures of compounds **8-11** it may be envisaged that the dimeric nature of **LXXXII** could allow for insertion of the isocyanate into the terminal alkoxide groups to form *iso*-carbamate groups without the need for the dimer to separate. The same pattern is observed for $\Delta H^{\neq}$, the enthalpy of activation with the reaction to form **13** being nearly a third of the value of that calculated for the reaction to form **12** (30.89 and 89.43 kJ mol^{-1} respectively). The values calculated for $\Delta S^{\neq}$, the entropy of formation, diverged significantly. For the reaction to form **13** this was found to be -176.08 J mol^{-1} K^{-1}, indicating that the insertion transition state is more ordered than the reactants. This is in keeping with the **LXXXII** dimer remaining intact, and the transition state involving the association and insertion of the ^{t}BuNCO. On the other hand the positive nature of $\Delta S^{\neq}$ for **12** at 12.61 J mol^{-1} K^{-1} is consistent with the transition state being less ordered than the reactants. This would be consistent with a polymeric solution structure for **5** which would break up into shorter oligomeric or dimeric units upon reaction with the isocyanate.

Table 4.6: EXSY kinetic data for the reaction of ^{t}BuNCO with 5 and LXXXII

	5 + ^{t}BuNCO (12)	**LXXXII + ^{t}BuNCO (13)**
Activation energy kJ mol^{-1}	92.18 ± 0.96	33.71 ± 2.04
$\Delta H^{\neq}$ kJ mol^{-1}	89.43 ± 0.95	30.89 ± 2.05
$\Delta S^{\neq}$ J mol^{-1} K^{-1}	12.61 ± 2.86	-176.08 ± 6.07

The kinetic data obtained for **12** shows some correlation with the kinetic data obtained for the reaction between **5** and CO_2 (Section 4.1). The activation energy for the reaction with CO_2 was found to be lower (70.3 kJ mol^{-1}) compared to the same reaction with ^{t}BuNCO (92.2 kJ mol^{-1}); the lower activation energy can be attributed to a lower steric interaction during the insertion reaction with CO_2, compared to the sterically larger ^{t}BuNCO. The same trend is also observed with $\Delta H^{\neq}$ with the reaction with ^{t}BuNCO (89.4 kJ mol^{-1}) higher than the reaction with CO_2 (68.0 kJ mol^{-1}). The entropy of the transition state also follows this trend, more interestingly for $\Delta S^{\neq}$ is the change in sign for the calculation depending on the heterocumulene involved. For the ^{t}BuNCO reaction $\Delta S^{\neq}$ is found to be positive (12.6 J mol^{-1} K^{-1}) while the reaction with CO_2 results in a negative $\Delta S^{\neq}$ (-7.37 J mol^{-1} K^{-1}). A negative $\Delta S^{\neq}$ value is also observed in the kinetic data for **13** (-175 J mol^{-1} K^{-1}) and by Fulton and co-workers when they investigated the reversible formation of **XLVIII** (-165 J mol^{-1} K^{-1}).[214]

4.2.2.2 Solution-based analysis of the homoleptic bis(*iso*-carbamate) compounds 14-17

Compound **14** was synthesised through the reaction of two equivalents of ^{i}Pr isocyanate with **5** in toluene. The ^{1}H NMR spectrum for **14** displayed four resonances attributed to the two different ^{i}Pr environments arising from the *iso*-carbamate ligand. The doublet resonance at δ 1.13 ppm and the septet at δ 4.94 ppm were assigned to the O^{i}Pr protons, while the doublet at δ 1.19 ppm and the septet at 4.04 ppm were attributed to the N-^{i}Pr substituent. The $^{13}C\{^{1}H\}$ NMR spectrum contained five resonances, with two at δ 22.9 and 24.3 ppm assigned to methyl groups and two at δ 45.9 and 69.6 ppm attributed to the methine carbons of the ^{i}Pr groups with the latter associated with the O-^{i}Pr substituent. A further resonance at δ 163.2 ppm could be assigned to the quaternary carbon of the N-C-O unit. A single resonance was observed in the $^{119}Sn\{^{1}H\}$ NMR spectrum at δ -360 ppm up field of the resonances observed for the heteroleptic compounds **8-11**, and the same as the resonance observed for compound **12**.

Compound **15** was synthesised through addition of two equivalents of ^{i}Pr isocyanate to **LXXXII**. The ^{1}H NMR spectrum for compound **15** contained three resonances, a singlet at δ 1.43 ppm assigned to the O-^{t}Bu group, and a doublet and septet at δ 1.19-1.21 and δ 3.94-4.03 ppm respectively which could attributed to the N-^{i}Pr substituent. The $^{13}C\{^{1}H\}$ NMR spectrum displayed two resonances attributed to the methyl groups of the ^{i}Pr and ^{t}Bu groups at δ 24.2 and 29.3 ppm. A further resonance observed at 49.1 ppm was assigned to the methine carbon of the ^{i}Pr group, while the resonance at δ 80.3 ppm could be attributed to the quaternary carbon of the ^{t}Bu substituent. A further resonance at 163.2 ppm is characteristic

of the backbone N-C(O)-O carbon. In the $^{119}Sn\{^{1}H\}$ NMR spectrum a single resonance was observed at δ -338 ppm, slightly downfield of that observed for compound **14**.

The addition of two equivalents of cyclohexyl isocyanate to **5** allowed the formation of compound **16**. Although the ^{1}H NMR spectrum was complicated by the overlap of resonances for the ^{i}Pr and cyclohexyl groups, a multiplet at δ 1.10-1.28 ppm was assigned to the methyl groups of the ^{i}Pr substituent overlapping with a CH_2 group in the cyclohexyl ring. A multiplet at 4.91-5.03 ppm was attributed to the methine proton of the ^{i}Pr group. A series of multiplet resonances, that upon integration were deduced to represent two protons each, were assigned to the cyclohexyl group at δ 1.44-1.57 ppm (two sets of two protons), δ 1.61-1.71ppm and δ 1.87-2.19ppm. A resonance further downfield at δ 3.64-3.73ppm integrated to a single proton and could be assigned to the CH group of the cyclohexyl ring bound to the nitrogen. The $^{13}C\{^{1}H\}$ NMR spectrum contained four resonances between δ 22.9 and 34.8 ppm that could be attributed to the methyl groups of the ^{i}Pr moiety and the CH_2 carbons in the cyclohexyl ring. The CH group of the cyclohexyl group was assigned to the resonance at δ 53.9 ppm, the methine carbon of the ^{i}Pr group was attributed to the resonance at δ 69.6 ppm and the resonance at δ 163.2ppm was assigned to the backbone N-C(O)-O carbon. A single peak in the $^{119}Sn\{^{1}H\}$ NMR at δ -355 ppm was comparable to the resonances observed for **12** and **14** (δ -360 ppm).

Compound **17** was prepared by adding two equivalents of cyclohexyl isocyanate to **LXXXII**. The ^{1}H NMR spectrum contained a singlet resonance for the ^{t}Bu group at δ 1.44 ppm, and a broad multiplet at δ 1.50-1.75 and further two multiplets at δ 1.80-1.91 and δ 3.57-3.76ppm assigned to the cyclohexyl protons. The $^{13}C\{^{1}H\}$ NMR spectrum comprised resonances at δ 26.5, 26.6, 29.3 and 34.6 ppm for the cyclohexyl CH_2 groups and the methyl groups of the ^{t}Bu substituent. Further resonances are observed at δ 54.2 ppm for the CH of the cyclohexyl moiety, δ 80.3 ppm for the quaternary carbon of the ^{t}Bu group and δ 163.1 ppm for the N-C(O)-O backbone carbon. A single resonance at δ -335 ppm is observed in the $^{119}Sn\{^{1}H\}$ NMR spectrum which was consistent with the shifts observed for both the dimeric and monomeric tin iso-carbamate compounds **8-16.**

4.2.2.3 Molecular structures of tin(II) bis(*iso*-carbamates)

The solution-based analysis of compounds **14-17** suggested that the products formed were the homoleptic bis(*iso*-carbamate) systems. This contrasted with the aryl isocyanate insertions used for compounds **8-11** which resulted in exclusive mono-insertion and the

formation of heteroleptic compounds. The coordination number of the tin, and the binding modes of the *iso*-carbamate ligands could not be determined by solution based analysis; the $^{119}Sn\{^{1}H\}$ NMR shifts are comparable to both the dimeric four-coordinate iso-carbamate compounds **8-11** and the monomeric four coordinate ureate compounds **1-4** described in Chapter 2. While compound **14** could be isolated as a crystalline material, the quality of crystals was not suitable for single crystal X-ray diffraction studies and attempts to grow better quality crystals were unsuccessful. The solid state structures for compounds **15-17** were, however, confirmed using single crystal X-ray diffraction analysis and can be observed in Figures 4.20-4.22. Table 4.7 details the collection parameters for the compounds while selected bond lengths and angles can be found in Table 4.8. Compound **15** was found to be orthorhombic and crystallised in the $C222_1$ space group, while compound **16** was found to be triclinic in the *P*-1 space group and compound **17** was found to be monoclinic in the space group $P2_1/a$.

Table 4.7: Crystallographic Parameters for compounds 15-17

Compound	**15**	**16**	**17**
Empirical Formula	$C_{16}H_{32}N_2O_4Sn$	$C_{20}H_{36}N_2O_4Sn$	$C_{22}H_{40}N_2O_4Sn$
Crystal System	Orthorhombic	Triclinic	Monoclinic
Space Group	$C222_1$	*P*-1	$P2_1/a$
Cell Constants			
a (Å)	9.7150(2)	9.9870(2)	9.4880(2)
b (Å)	10.7320(2)	11.2070(4)	29.6630(6)
c (Å)	20.0140(2)	11.2480(4)	10.0490(2)
α (°)	90	75.732(2)	90
β (°)	90	71.845(2)	114.8540(10)
γ (°)	90	81.512(2)	90
Volume (Å^3)	2086.69(7)	1155.92(6)	2566.27(9)
Density (mg/m^3)	1.385	1.400	1.334
Z	4	2	4
Measured reflections	20608	20291	34188
Unique reflections	2808	5279	4961
R_{int}	0.0409	0.0492	0.0451
R_1. w$R_2[I > 2\sigma(I)]$	0.0251, 0.0599	0.0284, 0.0634	0.0340, 0.0774
***R* indices (all data)**	0.0281, 0.0616	0.0371, 0.0672	0.0455, 0.0828

All three compounds were found to exist as monomeric compounds with the tin(II) centre bound to two κ^2-N,O *iso*-carbamate ligands bound to the tin through the amido-N and carbonyl oxygen atoms of the ligand. The tin(II) centres were found to be in a distorted square based pyramidal geometry with the stereochemically active lone pair situated at the apex of the pyramid. The distortion observed is comparable to that seen for the ureate systems described in Chapter 2 and the dimeric iso-carbamate compounds **8-11**, with the amido-N substituent pushed out of the plane expected for a square based pyramidal structure. This reduces the steric interaction between the two ligands bound to the tin(II) centre.

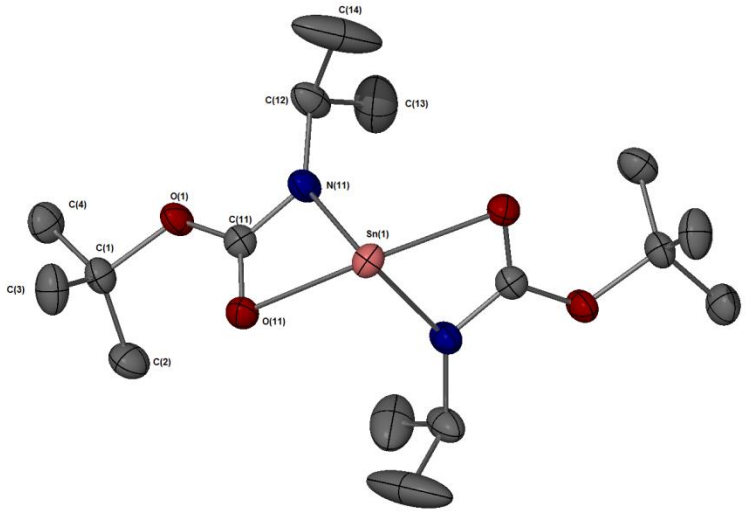

Figure 4.20: Crystal structure of compound 15. Ellipsoids shown at 50% probability, hydrogen atoms omitted for clarity.

As discussed earlier for compounds **8-11,** the orientation of the OR group on the iso-carbamate is important to allow orbital overlap if electron delocalisation is to occur across the N(C)O,OR system. For compounds **15-17** the OR group lies co-planar to the NCO core of the *iso*-carbamate ligand which allows orbital overlap and delocalisation of electron density across the backbone of the system to take place. This is reflected in the bond lengths observed for C(11)-O(1) which measure 1.337 to 1.347 Å, 0.1 Å shorter than the carbonyl derived O(1)-C(1) bonds which measure 1.459-1.477 Å.

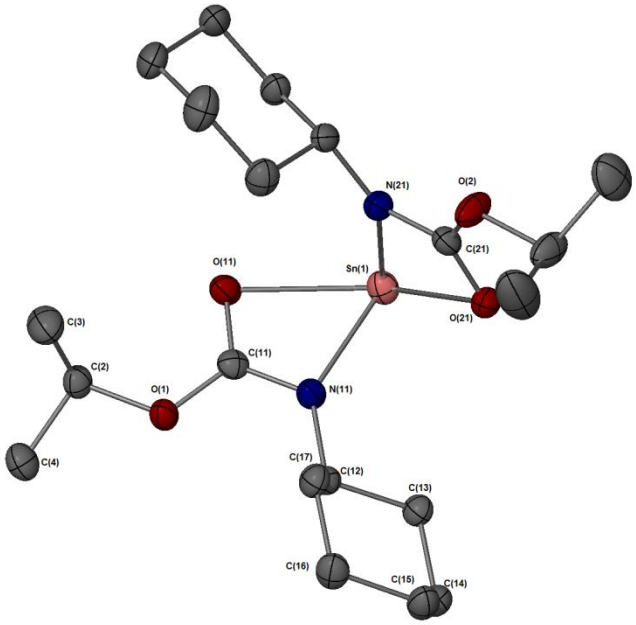

Figure 4.21: Crystal structure of compound 16. Ellipsoids shown at 50% probability, hydrogen atoms omitted for clarity.

The variation between the three different compounds is much less pronounced than that observed for the dimeric systems **8-1.** The influence of the amido-R group is negated by the *transoid* geometry, with the N-R groups on opposite corners of the basal plane of the square-based pyramid. For compounds **8-11** the interaction of the bridging alkoxides with the N-R group causes more significant variation in the bond lengths and mutual steric interactions around the tin(II) centre.

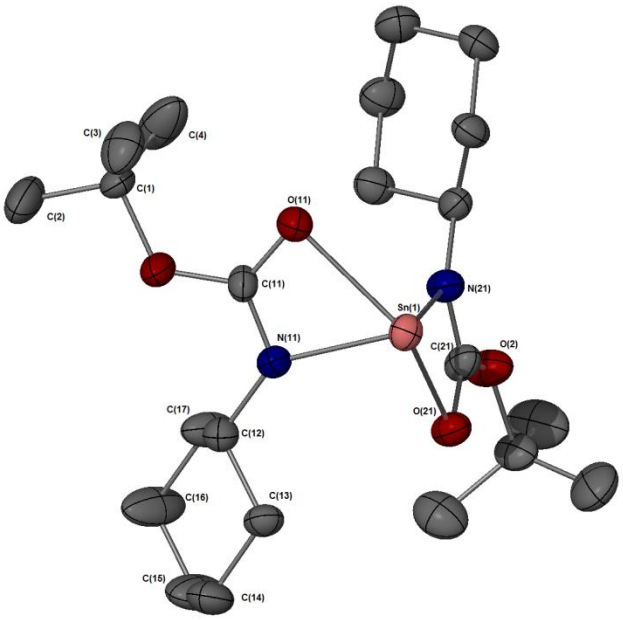

Figure 4.22: Crystal structure of compound 17. Ellipsoids shown at 50% probability, hydrogen atoms omitted for clarity.

Table 4.8: Selected bond lengths and bond angles for compounds 15-17.

Selected bond lengths (Å)			
	15	**16**	**17**
Sn(1)-O(11)	2.3752(18)	2.4285(15)	2.376(2)
Sn(1)-O(21)	-	2.3717(15)	2.399(2)
Sn(1)-N(11)	2.1723(18)	2.1703(17)	2.160(3)
Sn(1)-N(21)	-	2.1708(18)	2.180(3)
N(11)-C(11)	1.317(3)	1.312(3)	1.311(4)
N(11)-C(12)	1.469(3)	1.467(3)	1.462(4)
O(11)-C(11)	1.268(3)	1.267(2)	1.262(4)
O(1)-C(11)	1.338(3)	1.347(2)	1.337(4)
O(1)-C(1)	1.477(3)	1.459(2)	1.474(4)
Selected bond angles (°)			
	15	**16**	**17**
N(11)-Sn(1)-N(21)	-	94.44(7)	94.26(10)
N(11)-Sn(1)-O(11)	58.06(7)	57.47(6)	58.19(8)
N(11)-Sn(1)-O(21)	-	87.50(6)	86.30(9)
N(21)-Sn(1)-O(11)	-	86.61(6)	87.98(9)
C(11)-N(11)-Sn(1)	95.89(14)	96.90(13)	95.74(19)
C(11)-O(11)-Sn(1)	88.01(13)	86.38(12)	87.25(18)
O(1)-C(11)-O(11)	123.8(2)	122.29(18)	123.0(3)
C(1)-O(1)-C(11)	121.42(18)	118.20(16)	123.2(2)
C(12)-N(11)-C(11)	124.2(2)	122.60(17)	123.4(3)
N(11)-Sn(1)-N(11)#1	94.54(10)	-	-
N(11)-Sn(1)-O(11)#1	87.95(8)	-	-
O(11)-Sn(1)-O(11)#1	130.82(8)	-	-

4.2.2.4 Evaluation of compounds as potential CVD precursors by TGA

Samples of compounds **14-17** were prepared and provided to SAFC Hi-Tech for analysis by TGA. The results are illustrated below with the first derivative also shown. The TGA for **14** displays three major mass loss events from 60 °C to 290°C resulting in a residual mass of 6.5 % (Figure 4.23). The residual mass is well below the calculated residual masses for tin metal and SnO (29.4 % and 33.30 % respectively) and is, therefore, indicative of the compound exhibiting some volatility. The first mass loss event is observed between 60 °C and 165 °C and accounts for 30% of the total lost, while the second event between 170 °C and 235 °C accounts for 38% of the compound mass. The final mass loss event from 240 - 290 °C corresponds to 24% mass loss with a slow mass loss observed of 3% observed between 290 °C and the high temperature limit. Attempts to determine the possible decomposition products at each mass loss event were unsuccessful. In comparison the parent alkoxide **5** displayed a much sharper mass loss between 125-215 °C and had finished decomposing by 265°C, slightly lower than **14** (Figure 4.24). The secondary decomposition step observed for **14** is comparable to that of the parent alkoxide and could therefore indicate that the initial decomposition pathway involves the extrusion of the ^{i}Pr isocyanate.

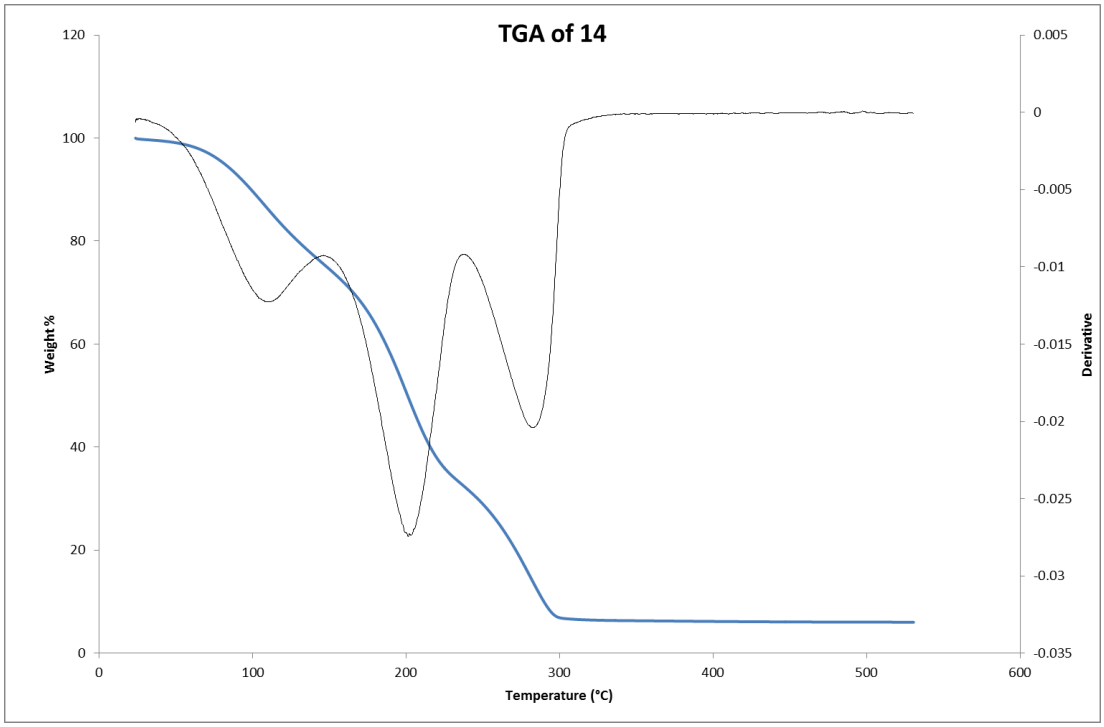

Figure 4.23: TGA of compound 14

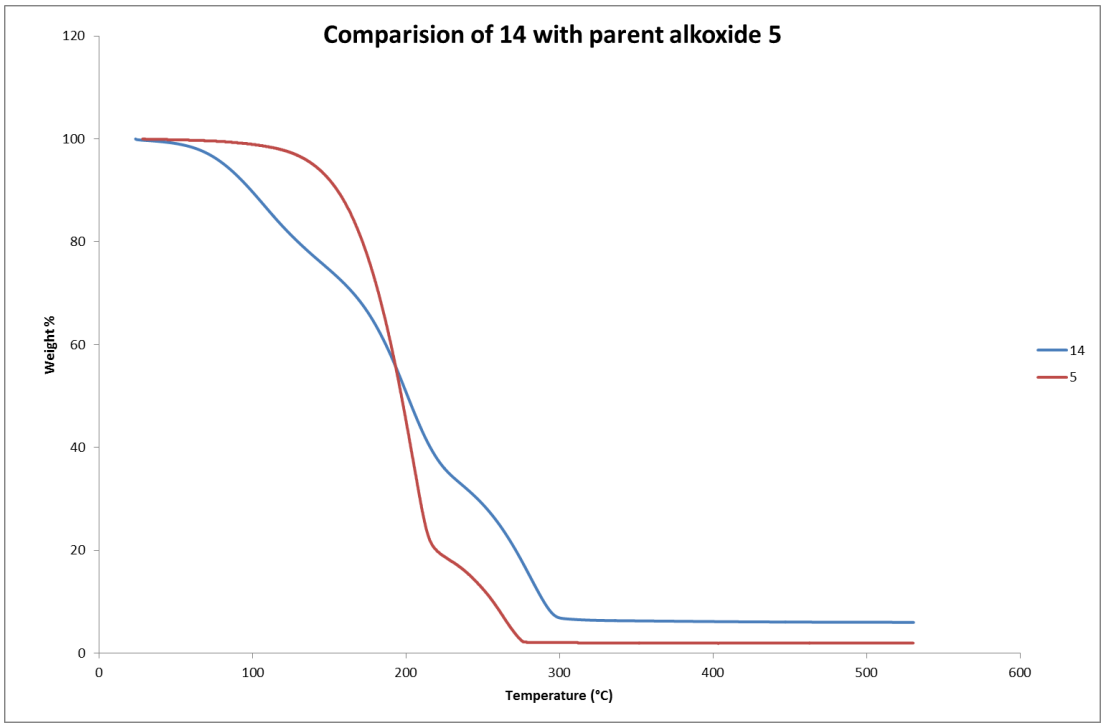

Figure 4.24: Comparison of TGA data for compounds 14 and 5

In contrast the TGA for compound **15** showed a single main mass loss event from 55-140 °C accounting for 60% of the compound's mass; this is proceeded by a gradual loss of 7% of the mass up to 420°C (Figure 4.23). In this case the residual mass of 33% is close to the calculated residual mass expected for SnO_2 (34.8%). The onset is slightly lower than that observed for the parent alkoxide **LXXXII** (Section 3.3, Figure 3.11) which begins to decompose at 60 °C and finish at 245 °C, with the residual mass much lower than that expected for tin metal at 2%.

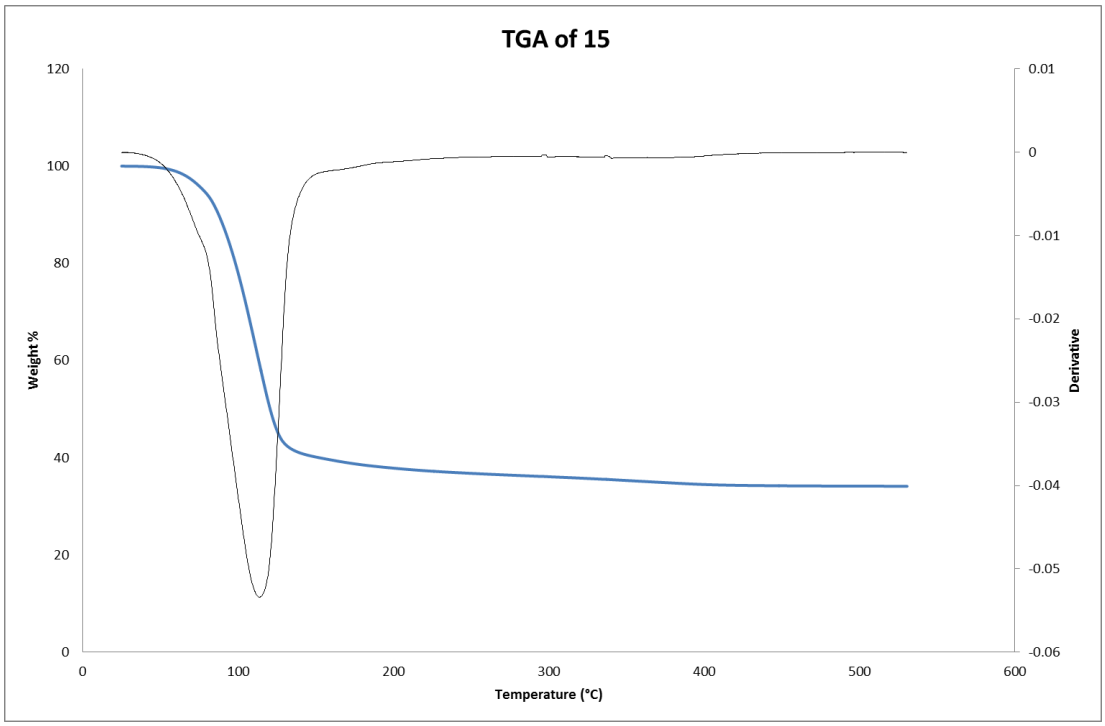

Figure 4.25: TGA of compound 15

The difference in the TGA data for compounds **14** and **15** is of significant interest as the two compounds have ligands that differ through the replacement of a hydrogen with a methyl group located on the O-R moiety (Figure 4.26). The TGA data suggest that, despite the close similarity in the precursor structures for **14** and **15,** they follow very different decomposition pathways. Although attempts to assign the possible decomposition products observed in the TGA of **14** at the three mass loss events were unsuccessful; comparison with the parent alkoxide **5** suggests that extrusion of ^{i}Pr isocyanate to reform **5** could be a possible pathway. This feasibility of this hypothesis is enhanced by the reversible nature of ^{t}Bu isocyanate insertion observed in the reaction to form **12**. Comparison of the TGA data for **15** with the parent alkoxide **LXXXII** indicates they do not behave in a similar way, with the residual mass for **15** significantly higher than that observed for **LXXXII**. The residual mass for **15** suggests that SnO_2 is formed, which would require the tin(II) centre to be oxidised to tin(IV) as part of decomposition pathway. A similar outcome has been observed previously by Maruyama and co-workers using **LI** and by Giebelhaus and co-workers using **LVIII** although the mechanism for oxidation of the tin centre is still unknown.[149,155]

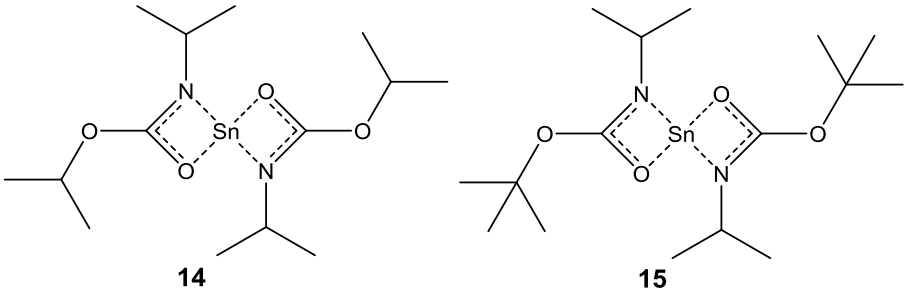

Figure 4.26: The molecular structures of compounds 14 and 15 for comparison

The TGA for compound **16** comprised two main mass loss events, with the first occurring between 80 °C and 200 °C and accounting for 88% of the mass of the compound (Figure 4.27). A second decrease is observed between 220 °C and 245 °C accounting for an additional 8% of the compound mass. The resulting residual mass is less than 5%, much lower than that calculated for tin metal (24.6 %) suggesting that the compound exhibits some volatility when heated. The large mass loss at the beginning of the analysis includes some of this volatilisation as the resulting mass is only 12%. This mass loss event has a small shoulder between 155 °C and 200 °C which accounts for 31% of the mass of the compound. Due to the volatilisation of the compound during this step determination of the decomposition products was not possible. The onset for **16** is lower than that observed for the parent alkoxide **5**. Although the weight loss is similar to that displayed by **5** all of the steps observed occur at lower temperatures suggesting that the formation of the iso-carbamate complex improves the precursor properties compared to just using the alkoxide. A comparison of the TGA of **16** with the TGA for **5** is shown in Figure 4.28.

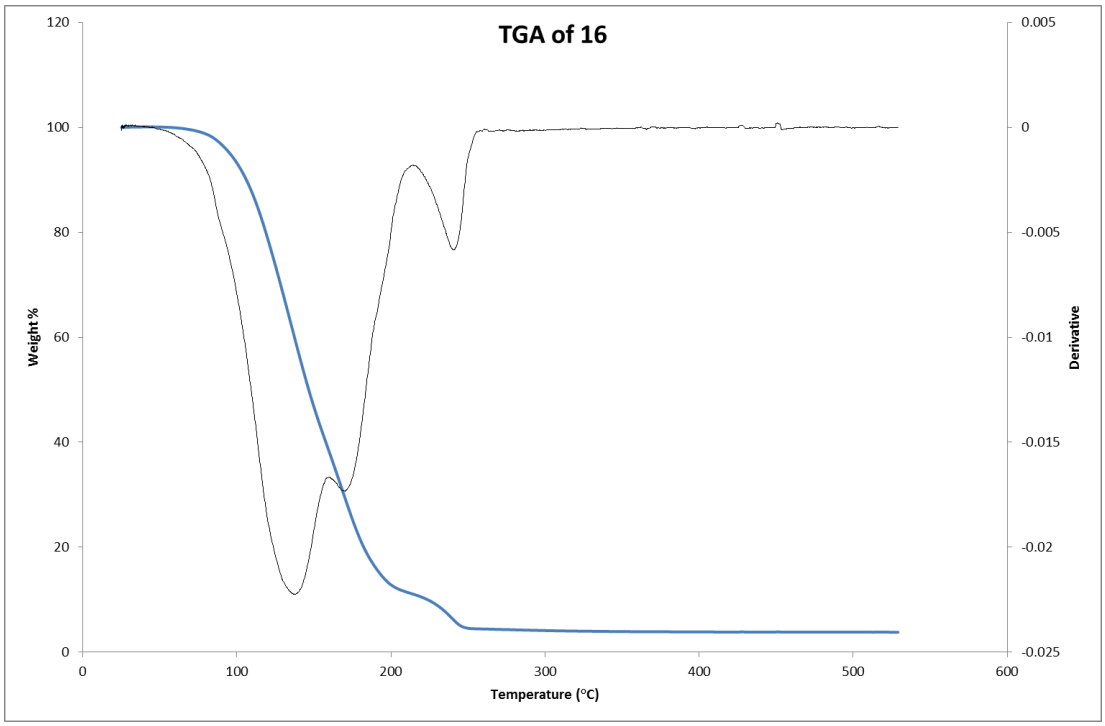

Figure 4.27: TGA of compound 16

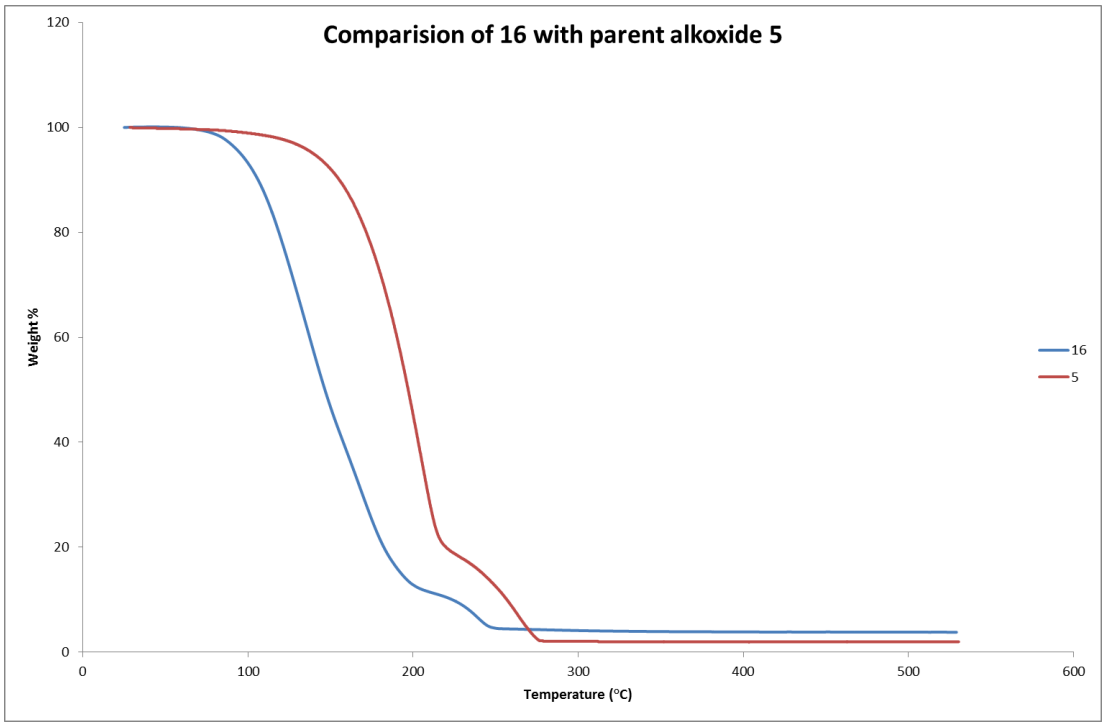

Figure 4.28: Comparison of TGA data for compounds 5 and 16

The TGA for compound **17** is similar to that for compound **16** with two main mass loss events, the first of which has a shoulder present. The initial mass loss is between 60 °C and

185 °C and accounts for 88% of the compound's mass, with the shoulder observed between 140 °C and 185 °C accounting for 31% (Figure 4.29). The second decomposition step is between 230 °C and 265°C and corresponds to a 6% mass loss, while the TGA shows a further slow loss of 2% between 265 °C and 550 °C. The residual mass is observed to be well below that expected for tin metal (23.2%) suggesting that the compound has some volatility. As observed with **16** the initial mass loss is thought to include some volatilisation of the product as the mass at 185 °C is only 12% and therefore determination of the decomposition products was not possible. The onset decomposition temperature for **17** is slightly lower than that observed for the parent alkoxide **LXXXII**, once mass loss has begun, **16** is approximately 50°C lower in temperature than the parent alkoxide. The residual mass for the parent alkoxide is, however, lower than that observed for **17**.

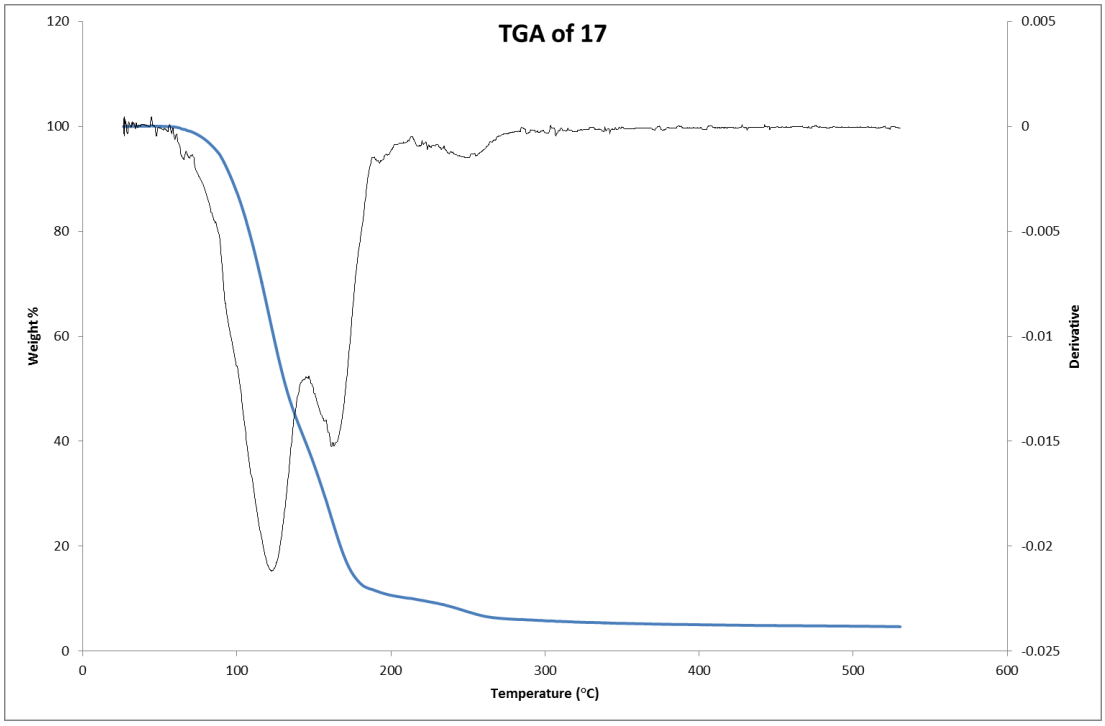

Figure 4.29: TGA of compound 17

Compounds **15**, **16** and **17** were also sent for vapour pressure analysis - see Appendix 2 for more information.

4.2.3 Iso-thiocyanate insertion into tin(II) alkoxide bonds

To allow further investigation of the reactivity of tin(II) alkoxides with different heterocumulenes, the reaction of **5** with organic iso-thiocyanates was also investigated with the aim of forming iso-monothiocarbamate compounds (Figure 4.30). While the *iso*-monothiocarbamate compounds contain oxygen and present an opportunity for tin oxide formation, the incorporation of sulphur into the ligand allows the possibility of tin sulphide formation using a single-source precursor. Compounds **18** and **19** were prepared through addition of two equivalents of the appropriate iso-thiocyanate to compound **5** in toluene. Removal of the solvent *in vacuo* resulted in yellow residues which were purified by recrystallisation from toluene at room temperature.

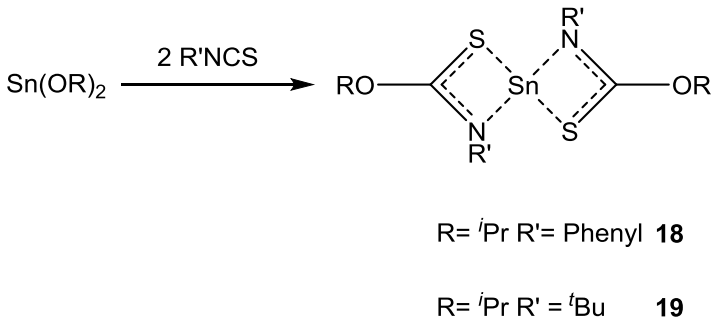

Figure 4.30: Synthetic route for the formation of tin(II) *iso*-monothiocarbamate

4.2.3.1 Solution-based analysis of tin bis(*iso*-monothiocarbamate) compounds

The ^{1}H NMR spectrum for compound **18** contained two resonances for the O^{i}Pr substituent with a doublet at δ 0.97-0.99 ppm ($^{3}J_{H-H}$ = 6Hz) and a septet at δ 5.03-5.15 ppm ($^{3}J_{H-H}$ = 6Hz) along with a multiplet at δ 6.13-6.73ppm for the aromatic protons of the phenyl group. The $^{13}C\{^{1}H\}$ NMR spectrum contained resonances at δ 22.6, 23.0 and 77.0 ppm for the ^{i}Pr moiety and at δ 125.4, 125.8, 126.9, 129.8, 130.5 and 144.7 for the phenyl group. The resonance for the backbone N-C(S)-O carbon was much further downfield than those observed for ureate and iso-carbamate compounds with a resonance of δ 180.8 ppm. A considerable shift in the $^{119}Sn\{^{1}H\}$ NMR spectrum was also observed with the tin resonance 600 ppm downfield of those observed for the ureate and iso-carbamate compounds at δ 309 ppm.

For compound **19** the ^{1}H NMR spectrum contained two resonances for the iso-propyl substituent with a doublet at δ 1.05-1.07 ppm ($^{3}J_{H-H}$ = 6Hz) and a septet at δ 4.95-5.08 ppm ($^{3}J_{H-H}$ = 6Hz) with a singlet observed at δ 1.35 ppm that corresponded to the ^{t}Bu group. The $^{13}C\{^{1}H\}$ NMR spectrum contained three resonances corresponding to methyl groups at δ 22.9, 29.2 and 29.9 ppm, and a further two resonances at δ 55.8 ppm for the quaternary carbon of the ^{t}Bu group and δ 75.8 ppm for the methine carbon of the ^{i}Pr moiety. The carbon located in the NC(S)O backbone could not be observed in the $^{13}C\{^{1}H\}$ NMR spectrum, this could be due to a fast relaxation time which resulted in a weak signal for compound **18**. The $^{119}Sn\{^{1}H\}$ NMR spectrum contained a single resonance at 304 ppm, consistent with that observed for compound **18** and well downfield of the ureate and *iso*-carbamate resonances observed for compounds **1-4** and **8-17**.

The solution based analysis of compounds **18** and **19** indicated that the reactions between **5** and two equivalents of phenyl iso-thiocyanate and ^{t}Bu iso-thiocyanate proceed in a similar fashion to that observed for compounds **14-17** to produce homoleptic tin(II) compounds bound to two *iso*-monothiocarbamate ligands. This conclusion is primarily based on the presence of a single set of resonances for the ^{i}Pr moiety suggesting that there is a single ligand environment. Evidence of a different tin(II) binding environment is present in the $^{119}Sn\{^{1}H\}$ NMR spectra with resonances at δ 309 and 304 ppm, significantly downfield of the parent alkoxide **5** which has a single resonance at δ -220 ppm.

4.2.3.2 Molecular structures of tin(II) bis(iso-monothiocarbamate) compounds

While solution-based analysis of compounds **18** and **19** suggested that the compounds exist as homoleptic tin compounds bound to two *iso*-monothiocarbamate ligands, the nuclearity and binding geometry at the tin(II) centres could not be determined. The solid state structures for compounds **18** and **19** were, thus, confirmed using single crystal X-ray diffraction analysis. Table 4.9 details the collection parameters for the compounds, while selected bond lengths and angles can be found in Table 4.10. Compound **18** was found to be monoclinic crystallising in the space group $P2_1/c$ while **19** was found to be orthorhombic in the space *Pnaa*.

Table 4.9: Crystallographic parameters for compound 18 and 19

Compound	**18**	**19**
Empirical Formula	$C_{20}H_{24}N_2O_2S_2Sn$	$C_{16}H_{32}N_2O_2S_2Sn$
Crystal System	Monoclinic	Orthorhombic
Space Group	$P2_1/c$	*Pnaa*
Cell Constants		
a (Å)	8.48600(10)	11.2290(2)
b (Å)	25.3860(2)	11.5980(3)
c (Å)	10.12000(1)	34.0920(7)
α (°)	90	90
β (°)	91.7630(10)	90
γ (°)	90	90
Volume (Å^3)	2179.07(4)	4439.94(17)
Density (mg/m^3)	1.546	1.398
Z	4	8
Measured reflections	34752	36455
Unique reflections	6612	6549
R_{int}	0.0510	0.0528
R_1. w$R_2[I > 2\sigma(I)]$	0.0250, 0.0549	0.0338, 0.0672
***R* indices (all data)**	0.0337, 0.0580	0.0551, 0.0726

The structures of compounds **18** and **19** are shown in Figures 4.31 and 4.32. Both compounds were found to exist as monomeric systems with each tin(II) centre bound to two *iso*-monothiocarbamate ligands in a κ^2-N, S motif binding through the amido - N substituent and the thionyl sulphur atom. The tin(II) centre again displays a distorted square based pyramidal geometry with the stereochemically active lone pair situated at the apex of the pyramid. The distortion observed is comparable to that seen for the ureate systems and the dimeric and monomeric iso-carbamate compounds, with the amido-N substituent pushed out of the plane expected for a square based pyramidal structure. This reduces the steric interaction between the ligands bound to the tin(II) centre. Due to the location of the lone pair at the apex of the square based pyramid the two ligands are compressed toward each other, resulting in a 106.2° angle between the planes of the two *iso*-monothiocarbamate ligands for both **18** and **19**.

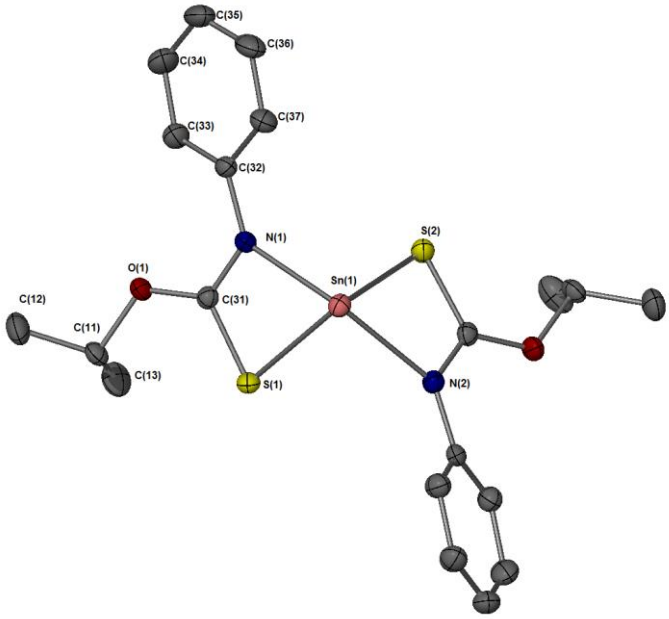

Figure 4.31: Crystal structure of compound 18. Ellipsoids shown at 50% probability, hydrogen atoms omitted for clarity.

As discussed with compounds **8-11** and **15-17** earlier the orientation of the OR group on the iso-carbamate is important to allow orbital overlap if electron delocalisation is to occur in the system. For compounds **18** and **19** the OR group is found to lie co-planar to the NCO backbone of the *iso*-monothiocarbamate ligand, allowing orbital overlap to occur and delocalisation of electrons across the backbone of the ligand system. This is reflected in the bond lengths observed for C(31)-O(1) which measure 1.336 to 1.341 Å, more than 0.1 Å shorter than the O(1)-C(11) bonds which measure 1.464-1.4768 Å.

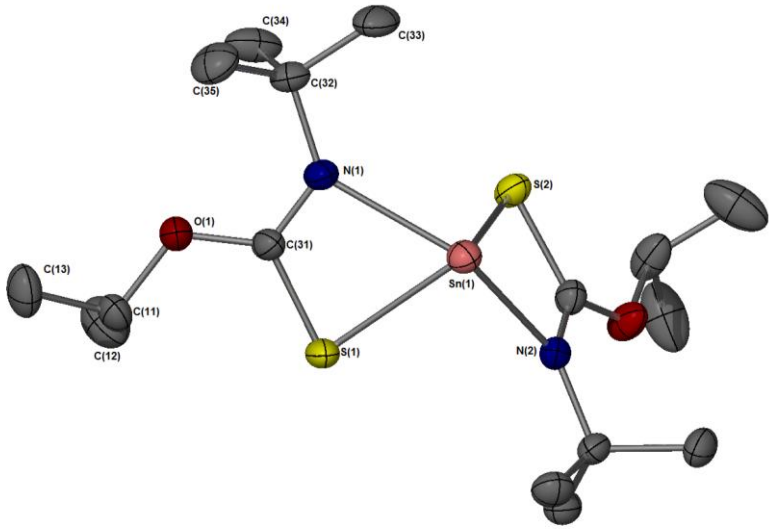

Figure 4.32: Crystal structure of compound 19. Ellipsoids shown at 50% probability, hydrogen atoms omitted for clarity.

For compounds **18** and **19** the Sn-N bond lengths are longer than those of the *iso*-carbamate ligands of **8-11** and **15-17** measuring 2.3651 - 2.3914 Å. For comparison the measured Sn-N bond lengths for **8-11** and **15-17** are 2.160-2.203 Å. The observed Sn-S bonds are also longer than the Sn-O bonds observed for the iso-carbamate ligands this can be readily attributed to the differences in bonding between sulphur and tin with the larger atomic radius of sulphur resulting in longer bonds. The Sn-S bond lengths observed for **18** and **19** are shorter that those observed for the tin(II) xanthate compounds $Sn(S_2COEt)_2$ and $Sn(S_2COMe)_2$ with the shortest Sn-S bond observed in the xanthates measuring 2.604 Å.[215,216] For comparison the longest Sn-S interaction observed for **18** is 2.5971(5) Å. It should be noted that the tin(II) xanthates have some variation in the Sn-S bond length due to anisobidentate chelation resulting in one long and one short interaction. This is also observed for tin(II) dithiocarbamate compounds, with the shorter Sn-S bonds found to be slightly shorter than compounds **18** and **19** at 2.568 Å.[217] The observed bond lengths for the *iso*-monothiocarbamate compounds are therefore found to be in between those observed for tin(II) xanthate and tin(II) dithiocarbamate compounds suggesting that the Sn-S interaction is stronger than xanthates, but slightly weaker than dithiocarbamate compounds. Given that both tin(II) xanthate and tin(II) dithiocarbamate compounds have been utilised as tin sulphide precursors, and the Sn-S bond length of the *iso*-monothiocarbamate compounds is comparable in length it would be feasible for compounds **18** and **19** to decompose to form tin sulphide.

Table 4.10: Selected bond lengths and angles for compounds 18 and 19

Selected bond lengths (Å)			Selected bond angles (°)		
	18	**19**		**18**	**19**
Sn(1)-N(1)	2.3786(13)	2.3914(17)	**N(1)-Sn(1)-N(2)**	128.68(5)	132.76(6)
Sn(1)-N(2)	2.3814(13)	2.3651(17)	**N(1)-Sn(1)-S(1)**	62.55(3)	62.87(4)
Sn(1)-S(1)	2.5906(4)	2.5773(6)	**N(1)-Sn(1)-S(2)**	83.46(3)	85.26(4)
Sn(1)-S(2)	2.5971(5)	2.5938(6)	**S(1)-Sn(1)-N(2)**	86.81(3)	87.01(4)
O(1)-C(31)	1.3363(18)	1.341(2)	**S(1)-C(31)-N(1)**	115.93(12)	116.93(16)
O(1)-C(11)	1.4768(19)	1.464(3)	**Sn(1)-S(1)-C(31)**	81.16(5)	81.00(7)
S(1)-C(31)	1.7382(16)	1.751(2)	**Sn(1)-N(1)-C(31)**	99.29(10)	98.78(12)
N(1)-C(31)	1.3004(19)	1.281(3)	**C(31-O(1)-C(11)**	120.17(13)	121.62(16)
N(1)-C(32)	1.415(2)	1.479(2)	**C(31)-N(1)-C(32)**	127.75(14)	125.27(18)

4.2.3.3 Evaluation of compound 19 as a potential CVD precursor by TGA

A sample of compound **19** was prepared and sent to SAFC Hi-Tech for analysis in the TGA. The TGA plot is shown in Figure 4.33 with the first derivative also shown. The TGA profile for compound **19** displays one main weight loss event with a slight shoulder. A sharp mass loss is observed at 105 °C which has a slight plateau at 140 °C before flattening out at 190 °C after a mass loss of 75%. There is a small secondary mass loss at 300 °C to 340 °C which accounts for a further 5% giving a residual mass of just 21%. This residual mass is lower than the mass calculated for tin metal (25.6%) which indicates that the compound could exhibit some volatility. Compound **19** was found to decompose at temperatures approximately 50 °C below that of the parent alkoxide **5** suggesting that the insertion reaction has an effect on the decomposition temperature and volatility of the compound.

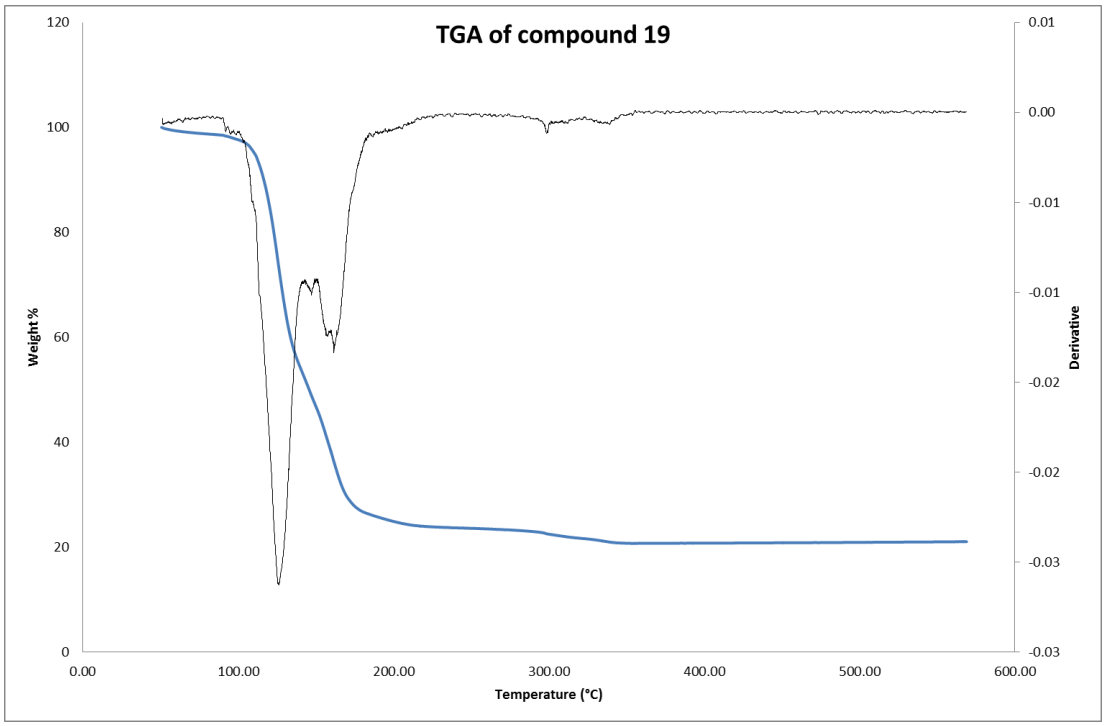

Figure 4.33: TGA of compound 19

As compound **19** contains sources for both sulphur and oxygen and the residual mass is much lower than that for tin metal attempts to determine the thermal decomposition product were unsuccessful. In order to carry out a bulk decomposition or CVD deposition study the synthesis of compound **19** was repeated, however it was found to be difficult to reproduce on a sufficiently large scale.

4.3 AACVD experiments using compound 15

Following evaluation of compounds **14**-**17** by TGA analysis compounds **15**, **16** and **17** were identified as potential CVD precursors based on the decomposition profiles observed; compounds **16** and **17** had low residual masses suggesting the compounds may exhibit some volatility and could be suitable for LPCVD studies however due to time constraints no deposition studies were carried out with these compounds. Compound **15** was selected for AACVD studies based on the residual mass observed in the TGA, which correlated with SnO_2 growth. Deposition studies were carried out using both a custom built hot-walled CVD reactor with the aerosol produced using a TSI generator and an EGS cold-walled CVD reactor with ultrasonic nebuliser used for aerosol generation (further details in Section 2.4.1).

4.3.1 AACVD of compound 15 using the EGS apparatus

For depositions carried out using the EGS apparatus a 0.1 M solution of compound **15** in toluene was prepared. Initial depositions were carried out on silicon wafers, glass microscope slides and plexiglass substrates at temperatures ranging from 150 °C to 400 °C. General deposition parameters are shown in Table 4.11. Deposited films had a slight yellow coloration which decreased in intensity as the deposition temperature was reduced. Samples showed strong adherence on glass substrates with minimal haze observed.

Table 4.11: Deposition parameters for AACVD experiments with 15 on EGS apparatus

Variable	Value
Precursor Concentration	0.1M
Substrate temperature	150-400 °C
Substrates	Glass slide, silicon wafer, plexiglass
Carrier gas flow rate (Argon)	1.5 L/min
Gas Flow Temperature	85 °C
Deposition Time	30-60 minutes

Film growth was observed at temperatures as low as 150 °C allowing preliminary studies into the deposition of tin oxide onto plastic substrates. The side arm of a pair of safety spectacles was selected for these initial studies and, while the plastic deformed slightly the deposition at 150 °C had a yellow hue suggesting that growth had been achieved (Figure 4.34).

Figure 4.34: Image of a film grown using compound 15 in the EGS reactor at 150°C on plastic.

4.3.1.1 Raman spectroscopy of depositions using 15 on the EGS apparatus

In an effort to ascertain the tin phases present in the films deposited using **15** the samples were analysed by Raman spectroscopy. Unlike depositions carried out previously using tin(II) ureate (Section 2.4) or tin(II) alkoxide (Section 3.3.3) systems, depositions carried out with **15** displayed no observable vibrations in the Raman spectrum when irradiated with either a red or green laser source. Further analysis was obtained through excitation using a 356 nm UV laser which did result in some features in the Raman spectrum. The Raman spectra of a thin film deposited on glass at 400°C is shown in Figure 4.35. Sharp resonances at 330, 1590 and 2330 cm^{-1} and a broad resonance between 430 and 780 cm^{-1} are observed, with the increasing intensity observed between 3000-3500cm^{-1} attributed to photoluminescence of the sample. The resonances at 1590 and 2330 cm^{-1} can be attributed to atmospheric oxygen and nitrogen respectively. Attempts to assign the resonances observed were unsuccessful with limited literature values for Raman spectra irradiated with this wavelength, and no reference material for tin species located.

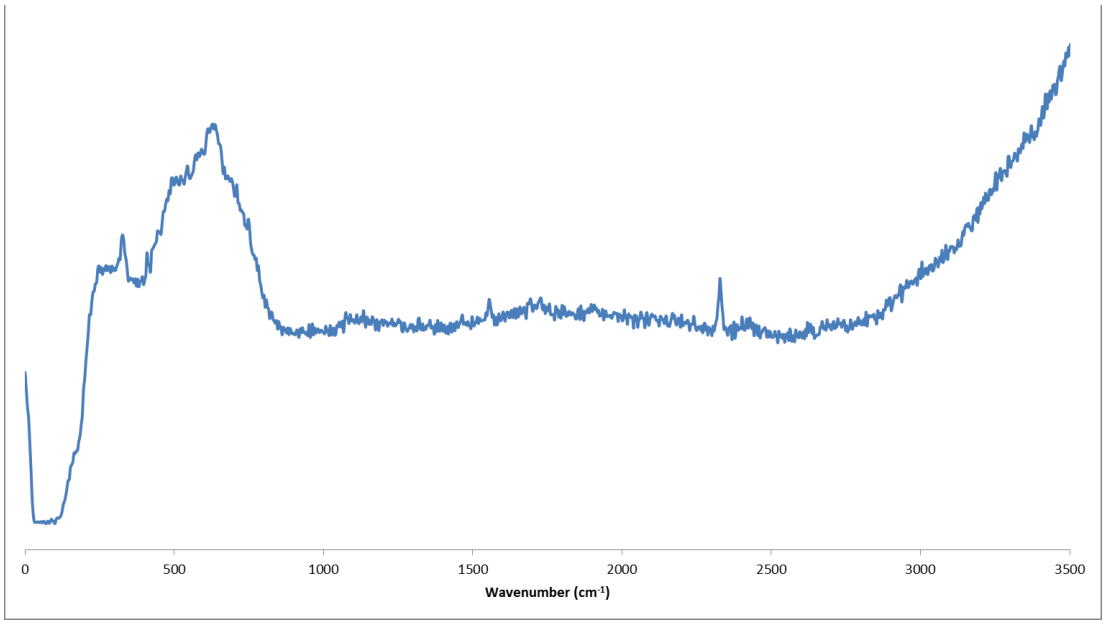

Figure 4.35: Raman spectrum of film grown at 400 °C on glass using compound 15

In order to rule out any spectral artefacts from the glass substrate analysis of a deposition on silicon at 400°C was carried out. The resultant spectrum had similar features, with sharp peaks at 330, 1590 and 2330 cm^{-1}, along with an additional sharp feature at 530cm^{-1} which corresponds to the silicon substrate within the broad vibration from 430-780cm^{-1} (Figure 4.36).

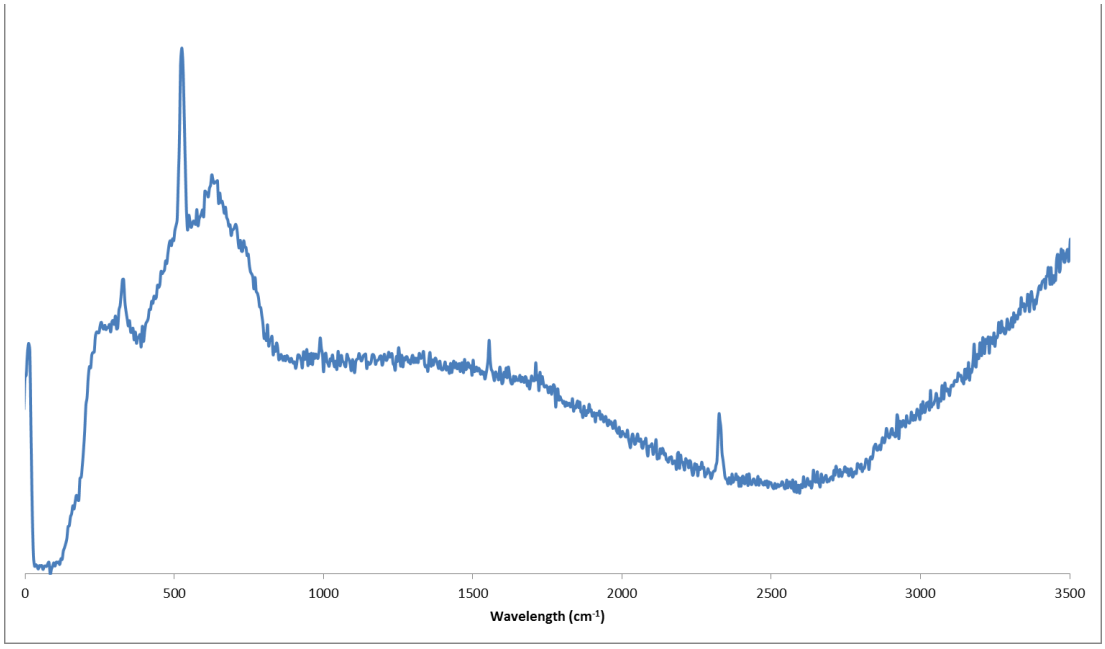

Figure 4.36: Raman spectrum of sample grown at 400 °C on silicon using compound 15

4.3.1.2 X-ray diffraction analysis

Further analysis of the films grown using compound **15** was conducted through X-ray diffraction. Samples grown on glass at 400 °C and 200 °C were analysed and are shown in Figure 4.37. The sample grown at 200 °C has no observable maxima suggesting an amorphous or microcrystalline sample. At a higher deposition temperature of 400 °C, however, two diffraction peaks are observed at 33.9 and 36.9°. The reflection at 33.9° can be attributed to the (101) Miller index for SnO_2, while the peak at 36.9° can be attributed to the (111) plane for SnO suggesting that a mixture of both SnO and SnO_2 has been deposited. Considering the elevated deposition temperature this could be due to disproportionation of SnO to SnO_2, with the intermediate Sn_2O_3 or Sn_3O_4 phases and the expected tin metal not observed. The deposition of both SnO_2 and SnO could occur due to incomplete oxidation of the precursor during the process and, given the residual mass information obtained from the TGA analysis suggested that SnO_2 was the major product; the incomplete oxidation could be due to the faster heating of the precursor that occurs during the CVD process.

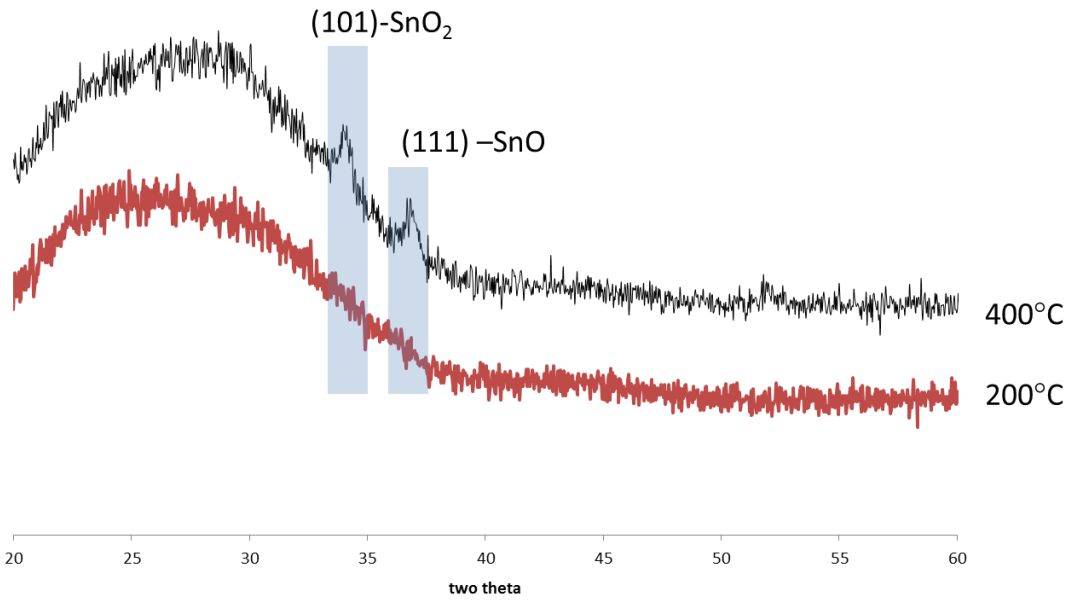

Figure 4.37: XRD patterns for films grown using compound 15 at 400 °C and 200 °C

Analysis of samples grown on silicon at 200 °C and 400 °C was also undertaken to remove the noise associated with glass substrates. The patterns are shown in Figure 4.38. Both samples display a sharp reflection at 33.1° which is attributed to an impurity in the silicon wafer. The sample at grown at 200 °C shows no reflections and is therefore either

microcrystalline or an amorphous deposition. The sample grown at 400 °C has three broad resonances which correspond to the (111), (101) and (211) Miller indices of SnO_2. Unlike the samples grown on glass there is no evidence of crystalline SnO in the X-ray diffraction patterns suggesting that the precursor was successfully oxidised from tin(II) to tin(IV) during the deposition process. This is consistent with the TGA analysis of compound **15** and has previously been observed for tin(II) compounds by Maruyama and Gielbelhaus. [149,155]

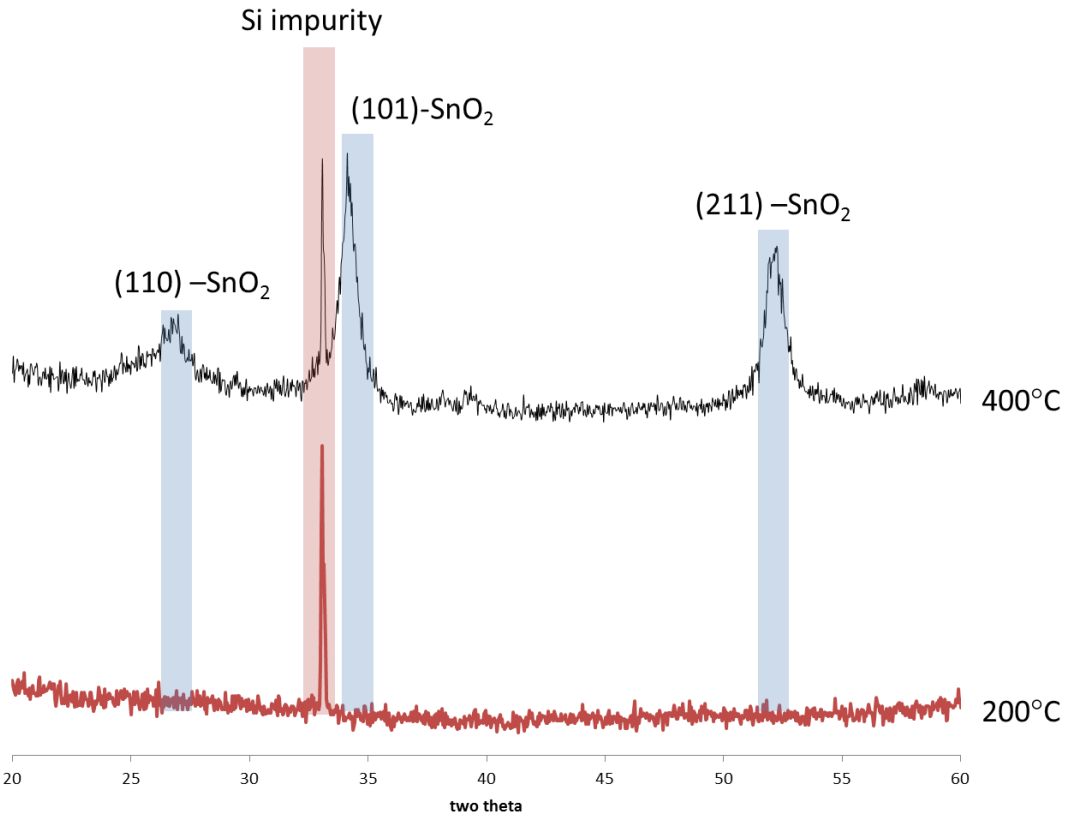

Figure 4.38: XRD patterns for films grown on silicon using compound 15 at 200°C and 400°C

Analysis of films grown using compound **15** showed that on glass substrates the deposited films either exhibit no crystalline phases or the presence of a mixture of SnO and SnO_2. Tin metal was not detected at 400 °C, which would be indicative of thermal disproportionation of SnO to SnO_2 and therefore the presence of both tin oxide materials maybe a result of partial oxidation of the tin(II) centre to tin(IV). Analysis of the depositions carried out on silicon substrates at 400°C have reflections for only SnO_2 suggesting that complete oxidation has occurred at this point.

4.3.1.3 XPS analysis of film grown using compound 15

In order to investigate the tin species were present in films deposited on glass substrates a sample grown using compound **15** at 350°C was sent to Newcastle University for XPS analysis at the NEXUS facility. As discussed in Section 2.4.7 XPS is a useful technique as it provides environmental and oxidation state information about the elements present in a sample. Initial compositional analysis confirmed that the films grown using compound **15** were thin or non-continuous, with silicon and other glass components detected before etching. The tin concentration (1.4%) was also low before etching; rising to 1.86% after etching. Analysis of the Sn 3d region shows two signals corresponding to the Sn 3d 3/2 and Sn 3d 5/2 regions of the XPS spectra at 486.45 eV and 494.88 eV. A third signal at 497.13 eV was also present, which did not match any previous reports for tin. After etching, the intensity of this third peak was enhanced while the signals observed for the Sn 3d 3/2 and Sn 3d 5/2 are found to shift slightly to 486.12 eV and 494.66 eV respectively (Figure 4.39).

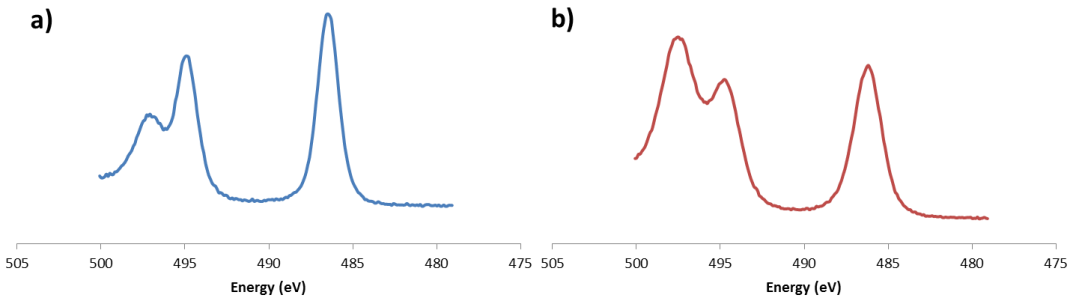

Figure 4.39: XPS spectra for sample grown on glass at 350 °C using compound 15 a) before etch b) after 20 second etch

A better understanding of the oxidation state of the tin detected in the Sn 3d region may be obtained through analysis of the valence band region of the XPS spectrum. As discussed in Section 2.4.7 there is a distinct difference between SnO and SnO_2 in the valence band; example spectra are shown below in Figure 4.40. The shape and low energy of the VB suggest that SnO is the dominant oxide present both before and after etching of the sample; the presence of SnO was detected in the XRD pattern at 400°C and therefore is not unexpected. The lack of evidence of SnO_2 could be attributed to the lower deposition temperature for this sample when compared to the XRD data.

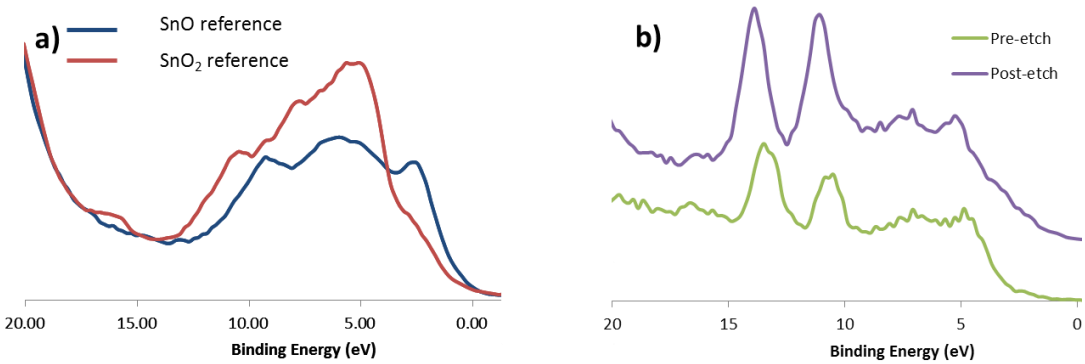

Figure 4.40: XPS data for a) reference spectra for SnO and SnO_2 b) Pre and post etch valence band region for deposition at 350°C using compound 15

4.3.2 AACVD of compound 15 using the TSI apparatus

Further deposition studies using compound **15** were carried out using the hot-walled CVD reactor and the TSI aerosol generator. Depositions were carried out using a 0.03M solution of **15** in toluene or THF on glass substrates at temperatures ranging from 200 to 400°C; further deposition parameters are shown in Table 4.12. A second series of depositions was also carried out with 5 mol% of $N(^nBu)_4.F$ as a 1M THF solution added as fluorine source, with the aim of depositing FTO from the solution at temperatures ranging from 125 to 400°C. The films deposited had a pale yellow colouration that became stronger at higher deposition temperatures, and the films showed minimal haze and good adherence to the substrate. Depositions at temperatures as low as 125°C were observed at run times of 1h, some 25°C lower than found in the EGS apparatus for the same deposition time.

Table 4.12: Deposition parameters for AACVD of compound 15

Variable	Value	
Precursor concentration	0.03M	0.03M +5mol% $N(^nBu)_4.F$
Solvent	Toluene, THF	Toluene
Substrate temperature	200-400°C	1025-400°C
Substrate	Glass slide	Glass slide
Carrier gas flow rate (Argon)	3.0L/min	3.0L/min
Deposition time	30-60 minutes	30-60 minutes

Depositions using the hot walled CVD reactor resulted in films with a stronger yellow - yellow brown colour than those carried out on the EGS apparatus. As discussed in Sections 2.5 and 3.3.3 this colouration has been linked to the deposition of SnO thin films, rather than SnO_2.

Attempts to reduce the colouration observed included annealing the samples post deposition in a flow of nitrogen containing 10% oxygen. The anneal process was carried out at for 1h using the cold walled EGS apparatus, which allowed the controlled introduction of oxygen at the same temperature of deposition. This resulted in the reduction in the yellow colour, with films becoming more transparent whilst staying adherent and with no observed impact on the haze of the thin films.

4.3.2.1 Raman spectroscopy

In an effort to ascertain the oxidation state of the tin species present in the deposited films, Raman spectroscopy was utilised as SnO and SnO_2 have different Raman spectra. Thin films grown using compound **15** in conjunction with $N(^nBu)_4.F$ were analysed, with samples grown at temperatures above 400 °C having Raman spectra that indicated the presence of SnO exclusively. A spectrum for a thin film grown using compound **15** with $N(^nBu)_4.F$ at 250°C is shown in Figure 4.41, with the two resonances at 109 and 209cm^{-1} corresponding to the B_{1g} and A_{1g} modes of SnO respectively.

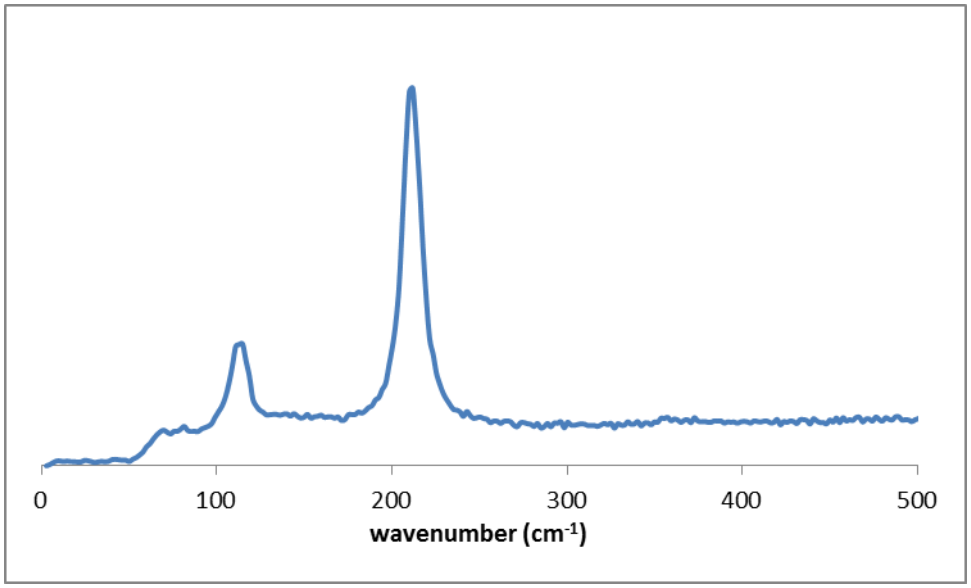

Figure 4.41: Raman spectrum of film deposited using compound 15 and $N(^nBu)_4.F$ at 400°C.

At temperatures below 250 °C the Raman spectrum became more difficult to interpret, possibly due to the resonances observed for the substrate. Figure 4.42 is the Raman spectrum for a deposition at 150 °C. The resonance at 145cm^{-1} is similar to resonances calculated for SnO_2 B_{1u} mode and observed for Sn_2O_3.[185,218] Due to the ambiguity of which phase this vibration represents, it is difficult to state that the Raman spectra of the low temperature depositions show a particular tin phase.

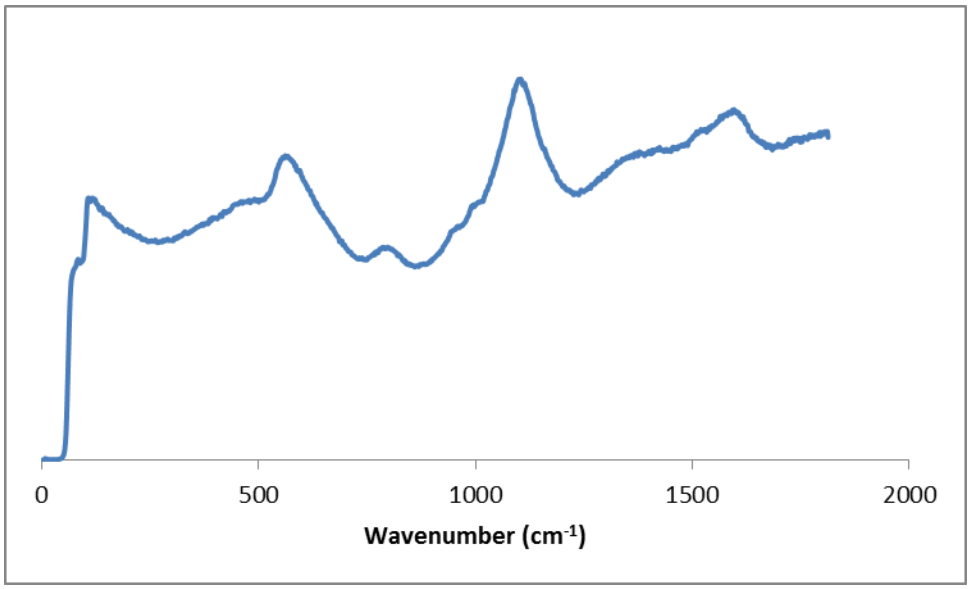

Figure 4.42: Raman spectrum of film deposited using compound 15 and $N(^nBu)_4.F$ at 150 °C.

Depositions of compound **15** on the EGS apparatus provided Raman spectra that also showed ambiguity of the precise nature of the tin material deposited. It should be noted that at higher temperature depositions there was no Raman data to indicate that SnO was present in the deposited thin films when the EGS apparatus was utilised. Although the potential presence of different phases at different deposition temperatures could be a result of the involvement of two different and competing decomposition pathways there is no data on the decomposition products for compound **15** at either low or elevated temperatures to support this.

Analysis of the annealed thin films by Raman spectroscopy did not yield any conclusive results either. Raman spectra of the thin films using visible light excitation, particularly the 532 nm laser, resulted in spectra that showed limited or no vibrations. The poor spectra were attributed to the thin nature of the films, with any tin based material masked by the glass slide baseline. In order to combat this effect, excitation was attempted using a UV 346 nm laser as an excitation source which has a weaker surface penetration and therefore could reduce the effect of the substrate. An example spectrum, shown in Figure 4.43, was taken from a deposition at 300 °C that was annealed for 1h at the same temperature. The Raman spectrum clearly shows several vibrational modes between 240 and 750 cm^{-1} along with two sharp resonances at 1590 and 2330 cm^{-1}, which can be attributed to CO_2 and N_2, before the sample is observed to fluoresce above 3000 cm^{-1}. It was not possible to fully interpret this part of the spectrum, and it may contain vibration assignable to several different tin containing species. The main Raman active modes of SnO_2 are expected between 100 and

780 cm^{-1} according to Katiyar and co-workers[185] however the active modes for SnO, Sn_2O_3 and Sn_3O_4 are also found in this area according to Diebold and co-workers.[29]

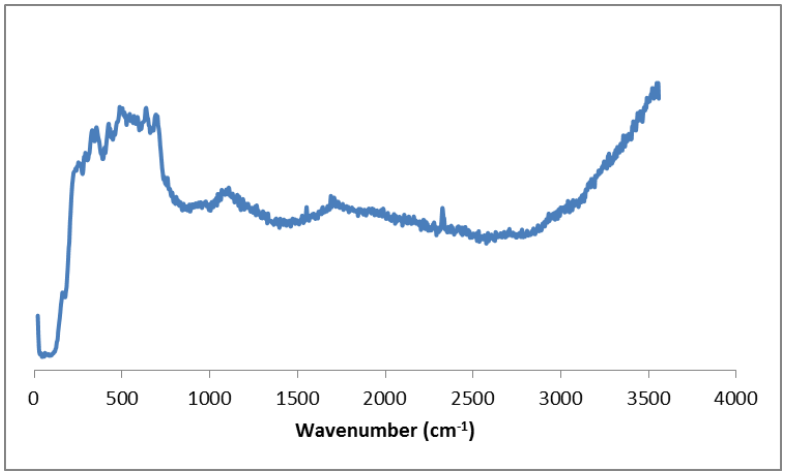

Figure 4.43: Raman spectrum of film deposited using compound 15 and $N(^nBu)_4.F$ at 300 °C and annealed in 10% oxygen for 1h at 300 °C.

4.3.2.2 X-ray diffraction analysis

To obtain further information into the composition of the thin films deposited using compound **15** samples were also analysed by X-ray diffraction analysis. The diffraction pattern of a thin film grown at 300 °C using compound **15** from a toluene solution is shown in Figure 4.44. The diffraction pattern shows a single peak that can be indexed to the (101) orientation of SnO.

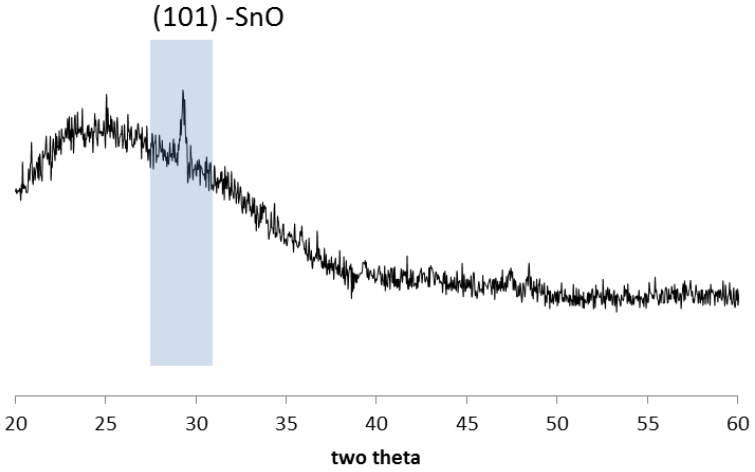

Figure 4.44: Powder diffraction pattern of film deposited at 300 °C using compound 15 in toluene.

In comparison the diffraction pattern for a deposition at the same temperature from a THF solution of compound **15** is shown in Figure 4.45. The pattern has reflections that can be attributed to both SnO (101) and (111) orientations, but also the (101) diffraction line for tin metal. This suggests that rather than oxidation of the tin(II) centre, there is possible disproportionation of SnO to tin metal and SnO_2 with the tin dioxide not exhibiting any crystalline properties. Alternatively the thermal decomposition has resulted in the reduction of the tin(II) centre to tin metal. This was not observed when depositions were carried out in the EGS apparatus; in fact the opposite was observed with the tin(II) centre showing some oxidation to SnO_2.

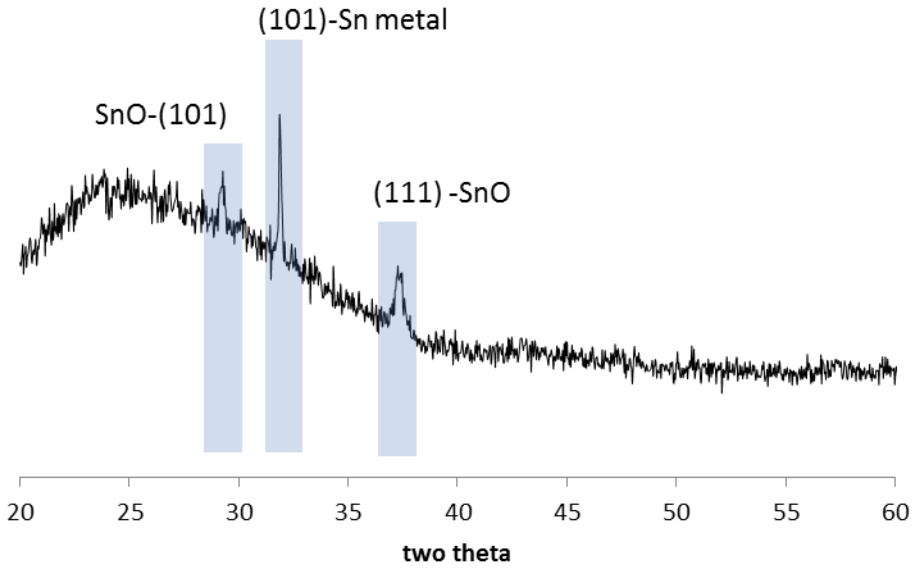

Figure 4.45: Powder diffraction pattern of film deposited at 300 °C using compound 15 in THF.

Depositions carried out using a mixture of toluene and THF were also carried out to determine if inclusion of small quantities of THF would have an impact on the deposition of compound **15**. Depositions were carried out with 20% of the toluene replaced with THF; the diffraction pattern for the deposition at 350 °C is shown in Figure 4.46. The resulting material does not have any diffraction peaks associated with tin metal, unlike depositions carried out in just THF. The orientation of the SnO deposited does seem to be affected by the presence of THF with a strong reflection in the (111) orientation and a very weak reflection in the (101). In contrast the (101) was the only observed reflection when deposition was carried out in just toluene.

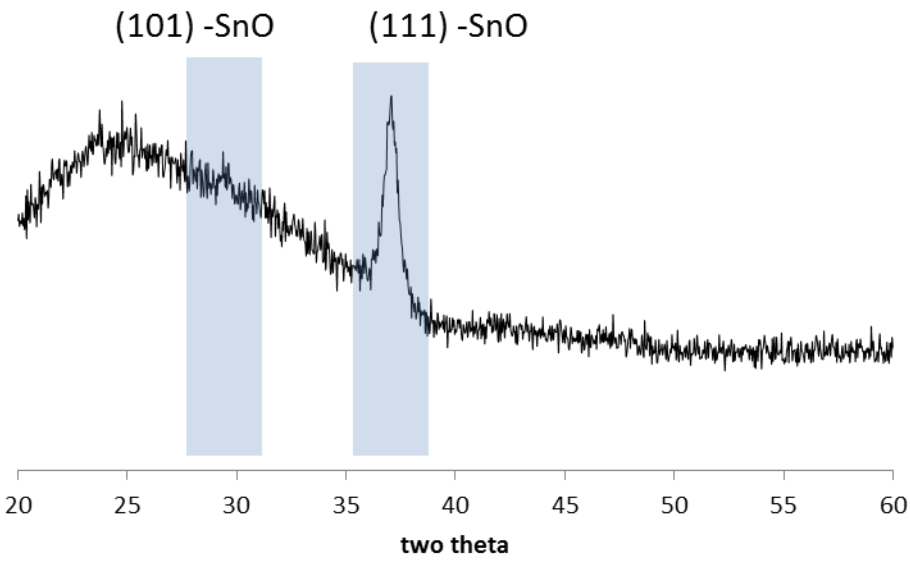

Figure 4.46: Powder diffraction pattern of film deposited at 350 °C using compound 15 in toluene / THF mixture.

For depositions carried out using a combination of compound **15** and 5 mol% N(nBu)4.F in toluene, diffraction patterns contained reflections that corresponded solely to SnO at temperatures between 200 and 350 °C. Depositions at temperatures lower than this resulted in amorphous or microcrystalline material with no observed maxima in the X-ray diffraction analysis. A diffraction pattern of a film grown at 300°C is shown in Figure 4.47. The three reflections have been indexed to SnO with the (001), (101) and (111) reflections observed. This is comparable to both the alkoxide depositions detailed in Section 3.3 and the depositions using ureate **3** using the TSI apparatus is Section 2.5.

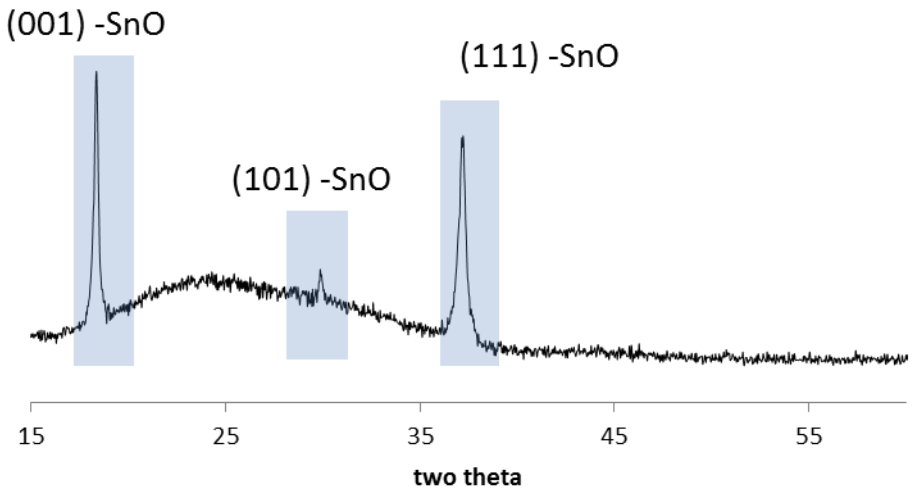

Figure 4.47: Powder diffraction pattern of film deposited at 300 °C using compound 15 and $N(^nBu)_4F$ in toluene.

4.3.2.3 XPS analysis

Attempts to analyse the thin films grown using compound **15** with 5 mol% of N(nBu)4.F using energy dispersive spectroscopy (EDS) in the scanning electron microscope (SEM) were unsuccessful due to the charging of the samples. To obtain information on the potential inclusion of fluorine in the deposited thin films and to try and gather more information on the oxidation state of the tin samples of the thin films, both before and after annealing, were sent to Newcastle University's NEXUS facility for XPS analysis.

For the thin film grown at 400 °C the XPS data showed that fluorine inclusion had been achieved with fluorine detected in the films after deposition and after annealing. Due to the film thickness or a high defect level, quantitative analysis of the fluorine content was not possible as signals corresponding to the glass substrate were also observed in the XPS spectrum. Figure 4.48 shows the F1s region of the XPS spectrum for the annealed sample. The carbon content was also particularly high even after etching the thin films which suggests carbon contamination throughout the film; - although due to the thin nature of the films this could be external contamination.

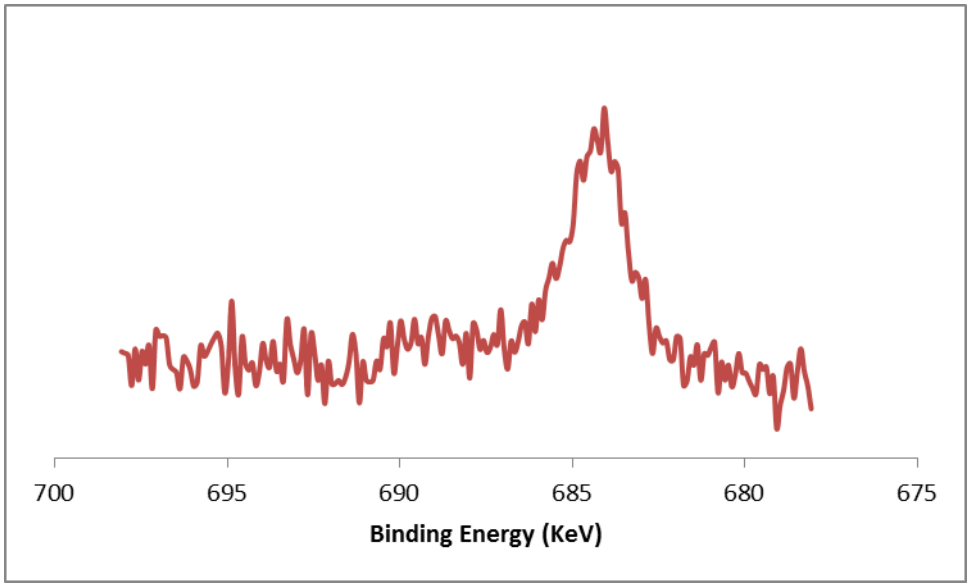

Figure 4.48: XPS spectrum of the F 1s region taken after 40 second etch on a sample deposited at 400 °C using compound 15 and 5 mol% $N(^{n}Bu)_4.F$

In order to determine the oxidation state of the tin present in the thin films the valence band region was analysed, with the spectra shown in Figure 4.49. Unlike with previous samples it was more difficult to determine the oxidation state of the tin due to the presence of both SnO and SnO_2 in the pre-annealed sample resulting in a spectrum that has features for both

oxidation states. After annealing the sample displayed a peak shape much more characteristic of SnO_2.

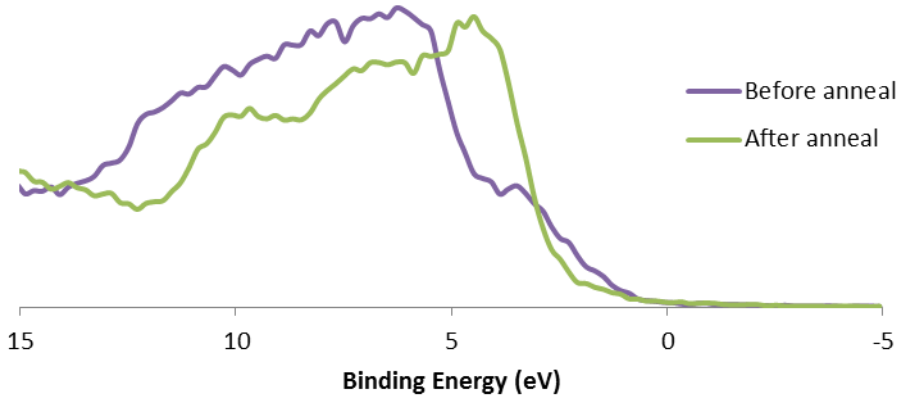

Figure 4.49: XPS spectra of the valence band region for samples deposited at 400 °C using compound 15 and 5 mol% $N(^nBu)_4F$ before and after 1h anneal.

4.4 Conclusions

The reaction of tin(II) alkoxides with different heterocumulene compounds has resulted in synthetic routes towards potential tin oxide and tin sulphide CVD precursor compounds. Initial experiments investigating the feasibility of forming tin(II) carbonate compounds through the insertion reaction of CO_2 into tin alkoxide bonds highlighted the facile nature of the reaction with the carbonate species existing in equilibrium with the parent alkoxide and free CO_2. Investigation of the reaction between **5** and CO_2 using EXSY NMR experiments allowed the gathering of some kinetic data for the transition state which was in close agreement with the $\Delta H°$ and $\Delta S°$ values reported for a similar reaction by Fulton and co-workers although a direct comparison is not suitable given the different measurement techniques used to calculate the equilibrium constants and therefore the physical parameters. Work by Johnson and co-workers calculated $\Delta H^{\neq}$ to be 48.2 ±18 kJ mol^{-1} for the reversible insertion of bis-tertiarybutyl carbodiimide into lithium dimethlyamide (Figure 4.50) using the same technique.[219] This is lower than the $\Delta H^{\neq}$ values calculated for **5** with CO_2 (67.99 kJ mol^{-1}), but given the lack of bulk around the lithium centre in comparison to the tin centre in **5** a lower $\Delta H^{\neq}$ would be expected.

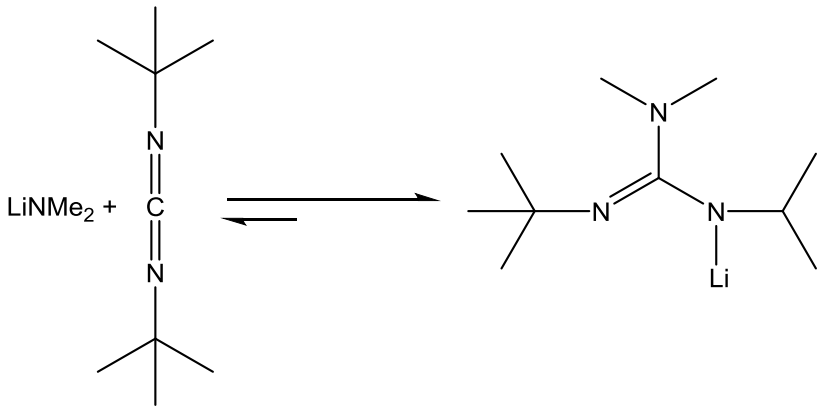

Figure 4.50: Reversible formation of a lithium guanidinate system.

The reactions between **5** and **LXXXII** with ^{t}BuNCO were also found to exist in equilibrium between the iso-carbamate and the parent alkoxide and isocyanate. The kinetic information gathered on these reversible processes through variable temperature EXSY NMR experiments revealed that the two processes had significantly different activation energies with the bulkier **LXXXII** having an activation energy equivalent to a third of the smaller compound **5** (33.7 kJ mol^{-1} and 92.2 kJ mol^{-1} respectively). It is postulated that the difference is a result of the nuclearity of the parent alkoxides with **5** known to exist in the solid state as

a polymer, while **LXXXII** is dimeric in the solid state; for the solution phase this is backed by ^{119}Sn NMR resonances that indicate the tin centres are subjected to different environments with **LXXXII** observed at δ -99 ppm and **5** at δ -220 ppm. This is also backed with the $\Delta S^{\neq}$ values with the reaction between **5** and ^{t}BuNCO having a small positive $\Delta S^{\neq}$ (12.61 J mol^{-1} K^{-1}) indicative of the transition state being less ordered than the reactants. This would be consistent with a polymeric solution structure for **5** which would break up into shorter oligomeric or dimeric units upon reaction with the isocyanate. For the reaction between **LXXXII** and tBuNCO $\Delta S^{\neq}$ is much smaller (-176.1 J mol^{-1} K^{-1}); consistent with the **LXXXII** dimer remaining intact, and the transition state involving the association and insertion of the ^{t}BuNCO.

The reaction of aromatic isocyanates with **5** and **LXXXII** resulted in the formation of the dimeric iso-carbamate compounds **8-11**; all four compounds existed as alkoxide bridged dimers with terminal iso-carbamate ligands when analysed in the solid state. The iso-carbamate ligands were arranged in a transoid arrangement across the molecule with the bulky NR constituents located on opposite sides of the molecule. This trend was also observed for the ureate compounds **1-3**, and can be attributed to reducing the steric interactions within the molecule. Solution based analysis of compounds **8-10** through ^{119}Sn{^{1}H} NMR resulted in resonances ranging from δ -315 to -347ppm. These are consistent with the ^{119}Sn{^{1}H} NMR resonances reported in the literature for tin(II) bis-amidinates (δ -255 to -397 ppm)[177–180], tin (II) bis-guanidinates (δ -377 to -432 ppm)[103] and the tin(II) bis ureate compounds **1-4** in Chapter 2 (δ -307 to -357 ppm). The binding environment for the tin iso-carbamates is different to that expected for the bis-amidinate, bis-guanidinate and bis-ureate systems with only one κ^2 - ligand bound to the tin centre, this is offset by the bridging alkoxide groups which results in a similar electronic environment and comparable electron donation into the tin(II) centre.

The reaction of alkyl isocyanates (other than ^{t}BuNCO) with **5** and **LXXXII** also resulted in the formation of tin(II) iso-carbamate compounds; however these did not have bridging alkoxide groups and instead were found to exist as monomeric bis iso-carbamate systems **14-17**. The solid state structures of compounds **14-17** were found to be directly comparable to the ureate compounds **1-4** with a central tin atom bound to two iso-carbamate ligands in a square based pyramidal geometry with the stereochemcially active lone pair of the tin located at the apex. The iso-carbamate ligands were orientated transoid to each other allowing the bulky NR groups to be on opposite sides of the molecule. The ^{119}Sn{^{1}H} NMR spectra contained single resonances between δ -335 and 360 ppm which is in agreement with analogous systems in the literature such as tin(II) bis-amidinates (δ -255 to -397 ppm)[177–180],

tin (II) bis-guanidinates (δ -377 to -432 ppm)[103] and the tin(II) bis ureate compounds **1**-**4** in Chapter 2 (δ -307 to -357 ppm).

In comparison the reaction of **5** with iso-thiocyanates resulted in the formation of homoleptic tin(II) bis-monothiocarbamate compounds **18** and **19** regardless of whether the R group was aromatic or alkyl. Compounds **18** and **19** had structures comparable to the bis-ureate compounds **1-4** and the iso-carbamate compounds **14-17** with two mono-thio carbamate ligands bound to a four-coordinate tin(II) centre in a square based pyramidal geometry via a κ^2 N, S binding motif. The $^{119}Sn\{^1H\}$ NMR spectra contained single resonances at δ 309 and 304 ppm for **18** and **19** respectively. These are significantly downfield of the resonances observed for the iso-carbamate compounds **8-17** which were situated between δ -315 and -360 ppm and can be explained by the direct interaction between the tin centre and the sulphur atoms on the mono-thiocarbamate ligand.

Evaluation of compounds **14-17** by TGA as potential CVD precursors showed that compounds **15**, **16** and **17** all exhibited properties that would make them candidates for deposition studies. Compound **14** was found to have a long decomposition pathway that included multiple mass loss events between 60 °C and 290 °C. The large decomposition window and the presence of multiple mass loss events suggested the compound was not a suitable CVD precursor although the low residual mass (10%) indicates the compound may have some volatility. In comparison compounds **16** and **17** showed much sharper decompositions between 80-245 °C and 60-265 °C respectively, although both contained shoulders in the decomposition approximately 40 °C before finishing. Both compounds **16** and **17** had residual masses lower than that expected for tin metal, this is indicative of some volatility. For compound **15** a single mass loss event was observed between 55 °C and 140 °C with a residual mass that correlated with SnO_2 observed. The low decomposition temperature, and the residual mass correlating to SnO_2 resulted in compound **15** been taken forward for AA-CVD studies. For comparison the tin(II) bis ureate **3** had decomposition profile that began at 90 °C and finished at 180 °C, this is approximately 40 °C higher than that observed for **15.**

Deposition studies were carried out using **15** on both the hot-walled and cold-walled reactor systems. The AA-CVD experiments using **15** in toluene on the EGS cold walled reactor resulted in the deposition of mixed valence tin oxide, with the XRD patterns containing diffraction peaks that corresponded to both SnO and SnO_2 at deposition temperatures in excess of 350°C. Depositions at lower temperatures contained no observable diffraction lines. This mixed valence deposition is comparable to the depositions reported in the literature for the **LV** using LPCVD apparatus,[153] although Boyle and co-workers also

identified the presence of tin metal. The presence of SnO_2, SnO and tin metal is in keeping with the disproportionation of SnO at elevated temperatures. As the depositions carried out with **15** did not contain any detectable tin metal the presence of SnO_2 could be due to oxidation of the tin(II) centre as part of the decomposition pathway of the compound. As previously discussed the potential for a tin(II) system to be oxidised during deposition has been reported by Maruyama and Gielbelhaus, [149,155] the TGA data for **15** also suggested that SnO_2 was the product, and therefore the presence of SnO in the XRD could be attributed to incomplete oxidation of the tin centre. Interrogation of the Raman spectra for depositions between 150 °C and 400 °C was inconclusive with the vibrations associated with SnO_2 not clearly present in the spectrum, however analysis of the XPS valence band region gave a strong indication that tin(IV) was the dominant oxidation state in the thin films.

On transfer to the hot walled reactor utilising the TSI aerosol generator the only tin oxide detected at 300-400 °C was SnO, this was confirmed through Raman spectroscopy and XRD analysis. The change from cold to hot-walled reactor was found to have a significant effect on the morphology and deposition parameters of the tin(II) alkoxides investigated in Chapter 3. The lack of oxidation of the tin(II) centre of compound **15** when the hot-walled reactor was utilised is indicative of a change of decomposition mechanism. Furthermore, depositions at 400°C utilising THF as a solvent, or on silicon substrates also showed the presence of tin metal in the PXRD analysis, suggesting that the tin centre was reduced rather than oxidised during these experiments. Given that that tin(II) oxide is prone to disproportionation to tin metal and tin(IV) oxide at elevated temperatures this may be the more likely mechanism - although there was no crystalline SnO_2 detected in the PXRD and the Raman spectra did not show the presence of SnO_2. The likelihood of disproportionation was strengthened when the samples were analysed by XPS, which showed that although the predominant product was SnO, SnO_2 was also present in the bulk of the sample.

In conclusion, the work presented in this chapter has shown that the reaction of tin(II) alkoxides **5** and **LXXXII** with isocyanates results in the formation of tin(II) iso-carbamate compounds. Further to this, compound **15** has been evaluated as a potential CVD precursor using AA-CVD resulting in the formation of tin oxide thin films between 150°C and 400 °C. The type of AA-CVD reactor used in these experiments is found to have a direct influence on the oxidation state of the tin oxide thin film grown, with the cold-walled reactor resulting in the formation of SnO_2 thin films, while a hot-walled reactor results in the growth of SnO thin films.

5. Conclusions and further work

5.1 Conclusions

The original aim of this project was to develop new precursors for the low temperature formation of tin oxide thin films by chemical vapour deposition. To achieve this the design rationale was to synthesise and characterise tin(II) precursors with a chemical structure analogous to the low temperature tin sulphide precursors, tin xanthates and tin dithiocarbamates, that have previously been studied. Figure 5.1 summarises some of different tin compounds that were synthesised as part of this research; the four main types of compound looked at were tin(II) bis-ureates (**1**-**4**), tin(II) iso-carbamates (**8**-**17**), attempts to make tin(II) carbonates and tin(II) alkoxide compounds (**5**-**7**).

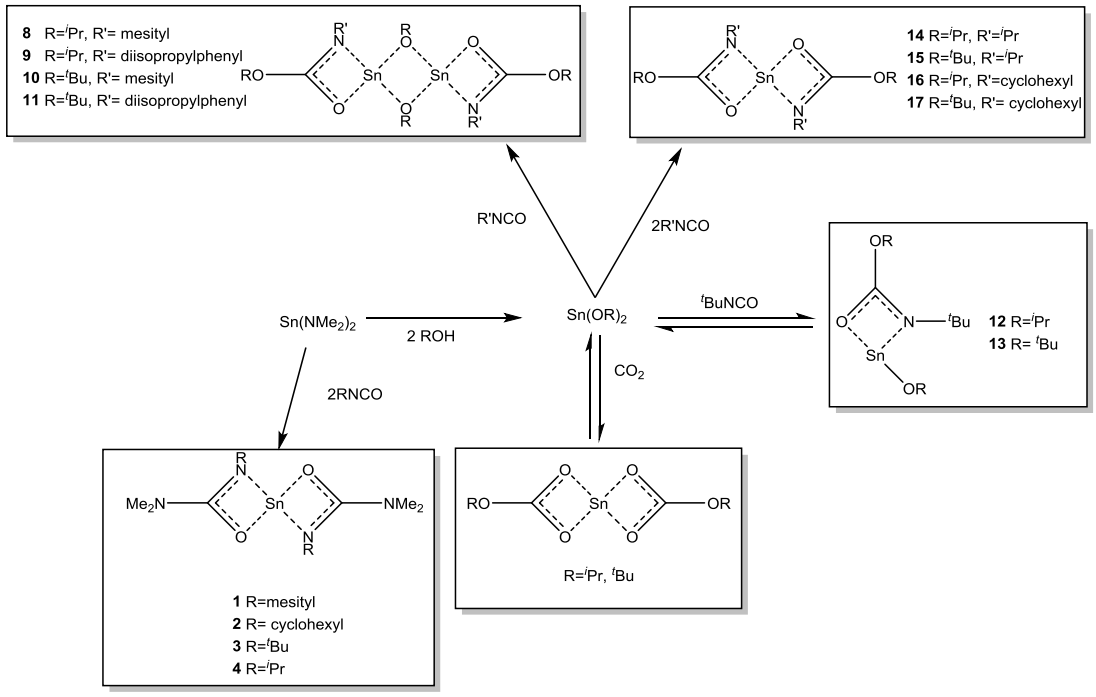

Figure 5.1: Reaction scheme of some of the compounds described in the thesis

The tin(II) bis-ureate and bis iso-carbamate compounds were found to contain tin environments that closely matched those for previously reported tin(II) bis-amidinate and guanindate compounds. The ureate compounds **1**-**4** had $^{119}Sn\{^{1}H\}$ NMR chemical shifts between δ -307 and -357 ppm, the bis iso-carbamate compounds **14**-**17** had shifts between δ -335 and -360 ppm; the chemical shifts observed in the literature for bis amidinate and guanidinate compounds range from δ -255 to -397 ppm[177–180] and δ -377 to -432 ppm[103]

respectively. Furthermore the geometries of the solid state structures for these compounds were also similar with the compounds adopting a square based pyramidal structure with a central tin atom; the stereochemically active lone pair of the tin was located at the apex of this structure. The ligands adopted a transoid configuration across the compounds with the sterically bulky NR groups located on opposite sides of the compound to minimise strain in the system for all of the bis-ureate and bis iso-carbamate compounds except for compound **3**. Interestingly compound **3** adopted a unique solid state structure with one ligand binding in a κ^2 N, O fashion and one κ^2 N, N' orientation. The κ^2 N, N' binding motif has been observed previously for a Pt ureate complex **LXXX,** however this is the only tin species found to bound in this manner so far.

Prior to deposition studies compounds were subjected to an initial evaluation via thermogravimetric analysis. To ensure that the insertion reactions and subsequent formation of the tin ureate and iso-carbamate compounds did not result in the formation of a precursor that exhibited lower volatility or poorer decomposition profile the TGA data was compared to the parent alkoxide or amide. It was found that the reaction of the tin(II) amide or alkoxide with an isocyanate resulted in a reduction in the onset temperature for thermal decomposition and furthermore was found to have a direct effect on the residual mass after decomposition. An example of this is shown in figure 5.2 for compound **16** and the parent alkoxide **5**.

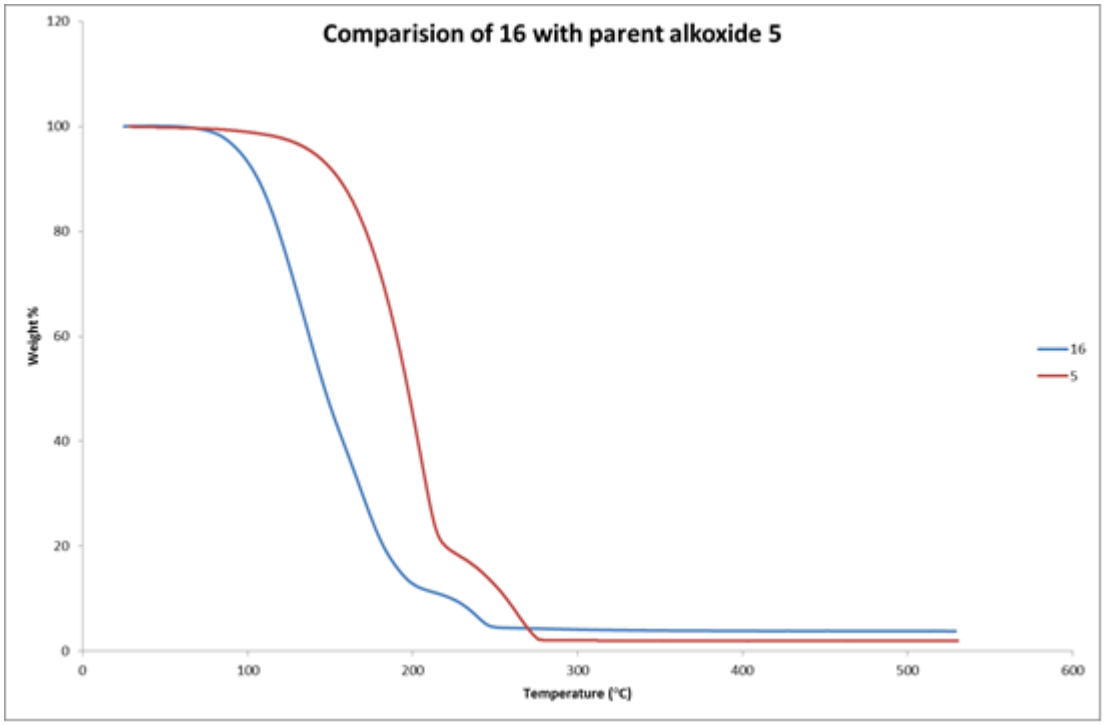

Figure 5.2: TGA data for compound 16 displayed alongside the parent alkoxide 5

As discussed earlier, the compounds described above were synthesised with the aim of utilising these in CVD experiments for the growth of metal oxide thin films. Deposition studies were carried out using compounds **3**, **5**, **7**, **LXXXII** and **15** using two different aerosol-assisted CVD apparatus (see section 2.4.1). Aerosol-assisted CVD was selected to ensure consistent mass transfer of the precursor to the substrate regardless of the volatility of the compounds used. Depositions carried out using the tin(II) bis-ureate **3** resulted in the exclusive growth of tin monoxide thin films between 250 and 350 °C, independent of the reactor system used. The oxidation state of the tin was confirmed using Raman spectroscopy, X-ray diffraction and XPS techniques and there was no detectable presence of tin metal or tin(IV) environments in the bulk of the samples. The tin(IV) oxide is the thermodynamically more stable of the two tin oxide materials and therefore this suggests that the decomposition route proceeds under kinetic control and could be utilised for the formation of other low oxidation metal oxide thin films.

Deposition experiments with tin(II) alkoxides **5**, **7** and **LXXXII** also resulted in the formation of SnO thin films when analysed by Raman spectroscopy and X-ray diffraction methods. The deposition temperature was found to be affected by the identity of the precursor with films grown from 250-450°C; the precursor also had an effect on the orientation of the SnO thin films, with preferred orientation observed for both compounds **5** and **7**. The unique morphology of depositions using **LXXXII** which results in micro-rods made of microspheres of SnO resulted in an un-orientated crystalline growth.

Given that previous LPCVD experiments with **5** and **LXXXII** resulted in mixed valence metal oxide thin films, with Sn^{2+}, Sn^{4+} and tin metal present, the selective growth of just SnO through AA-CVD highlighted how the delivery method can have an effect on the decomposition pathway. Based on the deposition results for **3**, **5**, **7** and **LXXXII** depositions of tin(II) precursors carried out by AA-CVD looked to result in kinetically controlled depositions resulting in SnO formation. Deposition studies carried out using the tin(II) bis iso-carbamate compound **15** disproved the theory that the oxidation control was provided by the deposition method as upon analysis of the thin films SnO_2 was found to be present alongside SnO. Furthermore depositions carried out on silicon substrates resulted in the presence of just SnO_2 when analysed by X-ray diffraction and XPS. The deposition of SnO_2 gives some confidence that the oxidative control displayed by **3**, **5**, **7** and **LXXXII** is in some part due to the precursor and the decomposition pathway and not just the method of delivery.

The precise decomposition pathway for the compounds used in deposition studies within this report is not known at this point and further studies are required to elucidate that information, in particular inline mass spectral data would be useful to determine the

decomposition products after deposition. However, the decomposition pathway is thought to be affected by the type of CVD chamber utilised in deposition studies. This is based on different observed crystallite orientation and morphology for depositions carried in a hot-walled CVD reactor and a cold walled CVD reactor. This is further exemplified with deposition studies using compound **15**; in a cold walled reactor SnO and SnO_2 diffraction lines were detected, however on transfer to a hot-walled reactor, only SnO diffraction lines were present. The different decomposition pathways can be attributed to where the compound is thought to be decomposing. For depositions in a hot-walled reactor the precursor will heat up in the gas phase and therefore the decomposition process may occur some distance from the substrate; in a cold-walled reactor the precursor is not heated until it is situated much closer to the substrate increasing the possibility of surface adhesion and during the decomposition process.

In conclusion this work has detailed the synthetic routes to two new types of tin(II) AACVD precursor, tin(II) bis-ureates (**1**-**4**) and tin(II) bis iso-carbamates (**14**-**17**) that have previously not been produced. Example compounds from each family of precursor have been selected and studied as potential precursors for the formation of tin oxide thin films. It has been found that depositions with tin(II) bis-ureate **3** result in the exclusive formation of tin monoxide thin films as low as 250°C. Depositions with tin(II) bis iso-carbamate **15** result in the formation of a mixed valence tin oxide thin film (SnO, and SnO_{2}-) in a cold-walled CVD reactor system, or exclusively SnO in a hot-walled reactor system.

5.2 Further work

The work within this project as highlighted the potential for using ureate and iso-carbamate ligands to stabilise metal centres for use in CVD experiments. The formation of ureate and iso-carbamate ligands in this work was based on the insertion of an organic isocyanate into the metal nitrogen, or metal oxygen bond of a tin amide or alkoxide compound. The formation of other metal ureate compounds could be investigated through analogous reactions; however the potential steric crowding around different metal centres or instability of the metal amide or alkoxide compounds may make this synthetic route less viable. An alternative route to the formation of metal ureate or iso-carbamate compounds may be achieved through the formation of the analogous urea or carbamic acid which could be reacted with the intended metal directly, or through a salt metathesis route (Figure 5.3).

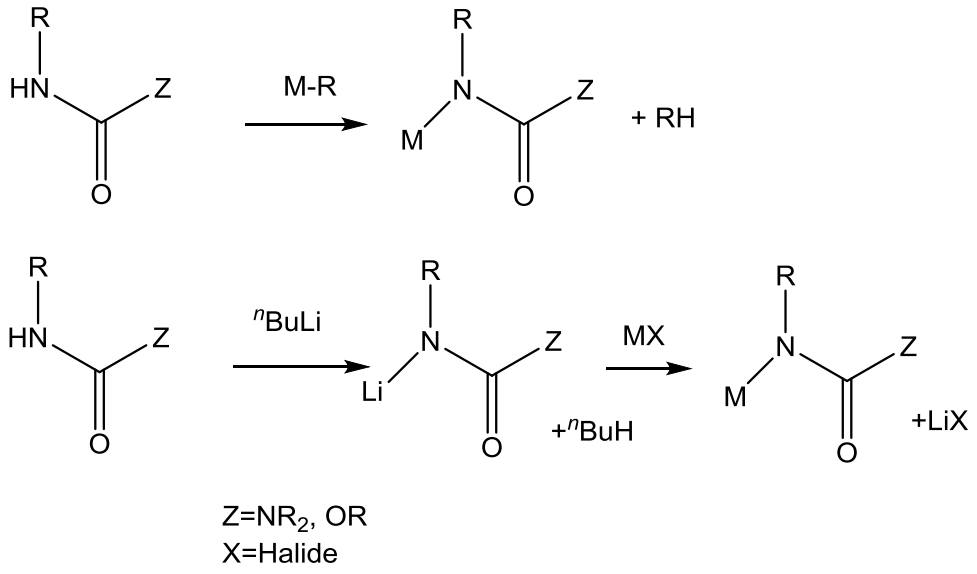

Figure 5.3: Potential synthetic routes to form metal ureate and metal iso-carbamate compounds

In Chapter four the synthesis of tin iso-monothiocarbamate was described and the TGA of compound **19** is discussed as a potential precursor for the formation of tin sulphide materials. The reaction of tin(II) amide and tin(II) alkoxide compounds with organic iso-thiocyanates is an area that could be explored further to give new single-source tin sulphide precursors. The approach could be extended further to include other metal sulphide target materials.

Addition of mass spectral data to the thermogravimetric data through a TGA-mass spectrometry machine would provide valuable data about the decomposition mechanism for the precursors developed throughout this project which would allow a greater understanding of the decomposition pathways allowing the precursors to be tuned further to provide lower deposition temperatures, or to preferentially form tin(II) or tin(IV) oxide materials.

The depositions discussed in this project focussed on the AA-CVD due to the relatively low measured volatility of the precursors. An alternative route to introduce the precursor into the deposition chamber would be to evaluate the precursors using LP-CVD experiments which may result in very different results. Further to this the introduction of an oxidant as a co-reagent can be carried out safely when depositions are not carried out with the use of a solvent which could allow for the low-temperature formation of SnO_2 using compound **3**.

6. Experimental section

6.1 General experimental details

All reactions dealt with potentially air and moisture-sensitive compounds and as such were carried out under an argon atmosphere using standard Schlenk line and glovebox techniques in an MBraun Labmaster glovebox at O_2, H_2O < 2.5 ppm. NMR experiments using air-sensitive compounds were conducted in Youngs tap NMR tubes prepared and sealed in a glovebox under argon. NMR spectra were recorded either on a Bruker AV-400 spectrometer at 100.6 MHz (^{13}C), Bruker AV-300 at 75.5 MHz (^{13}C), spectrometer or a Bruker AV-250 spectrometer at 62.9 MHz (^{13}C). The ^{1}H NMR and ^{13}C NMR spectra were referenced relative to residual solvent resonances. Me_4Sn was used as a standard for ^{119}Sn NMR measurements. Unless otherwise stated data quoted was recorded at 298 K. Elemental analysis was performed by Mr. Stephen Boyer at SACS, London Metropolitan University. Solvents for air and moisture-sensitive reactions were provided by an Innovative Technology Solvent Purification System, or dried / degassed manually according to established laboratory procedures. Single-crystal X-ray diffraction data were collected at 150 K on a Nonius KappaCCD diffractometer, equipped with an Oxford Cryostream, using graphite-monochromated Mo Kα radiation (λ = 0.71073 Å). Crystal data were processed using the Nonius software. Structure solution, followed by full-matrix least-squares refinement, was performed using the WINGX-1.80 suite of programs throughout.[220]

TGA analysis of the complexes was performed at SAFC Hitech, Bromborough, UK, using a Shimadzu TGA-51 Thermogravimetric Analyser. Data points were collected every second at a ramp rate of 20 °C min^{-1} in a flowing (50 ml min^{-1}) N_2 stream. Thin films were deposited using either a cold wall or hot wall CVD conditions onto glass microscope slides or silicon wafers. The cold wall reactor (Electro-gas Systems Ltd, UK) consisted of a tubular quartz reactor containing a silicon carbide coated graphite susceptor. The temperature of the susceptor was monitored using a k-type thermocouple coupled with a proportional–integral–derivative controller (PID controller) and heated with a water cooled IR lamp mounted externally beneath the reaction tube. The hot wall system comprised of a TSI 3076 Constant Output Atomiser using argon at 20 psi to generate the aerosol and act as carrier gas. The aerosol was passed through a quartz tube containing the substrate, heated by an Elite thermal Systems Ltd tube furnace. FE-SEM analysis of the films was undertaken on a JEOL 6301F. EDX analysis was performed using a JEOL 6480 LV SEM microscope. AFM analysis was performed using a Digital Instruments Nanoscope IIIa, with TAP300 tips in contact mode (tip radius <10 nm). Powder XRD of the films was performed on a Bruker D8 Advance powder diffractometer, using a Cu anode X-ray source (Kα wavelength = 1.5406 Å) at the

University of Bath. X-ray photoelectron spectra were recorded on a Thermo Scientific K-Alpha instrument with a monochromated Al K source having an X-ray energy of 1486.6eV (thermo scientific Ltd, East Grinstead, UK) at NEXUS. Spectra were quantified using the CasaXPS software (CasaSoftware Ltd, Teignmouth, UK).

6.2 Chapter 2 - Tin(II) amide and tin(II) ureate complexes

6.2.1 $[Sn(NMe_2)_2]_2$

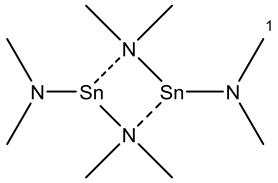

The synthesis of $[Sn(NMe_2)_2]_2$ was carried out following literature preparations.[175,176] A solution of butyl-lithium in hexanes (40 ml, 0.05 mol) was cooled to −78 °C. To this $HNMe_2$ (7 mL, 0.05 mol) was condensed, forming a white precipitate which dissolved on addition on an excess of $HNMe_2$ (7 mL, 0.05 mol). The solution was kept cold, and slowly added to $SnCl_2$ (4.74 g, 0.025 mol) in Et_2O (20 mL). The resulting pale yellow solution was gently warmed to room temperature whilst stirring. The solvent was removed *in vacuo*, and the remaining solid was extracted into hexanes (30 mL). The yellow solution was filtered from the white precipitate and the hexanes removed *in vacuo* to afford a pale yellow solid. Further purification was afforded by recrystallisation from hexanes.

^{1}H NMR (300 MHz, d^8 tol); δ 2.76 (s, broad) (**1**)

$^{13}C\{^{1}H\}$ NMR (75.5 MHz, d^8 tol); δ 44.7 (**1**)

$^{119}Sn\{^{1}H\}$ NMR (112 MHz, d^8 tol); δ 121

6.2.2 Compound 1

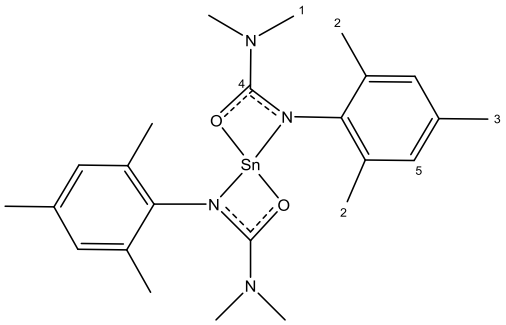

In an argon filled glovebox mesityl isocyanate (272 mg, 1.94 mmol) was added to a solution of $[Sn(NMe_2)_2]_2$ (200 mg, 0.485 mmol) in toluene (5 mL). The solution was vigorously stirred. Removal of toluene through gentle evaporation resulted in a white crystalline material in quantitative yield.

^{1}H NMR (300 MHz, d^{8} Tol); δ 2.17 (s, 3H, (**3**)), 2.35 (s, 6H, (**2**)), 2.37 (s, 6H, (**1**)), 6.75 (s, 2H, (**5**))

^{13}C{^{1}H} NMR (75.5 MHz, d^{8} Tol); δ 19.4 (**3**), 20.9 (**2**), 36.5(**1**), 128.9, 132.7, 133.9, 141.1 (Aromatic), 164.4 (**4**)

^{119}Sn NMR (112 MHz, d^{8} Tol); δ −353

EA: Expected C 54.46%, H 6.48 %, N 10.59%. Found C 54.37%, H 6.57%, N 10.62%

6.2.3 Compound 2

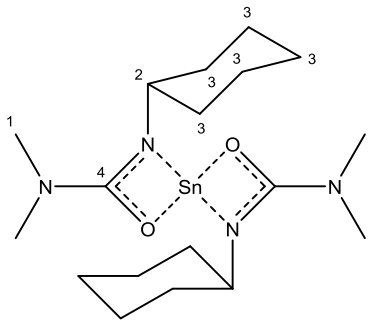

In an argon filled glovebox cyclohexyl isocyanate (274mg, 1.94 mmol) was added to a solutuion of [Sn(NMe$_2$)$_2$]$_2$ (200mg, 0.485 mmol) in toluene (5 mL). The solution was vigorously stirred. Removal of toluene through gentle evaporation resulted in a white crystalline material in quantitative yield.

^{1}H NMR (300 MHz, d^{8} Tol); δ 1.1-1.2 (m, 2H, (**3**)), 1.52-1.75 (m, 6H, (**3**)), 1.84-1.95 (m, 2H, (**3**)), 2.59 (s, 6H, (**1**)), 3.45-3.6 (m, 1H, (**2**))

^{13}C{^{1}H} NMR (75.5 MHz, d^{8} Tol); δ 26.2, 26.3, 35.6, 38.6 (**1** and **3**), 55.3 (**2**), 166.8 (**4**)

^{119}Sn NMR (111.8 MHz, d^{8} Tol); δ -310

EA: Expected C 47.29 %, H 7.50 %, N 12.25 %. Found C 47.44 %, H 7.36 %, N 12.04 %

6.2.4 Compound 3

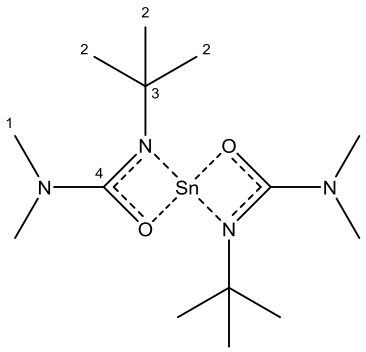

In an argon filled glove box ^{t}Bu isocyanate (192 mg, 1.94 mmol) was added to a solution of $[Sn(NMe_2)_2]_2$ (200 mg, 0.485 mmol) in toluene (5 mL). The solution was vigorously stirred. Removal of toluene through gentle evaporation resulted in a white crystalline material in quantitative yield.

^{1}H NMR (300 MHz, d^{8} Tol); δ 1.37 (s, 9H, (**2**)), 2.44 (s, 6H, (**1**))

^{13}C{^{1}H} NMR (75.5 MHz, d^{8} Tol); δ 31.4 (**2**), 41.4 (**1**), 53.0 (**3**), 167.0 (**4**)

^{119}Sn NMR (111.9 MHz, d^{8} Tol); δ -357

EA: Expected C 41.51%, H 7.46 %, N 13.83%. Found C 41.47%, H 7.54%, N 13.69%

6.2.5 Compound 4

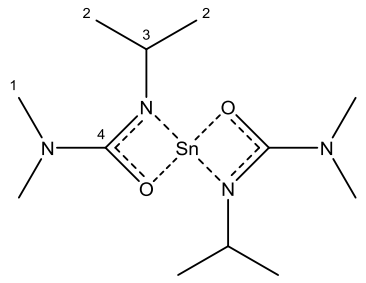

In an argon filled glovebox ^{i}Pr isocyanate (41.2 mg, 0.48 mmol) was added to a solution of $[Sn(NMe_2)_2]_2$ (50 mg, 0.12 mmol) in d_8-toluene (0.5 mL) in a Youngs tap NMR tube. The reaction mixture was analysed in situ by multinuclear NMR spectroscopy, the following resonances were observed:

^{1}H NMR (300 MHz, d^{8} Tol); δ 1.23-1.25 (d, 6H, (**2**)), 2.57 (s, 6H, (**1**)), 3.89-4.01 (sept, J_{H-H}=6.4Hz, 1H)

^{13}C{^{1}H} NMR (75.5 MHz, d^{8} Tol); δ 25.2 (**2**), 38.9 (**1**), 47.1 (**3**), 167.2 (**4**)

^{119}Sn NMR (111.8 MHz, d^{8} Tol); δ -307

Attempts to isolate the compound resulted in the isolation of an orange oil. Analysis of the oil by multinuclear NMR showed suggested that compound **4** was present alongside an unidentified decomposition product. The NMR of the solution showed the presence of only one tin environment, matching that of compound **4**. The spectral data is shown below:

^{1}H NMR (300 MHz, d^{8} Tol); δ 1.08-1.10 (d, J_{H-H}=6.4Hz, 12H), 1.22-1.24 (d, J_{H-H}=6.4Hz, 6H, (**2**)), 2.58 (s, 12H, (**1**)), 2.60 (s, 6H), 3.98-4.00 (sept, J_{H-H}=6.4Hz 2H) 4.08-4.14 (sept, J_{H-H}=6.4Hz, 1H, (**3**))

^{13}C{^{1}H} NMR (75.5 MHz, d^{8} Tol); δ 23.9(decomp), 25.2 (**2**), 36.2(decomp), 38.9 (**1**), 43.0(decomp), 47.1 (**3**), 158.2(decomp), 167.2 (**4**)

^{119}Sn NMR (111.8 MHz, d^{8} Tol); δ -307

6.3 Chapter 3 - Tin(II) alkoxides

6.3.1 $[Sn\{N(SiMe_3)_2\}_2]_2$

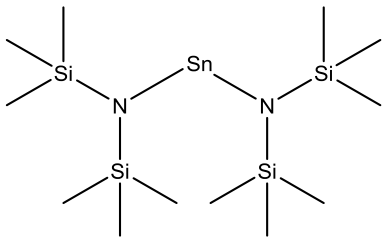

To a solution of $SnCl_2$ (9.5g, 50.2mmol) in Et_2O (100mL) was added $LiN(SiMe_3)_2$ (16.8g, 100.4 mmol) producing an orange precipitate. The solvent was removed in vacuo and redissolved in toluene. This solution was filtered and the toluene removed in vacuo to give an orange oil. This was purified by vacuum distillation to afford bright orange oil that crystallised at 5°C to give orange crystals.[212]

^{1}H NMR (300 MHz, d^{8} toluene); δ 0.19 (s, broad. CH_3)

^{119}Sn NMR (111.8 MHz, d^{8} toluene); δ 775

6.3.2 LXXXII

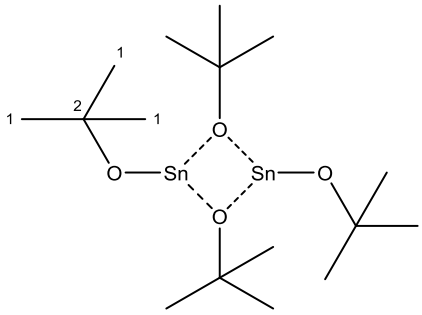

Compound **LXXXII** was prepared according to literature procedures.[202–204] A solution of $[Sn\{N(SiMe_3)_2\}_2]_2$ in toluene was cooled to -78 °C. To this a ^{t}BuOH was slowly added resulting in the orange solution becoming a clear. Removal of the solvent and volatiles in vacuo resulted in an off-white precipitate. This was further purified through recrystallisation from hexanes at -30°C.

^{1}H NMR (300 MHz, d^8 toluene); δ 1.27 (s, broad. (**1**)).

^{13}C{^{1}H} NMR (75.5 MHz, d_8-toluene); δ 32.5 (**1**), 79.8 (**2**)

^{119}Sn NMR (111.8 MHz, d^8 toluene); δ -94 [202]

6.3.3 Compound 5

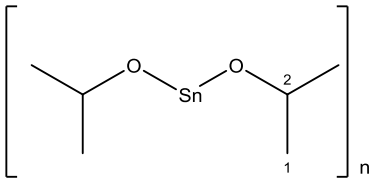

$[Sn(NMe_2)_2]_2$ (1.0 g, 4.8 mmol) was added to an excess of ^{i}PrOH (15 mL, 196 mmol) and left to stir for 20min. The solvent was removed in vacuo to give an off-white precipitate. The precipitate was dissolved in the minimum volume of toluene and cooled to -40°C producing clear needle-like crystals.

^{1}H NMR (300 MHz, d_8 tol); δ 1.29-1.31 (d, J_{H-H} = 6.4 Hz, 6H, (**1**)), 4.51-4.63 (sept, J_{H-H} = 6.4 Hz, 1H, (**2**)).

^{13}C{^{1}H} NMR (75.5 MHz, d_8 tol); δ 28.4 (**1**), 65.9 (**2**).

^{119}Sn NMR (111.8 MHz, d_8 tol); δ -220

EA: Expected C 30.42%, H 5.96%. Found C 30.23% H 6.01%.

6.3.4 Compound 6

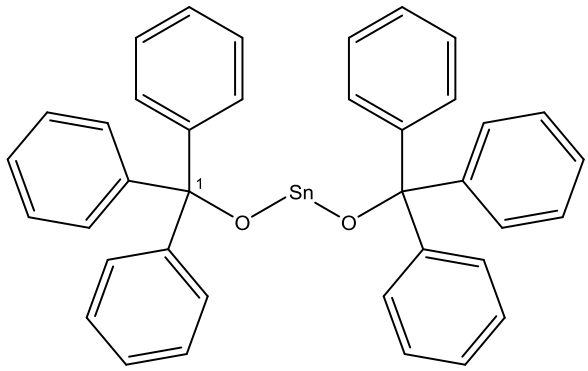

To a solution of $[Sn\{N(SiMe_3)_2\}_2]_2$ (572 mg, 5.5 mmol) in THF (20mL) was added triphenyl methanol (500 mg, 22 mmol) and left to stir for 20min. The solvent was removed *in vacuo* to give an off-white precipitate. The precipitate was re-dissolved in hot THF and allowed to cool slowly to room temperature resulting in crystals suitable for X-ray diffraction studies.

^{1}H NMR (300 MHz, d_8 THF); δ 7-7.4 (m, aromatic H).

$^{13}C\{^{1}H\}$ NMR (75.5 MHz, d_8 THF); δ 127.3, 128.2, 129.0, 149.0 (aromatic)

^{119}Sn NMR (111.8 MHz, d_8 THF); δ -66

EA: Expected C 71.61%, H 4.74%. Found C 71.75% H 4.82%.

6.3.5 Compound 7

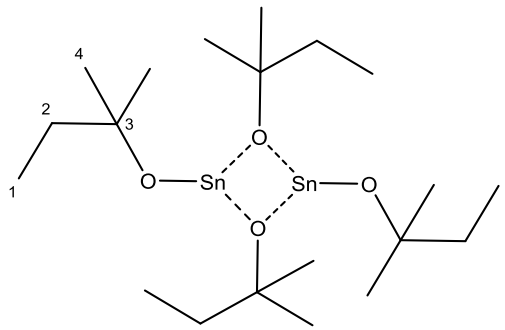

To a solution of $[Sn\{N(SiMe_3)_2\}_2]_2$ (3.1 g, 3.5 mmol) in THF (20 mL) was added 2-methyl-2-butanol (1.2 g, 14 mmol) and left to stir for 20min. The solvent was removed *in vacuo* to give pale yellow oil.

^{1}H NMR (300 MHz, d_8-tol); δ 0.99-1.04 (t, J_{H-H} =7.5Hz, 3H, (**1**)), 1.36 (s, 6H (**4**)), 1.57-1.68 (quartet, J_{H-H} = 7.5, 2H, (**4**))

^{13}C{^{1}H} NMR (75.5 MHz, d_8-tol); δ 28.6, 31.8, 33.8 (**1**, **2** & **4**), 73.2 (**3**)

^{119}Sn NMR (111.8 MHz, d_8-tol); δ -99

EA: Expected C 40.99%, H 7.57%. Found C 40.88% H 7.56%.

6.4 Chapter 4 - Tin(II) carbonate and iso-carbamate compounds

6.4.1 Tin(II) carbonate compounds

Attempts to isolate tin(II) carbonate compounds were unsuccessful. The general method used for preparing samples for 2D-EXSY NMR analysis is detailed for experiments using compound **5**:

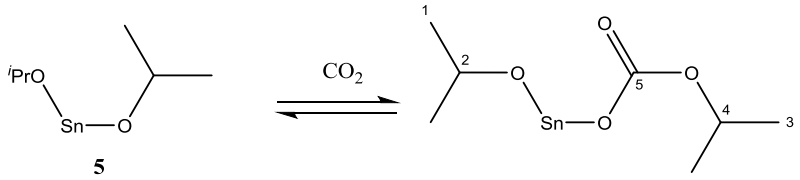

5

A sample of **5** (100mg, 0.42mmol) was dissolved in d_8-tol (0.5mL) in a Youngs tap NMR tube. The sample was degassed by freeze thaw technique and the headspace was evacuated and refilled with the CO_2 and shaken to promote mass transfer.

^{1}H NMR (300 MHz, d_8-tol); δ 1.15-1.19 (d, J_{H-H}=6.4Hz (**1**)), 1.23-1.27 (d, J_{H-H}=6 Hz, (**3**)), 4.51(sept, J_{H-H}=6.4Hz (**2**)), 4.85 (m, J_{H-H}=6 Hz (**4**)).

^{13}C{^{1}H} NMR (75.5 MHz, d_8-tol); δ 22.7 (**3**), 28.1 (**1**), 67.1 (**2**), 70.4 (**4**), 161.6 (**5**)

^{119}Sn NMR (111.8 MHz, d_8-tol); δ -368

6.4.2 Compound 8

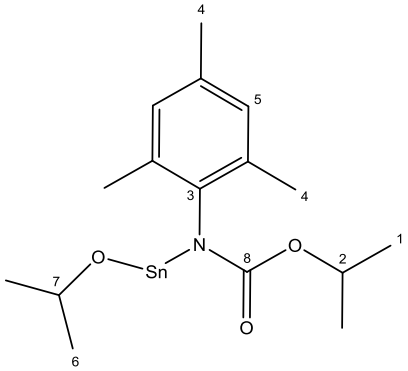

In an argon filled glove box mesityl isocyanate (136 mg, 0.84 mmol) was added to a solution of **5** (200 mg, 0.84 mmol) in toluene (5mL). The solution was vigorously stirred. Removal of toluene through gentle evaporation resulted in a white crystalline material in quantitative yield.

^{1}H NMR (300 MHz, d_8-tol); δ 0.99-1.01 (d, J_{H-H} =6 Hz, 12H (**1**, **6**)), 2.12 (s, 9H, (**4**)), 4.19-4.30 (sept, J_{H-H} = 6Hz, 1H, (**7**)), 4.96-5.08 (sept, J_{H-H} =6 Hz, 1H, (**2**)), 6.98 (s, 2H (**5**)).

^{13}C{^{1}H} NMR (75.5 MHz, d_8-tol); δ 20.2, 21.2, 21.7 (**4**), 22.7(**1**, **6**), 69.0, 69.1 (**2**, **7**), 139.7, 134.7, 134.3, 129.7 (aryl) 161.9 (**8**).

^{119}Sn NMR (111.8 MHz, d_8-tol); δ −315

EA: Expected C 48.27%, H 6.33%, N 3.52%. Found C 48.46%, H 6.43%, N 3.37%

6.4.3 Compound 9

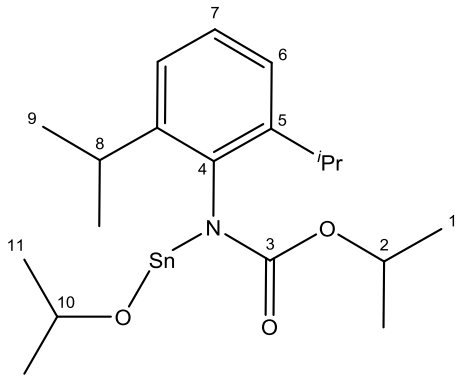

In an argon filled glove box 2,4-diisopropylphenyl isocyanate (171 mg, 0.84 mmol) was added to a solution of **5** (200 mg, 0.84 mmol) in toluene (5 mL). The solution was vigorously stirred. Removal of toluene through gentle evaporation resulted in a white crystalline material in quantitative yield.

^{1}H NMR (300 MHz, d_8-tol); δ 1.02-1.04 (d, J_{H-H} =6.4, 6H (**9**)), 1.05-1.07 (d, J_{H-H} =6.4, 6H (**1**, **11**)), 1.30-1.32 (d, J_{H-H} =6.8, 6H, (**9**)), 1,35-1.37 (d, J_{H-H} =6.8, 6H (**9**), 3.58-3.71 (m, 2H, (**8**)), 4.2-4.32 (sept, J_{H-H} =6.4Hz, 1H, (**10**)),4.94-5.07 (sept, J_{H-H} =6.4Hz, 1H, (**2**)), 6.95-7.15 (**6**, **7**).

^{13}C{^{1}H} NMR (75.5 MHz, d_8-tol); δ 22.6, 24.6, 25.7, (**1**, **9**, **11**), 29.4 (**8**), 69.1, 69.7 (**2**, **10**), 123.7, 138.2, 139.2, 145.5 (**4**, **5**, **6**, **7**), 162.4 (**3**).

^{119}Sn NMR (111.8 MHz, d_8-tol); δ -347

6.4.4 Compound 10

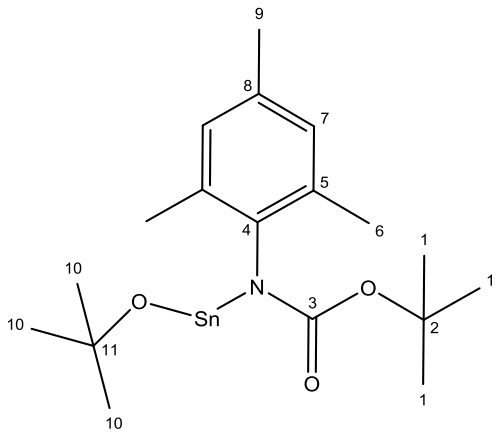

In an argon filled glove box mesityl isocyanate (122 mg, 0.754 mmol) was added to a solution of **LXXXII** (200mg, 0.754 mmol) in toluene (5 mL). The solution was vigorously stirred. Removal of toluene through gentle evaporation resulted in a white crystalline material in quantitative yield.

^{1}H NMR (300 MHz, d_8-tol); 1.60 (s, 9H, (**1**)), 1.63 (s, 9H (**10**)), 2.46 (s, 3H (**6**)), 2.51 (s, 3H (**6**)), 2.56 (s, 3H (**9**)), 7.04 (s, 2H (**7**)).

^{13}C{^{1}H} NMR (75.5 MHz, d_8-tol); 29.1, 30.9, 32.5, 35.3 (**1**, **6**, **9, 10**), 76.9(**2**), 79.8 (**11**), 129, 134, 135.1, 140.9, (**4**, **5**, **7**, **8**), 162.0 (**3**)

^{119}Sn NMR (111.8 MHz, d_8-tol); -317

EA: Expected C 50.73%, H 6.86 %, N 3.29 %. Found C 50.68 %, H 6.89 %, N 3.29 %

6.4.5 Compound 11

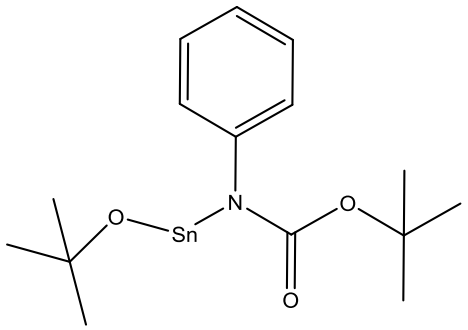

In an argon filled glove box phenyl isocyanate (23 mg, 0.189 mmol) was added to a solution of **LXXXII** (50 mg, 0.189 mmol) in d_8-tol (0.5 mL). A pale yellow crystalline product crashed out after 15 minutes. The pale yellow crystals were produced quantitatively and

were suitable for single crystal X-ray diffraction experiments. Attempts to analyse compound **11** using solution based spectroscopy were unsuccessful due to the low solubility in a range of NMR solvents.

EA: Expected C 46.91%, H 6.04%, N 3.65%. Found: C 46.80%,H 6.12%,N 3.73%

6.4.6 Compound 12

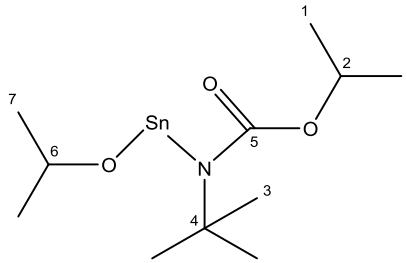

In an argon filled glovebox ^{t}Bu isocyanate (83 mg, 0.84 mmol) was added to a solution of **5** (100 mg, 0.42 mmol) in d_8-tol (0.5 mL) in a Youngs tap NMR tube. The sample was analysed using multinuclear and 2D NMR spectroscopy experiments in situ; attempts to isolate **12** were unsuccessful due to the reversible nature of the insertion reaction. The NMR data for the insertion product identified in the exchange NMR experiments is detailed below:

^{1}H NMR (300 MHz, C_6D_6); δ 0.92 (s, free ^{t}BuNCO), 1.11-1.13 (d, J_{H-H}=6Hz, (**7**)), 1.34-1.35 (d J_{H-H}=6Hz, (**1**)),1.42 (s, (**3**)), 4.56 (sept, J_{H-H}=6Hz, (**6**)), 4.94-5.02 (sept, J_{H-H} = 6Hz, (**2**)).

^{13}C{^{1}H} NMR (300MHz, C_6D_6); δ 22.8, 28.8 (**1**, **7**), 31.0, 31.9 (**3,** free ^{t}BuNCO), 52.1, 55.5 (**2**, **6**), 69.9 (**4**), 163.4 (**5**)

^{119}Sn NMR (111.8 Hz, C_6D_6); δ -360

6.4.7 Compound 13

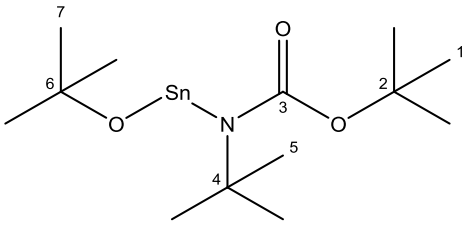

In an argon filled glovebox ^{t}Bu isocyanate (75 mg, 0.84 mmol) was added to a solution of **LXXXII** (100 mg, 0.377 mmol) in d_8-tol (0.5 mL) in a Youngs tap NMR tube. The sample was analysed using multinuclear and 2D NMR spectroscopy experiments in situ; attempts to isolate **13** were unsuccessful due to the reversible nature of the insertion reaction. The NMR data for the insertion product identified in the exchange NMR experiments is detailed below:

^{1}H NMR (300 MHz, d_8-tol); δ 0.98 (s, free ^{t}BuNCO), 1.35 (s, **7**), 1.41 (s, **1**), 1.43 (s, **5**)

^{13}C{^{1}H} NMR (300MHz, d_8-tol); δ 29.4, 30.9, 32.1, 35.4 (**1**, **5, 7** free ^{t}BuNCO), 51.9, 55.5 (**4,** free ^{t}BuNCO), 80.8 (**2**, **6**), 163.3 (**3**)

^{119}Sn NMR (111.8 Hz, d_8-tol); δ -377

6.4.8 Compound 14

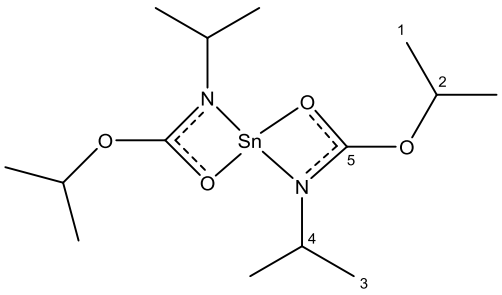

In an argon filled glove box ^{i}Pr isocyanate (287 mg, 3.36 mmol) was added to a solution of **5** (400 mg, 1.68 mmol) in toluene (5 mL). The solution was vigorously stirred. Removal of toluene through gentle evaporation resulted in a white crystalline material in quantitative yield.

^{1}H NMR (300 MHz, d_8-tol) δ 1.13 (d, *J*=6 Hz, 6H, (**1**)) 1.19 (d, *J*=6.4 Hz, 6 H, (**3**)) 4.04 (sept, *J*=6.4 Hz, 1 H, (**4**)) 4.94 (sept, *J*=6Hz, 1 H, (**2**))

^{13}C{^{1}H} NMR (75.5 MHz, d_8-tol); δ 22.9, 24.3 (**1**, **3**), 45.9, 69.6 (**2**, **4**) 163.2 (**5**)

^{119}Sn NMR (111.8 MHz, d_8-tol); δ -360

EA: Expected C 41.30%, H 6.93%, N 6.88% Found C 41.13% H 7.04%, N 6.74%.

6.4.9 Compound 15

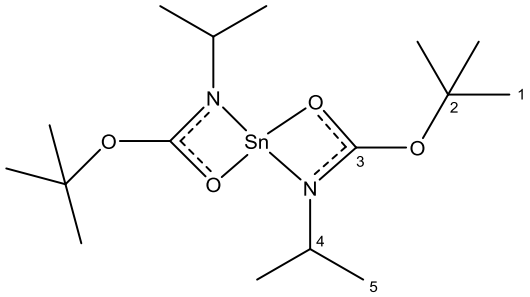

In an argon filled glove box ^{i}Pr isocyanate (266 mg, 3.12 mmol) was added to a solution of **LXXXII** (400 mg, 1.56 mmol) in toluene (5 mL). The solution was vigorously stirred before being concentrated *in vacuo* to produce a yellow crystalline material. Further purification was achieved by taking the yellow crystalline product and dissolving in 2 mL of hexane, filtering and concentrating through gentle evaporation resulted in a white crystalline material. Yield 400 mg (0.91 mmol, 58%).

^{1}H NMR (300 MHz, d_8-tol) δ ppm 1.19-1.21 (d, J_{H-H}=6.4Hz, 6H (**5**)), 1.43 (s, 9H (**1**)) 3.94-4.03 (sept, J_{H-H}=6.4Hz, 1H, (**4**))

^{13}C{^{1}H} NMR (75.5 MHz, d_8-tol);) δ ppm 24.2 (**5**), 29.3 (**1**), 49.1 (**4**), 80.30 (**2**), 163.2 (**3**)

^{119}Sn NMR (111.8 MHz, d_8-tol); δ ppm -338

EA: Expected C 44.16%, H 7.41%, N 6.44% Found C 43.89% H 7.44%, N 6.49%.

6.4.10 Compound 16

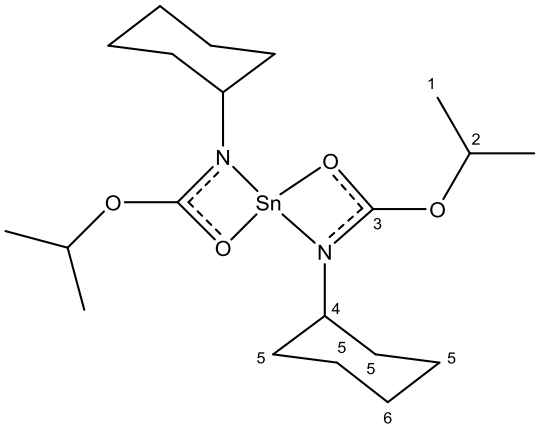

In an argon filled glovebox cyclohexyl isocyanate (431 uL, 3.38 mmol) was added to a solution of **5** (400 mg, 1.68 mmol) in toluene (5 mL). The solution was concentrated *in vacuo* to give a yellow crystalline material in quantitative yield. Recrystallisation from hexanes at -30°C resulted in crystals suitable for X-ray diffraction analysis.

^{1}H NMR (300 MHz, d^{8} Tol) δ ppm 1.10-1.28 (m, 10H (**1**, **5**)) 1.44-1.57 (m, 4H (**5**) 1.67-1.71 (m, 2H (**6**)), 3.64-3.74 (m, 1H (**4**)), 4.91-5.03 (sept, J_{H-H}=6 Hz 1H (**2**))

^{13}C{^{1}H} NMR (75.5 MHz, d^{8} Tol); δ ppm 22.9 (**1**), 26.5, 26.7, 34.8 (**5**,) 53.9 (**4**), 69.6 (**2**), 163.2 (**3**)

^{119}Sn NMR (111.8 MHz, d^{8} Tol); δ ppm -355

EA: Expected C 51.27%, H 7.82 %, N 5.59 Found: C 51.22%, H 7.75%, N 5.44.

6.4.11 Compound 17

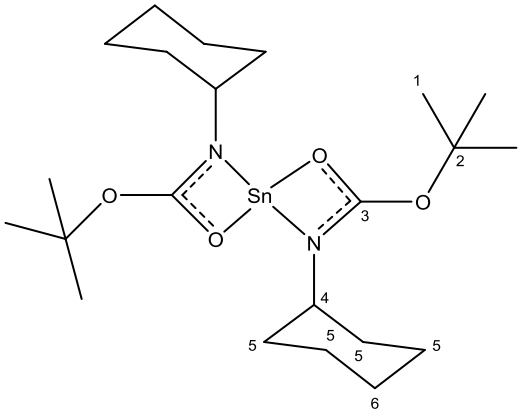

In an argon filled glovebox cyclohexyl isocyanate (399 uL, 3.12 mmol) was added to a solution of **LXXXII** (400 mg, 1.56 mmol) in hexanes (5 mL). The solution was stirred vigorously before the solvent was gently evaporated off to give colourless crystals of X-ray quality in quantitative yield.

^{1}H NMR (300MHz, d_8-tol); δ 1.44 (s, 9H, (**1**)), 1.50-1.75 (m, 8H, (**5**)), 1.80-1.91 (m, 2H, (**6**)), 3.57-3.76 (m, 1H, (**4**)).

^{13}C{^{1}H} NMR (75.5 MHz, d_8-tol); δ 26.5, 26.6, 29.3, 34.6 (**1**, **5**, **6**), 54.2 (**4**), 80.3 (**2**), 163.1 (**3**)

^{119}Sn NMR (111.8 MHz, d_8-tol); δ -335

EA: Expected C 51.28 %, H 7.82 %, N 5.44 %. Found C 51.07 %, H 7.85 %, N 5.52 %.

6.5 Chapter 4 - Tin(II) iso-mono thio carbamates

6.5.1 Compound 18

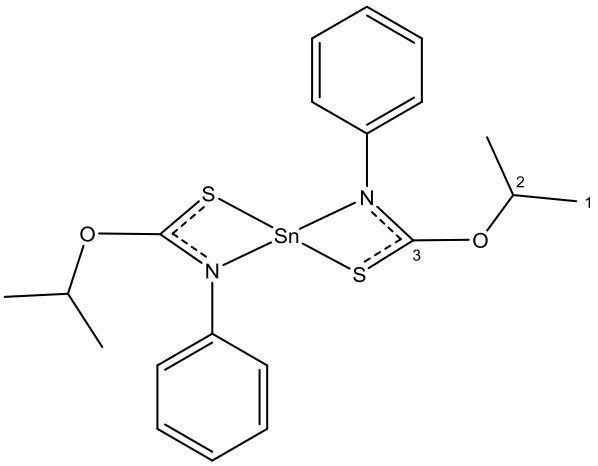

In an argon filled glovebox phenyl isocyanate (201 mg, 1.60 mmol) was added to a solution of **5** (200 mg, 0.8 mmol) in toluene (5 mL). The solution was stirred vigorously before the solvent was gently evaporated off to give yellow crystals of X-ray quality in quantitative yield.

^{1}H NMR (300 MHz, d_8-tol); δ 0.97-0.99 (d, J_{H-H} =6Hz, 6H, (**1**)), 5.03-5.15 (sept, J_{H-H} = 6Hz, 1H, (**2**)), 6.13-6.73 (m, 5H, aromatic).

^{13}C{^{1}H} NMR (75.5 MHz, d_8-tol); δ 22.6, 23.0 (**1**), 76.0 (**2**), 125.4, 125.8, 126.9, 129.8, 130.5, 144.7 (aryl group), 180.8 (**3**).

^{119}Sn NMR (111.9 MHz, d_8-tol); δ 309

EA: Expected C 47.36%, H 4.77%, N 5.52%. Found C 47.48%, H 4.92%, N 5.41%

6.5.2 Compound 19

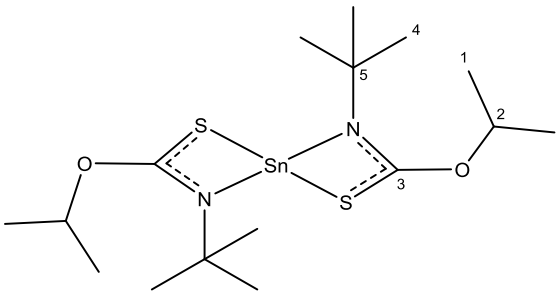

In an argon filled glovebox ^{t}Bu thio-isocyanate (194mg), 1.6 mmol) was added to a solution of **5** (200 mg, 0.8 mmol) in toluene (5 mL). The solution was stirred vigorously before being left to gently evaporate resulting in yellow crystals in quantitative yield.

^{1}H NMR (300 MHz, C_6D_6); δ 1.07-1.05 (d, J_{H-H}=6Hz, 6H, (**1**)), 1.35 (s, 9H (**4**)), 5.08-4.95 (s, J_{H-H}=6.Hz, 1H (**2**))

$^{13}C\{^{1}H\}$ NMR (75.5 MHz, C_6D_6); δ 22.9 (**1**), 29.2, 29.9 (**4**), 55.8 (**5**), 75.8 (**2**)

^{119}Sn NMR (111.9 MHz, C_6D_6); δ 304

EA: Expected C 41.13%, H 6.90%, N 6.44% Found C 41.10% H 6.99%, N 6.03%.

7. References

1. G. H. Lee, T. Kawazoe, and M. Ohtsu, *Solid State Commun.*, 2002, **124**, 163–165.

2. K. M. Reddy, *Mater. Chem. Phys.*, 2003, **78**, 239–245.

3. V. Kumar and S. Masudy-Panah, *Nanoelectron. Conf. 2013 IEEE 5th Int.*, 2013, 443–445.

4. S. Van den Berghe, F. Miserque, T. Gouder, B. Gaudreau, and M. Verwerft, *J. Nucl. Mater.*, 2001, **294**, 168–174.

5. L. Leontie, *J. Optoelectron. Adv. Mater.*, 2006, **8**, 1221–1224.

6. S. Baco, A. Chik, and F. M. Yassin, *J. Sci. Technol.*, 2012, **4**, 61–72.

7. N. F. Quackenbush, J. P. Allen, D. O. Scanlon, S. Sallis, J. A. Hewlett, A. S. Nandur, B. Chen, K. E. Smith, C. Weiland, D. a. Fischer, J. C. Woicik, B. E. White, G. W. Watson, and L. F. J. Piper, *Chem. Mater.*, 2013, **25**, 3114–3123.

8. P. Erhart, A. Klein, R. Egdell, and K. Albe, *Phys. Rev. B*, 2007, **75**, 153205.

9. P. . Patil and L. . Kadam, *Appl. Surf. Sci.*, 2002, **199**, 211–221.

10. H. Sato, T. Minami, S. Takata, and T. Yamada, *Thin Solid Films*, 1993, **236**, 27–31.

11. Y. Ogo, H. Hiramatsu, K. Nomura, H. Yanagi, T. Kamiya, M. Hirano, and H. Hosono, *Appl. Phys. Lett.*, 2008, **93**, 032113.

12. G. Hautier, A. Miglio, G. Ceder, G.-M. Rignanese, and X. Gonze, *Nat. Commun.*, 2013, **4**, 2292–2299.

13. H. Kawazoe, H. Yanagi, K. Ueda, and H. Hosono, *MRS Bull.*, 2000, **25**, 28–36.

14. S. Fraga, J. Karwowski, and K. M. S. Saxena, *Handbook of Atomic Data*, Elsevier Scientific Publishing Company,New York, NY, 1976.

15. H. Kawazoe, M. Yasukawa, H. Hyodo, M. Kurita, H. Yanagi, and H. Hosono, *Nature*, 1997, **389**, 939–942.

16. R. Nagarajan, A. D. Draeseke, A. W. Sleight, and J. Tate, *J. Appl. Phys.*, 2001, **89**, 8022–8025.

17. H. Ohta, M. Orita, M. Hirano, I. Yagi, and K. Ueda, *J. Appl. Phys.*, 2002, **91**, 3074–3078.

18. A. Kudo, H. Yanagi, H. Hosono, and H. Kawazoe, *Appl. Phys. Lett.*, 1998, **73**, 220.

19. K. Ueda, S. Inoue, S. Hirose, H. Kawazoe, and H. Hosono, *Appl. Phys. Lett.*, 2000, **77**, 2701–2703.

20. B. G. Lewis and D. C. Paine, *MRS Bull.*, 2000, 22–27.

21. R. Gordon, *J. Non-Cryst. Solids*, 1997, **218**, 81–91.

22. R. G. Gordon, *MRS Bull.*, 2000, **25**, 52–57.

23. J. R. Bellingham, W. A. Phillips, and C. J. Adkins, *J. Mater. Sci. Lett.*, 1992, **11**, 263–265.

24. L. Davis, *Thin Solid Films*, 1993, **236**, 1–5.

25. K. Molloy, *J. Chem. Res.*, 2008, **2008**, 2277–2288.

26. http://www.printedelectronicsworld.com/articles/ito-alternatives-to-gain-speed-in-the-2-billion-tcf-market-00004561.asp?sessionid=1 (accessed 15/08/13)

27. http://www.electroiq.com/articles/set/2012/07/ito-alternatives-infiltrating-transparent-conductive-films-market.html (accessed 15/08/13)

28. F. Lawson, *Nature*, 1967, **215**, 955–956.

29. M. Batzill and U. Diebold, *Prog. Surf. Sci.*, 2005, **79**, 47–154.

30. A. A. Bolzan, C. Fong, B. J. Kennedy, and C. J. Howard, *Acta Crystallogr. Sect. B Struct. Sci.*, 1997, **53**, 373–380.

31. J. Wager, D. Keszler, and R. Presley, *Transparent Electronics*, Springer US, 2008.

32. P. G. Harrison, *Chemistry of Tin*, Blackie, Glasgow, 1989.

33. M. J. Fuller and G. Croft, *Nature*, 1977, **269**, 585–586.

34. P. G. Harrison, C. Bailey, and W. Azelee, *J. Catal.*, 1999, **186**, 147–159.

35. P. W. Park, H. H. Kung, D. Kim, and M. C. Kung, *J. Catal.*, 1999, **184**, 440–454.

36. F. Solymosi and J. Kiss, *J. Catal.*, 1978, **51**, 42–51.

37. M. J. Fuller and M. E. Warwick, *J. Catal.*, 1976, **42**, 418–424.

38. G. C. Bond, L. R. Molloy, and M. J. Fuller, *J. Chem. Soc., Chem. Commun.*, 1975, 796–797.

39. M. J. Fuller and M. E. Warwick, *J. Catal.*, 1974, **34**, 445–453.

40. M. J. Fuller and M. E. Warwick, *J. Catal.*, 1973, **29**, 441–450.

41. P. Mars and D. W. van Krevelen, *Chem. Eng. Sci.*, 1954, **3**, 41–59.

42. J. Haber and M. Witko, *J. Catal.*, 2003, **216**, 416–424.

43. W. Gopel, *Prog. Surf. Sci.*, 1985, **20**, 9–103.

44. I. Sayago, J. Gutiérrez, and L. Arés, *Sensors Actuators B Chem.*, 1995, **26-27**, 19–23.

45. G. Sberveglieri, G. Faglia, S. Groppelli, and P. Nelli, *Sensors Actuators B Chem.*, 1992, **8**, 79–88.

46. B. Marquis and J. Vetelino, *Sensors Actuators B Chem.*, 2001, **77**, 100–110.

47. C. Di Natale, A. D'Amico, F. A. M. Davide, G. Faglia, P. Nelli, and G. Sberveglieri, *Sensors Actuators B Chem.*, 1994, **20**, 217–224.

48. J. Tamaki, T. Maekawa, N. Miura, and N. Yamazoe, *Sensors Actuators B Chem.*, 1992, **9**, 197–203.

49. R. Binions, C. J. Carmalt, and I. P. Parkin, *Meas. Sci. Technol.*, 2007, **18**, 190–200.

50. D. S. Ginley and J. D. Perkins, in *Handbook of Transparent Conductors*, eds. D. S. Ginley, H. Hosono, and D. C. Paine, Springer, New York, 2010, pp. 1–26.

51. L. Dominici, F. Michelotti, T. M. Brown, A. Reale, and A. Di Carlo, *Opt. Express*, 2009, **17**, 10155–67.

52. X. Q. Pan and L. Fu, *J. Electroceramics*, 2001, **7**, 35–46.

53. D. M. Adams, A. G. Christy, J. Haines, and S. M. Clark, *Phys. Rev. B*, 1992, **46**, 358–367.

54. W. J. Moore Jr and L. Pauling, *J. Am. Chem. Soc.*, 1941, **63**, 1392–1394.

55. N. E. Christensen, A. Svane, and E. L. Peltzer y Blancá, *Phys. Rev. B*, 2005, **72**, 014109.

56. I. Lefebvre, M. Szymanski, J. Olivier-Fourcade, and J. Jumas, *Phys. Rev. B*, 1998, **58**, 1896–1906.

57. J. P. Allen, D. O. Scanlon, S. C. Parker, and G. W. Watson, *J. Phys. Chem. C*, 2011, **115**, 19916–19924.

58. J. Köhler, J. Tong, R. Dinnebier, and A. Simon, *Zeitschrift für Anorg. und Allg. Chemie*, 2012, **638**, 1970–1975.

59. J. D. Donaldson, W. Moser, and W. B. Simpson, *J. Chem. Soc.*, 1961, 839–841.

60. J. A. Caraveo-Frescas, P. K. Nayak, H. A. Al-Jawhari, D. B. Granato, U. Schwingenschlögl, and H. N. Alshareef, *ACS Nano*, 2013, **7**, 5160–5167.

61. K. Okamura, B. Nasr, R. Brand, and H. Hahn, *J. Mater. Chem.*, 2012, **22**, 4607.

62. W. Guo, L. Fu, Y. Zhang, K. Zhang, L. Y. Liang, Z. M. Liu, H. T. Cao, and X. Q. Pan, *Appl. Phys. Lett.*, 2010, **96**, 042113.

63. H. Yabuta, N. Kaji, R. Hayashi, H. Kumomi, K. Nomura, T. Kamiya, M. Hirano, and H. Hosono, *Appl. Phys. Lett.*, 2010, **97**, 072111.

64. L. Y. Liang, Z. M. Liu, H. T. Cao, Z. Yu, Y. Y. Shi, A. H. Chen, H. Z. Zhang, Y. Q. Fang, and X. L. Sun, *J. Electrochem. Soc.*, 2010, **157**, H598–H602.

65. Y. Ogo, H. Hiramatsu, and K. Nomura, *Phys. Status Solidi A*, 2009, **206**, 2187–2191.

66. H. Hosono, Y. Ogo, H. Yanagi, and T. Kamiya, *Electrochem. Solid-State Lett.*, 2011, **14**, H13–H16.

67. D. B. Granato, J. A. Caraveo-Frescas, H. N. Alshareef, and U. Schwingenschlögl, *Appl. Phys. Lett.*, 2013, **102**, 212105.

68. P. Hsu, W. Chen, and Y. Tsai, *Jpn. J. Appl. Phys.*, 2013, **52**, 05DC07.

69. H. Lee, K. Kim, J.-J. Woo, D.-J. Jun, Y. Park, Y. Kim, H. W. Lee, Y. J. Cho, and H. M. Cho, *Chem. Vapor. Depos.*, 2011, **17**, 191–197.

70. H. Giefers, F. Porsch, and G. Wortmann, *Solid State Ionics*, 2005, **176**, 199–207.

71. F. Gauzzi and B. Verdini, *Inorg. Chim. Acta*, 1985, **104**, 1–7.

72. M. Moreno, G. Punte, and G. Rigotti, *Solid State Ionics*, 2001, 81–86.

73. A. Jones and M. Hitchman, in *Chemical Vapour Deposition: Precursors, Processes and Applications*, eds. A. C. Jones and M. L. Hitchman, Royal Society of Chemistry, 2009, pp. 1–36.

74. A. C. Jones and P. O'Brien, *CVD of Compound Semiconductors*, VCH, Cambridge, 2008.

75. J.-H. Ryou, R. D. Dupuis, and R. Kanjolia, in *Chemical Vapour Deposition: Precursors, Processes and Applications*, eds. A. C. Jones and M. L. Hitchman, Royal Society of Chemistry, 2009, pp. 272–319.

76. M. A. Malik and P. O'Brien, in *Chemical Vapour Deposition: Precursors, Processes and Applications*, eds. A. C. Jones and M. L. Hitchman, Royal Society of Chemistry, 2009, pp. 125–145.

77. S. P. Krumdieck, in *Chemical Vapour Deposition: Precursors, Processes and Applications*, eds. A. C. Jones and M. L. Hitchman, Royal Society of Chemistry, 2009, pp. 37–92.

78. P. Marchand, I. A. Hassan, I. P. Parkin, and C. J. Carmalt, *Dalton Trans.*, 2013, **42**, 9406–9422.

79. S. E. Alexandrov and M. L. Hitchman, in *Chemical Vapour Deposition: Precursors, Processes and Applications*, eds. A. C. Jones and M. L. Hitchman, Royal Society of Chemistry, 2009, pp. 494–534.

80. S. J. C. Irvine and D. Lamb, in *Chemical Vapour Deposition: Precursors, Processes and Applications*, eds. A. C. Jones and M. L. Hitchman, Royal Society of Chemistry, 2009, pp. 477–493.

81. S. A. Rushworth, L. M. Smith, A. J. Kingsley, R. Odedra, R. Nickson, and P. Hughes, *Microelectron. Reliab.*, 2005, **45**, 1000–1002.

82. A. C. Jones, H. C. Aspinal, and P. R. Chalker, in *Chemical Vapour Deposition: Precursors, Processes and Applications*, eds. A. C. Jones and M. L. Hitchman, Royal Society of Chemistry, 2009, pp. 357–412.

83. A. P. Duncan, S. M. Mullins, J. Arnold, and R. G. Bergman, *Organometallics*, 2001, **20**, 1808–1819.

84. D. Wood, G. P. A. Yap, and D. S. Richeson, *Inorg. Chem.*, 1999, **38**, 5788–5794.

85. J. P. Coyle, W. H. Monillas, G. P. a Yap, and S. T. Barry, *Inorg. Chem.*, 2008, **47**, 683–689.

86. A. P. Milanov, T. Toader, H. Parala, D. Barreca, A. Gasparotto, C. Bock, H.-W. Becker, D. K. Ngwashi, R. Cross, S. Paul, U. Kunze, R. a. Fischer, and A. Devi, *Chem. Mater.*, 2009, **21**, 5443–5455.

87. K. Xu, A. P. Milanov, M. Winter, D. Barreca, A. Gasparotto, H.-W. Becker, and A. Devi, *Eur. J. Inorg. Chem.*, 2010, **2010**, 1679–1688.

88. M. Eleter, S. Daniele, V. Brize, C. Dubourdieu, C. Lachaud, N. Blasco, and A. Pinchart, *ECS Trans.*, 2009, **25**, 151–158.

89. A. P. Milanov, R. Bhakta, A. Baunemann, H.-W. Becker, R. Thomas, P. Ehrhart, M. Winter, and A. Devi, *Inorg. Chem.*, 2006, **45**, 11008–11018.

90. A. Milanov, T. Thiede, M. Hellwig, H. Parala, C. Bock, H.-W. Becker, D. K. Ngwashi, R. Cross, S. Paul, U. Kunze, R. A. Fischer, and A. Devi, *ECS Trans.*, 2009, **25**, 143–150.

91. D. Bekermann, D. Barreca, and A. Devi, *ECS Trans.*, 2008, **16**, 235–242.

92. D. Rische, H. Parala, A. Baunemann, T. Thiede, and R. Fischer, *Surf. Coatings Technol.*, 2007, **201**, 9125–9130.

93. D. Rische, H. Parala, and E. Gemel, *Chem. Mater.*, 2006, **18**, 6075–6082.

94. T. B. Thiede, M. Krasnopolski, A. P. Milanov, T. de los Arcos, A. Ney, H.-W. Becker, D. Rogalla, J. Winter, A. Devi, and R. A. Fischer, *Chem. Mater.*, 2011, **23**, 1430–1440.

95. T. Chen, C. Xu, T. H. Baum, G. T. Stauf, J. F. Roeder, A. G. DiPasquale, and A. L. Rheingold, *Chem. Mater.*, 2010, **22**, 27–35.

96. A. P. Milanov, T. B. Thiede, A. Devi, and R. A. Fischer, *J. Am. Chem. Soc.*, 2009, **131**, 17062–17063.

97. C. J. Carmalt, A. C. Newport, S. a O'Neill, I. P. Parkin, A. J. P. White, and D. J. Williams, *Inorg. Chem.*, 2005, **44**, 615–619.

98. S. E. Potts, C. J. Carmalt, C. S. Blackman, F. Abou-Chahine, D. Pugh, and H. O. Davies, *Organometallics*, 2009, **28**, 1838–1844.

99. T. A. George, K. Jones, and M. F. Lappert, *J. Chem. Soc.*, 1965, 2157–2165.

100. M. Brym, M. D. Francis, G. Jin, C. Jones, D. P. Mills, and A. Stasch, *Organometallics*, 2006, **25**, 4799–4807.

101. S. P. Green, C. Jones, K.-A. Lippert, D. P. Mills, and A. Stasch, *Inorg. Chem.*, 2006, **45**, 7242–7251.

102. C. Jones, *Coord. Chem. Rev.*, 2010, **254**, 1273–1289.

103. T. Chlupaty, Z. Padelkova • , F. DeProft, R. Willem, and A. Ruzicka, *Organometallics*, 2012, **31**, 2203–2211.

104. M. R. Hill, A. W. Jones, J. J. Russell, N. K. Roberts, and R. N. Lamb, *J. Mater. Chem.*, 2004, **14**, 3198–3202.

105. K. C. Yang, C. C. Chang, and C. S. Yeh, *Organometallics*, 2001, **20**, 126–137.

106. A. Petrella, H. Deng, N. K. Roberts, and R. N. Lamb, *Chem. Mater.*, 2002, **14**, 4339–4342.

107. A. Belforte, F. Calderazzo, U. Englert, and J. Strahle, *Inorg. Chem.*, 1991, **30**, 3778–3781.

108. G. A. Horley, M. F. Mahon, K. C. Molloy, P. W. Haycock, and C. P. Myers, *Inorg. Chem.*, 2002, **41**, 5052–5058.

109. C. P. Myers, P. W. Haycock, M. Pichot, G. A. Horley, K. C. Molloy, S. A. Rushworth, and L. M. Smith, *Chem. Vapor. Depos.*, 2004, **10**, 35–44.

110. D. D. B. Dell'Amico, F. Calderazzo, L. Labella, F. Marchetti, and G. Pampaloni, *Chem. Rev.*, 2003, **103**, 3857–97.

111. L. Abis, D. Dell'Amico, and F. Calderazzo, *J. Mol. Catal. A-Chem.*, 1996, **108**, L113–L117.

112. A. P. Dove, V. C. Gibson, E. L. Marshall, H. S. Rzepa, A. J. P. White, and D. J. Williams, *J. Am. Chem. Soc.*, 2006, **128**, 9834–9843.

113. A. Jana, H. W. Roesky, C. Schulzke, A. Döring, T. Beck, A. Pal, and R. Herbst-Irmer, *Inorg. Chem.*, 2009, **48**, 193–197.

114. L. Harris, M. Coles, and J. Fulton, *Inorg. Chim. Acta*, 2011, **369**, 97–102.

115. E. C. Y. Tam, N. C. Johnstone, L. Ferro, P. B. Hitchcock, and J. R. Fulton, *Inorg. Chem.*, 2009, **48**, 8971–8976.

116. L. R. Sita, J. R. Babcock, and R. Xi, *J. Am. Chem. Soc.*, 1996, **118**, 10912–10913.

117. Y. Rad'kov and E. Fedorova, *J. Gen. Chem.*, 1986, **56**, 386–389.

118. C. Stewart, D. Dickie, Y. Tang, and R. A. Kemp, *Inorg. Chim. Acta*, 2011, **376**, 73–79.

119. C. A. Stewart, D. A. Dickie, B. Moasser, and R. A. Kemp, *Polyhedron*, 2012, **32**, 14–23.

120. R. Pothiraja, A. P. Milanov, D. Barreca, A. Gasparotto, H.-W. Becker, M. Winter, R. a Fischer, and A. Devi, *Chem. Commun.*, 2009, 1978–80.

121. A. J. Bloodworth and A. G. Davies, *J. Chem. Soc.*, 1965, 5238–5244.

122. A. G. Davies and P. G. Harrison, *J. Chem. Soc. C*, 1967, 1313–1317.

123. P. G. Harrison and J. J. Zuckerman, *J. Chem. Soc. D*, 1969, 321a–321a.

124. A. M. Willcocks, T. Pugh, J. a Hamilton, A. L. Johnson, S. P. Richards, and A. J. Kingsley, *Dalton Trans.*, 2013, **42**, 5554–65.

125. J. R. Babcock and L. R. Sita, *J. Am. Chem. Soc.*, 1998, **120**, 5585–5586.

126. J. R. Babcock, L. Liable-Sands, A. L. Rheingold, and L. R. Sita, *Organometallics*, 1999, **18**, 4437–4441.

127. X. Rimo and L. R. Sita, *Inorg. Chim. Acta*, 1998, **270**, 118–122.

128. A. J. Bloodworth, A. G. Davies, and S. C. Vasishtha, *J. Chem. Soc. C*, 1967, 1309–1313.

129. S. J. Blunden, R. Hill, and J. N. R. Ruddick, *J. Organomet. Chem.*, 1984, **267**, c5–c8.

130. J.-C. Choi, T. Sakakura, and T. Sako, *J. Am. Chem. Soc.*, 1999, **121**, 3793–3794.

131. D. Ballivet-Tkatchenko, O. Douteau, and S. Stutzmann, *Organometallics*, 2000, **19**, 4563–4567.

132. A. M. B. van Mol, Y. Chae, A. H. McDaniel, and M. D. Allendorf, *Thin Solid Films*, 2006, **502**, 72–78.

133. M. D. Allendorf and A. M. B. van Mol, *Top. Organomet. Chem.*, 2005, **9**, 1–48.

134. R. N. Ghoshtagore, *J. Electrochem. Soc.*, 1978, **124**, 110–117.

135. M. D. Allendorf, T. M. Besmann, R. J. Kee, and M. T. Swihart, in *Chemical Vapour Deposition: Precursors, Processes and Applications*, eds. A. C. Jones and M. L. Hitchman, Royal Society of Chemistry, 2009, pp. 93–157.

136. D. Lide, *CRC Handbook of Chemistry and Physics*, CRC Press, Boca Raton, FLA, USA, 90th edn., 2009.

137. A. G. Zawadzki, C. J. Giunta, and R. G. Gordon, *J. Phys. Chem.*, 1992, **96**, 5364–5379.

138. C. J. Giunta, D. A. Strickler, and R. G. Gordon, *J. Phys. Chem.*, 1993, **97**, 2275–2283.

139. N. N. Talaty, K. Beck, H. Citeau, K. Kirschbaum, and D. M. Giolando, *Zeitschrift für Anorg. und Allg. Chemie*, 2009, **635**, 53–63.

140. L. M. Atagi, D. M. Hoffman, J.-R. Liu, Z. Zheng, W.-K. Chu, R. R. Rubiano, R. W. Springer, and D. C. Smith, *Chem. Mater.*, 1994, **6**, 360–361.

141. J. Kane, H. P. Schweizer, and W. Kern, *J. Electrochem. Soc.*, 1975, **122**, 1144–1149.

142. D. J. Houlton, A. C. Jones, P. W. Haycock, E. W. Williams, J. Bull, and G. W. Critchlow, *Chem. Vapor. Depos.*, 1995, **1**, 26–28.

143. S. Mathur, V. Sivakov, H. Shen, S. Barth, C. Cavelius, a. Nilsson, and P. Kuhn, *Thin Solid Films*, 2006, **502**, 88–93.

144. D. J. Teff, C. D. Minear, D. V. Baxter, and K. G. Caulton, *Inorg. Chem.*, 1998, **37**, 2547–2553.

145. Y. Yadava, G. Denicolo, A. Arias, and I. Hummelgen, *Mater. Chem. Phys.*, 1997, **48**, 263–267.

146. F. J. Yusta, M. L. Hitchman, and S. H. Shamlian, *J. Mater. Chem.*, 1997, **7**, 1421–1427.

147. J. Zhao, S. Wu, J. Liu, H. Liu, S. Gong, and D. Zhou, *Sensors Actuators B Chem.*, 2010, **145**, 788–793.

148. M. Maleki and S. M. Rozati, *Bull. Mater. Sci.*, 2013, **36**, 217–221.

149. T. Maruyama and Y. Ikuta, *Sol. Energy Mater. Sol. Cells*, 1992, **28**, 209–215.

150. K.-M. Chi, C.-C. Lin, Y.-H. Lu, and J.-H. Liao, *J. Chinese Chem. Soc.*, 2000, **47**, 425–431.

151. T. Maruyama and K. Tabata, *J. Appl. Phys.*, 1990, **68**, 4282–4285.

152. T. Maruyama and T. Morishita, *Thin Solid Films*, 1994, **251**, 19–22.

153. T. J. Boyle, T. L. Ward, S. M. De'Angeli, H. Xu, and W. F. Hammetter, *Chem. Mater.*, 2003, **15**, 765–775.

154. T. J. Boyle, T. M. Alam, M. A. Rodriguez, and C. A. Zechmann, *Inorg. Chem.*, 2002, **41**, 2574–2582.

155. I. Giebelhaus, R. Müller, W. Tyrra, I. Pantenburg, T. Fischer, and S. Mathur, *Inorg. Chim. Acta*, 2011, **372**, 340–346.

156. T. Ishida, O. Tabata, J. Il Park, S. H. Shin, H. Magara, S. Tamura, S. Mochizuki, and T. Mihara, *Thin Solid Films*, 1996, **281-282**, 228–231.

157. H. L. Ma, D. H. Zhang, S. Z. Win, S. Y. Li, and Y. P. Chen, *Sol. Energy Mater. Sol. Cells*, 1996, **40**, 371–380.

158. K. H. Yoon and J. S. Song, *Sol. Energy Mater. Sol. Cells*, 1993, **28**, 317–327.

159. J. Proscia and R. G. Gordon, *Thin Solid Films*, 1992, **214**, 175–187.

160. J. E. Stanley, A. C. Swain, K. C. Molloy, D. W. H. Rankin, H. E. Robertson, B. F. Johnston, and M. F. Mahon, *Appl. Organomet. Chem.*, 2005, **19**, 644–657.

161. S. Suh, Z. Zhang, W.-K. Chu, and D. M. Hoffman, *Thin Solid Films*, 1999, **345**, 240–243.

162. J. E. Stanley, A. C. Swain, K. C. Molloy, D. W. H. Rankin, H. E. Robertson, B. F. Johnston, and M. F. Mahon, *Appl. Organomet. Chem.*, 2005, **19**, 658–671.

163. S. Suh, D. M. Hoffman, L. M. Atagi, D. C. Smith, J.-R. Liu, and W.-K. Chu, *Chem. Mater.*, 1997, **9**, 730–735.

164. K. C. Molloy and J. E. Stanley, *Appl. Organomet. Chem.*, 2009, **23**, 62–67.

165. I. Barbul, A. L. Johnson, G. Kociok-Köhn, K. C. Molloy, C. Silvestru, and A. L. Sudlow, *ChemPlusChem*, 2013, **78**, 866–874.

166. P. O'Brien, J. Walsh, and I. Watson, *J. Chem. Soc., Dalton Trans.*, 1996, 2491–2496.

167. S. Dowland, T. Lutz, A. Ward, S. P. King, A. Sudlow, M. S. Hill, K. C. Molloy, and S. A. Haque, *Adv. Mater.*, 2011, **23**, 2739–2744.

168. H. C. Leventis, S. P. King, A. Sudlow, M. S. Hill, K. C. Molloy, and S. A. Haque, *Nano Lett.*, 2010, **10**, 1253–1258.

169. N. Alam, M. S. Hill, G. Kociok-Köhn, M. Zeller, M. Mazhar, and K. C. Molloy, *Chem. Mater.*, 2008, **20**, 6157–6162.

170. J. M. Clark, G. Kociok-Köhn, N. J. Harnett, M. S. Hill, R. Hill, K. C. Molloy, H. Saponia, D. Stanton, and A. Sudlow, *Dalton Trans.*, 2011, **40**, 6893–6900.

171. K. Ramasamy, V. L. Kuznetsov, K. Gopal, M. A. Malik, J. Raftery, P. P. Edwards, and P. O'Brien, *Chem. Mater.*, 2013, **25**, 266–276.

172. A. V. Lee and L. L. Schafer, *Eur. J. Inorg. Chem.*, 2007, **2007**, 2245–2255.

173. G. Chandra, A. D. Jenkins, M. F. Lappert, and R. C. Srivastava, *J. Chem. Soc. A*, 1970, 2550–2559.

174. M. F. Lappert and A. Sanger, *J. Chem. Soc. A*, 1971, 1314–1320.

175. P. Foley and M. Zeldin, *Inorg. Chem.*, 1975, **14**, 2264–2267.

176. M. M. Olmstead and P. P. Power, *Inorg. Chem.*, 1984, **23**, 413–415.

177. T. Chlupatý, Z. Padělková, A. Lyčka, J. Brus, and A. Růžička, *Dalton Trans.*, 2012, **41**, 5010–5019.

178. S. R. Foley, Y. Zhou, G. P. A. Yap, and D. S. Richeson, *Inorg. Chem.*, 2000, **39**, 924–929.

179. C. Jones, S. J. Bonyhady, N. Holzmann, G. Frenking, and A. Stasch, *Inorg. Chem.*, 2011, **50**, 12315–12325.

180. N. Nimitsiriwat, V. C. Gibson, E. L. Marshall, A. J. P. White, S. H. Dale, and M. R. J. Elsegood, *Dalton Trans.*, 2007, 4464–4471.

181. D. C. Leitch, J. D. Beard, R. K. Thomson, V. A. Wright, B. O. Patrick, and L. L. Schafer, *Eur. J. Inorg. Chem.*, 2009, **2009**, 2691–2701.

182. J. Ruiz, V. Rodríguez, C. Vicente, J. Pérez, G. López, P. a Chaloner, and P. B. Hitchcock, *Inorg. Chim. Acta*, 2003, **351**, 114–118.

183. J. Barroso-Flores and J. A. Cogordan, *J. Organomet. Chem.*, 2006, **691**, 4937–4944.

184. L. Sangaletti and L. Depero, *J. Mater. Res.*, 1998, 2457–2460.

185. R. S. Katiyar, P. Dawson, M. M. Hargreave, and R. Wilkinson, G, *J. Phys. C*, 1971, **4**, 2421–2431.

186. K.-C. Kim, D.-H. Lee, and S. Maeng, *Mater. Lett.*, 2012, **86**, 119–121.

187. L. Y. Liang, Z. M. Liu, H. T. Cao, and X. Q. Pan, *ACS Appl. Mater. Interfaces*, 2010, **2**, 1060–1065.

188. B. Kumar, D. Lee, and S. Kim, *J. Phys. Chem. C*, 2010, 11050–11055.

189. F. Izumi, *J. Solid State Chem.*, 1981, **38**, 381–385.

190. A. Patterson, *Phys. Rev.*, 1939, **56**, 978–982.

191. J. Themlin, M. Chtaïb, L. Henrard, P. Lambin, J. Darville, and J.-M. Gilles, *Phys. Rev. B*, 1992, **46**, 2460–2466.

192. E. Amberger and M.-R. Kula, *Angew. Chemie Int. Ed.*, 1963, **2**, 395–395.

193. E. Amberger and M. R. Kula, *Chem. Ber.*, 1963, **96**, 2562–2565.

194. P. R. Deacon, M. F. Mahon, K. C. Molloy, and P. C. Waterfield, *J. Chem. Soc., Dalton Trans.*, 1997, 3705–3712.

195. P. F. R. Ewings and P. G. Harrison, *J. Chem. Soc., Dalton Trans.*, 1975, 2015–2017.

196. P. F. R. Ewings and P. G. Harrison, *J. Chem. Soc., Dalton Trans.*, 1975, 1717–1721.

197. P. F. R. Ewings, P. G. Harrison, and D. E. Fenton, *J. Chem. Soc., Dalton Trans.*, 1975, 821–826.

198. P. F. R. Ewings, D. E. Fenton, and P. G. Harrison, *Inorg. Nucl. Chem. Lett.*, 1974, **10**, 43–45.

199. J. S. Morrison and H. M. Haendler, *J. Inorg. Nucl. Chem.*, 1967, **29**, 393–400.

200. P. G. Harrison, *J. Chem. Soc., Chem. Commun.*, 1972, 544–544.

201. S. Suh and D. Hoffman, *Inorg. Chem.*, 1996, **35**, 6164–6169.

202. M. Veith and F. Toellner, *J. Organomet. Chem.*, 1983, **246**, 219–226.

203. T. Fjeldberg, P. B. Hitchcock, M. F. Lappert, S. J. Smith, and A. J. Thorne, *J. Chem. Soc., Chem. Commun.*, 1985, **2**, 939–941.

204. M. Veith, P. Hobein, and R. Roesler, *Z. Naturforsch. B. Chem. Sci.*, 1989, **44**, 1067–1081.

205. M. Veith, C. Belot, V. Huch, and M. Zimmer, *Zeitschrift für Anorg. und Allg. Chemie*, 2009, **635**, 942–948.

206. B. Cetinkaya, I. Gumrukcu, M. F. Lappert, J. L. Atwood, and R. Shakir, *J. Am. Chem. Soc.*, 1980, **102**, 2088–2089.

207. C. Stanciu, A. F. Richards, M. Stender, M. M. Olmstead, and P. P. Power, *Polyhedron*, 2006, **25**, 477–483.

208. D. A. Dickie, I. S. MacIntosh, D. D. Ino, Q. He, O. A. Labeodan, M. C. Jennings, G. Schatte, C. J. Walsby, and J. A. C. Clyburne, *Can. J. Chem.*, 2008, **86**, 20–31.

209. T. J. Boyle, T. Q. Doan, L. A. M. Steele, C. Apblett, S. M. Hoppe, K. Hawthorne, R. M. Kalinich, and W. M. Sigmund, *Dalton Trans.*, 2012, **41**, 9349–64.

210. D. M. Barnhart, D. L. Clark, and J. G. Watkin, *Acta Crystallogr. Sect. C Cryst. Struct. Commun.*, 1994, **50**, 702–704.

211. D. Schaeffer Jr, C and J. J. Zuckerman, *J. Am. Chem. Soc.*, 1974, **96**, 7160–7162.

212. D. H. Harris and M. F. Lappert, *J. Chem. Soc., Chem. Commun.*, 1974, 895–896.

213. O. G. Shirobokov, S. I. Gorelsky, R. Simionescu, L. G. Kuzmina, and G. I. Nikonov, *Chem. Commun.*, 2010, **46**, 7831–7833.

214. L. Ferro, P. B. Hitchcock, and M. P. Coles, *Inorg. Chem.*, 2011, **50**, 1879–1888.

215. A. L. Sudlow, PhD Thesis, University of Bath, 2012.

216. T. J. King, P. G. Harrison, and P. F. R. Ewings, *J. Chem. Soc., Dalton Trans.*, 1976, 1399–1403.

217. E. R. T. Tiekink, *Appl. Organomet. Chem.*, 2008, **22**, 533–550.

218. K. McGuire, Z. W. Pan, Z. L. Wang, D. Milkie, J. Menéndez, and A. M. Rao, *J. Nanosci. Nanotechnol.*, 2002, **2**, 499–502.

219. A. M. Willcocks, T. P. Robinson, C. Roche, T. Pugh, S. P. Richards, A. J. Kingsley, J. P. Lowe, and A. L. Johnson, *Inorg. Chem.*, 2012, **51**, 246–257.

220. Z. Otwinowski and W. Minor, in *Methods in Enzymology: Macro-molecular Crystallography, Part A*, eds. C. W. Carter and R. M. Sweet Jr, Elsevier, New Y~~r~~ork, 1997, vol. 276, pp. 1307–1326.

221. A. M. B. van Mol, J. P. A. M. Driessen, J. L. Linden, M. H. J. M. de Croon, C. I. M. A. Spee, and J. C. Schouten, *Chem. Vapor. Depos.*, 2001, 7, 101–104.

A2. Appendix 2

A2.1 Vapour pressure measurements

Vapour pressure data were obtained for compounds **3**, **5**, **7**, **LXXXII**, **15**, **16** and **17** through collaboration with SAFC HiTech. Vapour pressure measurements were carried out using a TGA apparatus using a process developed by SAFC HiTech. The precise method has not been disclosed however the process relies on measuring the vapour pressure through several back to back isothermal analyses on the same sample. The measurements are repeated on fresh samples until consistent data are obtained. The data have a correction factor applied to them derived from a standard which is determined from non-TGA vapour pressure measurements. The accuracy of the vapour pressure data determined using this method is affected by the standard used and how relevant it is to the precursor, SAFC Hitech used the best available standard based on the data they had on the compound.

The Clausius-Clapeyron equation is used to express vapour pressure as a function of temperature; this can be used to calculate the latent heat of vapourisation or latent heat of sublimation for the compound. The measurements were made using a TGA based method that relies on approximations and therefore is unsuitable for this calculation. Extrapolation of a plot of logP vs 1/T can be utilised to produce a vapour pressure equation (equation 5) which allows the correlation between pressure and temperature to be calculated at different points along the graph so that optimum pressures or temperatures can be determined. The vapour pressure equation contains the pressure (P - Torr), temperature (T-Kelvin) and two constants *a* and *b* which are compound dependent. For compound **3** the constants for *a* and *b* were found to be -3666 ± 11.69 and 9.8 ± 0.03 respectively. These constants allow the vapour pressure or temperature to be estimated to fit the conditions expected for the deposition.

$$\log_{10} P = -\frac{a}{T} + b \qquad (5)$$

In Table A1.1 the calculated vapour pressures for several compounds are shown alongside the upper and lower 95% confidence figures calculated using regression analysis in Excel 2010. The huge variation in calculated vapour pressure for many of the compounds highlights the uncertainty in this method of calculating the vapour pressure.

Table A2.1: Results of vapour pressure calculations

	Pressure calculated at 50 °C using:		
Compound	**Calculated constants**	**lower 95%**	**upper 95%**
3	0.03	0.02	0.04
5	0.02	0.00	34448.64
7	0.08	0.00	126.61
LXXXII	0.09	0.00	27.21
15	0.76	0.00	5266.91
16	0.06	0.00	145.79
17	0.06	0.00	81393910343400.70

The vapour pressure curves for the compounds are shown below including a short discussion.

A2.1.1 Vapour pressure information for compound 3

The TGA data for compound **3** contained a residual mass much lower than that expected for tin metal, which suggests the compound has some degree of volatility. In Figure A2.1 the vapour pressure curves for three different samples of compound **3** are shown. The vapour pressure data shows a good correlation between samples with the only significant deviation observed for sample one at 110°C.

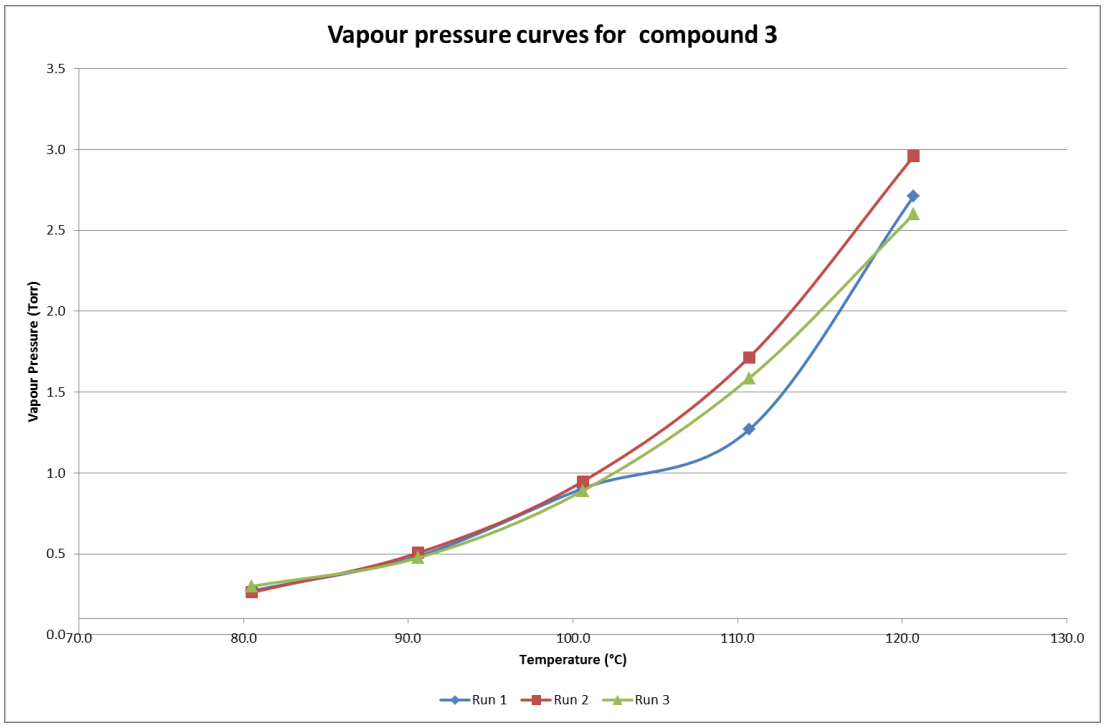

Figure A2.1: Vapour pressure data for compound 3.

Although the vapour pressure of **3** is not particularly good, the observation of a vapour pressure in excess of 1 Torr at 100 °C indicates it could provide suitable volatility in an LPCVD process. The vapour pressures of some common tin oxide CVD precursors, alongside the vapour pressure for compound **3** at 90°C are shown in Table A1.2. The vapour pressures of these compounds are significantly higher than that observed for compound **3** highlighting their applicability in atmospheric pressure CVD depositions.

Table A2.2: Vapour pressures at 90 °C for a selection of conventional tin oxide precursors.

Compound	Vapour Pressure (Torr) at 90 °C	Reference
Dimethyltin dichloride	11.04	[221]
Tin tetrachloride	343.13	[221]
Tetramethyltin	347.18	[221]
Monomethyltin trichloride	39.89	[221]
Trimethyltin chloride	7.60	[221]
Monobutyltin trichloride	4.39	[221]
3	0.491	This work

A2.1.2 Vapour pressure measurements of tin(II) alkoxides

Encouraged by the thermal analysis of compounds **5**, **7** and **LXXXII** samples were also subjected to vapour pressure measurements by SAFC Hi-tech. These can be seen in Figures A2.2-A2.4.

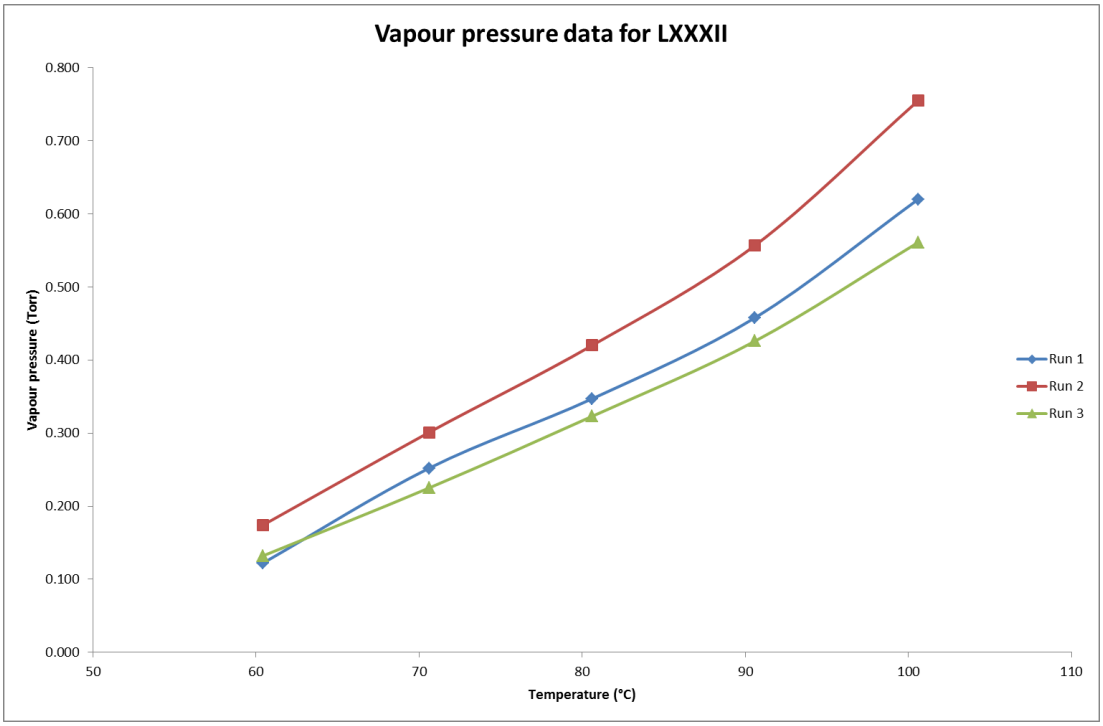

Figure A2.1: Vapour pressure measurements for compound LXXXII

The TGA data for compound **LXXXII** contained a residual mass much lower than that expected for tin metal, which suggests the compound has some degree of volatility. In Figure 2.2 the vapour pressure curves for three different samples of compound **LXXXII** are shown. The vapour pressure data shows a good correlation between samples with all three showing a similar pattern with the volatility beginning to increase above 90°C. The average vapour pressure at 90°C for **LXXXII** is 0.48 Torr, this is comparable to that observed for compound **3** in Table A2.1, which had a vapour pressure of 0.49 at 90 °C. These are much lower than the vapour pressures observed for conventional tin oxide precursors detailed in Table 2.2.

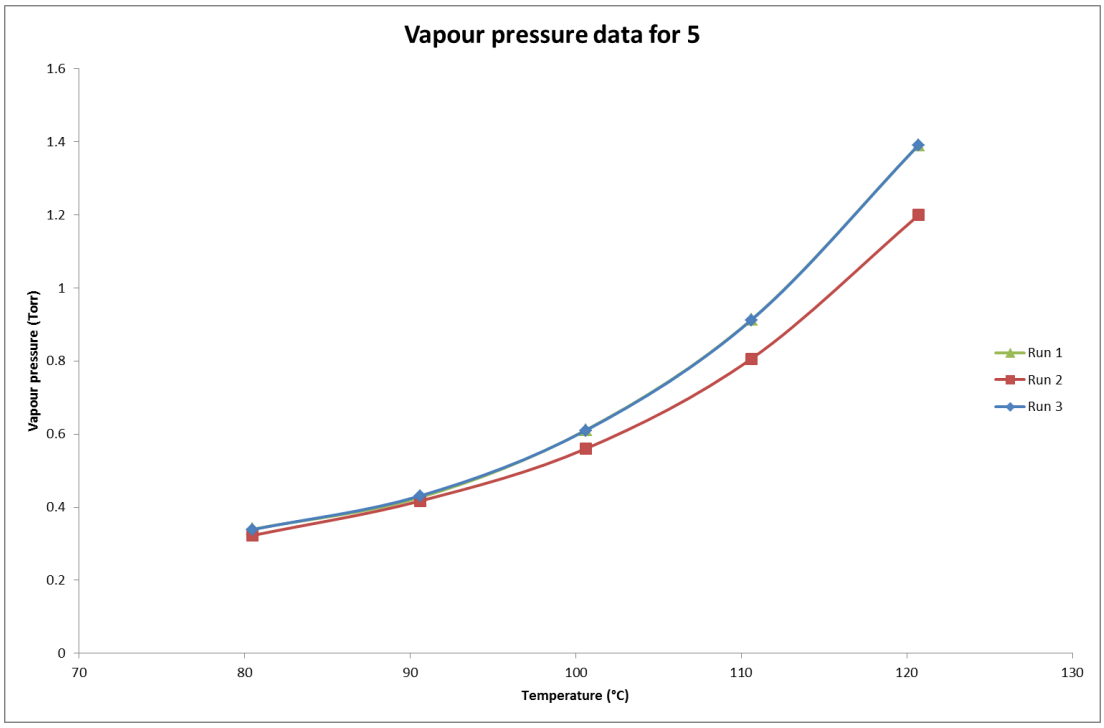

Figure A2.2: Vapour pressure data for compound 5

For compound **5** the vapour pressure data for the three samples analysed are consistent with runs one and three transposed on top of each other as shown in Figure A2.3. The exponential increase in volatility is more noticeable in this sample compared to the vapour pressure date for **LXXXII**. The average vapour pressure for compound **5** was found to be 0.43 Torr; this is lower than the vapour pressures observed for **LXXXII** and **3**. The lower volatility could be attributed to the nuclearity of the material; compound **5** was found to be polymeric, while **LXXXII** is dimeric in both solid and gas phase analyses,[203] therefore more bonds could require breaking to volatilise **5**.

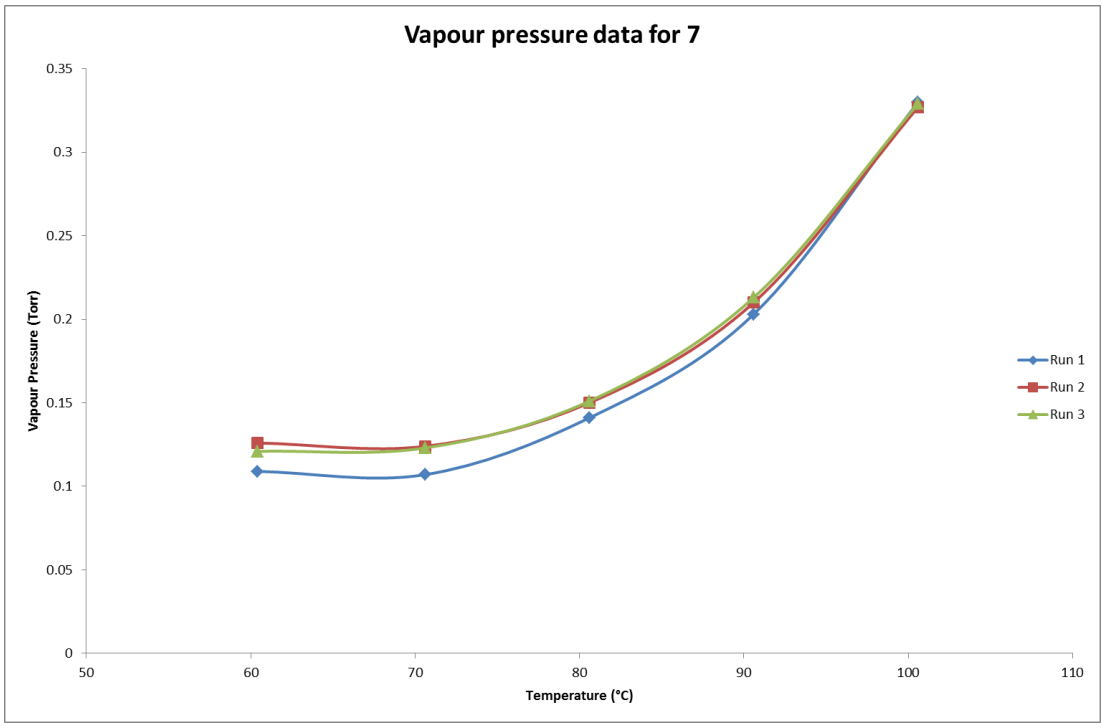

Figure A2.3: Vapour pressure data for compound 7

The vapour pressure data for compound **7** is presented in Figure A2.4; the data presented shows a similar level of consistency across the three samples as was observed for compound **5** with runs two and three particularly similar. The average vapour pressure for compound **7** at 90°C is much lower than that observed for the other tin(II) alkoxides analysed in this chapter, measuring just 0.20 Torr. Solution based analysis of compound **7** indicated that the compound had a similar tin environment to **LXXXII**, as a solid state structure could not be determined the exact nature of the tin environment is not known. The lower vapour pressure observed for **7** may be attributed to the additional CH_2 group situated on the alkyl chain. This allows the CH_3 unit to be further removed from the tin centre and offers increased rotation and flexibility; increasing these parameters may result in increased intermolecular interactions through hydrogen bonding increasing the energy required to enter the gas phase.

A2.1.3 Evaluation of compounds 15-17 as potential CVD precursors by vapour pressure measurements

Compounds **15-17** were also subjected to vapour pressure measurements to give a greater insight into the volatility of the precursors. The vapour pressure measurements were carried out by collaborators at SAFC HiTech and the resultant curves can be observed in Figures A2.5-A2.7.

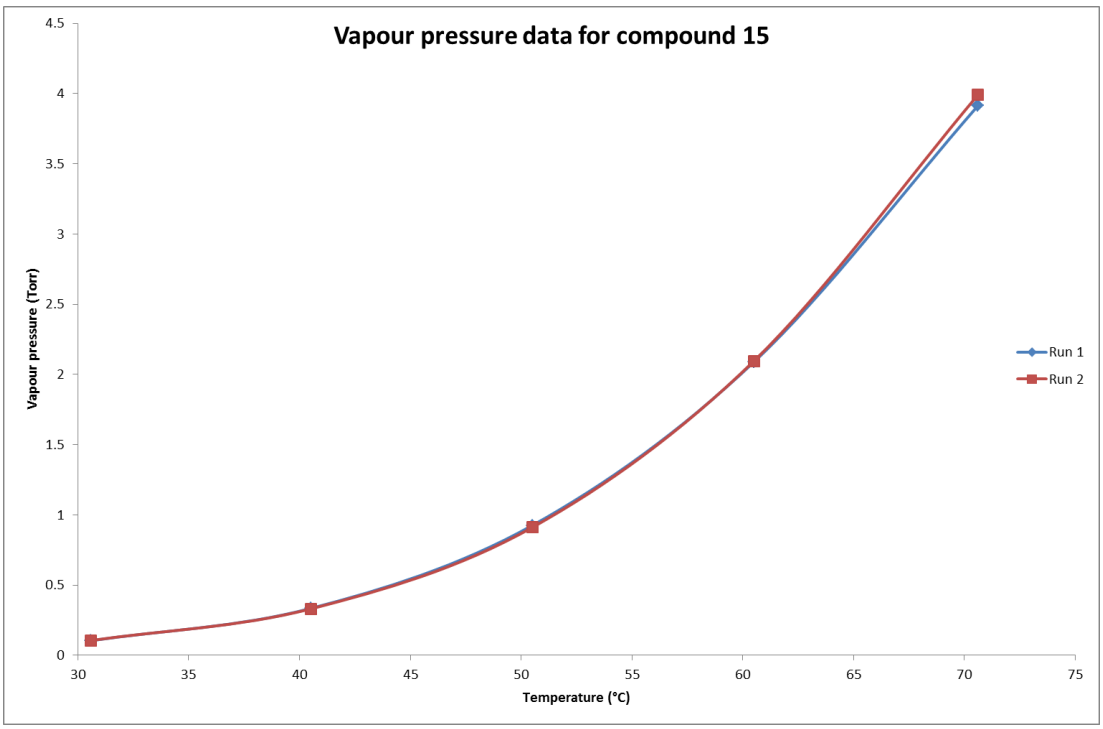

Figure A2.4: Vapour pressure data for compound 15

The vapour pressure data for compound **15** are shown above in Figure A2.5; the precursor shows a good level of volatility with a vapour pressure of 3.9 Torr at 70 °C. The TGA data for compound **15** showed a final mass of 33% which is close to that calculated for SnO_2 (34.8%). Based on this information the compound was expected to show limited volatility, therefore this observed vapour pressure is unexpected. Further comparison of the TGA and vapour pressure data does show that the material loses mass from 55°C (Figure 4.24) and therefore this could have an effect on the vapour pressure data.

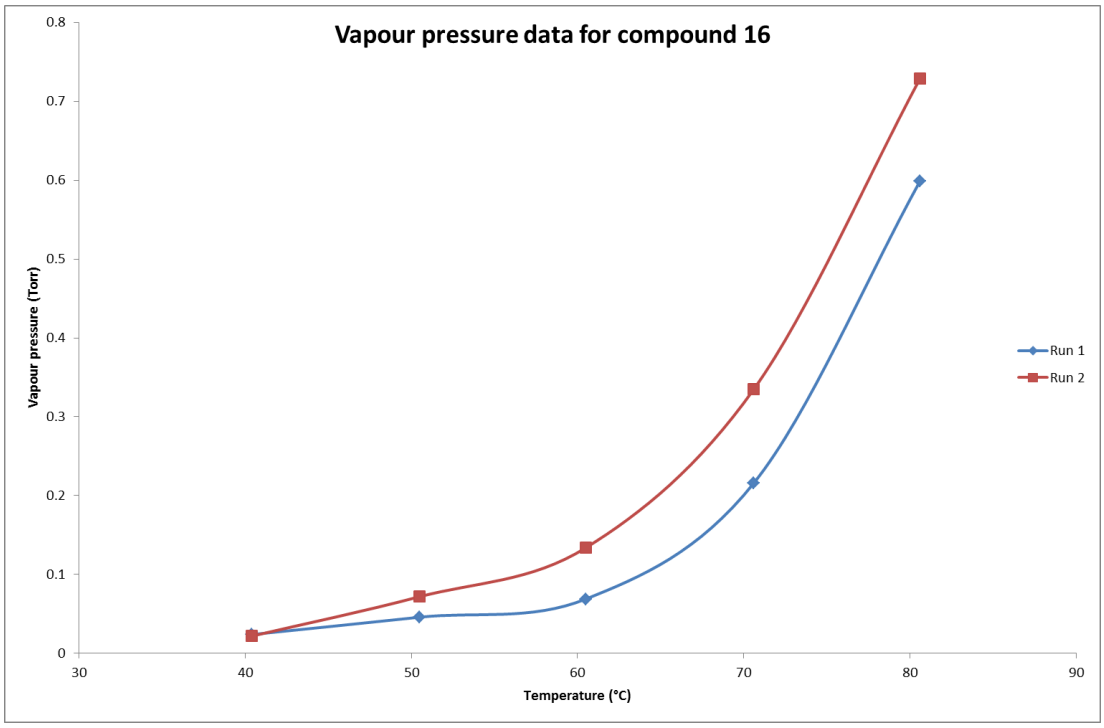

Figure A2.5: Vapour pressure data for compound 16

The vapour pressure data for compound **16** is shown above in Figure A2.6; the two runs show the same comparable changes in pressure as the temperature increases, although run 1 displayed partial pressures approximately 0.05 Torr lower than run 2 from 60 °C. The data show that compound **16** has limited volatility compared to previous tin oxide precursors published in the literature (Table A2.2), with a pressure of 0.2-0.3 Torr at 70 °C.

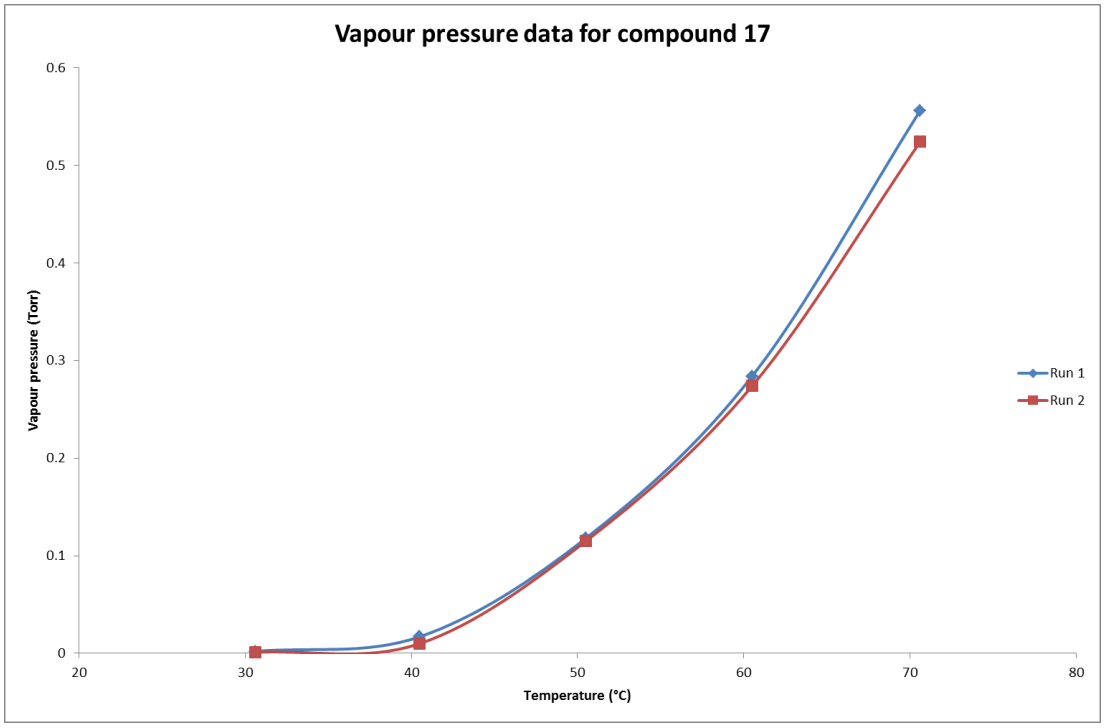

Figure A2.6: Vapour pressure data for compound 17

The vapour pressure data for compound **17** are shown in Figure A2.7; the two runs show good correlation throughout the temperature range assessed, however the vapour pressure data for compound **17** suggests the compound has a poor volatility with a pressure of 0.5 Torr observed at 70 °C. The vapour pressures for compounds **16** and **17** are similar with compound **16** approximately 0.2 Torr lower at 70 °C. This similarity was expected as the compounds have a similar chemical composition, with compound **17** having a CH_3 group replacing the proton on the ^{i}Pr moiety of the iso-carbamate backbone.

Comparison of the vapour pressure data for compounds **15**, **16**, and **17** indicates that compound **15** has the highest vapour pressure at 60 °C with a measured pressure of 2 Torr, much higher than the pressures recorded for **16** and **17** at 0.1 and 0.28 Torr respectively. When compared to the other precursors evaluated within this thesis compound **15** has the highest vapour pressure of all the compounds assessed at 60 °C with compounds **3**, **5**, **7** and **LXXXII** all exhibiting pressures below 0.2 Torr at this temperature. Further to this the vapour pressure of compound **15** is also greater than dimethyltin dichloride (1.1 Torr), trimethyltin chloride (1.4 Torr) and butyltin trichloride (0.8 Torr),[221] these results suggest the compound could have significant use in atmospheric pressure deposition as well as low pressure deposition processes.